The human toll of NIH's 'China initiative' pp. 1171 & 1180

Oxytocin and ancestral empathy pp. 1186 & 1232

Synthesis of soapbark tree vaccine adjuvants pp. 1187 & 1252

Science

$15
24 MARCH 2023
science.org
AAAS

MICROSPHERES

Multiple metal-carbide sheets pack into spherical shapes

pp. 1189 & 1242



VISIT…

LANZAROTE Caliente.com

NOMIS & Science
YOUNG EXPLORER AWARD 2023

Research at the intersection of the social and life sciences

Unconventional. Interdisciplinary. Bold.

The **NOMIS & *Science* Young Explorer Award** recognizes and rewards early-career M.D., Ph.D., or M.D./Ph.D. scientists that perform research at the intersection of the social and life sciences. Essays written by these bold researchers on their recent work are judged for clarity, scientific quality, creativity, and demonstration of cross-disciplinary approaches to address fundamental questions.

A cash prize of up to USD 15,000 will be awarded to essay winners, and their engaging essays will be published in *Science*. Winners will also be invited to share their work and forward-looking perspective with leading scientists in their respective fields at an award ceremony.

Apply by May 15, 2023

at www.science.org/nomis

NOMIS FOUNDATION
Creating the Spark

Science
AAAS


OPEN ACCESS
Pushing the Boundaries of Knowledge
As AAAS's first multidisciplinary, open access journal, Science Advances publishes research that reflects the selectivity of high impact, innovative research you expect from the Science family of journals, published in an open access format to serve a vast and growing global audience. Check out the latest findings or learn how to submit your research: science.org/journal/sciadv
Science Advances
AAAS
GOLD OPEN ACCESS, DIGITAL, AND FREE TO ALL READERS

NEWS FROM Science | AAAS

Subscribe to **News from Science** for unlimited access to authoritative, up-to-the-minute news on research and science policy.



bit.ly/NewsFromScience

Indiana University O'Neill School of Public and Environmental Affairs is proud to announce the inaugural recipient of the **Ron Hites Prize in Environmental Science.**



Congratulations to **Dr. Alessandra Cincinelli**, associate professor in the Department of Chemistry at the University of Florence and leading researcher in environmental science and analytic chemistry focusing on the measurement of legacy compounds and emerging contaminants.

The Ron Hites Prize in Environmental Science recognizes those whose work is having a transformative impact on environmental science and has contributed to solving complex environmental challenges. Nominations for future awards may be made at go.iu.edu/4LKJ by December 31, 2023.

O'NEILL
SCHOOL OF PUBLIC AND ENVIRONMENTAL AFFAIRS
Indiana University

CONTENTS

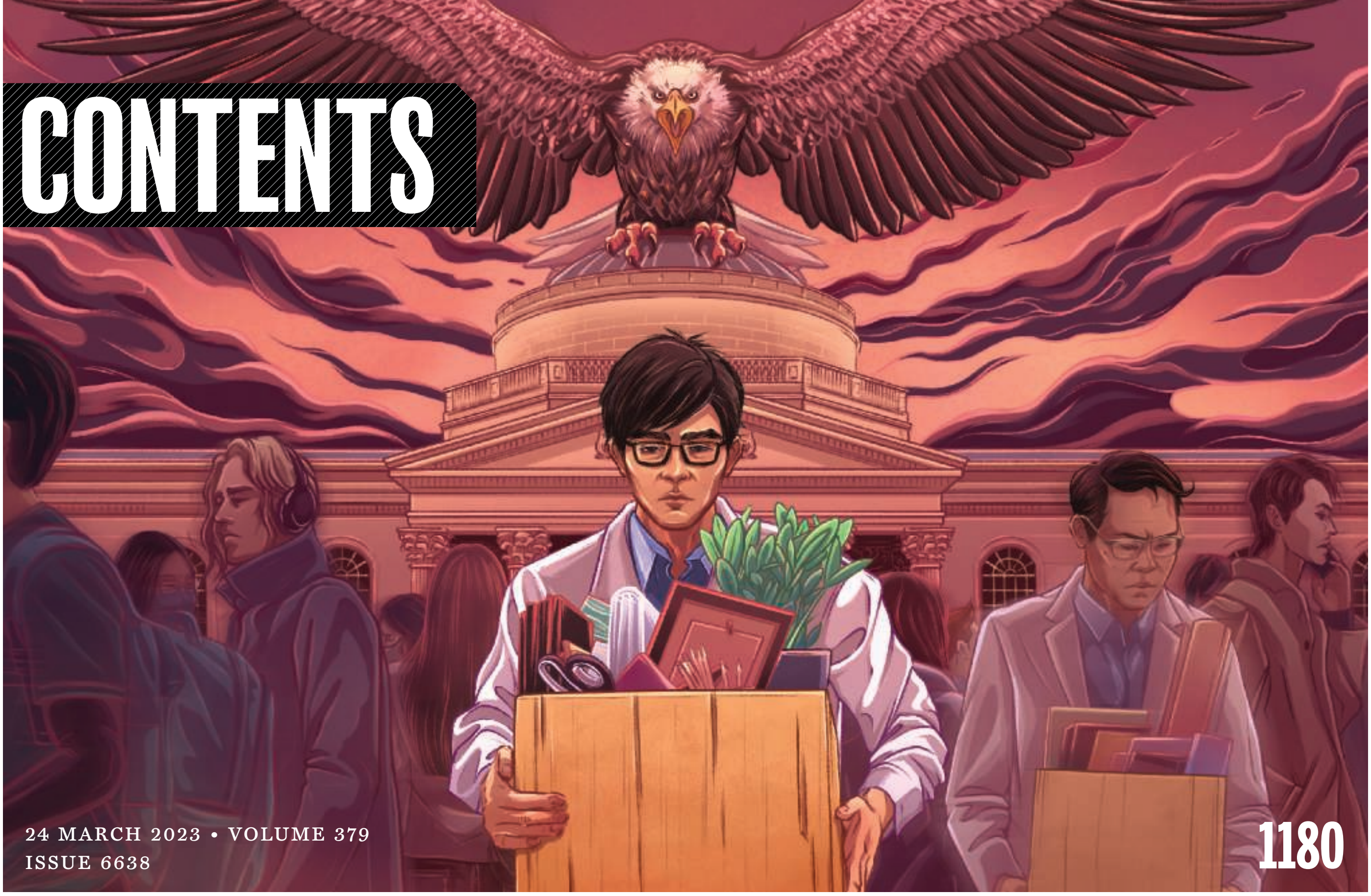


ILLUSTRATION: JASON LYON

NEWS

IN BRIEF

1172 News at a glance

IN DEPTH

1174 New Long Covid cases decline with Omicron
Virus biology, widespread vaccination may be driving down risk of persistent symptoms
By J. Couzin-Frankel

1175 New clues to pandemic's origin surface, causing uproar
Genetic sequences from Wuhan market may point to animal that spread SARS-CoV-2, but data remain hidden *By J. Cohen*

1176 A call for change at storied physics lab
Energy department opens new competition to run struggling Fermilab *By A. Cho*

1178 China's research enterprise undergoes shake-up
Revamp aims to respond to U.S. challenge and promote "self-reliance" in science *By D. Normile*

1179 Earth may face higher risk of catastrophic asteroid strikes
Sizes of geologically recent impact craters revised upward with sharper satellite imagery
By P. Voosen
PODCAST

FEATURES

1180 Pall of suspicion
The National Institutes of Health's "China initiative" has upended hundreds of lives and destroyed scores of academic careers
By J. Mervis
EDITORIAL p. 1171

INSIGHTS

PERSPECTIVES

1186 The spread of fear in an empathetic fish
An evolutionarily ancient signaling pathway mediates emotional contagion
By R. S. DeAngelis and H. A. Hofmann
RESEARCH ARTICLE p. 1232

1187 A booster for vaccines from plants
Reconstituting a plant biosynthetic pathway enables a sustainable supply of vaccine adjuvants
By H. H. Chubatsu Nunes and T.-T. T. Dang
RESEARCH ARTICLE p. 1252

1189 A direct and clean route to MXenes
New, scalable methods synthesize two-dimensional carbide and nitride materials
By D. D. Robertson and S. H. Tolbert
RESEARCH ARTICLE p. 1242

1190 Four-dimensional optics using time-varying metamaterials
Optical platforms using material parameters that change with time have diverse applications *By N. Engheta*

POLICY FORUM

1192 A global approach for natural history museum collections
Integration of the world's natural history collections can provide a resource for decision-makers *By K. R. Johnson* et al.

BOOKS *ET AL.*

1195 College towns as talent hubs
Communities can leverage institutions of higher education to lure knowledge workers to new regions *By J. Wai*

1196 Seeing fast and thinking slow
A philosopher explores perception and cognition *By C. Firestone and I. Phillips*

LETTERS

1197 Beyond protected areas for koala conservation
By B. A. Williams et al.

1198 Storylistening's role in policy advice
By P. Calow

1198 Response
By C. Craig and S. Dillon

RESEARCH

IN BRIEF

1201 From *Science* and other journals

RESEARCH ARTICLES

1204 Plant science
A Gγ protein regulates alkaline sensitivity in crops *H. Zhang* et al.
RESEARCH ARTICLE SUMMARY; FOR FULL TEXT: DOI.ORG/10.1126/SCIENCE.ADE8416

1205 Venus
Surface changes observed on a Venusian volcano during the Magellan mission
R. R. Herrick and S. Hensley

1209 Molecular biology
Structure and mechanism of the plant RNA polymerase V *G. Xie* et al.

1214 Kondo insulators
Visualizing the atomic-scale origin of metallic behavior in Kondo insulators *H. Pirie* et al.

1218 Ferroelectrics
Ferroelectricity in layered bismuth oxide down to 1 nanometer *Q. Yang* et al.

1225 3D porous materials
Programming 3D curved mesosurfaces using microlattice designs
X. Cheng et al.



1225
Finite element view, with color representation of height, of an ant



1238
A white-tailed jackrabbit in its white winter pelage

1232 Comparative emotion
Evolutionarily conserved role of oxytocin in social fear contagion in zebrafish
I. Akinrinade et al.
PERSPECTIVE p. 1186

1238 Climate adaptation
The evolution of white-tailed jackrabbit camouflage in response to past and future seasonal climates
M. S. Ferreira et al.

1242 Nanomaterials
Direct synthesis and chemical vapor deposition of 2D carbide and nitride MXenes *D. Wang* et al.
PERSPECTIVE p. 1189

1248 3D printing
A silicone-based support material eliminates interfacial instabilities in 3D silicone printing *S. Duraivel* et al.

1252 Plant science
Elucidation of the pathway for biosynthesis of saponin adjuvants from the soapbark tree *J. Reed* et al.
PERSPECTIVE p. 1187; PODCAST

DEPARTMENTS

1171 Editorial
Eroding trust and collaboration *By H. H. Thorp*
NEWS STORY p. 1180

1266 Working Life
Embrace compassion *By J. Larsen*

ON THE COVER

This color-enhanced scanning electron microscopy image shows Ti_2CCl_2 MXenes grown by chemical vapor deposition. The two-dimensional layers of this material grew perpendicular to the substrate and then folded into microspherical structures. Ion intercalation between two-dimensional MXene sheets has potential for energy storage and other applications. See pages 1189 and 1242.
Image: D. Wang et al., Science ***379***, *1242 (2023)*



Science Staff 1170
Science Careers 1265

SCIENCE (ISSN 0036-8075) is published weekly on Friday, except last week in December, by the American Association for the Advancement of Science, 1200 New York Avenue, NW, Washington, DC 20005. Periodicals mail postage (publication No. 484460) paid at Washington, DC, and additional mailing offices. Copyright © 2023 by the American Association for the Advancement of Science. The title SCIENCE is a registered trademark of the AAAS. Domestic individual membership, including subscription (12 months): $165 ($74 allocated to subscription). Domestic institutional subscription (51 issues): $2411; Foreign postage extra: Air assist delivery: $107. First class, airmail, student, and emeritus rates on request. Canadian rates with GST available upon request, GST #125488122. Publications Mail Agreement Number 1069624. **Printed in the U.S.A.**
Change of address: Allow 4 weeks, giving old and new addresses and 8-digit account number. **Postmaster:** Send change of address to AAAS, P.O. Box 96178, Washington, DC 20090–6178. **Single-copy sales:** $15 each plus shipping and handling available from backissues.science.org; bulk rate on request. **Authorization to reproduce** material for internal or personal use under circumstances not falling within the fair use provisions of the Copyright Act can be obtained through the Copyright Clearance Center (CCC), www.copyright.com. The identification code for *Science* is 0036-8075. *Science* is indexed in the *Reader's Guide to Periodical Literature* and in several specialized indexes.

CREDITS (FROM TOP TO BOTTOM): AMEDIO CORTESE; YIHUI ZHANG

Science AAAS

Editor-in-Chief Holden Thorp, hthorp@aaas.org

Executive Editor Valda Vinson

Editor, Research Jake S. Yeston **Editor, Insights** Lisa D. Chong **Managing Editor** Lauren Kmec

DEPUTY EDITORS Gemma Alderton (UK),Stella M. Hurtley (UK), Phillip D. Szuromi, Sacha Vignieri **SR. EDITORS** Caroline Ash (UK), Michael A. Funk, Brent Grocholski, Di Jiang, Priscilla N. Kelly, Marc S. Lavine (Canada), Mattia Maroso, Yevgeniya Nusinovich, Ian S. Osborne (UK), L. Bryan Ray, Seth Thomas Scanlon (UK), H. Jesse Smith, Keith T. Smith (UK), Jelena Stajic, Peter Stern (UK), Valerie B. Thompson, Brad Wible **ASSOCIATE EDITORS** Bianca Lopez, Madeleine Seale (UK), Corinne Simonti, Yury V. Suleymanov, Ekeoma Uzogara **LETTERS EDITOR** Jennifer Sills **LEAD CONTENT PRODUCTION EDITORS** Chris Filiatreau, Harry Jach **SR. CONTENT PRODUCTION EDITOR** Amelia Beyna **CONTENT PRODUCTION EDITORS** Robert French, Julia Haber-Katris, Nida Masiulis, Abigail Shashikanth, Suzanne M. White **SR. EDITORIAL MANAGERS** Carolyn Kyle, Beverly Shields **SR. PROGRAM ASSOCIATE** Maryrose Madrid **EDITORIAL ASSOCIATE** Joi S. Granger **SR. EDITORIAL COORDINATORS** Aneera Dobbins, Jeffrey Hearn, Lisa Johnson, Jerry Richardson, Alice Whaley (UK), Anita Wynn **EDITORIAL COORDINATORS** Maura Byrne, Clair Goodhead (UK), Alexander Kief, Ronmel Navas, Isabel Schnaidt, Qiyam Stewart, Brian White **RESEARCH & DATA ANALYST** Jessica L. Slater **ADMINISTRATIVE COORDINATOR** Karalee P. Rogers **ASI DIRECTOR, OPERATIONS** Janet Clements (UK) **ASI OFFICE MANAGER** Victoria Smith **ASI SR. OFFICE ADMINISTRATORS** Dawn Titheridge (UK), Jessica Waldock (UK)

News Editor Tim Appenzeller

NEWS MANAGING EDITOR John Travis **INTERNATIONAL EDITOR** David Malakoff **DEPUTY NEWS EDITORS** Rachel Bernstein, Shraddha Chakradhar, Elizabeth Culotta, Martin Enserink, Lila Guterman, David Grimm, Eric Hand (Europe) **SR. CORRESPONDENTS** Daniel Clery (UK), Jon Cohen, Jeffrey Mervis, Elizabeth Pennisi **ASSOCIATE EDITORS** Jeffrey Brainard, Michael Price, Kelly Servick **NEWS REPORTERS** Adrian Cho, Jennifer Couzin-Frankel, Jocelyn Kaiser, Rodrigo Pérez Ortega (Mexico City), Robert F. Service, Erik Stokstad, Paul Voosen, Meredith Wadman **CONTRIBUTING CORRESPONDENTS** Warren Cornwall, Andrew Curry (Berlin), Ann Gibbons, Sam Kean, Eli Kintisch, Kai Kupferschmidt (Berlin), Andrew Lawler, Mitch Leslie, Eliot Marshall, Virginia Morell, Dennis Normile (Tokyo), Elisabeth Pain (Careers), Charles Piller, Gabriel Popkin, Michael Price, Joshua Sokol, Richard Stone, Emily Underwood, Gretchen Vogel (Berlin), Lizzie Wade (Mexico City) **CAREERS** Katie Langin (Associate Editor) **COPY EDITORS** Julia Cole (Senior Copy Editor), Morgan Everett, Cyra Master (Copy Chief) **ADMINISTRATIVE SUPPORT** Meagan Weiland

Creative Director Beth Rakouskas

DESIGN MANAGING EDITOR Chrystal Smith **GRAPHICS MANAGING EDITOR** Chris Bickel **PHOTOGRAPHY MANAGING EDITOR** Emily Petersen **MULTIMEDIA MANAGING PRODUCER** Kevin McLean **WEB CONTENT STRATEGY MANAGER** Kara Estelle-Powers **DESIGN EDITOR** Marcy Atarod **SCIENTIFIC ILLUSTRATORS** Austin Fisher, Kellie Holoski, Ashley Mastin **SENIOR GRAPHICS SPECIALISTS** Holly Bishop, Nathalie Cary **GRAPHICS EDITOR** Drew An-Pham **SENIOR PHOTO EDITOR** Charles Borst **PHOTO EDITOR** Elizabeth Billman **SENIOR PODCAST PRODUCER** Sarah Crespi **VIDEO PRODUCER** Meagan Cantwell **SOCIAL MEDIA STRATEGIST** Jessica Hubbard **SOCIAL MEDIA PRODUCER** Sabrina Jenkins **WEB DESIGNER** Jennie Pajerowski

Chief Executive Officer and Executive Publisher Sudip Parikh

Publisher, Science Family of Journals Bill Moran

DIRECTOR, BUSINESS SYSTEMS AND FINANCIAL ANALYSIS Randy Yi **DIRECTOR, BUSINESS OPERATIONS & ANALYSIS** Eric Knott **MANAGER, BUSINESS OPERATIONS** Jessica Tierney **MANAGER, BUSINESS ANALYSIS** Cory Lipman **MANAGER, WEB ANALYTICS** Samantha Cressman **BUSINESS ANALYSTS** Kurt Ennis, Maggie Clark **FINANCIAL ANALYST** Isacco Fusi **BUSINESS OPERATIONS ADMINISTRATOR** Taylor Fisher **SENIOR PRODUCTION MANAGER** Jason Hillman **SENIOR MANAGER, PUBLISHING AND CONTENT SYSTEMS** Marcus Spiegler **CONTENT OPERATIONS MANAGER** Rebecca Doshi **SENIOR CONTENT & PUBLISHING SYSTEMS SPECIALIST** Jacob Hedrick **SENIOR PRODUCTION SPECIALIST** Kristin Wowk **PRODUCTION SPECIALISTS** Kelsey Cartelli, Audrey Diggs **DIGITAL PRODUCTION MANAGER** Lisa Stanford **SENIOR DIGITAL ADVERTISING SPECIALIST** Kimberley Oster **ADVERTISING PRODUCTION OPERATIONS MANAGER** Deborah Tompkins **DESIGNER, CUSTOM PUBLISHING** Jeremy Huntsinger **SR. TRAFFIC ASSOCIATE** Christine Hall **SPECIAL PROJECTS ASSOCIATE** Sarah Dhere

ASSOCIATE DIRECTOR, BUSINESS DEVELOPMENT Justin Sawyers **GLOBAL MARKETING MANAGER** Allison Pritchard **DIGITAL MARKETING MANAGER** Aimee Aponte **JOURNALS MARKETING MANAGER** Shawana Arnold **MARKETING ASSOCIATES** Ashley Hylton, Mike Romano, Lorena Chirinos Rodriguez, Jenna Voris **SENIOR DESIGNER** Kim Huynh

DIRECTOR AND SENIOR EDITOR, CUSTOM PUBLISHING Erika Gebel Berg **ASSISTANT EDITOR, CUSTOM PUBLISHING** Jackie Oberst **PROJECT MANAGER** Melissa Collins

DIRECTOR, PRODUCT & PUBLISHING DEVELOPMENT Chris Reid **DIRECTOR, BUSINESS STRATEGY AND PORTFOLIO MANAGEMENT** Sarah Whalen **DIRECTOR, PRODUCT MANAGMENT** Kris Bishop **PRODUCT DEVELOPMENT MANAGER** Scott Chernoff **SR. PRODUCT ASSOCIATE** Robert Koepke **PRODUCT ASSOCIATES** Caroline Breul, Anne Mason

ASSOCIATE DIRECTOR, INSTITUTIONAL LICENSING MARKETING Kess Knight **BUSINESS DEVELOPMENT MANAGER** Rasmus Andersen **ASSOCIATE DIRECTOR, INSTITUTIONAL LICENSING SALES** Ryan Rexroth **INSTITUTIONAL LICENSING MANAGER** Marco Castellan, Claudia Paulsen-Young **SENIOR MANAGER, INSTITUTIONAL LICENSING OPERATIONS** Judy Lillibridge **SENIOR OPERATIONS ANALYST** Lana Guz **SYSTEMS & OPERATIONS ANALYST** Ben Teincuff **FULFILLMENT ANALYST** Aminta Reyes

ASSOCIATE DIRECTOR, US ADVERTISING Stephanie O'Connor **US MID WEST, MID ATLANTIC AND SOUTH EAST SALES** Chris Hoag **US WEST COAST SALES** Lynne Stickrod **ASSOCIATE DIRECTOR, ROW** Roger Goncalves **SALES REP, ROW** Sarah Lelarge **SALES ADMIN ASSISTANT, ROW** Victoria Glasbey **DIRECTOR OF GLOBAL COLLABORATION AND ACADEMIC PUBLISHING RELATIONS, ASIA** Xiaoying Chu **ASSOCIATE DIRECTOR, INTERNATIONAL COLLABORATION** Grace Yao **SALES MANAGER** Danny Zhao **MARKETING MANAGER** Kilo Lan **ASCA CORPORATION, JAPAN** Rie Rambelli (Tokyo), Miyuki Tani (Osaka)

DIRECTOR, COPYRIGHT, LICENSING AND SPECIAL PROJECTS Emilie David **RIGHTS AND PERMISSIONS ASSOCIATE** Elizabeth Sandler **LICENSING ASSOCIATE** Virginia Warren **RIGHTS AND LICENSING COORDINATOR** Dana James **CONTRACT SUPPORT SPECIALIST** Michael Wheeler

MAIN HEADQUARTERS
Science/AAAS
1200 New York Ave. NW
Washington, DC 20005

SCIENCE INTERNATIONAL
Clarendon House
Clarendon Road
Cambridge, CB2 8FH, UK

SCIENCE CHINA
Room 1004, Culture Square
No. 59 Zhongguancun St.
Haidian District, Beijing, 100872

SCIENCE JAPAN
ASCA Corporation
Sibaura TY Bldg. 4F, 1-14-5
Shibaura Minato-ku
Tokyo, 108-0073 Japan

EDITORIAL
science_editors@aaas.org

NEWS
science_news@aaas.org

INFORMATION FOR AUTHORS
science.org/authors/science-information-authors

REPRINTS AND PERMISSIONS
science.org/help/reprints-and-permissions

MEDIA CONTACTS
scipak@aaas.org

MULTIMEDIA CONTACTS
SciencePodcast@aaas.org
ScienceVideo@aaas.org

INSTITUTIONAL SALES AND SITE LICENSES
science.org/librarian

PRODUCT ADVERTISING & CUSTOM PUBLISHING
advertising.science.org/products-services
science_advertising@aaas.org

CLASSIFIED ADVERTISING
advertising.science.org/science-careers
advertise@sciencecareers.org

JOB POSTING CUSTOMER SERVICE
employers.sciencecareers.org
support@sciencecareers.org

MEMBERSHIP AND INDIVIDUAL SUBSCRIPTIONS
science.org/subscriptions

MEMBER BENEFITS
aaas.org/membership/benefits

AAAS BOARD OF DIRECTORS
CHAIR Susan G. Amara
PRESIDENT Gilda A. Barabino
PRESIDENT-ELECT Keith Yamamoto
TREASURER Carolyn N. Ainslie
CHIEF EXECUTIVE OFFICER Sudip Parikh
BOARD Cynthia M. Beall
Ann Bostrom
Janine Austin Clayton
Kaye Husbands Fealing
Maria M. Klawe
Jane Maienschein
Robert B. Millard
Babak Parviz
William D. Provine
Juan S. Ramírez Lugo
Susan M. Rosenberg

Science serves as a forum for discussion of important issues related to the advancement of science by publishing material on which a consensus has been reached as well as including the presentation of minority or conflicting points of view. Accordingly, all articles published in *Science*—including editorials, news and comment, and book reviews—are signed and reflect the individual views of the authors and not official points of view adopted by AAAS or the institutions with which the authors are affiliated.

BOARD OF REVIEWING EDITORS (Statistics board members indicated with **S**)

Erin Adams, *U. of Chicago*
Takuzo Aida, *U. of Tokyo*
Leslie Aiello, *Wenner-Gren Fdn.*
Deji Akinwande, *UT Austin*
Judith Allen, *U. of Manchester*
Marcella Alsan, *Harvard U.*
James Analytis, *UC Berkeley*
Paola Arlotta, *Harvard U.*
Delia Baldassarri, *NYU*
Nenad Ban, *ETH Zürich*
Christopher Barratt, *U. of Dundee*
Nandita Basu, *U. of Waterloo*
Franz Bauer, *Pontificia U. Católica de Chile*
Ray H. Baughman, *UT Dallas*
Carlo Beenakker, *Leiden U.*
Yasmine Belkaid, *NIAID, NIH*
Philip Benfey, *Duke U.*
Kiros T. Berhane, *Columbia U.*
Joseph J. Berry, *NREL*
Alessandra Biffi, *Harvard Med.*
Chris Bowler, *École Normale Supérieure*
Ian Boyd, *U. of St. Andrews*
Malcolm Brenner, *Baylor Coll. of Med.*
Emily Brodsky, *UC Santa Cruz*
Ron Brookmeyer, *UCLA* (**S**)
Christian Büchel, *UKE Hamburg*
Dennis Burton, *Scripps Res.*
Carter Tribley Butts, *UC Irvine*
Johannes Buchner, *TUM*
György Buzsáki, *NYU School of Med.*
Mariana Byndloss, *Vanderbilt U. Med. Ctr.*
Annmarie Carlton, *UC Irvine*
Simon Cauchemez, *Inst. Pasteur*
Ling-Ling Chen, *SIBCB, CAS*
Wendy Cho, *UIUC*
Ib Chorkendorff, *Denmark TU*
Chunaram Choudhary, *Københavns U.*
Karlene Cimprich, *Stanford U.*
Laura Colgin, *UT Austin*
James J. Collins, *MIT*
Robert Cook-Deegan, *Arizona State U.*
Virginia Cornish, *Columbia U.*
Carolyn Coyne, *Duke U.*
Roberta Croce, *VU Amsterdam*
Christina Curtis, *Stanford U.*
Ismaila Dabo, *Penn State U.*
Jeff L. Dangl, *UNC*
Nicolas Dauphas, *U. of Chicago*
Frans de Waal, *Emory U.*
Claude Desplan, *NYU*
Sandra Díaz, *U. Nacional de Córdoba*
Samuel Díaz-Muñoz, *UC Davis*
Ulrike Diebold, *TU Wien*
Stefanie Dimmeler, *Goethe-U. Frankfurt*
Hong Ding, *Inst. of Physics, CAS*
Dennis Discher, *UPenn*
Jennifer A. Doudna, *UC Berkeley*
Ruth Drdla-Schutting, *Med. U. Vienna*
Raissa M. D'Souza, *UC Davis*
Bruce Dunn, *UCLA*
William Dunphy, *Caltech*
Scott Edwards, *Harvard U.*
Todd Ehlers, *U. of Tübingen*
Nader Engheta, *UPenn*
Karen Ersche, *U. of Cambridge*
Beate Escher, *UFZ & U. of Tübingen*
Barry Everitt, *U. of Cambridge*
Vanessa Ezenwa, *U. of Georgia*
Toren Finkel, *U. of Pitt. Med. Ctr.*
Natascha Förster Schreiber, *MPI Extraterrestrial Phys.*
Peter Fratzl, *MPI Potsdam*
Elaine Fuchs, *Rockefeller U.*
Caixia Gao, *Inst. of Genetics and Developmental Bio., CAS*
Daniel Geschwind, *UCLA*
Lindsey Gilson, *U. of Cape Town*
Ramon Gonzalez, *U. of South Florida*
Gillian Griffiths, *U. of Cambridge*
Nicolas Gruber, *ETH Zürich*
Hua Guo, *U. of New Mexico*
Taekjip Ha, *Johns Hopkins U.*
Daniel Haber, *Mass. General Hos.*
Sharon Hammes-Schiffer, *Yale U.*
Wolf-Dietrich Hardt, *ETH Zürich*
Louise Harra, *UCL*
Kelley Harris, *U. of Wash*
Carl-Philipp Heisenberg, *IST Austria*
Janet G. Hering, *Eawag*
Christoph Hess, *U. of Basel & U. of Cambridge*
Heather Hickman, *NIAID, NIH*
Hans Hilgenkamp, *U. of Twente*
Janneke Hille Ris Lambers, *ETH Zürich*
Kai-Uwe Hinrichs, *U. of Bremen*
Deirdre Hollingsworth, *U. of Oxford*
Randall Hulet, *Rice U.*
Auke Ijspeert, *EPFL*
Gwyneth Ingram, *ENS Lyon*
Darrell Irvine, *MIT*
Akiko Iwasaki, *Yale U.*
Stephen Jackson, *USGS & U. of Arizona*
Erich Jarvis, *Rockefeller U.*
Peter Jonas, *IST Austria*
Johanna Joyce, *U. de Lausanne*
Matt Kaeberlein, *U. of Wash.*
William Kaelin Jr., *Dana-Farber*
Daniel Kammen, *UC Berkeley*
Kisuk Kang, *Seoul Nat. U.*
V. Narry Kim, *Seoul Nat. U.*
Nancy Knowlton, *Smithsonian*
Etienne Koechlin, *École Normale Supérieure*
Alex L. Kolodkin, *Johns Hopkins U.*
LaShanda Korley, *U. of Delaware*
Paul Kubes, *U. of Calgary*
Chris Kuzawa, *Northwestern U.*
Laura Lackner, *Northwestern U.*
Gabriel Lander, *Scripps Res.* (**S**)
Mitchell A. Lazar, *UPenn*
Hedwig Lee, *Duke U.*
Ryan Lively, *Georgia Tech*
Luis Liz-Marzán, *CIC biomaGUNE*
Omar Lizardo, *UCLA*
Jonathan Losos, *WUSTL*
Ke Lu, *Inst. of Metal Res., CAS*
Christian Lüscher, *U. of Geneva*
Jean Lynch-Stieglitz, *Georgia Tech*
David Lyons, *U. of Edinburgh*
Fabienne Mackay, *QIMR Berghofer*
Zeynep Madak-Erdogan, *UIUC*
Vidya Madhavan, *UIUC*
Anne Magurran, *U. of St. Andrews*
Ari Pekka Mähönen, *U. of Helsinki*
Asifa Majid, *U. of Oxford*
Oscar Marín, *King's Coll. London*
Charles Marshall, *UC Berkeley*
Christopher Marx, *U. of Idaho*
David Masopust, *U. of Minnesota*
Geraldine Masson, *CNRS*
Rodrigo Medellín, *U. Nacional Autónoma de México*
C. Jessica Metcalf, *Princeton U.*
Tom Misteli, *NCI, NIH*
Jeffery Molkentin, *Cincinnati Children's Hospital Medical Center*
Alison Motsinger-Reif, *NIEHS, NIH* (**S**)
Danielle Navarro, *U. of New South Wales*
Daniel Nettle, *Newcastle U.*
Daniel Neumark, *UC Berkeley*
Thi Hoang Duong Nguyen, *MRC LMB*
Beatriz Noheda, *U. of Groningen*
Helga Nowotny, *Vienna Sci. & Tech. Fund*
Pilar Ossorio, *U. of Wisconsin*
Andrew Oswald, *U. of Warwick*
Isabella Pagano, *Istituto Nazionale di Astrofisica*
Elizabeth Levy Paluck, *Princeton U.*
Giovanni Parmigiani, *Dana-Farber* (**S**)
Daniel Pauly, *U. of British Columbia*
Ana Pêgo, *U. do Porto*
Julie Pfeiffer, *UT Southwestern Med. Ctr.*
Philip Phillips, *UIUC*
Matthieu Piel, *Inst. Curie*
Kathrin Plath, *UCLA*
Martin Plenio, *Ulm U.*
Katherine Pollard, *UCSF*
Elvira Poloczanska, *Alfred-Wegener-Inst.*
Julia Pongratz, *Ludwig Maximilians U.*
Philippe Poulin, *CNRS*
Lei Stanley Qi, *Stanford U.*
Trevor Robbins, *U. of Cambridge*
Joeri Rogelj, *Imperial Coll. London*
Amy Rosenzweig, *Northwestern U.*
John Rubenstein, *SickKids*
Mike Ryan, *UT Austin*
Miquel Salmeron, *Lawrence Berkeley Nat. Lab*
Nitin Samarth, *Penn State U.*
Erica Ollmann Saphire, *La Jolla Inst.*
Joachim Saur, *U. zu Köln*
Alexander Schier, *Harvard U.*
Wolfram Schlenker, *Columbia U.*
Susannah Scott, *UC Santa Barbara*
Anuj Shah, *U. of Chicago*
Vladimir Shalaev, *Purdue U.*
Jie Shan, *Cornell U.*
Beth Shapiro, *UC Santa Cruz*
Jay Shendure, *U. of Wash.*
Steve Sherwood, *U. of New South Wales*
Brian Shoichet, *UCSF*
Robert Siliciano, *JHU School of Med.*
Lucia Sivilotti, *UCL*
Emma Slack, *ETH Zürich & U. of Oxford*
Richard Smith, *UNC* (**S**)
John Speakman, *U. of Aberdeen*
Allan C. Spradling, *Carnegie Institution for Sci.*
V. S. Subrahmanian, *Northwestern U.*
Eriko Takano, *U. of Manchester*
A. Alec Talin, *Sandia Natl. Labs*
Patrick Tan, *Duke-NUS Med. School*
Sarah Teichmann, *Wellcome Sanger Inst.*
Rocio Titiunik, *Princeton U.*
Shubha Tole, *Tata Inst. of Fundamental Res.*
Maria-Elena Torres Padilla, *Helmholtz Zentrum München*
Kimani Toussaint, *Brown U.*
Barbara Treutlein, *ETH Zürich*
Jason Tylianakis, *U. of Canterbury*
Wim van der Putten, *Netherlands Inst. of Ecology*
Matthew Vander Heiden, *MIT*
Ivo Vankelecom, *KU Leuven*
Judith Varner, *UC San Diego*
Henrique Veiga-Fernandes, *Champalimaud Fdn.*
Reinhilde Veugelers, *KU Leuven*
Bert Vogelstein, *Johns Hopkins U.*
Julia Von Blume, *Yale School of Med.*
David Wallach, *Weizmann Inst.*
Jane-Ling Wang, *UC Davis* (**S**)
Jessica Ware, *Amer. Mus. of Natural Hist.*
David Waxman, *Fudan U.*
Alex Webb, *U. of Cambridge*
Chris Wikle, *U. of Missouri* (**S**)
Terrie Williams, *UC Santa Cruz*
Ian A. Wilson, *Scripps Res.* (**S**)
Hao Wu, *Harvard U.*
Li Wu, *Tsinghua U.*
Wei Xie, *Tsinghua U.*
Amir Yacoby, *Harvard U.*
Benjamin Youngblood, *St. Jude*
Yu Xie, *Princeton U.*
Jan Zaanen, *Leiden U.*
Kenneth Zaret, *UPenn School of Med.*
Lidong Zhao, *Beihang U.*
Bing Zhu, *Inst. of Biophysics, CAS*
Xiaowei Zhuang, *Harvard U.*
Maria Zuber, *MIT*

EDITORIAL

Eroding trust and collaboration



H. Holden Thorp
Editor-in-Chief, *Science* journals.
hthorp@aaas.org; @hholdenthorp

It wasn't that long ago when scientific collaboration between the United States and China was enthusiastically encouraged as a means to accomplish the best science. American universities established campuses in China, set up exchange programs for students and trainees, and hired highly productive Chinese researchers. That all changed in 2018, when then-President Trump launched the China Initiative to rid US academia of Chinese spies. As reporter Jeffrey Mervis describes in this issue of *Science*, the National Institutes of Health (NIH)—the largest federal funder of biomedical research—vigorously responded to this charge. The agency's allegations and investigations have not only destroyed careers but also eroded trust in the agency and federal government across the scientific community.

This is probably not how Michael Lauer wants to be remembered. As the deputy director for extramural research at NIH, he probably hoped he'd be known for the many good things he's helped facilitate, particularly the substantial increases in funding during his tenure. But history is not always kind. Lauer has been heavy-handed with regard to policing foreign influence from China, allowing the agency to engage in secretive hardball to target researchers who receive NIH support and who are affiliated with Chinese collaborators.

"The…allegations… have not only destroyed careers but also eroded trust…"

Of course, Congress and the NIH get to set the rules of engagement, but the rules changed abruptly and without warning, with no allowance for the fact that researchers had been doing what they were previously encouraged to do, and with absolutely no acknowledgment of the likely repercussions. Chinese-born researchers working in the United States had competed successfully for federal funding for decades. So, it's reasonable for them and their colleagues to wonder why the rug has been pulled out from under them and to ask what has so suddenly changed. When pressed publicly for details, the NIH and the institutions have given legalistic responses that provide little reassurance.

It's hard not to conclude that the answer to what changed is Donald Trump's term as president along with the rise in power of conservative members of Congress bent on reviving the dark spirit of McCarthyism, with China substituted for the Soviet Union. The result was threatening letters from Lauer and a complete change in tone from the institutions. As Mervis's story shows, since 2018, 100 institutions have received letters concerning 246 faculty members, most of them Asian and most working with Chinese collaborators. Altogether, 103 have been forced out, and many more have been enjoined from receiving NIH funds, which is almost always a career killer. Because the letters contain language portraying these scientists as being "unwelcome in the NIH ecosystem," very few institutions in the United States will hire them.

Is it possible that all of the nefarious activities implied by these actions were real? Sure. As Lauer told *Science*, "The fact that more than 60% of these cases have resulted in an employment separation, or a university taking the step of excluding a scientist from [seeking an NIH grant] for a significant period of time, means that something really, really serious has occurred." But if true, did it suddenly begin in 2018 when Lauer started sending his letters? Doubtful. If it's real now, it's been real for a while. The NIH has not given adequate answers as to why this all started so abruptly.

Given the statements that Lauer has made in his letters, it's no wonder the institutions have clammed up. But they owe their faculty, students, trainees, and staff an explanation as well. As Mervis describes, everyone who has asked about the firing of the outstanding researcher Yue Xiong at the University of North Carolina at Chapel Hill (where I used to be the chancellor) has been ghosted by the administration. Has the national security apparatus demanded administrators' silence? Or is it the need for institutions to maintain their good standing with NIH?

The institutions and the NIH need to resolve this. Given the information available in the public domain, the scientific community could easily conclude that this is a xenophobic program to harm Chinese scientists and cut off international scientific cooperation. The federal government needs to figure out a way to let the NIH and the institutions reassure the community that this is all worth it.

–H. Holden Thorp

PHOTO: CAMERON DAVIDSON

10.1126/science.adh8832

NEWS

2364 Reports of babesiosis, a severe tickborne disease, across 10 U.S. states in 2019—double the number in 2011, perhaps because ticks are thriving in a warming climate.

IN BRIEF

Edited by **Michael Price**



PUBLIC HEALTH

Next-gen bed nets get go-ahead

A new type of malaria-fighting bed net received a major endorsement from the World Health Organization (WHO) last week. The net combines two chemicals to more effectively kill the mosquitoes that transmit the parasite behind malaria, a disease that killed an estimated 619,000 people in 2022, most of them young children in sub-Saharan Africa. Insecticide-treated bed nets have helped drive malaria rates down dramatically. But in recent years, resistance to the insecticide used to treat nets, pyrethroid, has been spreading. That has contributed to the rebound of malaria in many places. The new nets are treated with pyrethroid and a second chemical called chlorfenapyr. It is a relatively new insecticide that targets the insects' muscles, preventing them from moving. The new nets are more expensive, but two large studies found the extra killing power seems to pay off, reducing the incidence of malaria in children by nearly half compared with pyrethroid-only nets. That prompted WHO on 14 March to strongly recommend their use in regions where pyrethroid resistance has spread.

Insecticide-treated bed nets are a key tool in the fight against malaria.

PHOTO: YASUYOSHI CHIBA/AFP/GETTY IMAGES

Polio cases tied to new vaccine

VACCINES | The Global Polio Eradication Initiative (GPEI) reported last week that seven African children, six in the Democratic Republic of the Congo and one in Burundi, were recently paralyzed by strains of poliovirus derived from a new version of the Albert Sabin© live oral polio vaccine. These are the first cases linked to the vaccine, novel oral polio vaccine type 2 (nOPV2), which has been genetically tweaked to avoid just this problem. Vaccine-derived strains can arise in places where vaccination rates are low and the weakened vaccine virus can keep spreading person to person and revert to its paralytic form. Since nOPV2 was rolled out 2 years ago, GPEI has administered almost 600 million doses in response to outbreaks in 28 countries. Experts say these reversions, though disappointing, seem to be extremely rare, and the vaccine appears much more genetically stable than its predecessor. The new cases, they add, underscore the need to boost vaccine coverage in order to head off such reversions in the first place.

Planting trees for papers

PUBLISHING | The Company of Biologists, a nonprofit publisher, has a new, green plan to acknowledge the contributions of authors and peer reviewers: Over 2 years starting from January, it will plant a tree for each peer review and each paper it publishes. The idea came from Steven Kelly, a plant biologist at the University of Oxford and editor-in-chief of *Open Biology*, one of the organization's five journals. The publisher will use £80,000 of its endowment to plant a new forest intended for environmental education. Approximately 3750 new trees will be planted on a former mining site outside Nottingham, England. The funds will also support restoration of 12 hectares at an ancient forest called Great Knott Wood. About 260 papers so far appear as trees in a virtual forest online. The publisher will begin to acknowledge trees planted for peer reviews next month.

Biden OKs COVID-19 data release

COVID-19 | U.S. intelligence agencies must declassify information related to China's Wuhan Institute of Virology (WIV) and the origin of the COVID-19 pandemic within 90 days, according to a bill signed into law on 20 March by President Joe Biden. Both chambers of Congress passed the declassification bill with strong bipartisan support. WIV has received intense scrutiny thanks to its long history of working with bat coronaviruses, including a distant cousin of SARS-CoV-2, the cause of the pandemic. Some suspect WIV accidentally released the virus, perhaps after engineering a strain from bats to be more infectious in humans. U.S. intelligence agencies have delivered conflicting assessments on that possibility, but released little of the data behind their conclusions. The law asks for details about WIV researchers who allegedly became sick with a respiratory illness in the fall of 2019, before a COVID-19 outbreak clearly surfaced in Wuhan in December.

S. Korea, Japan reup science ties

DIPLOMACY | In 2019, a long-running dispute over compensation claims for World War II–era forced labor ruptured ties between Japan and South Korea. Now, the two countries appear to be on the cusp of resuming cooperation on science and technology projects. In a sign of thawing relations, South Korean President Yoon Suk Yeol last week met Japanese Prime Minister Fumio Kishida for the two countries' first top-level summit in a decade. Just before the meeting, Park Yun-kyu, vice minister of South Korea's science ministry, announced Seoul is "considering expanding cooperation [with Japan in] artificial intelligence, 5G and 6G wireless networks, space satellites, and quantum technologies." Park said working-level talks will set the stage for a later ministerial meeting, though he did not set a schedule.



The weedy sea dragon population has fallen by about half.

PHOTO: GARY BELL/OCEANWIDE/MINDEN PICTURES

CONSERVATION

Australia's coastal species decline

More than half of the marine species along Australia's shallow coral and rocky reefs are suffering, in part because of warming oceans, according to a new study. Researchers analyzed more than a decade's worth of population data on more than 1000 species of fish, seaweeds, and invertebrates. Between 2008 and 2021, 57% of the species declined, with almost one-third of them losing 30% of their population, the team reports in *Nature*. That puts many species in the "threatened" category; 28 species declined so much they now fall into the "critically endangered" category. One example is an iconic native seahorse called the weedy sea dragon (*Phyllopteryx taeniolatus*, pictured), whose numbers fell by 59%. Species in temperate regions suffered more than those in tropical areas, particularly in years following heat waves. In cool areas, warming temperatures also brought tropical invaders.

Health hints in Beethoven's hair

GENETICS | Composer Ludwig van Beethoven had troubled health, including hearing loss, gastrointestinal problems, and liver disease. He asked that scientists study his body after he died in hopes of finding the causes of his illnesses. Now, researchers investigating his genome have made good on his request. They tracked down locks of the composer's hair and analyzed its DNA. They failed to find any genetic cause for Beethoven's hearing loss or gastrointestinal issues, but they learned his genes put him at a heightened risk of liver cirrhosis. Fragments of hepatitis B DNA also lurked in his hair, suggesting he had been infected with the virus late in life. That infection combined with Beethoven's heavy drinking, researchers report in *Current Biology*, may explain his death due to liver disease.

How 'Oumuamua hit the gas

ASTRONOMY | In 2017, the bizarre object called 'Oumuamua whizzed into the Solar System, moving so fast it could only have hailed from interstellar space. When it whipped around the Sun, it sped up slightly. But it lacked the icy tail of a typical comet, so that acceleration could not be explained by the release of gas from that water ice. This week in *Nature*, researchers put forth a model they say finally solves the mystery: As 'Oumuamua journeyed through interstellar space, cosmic radiation converted much of its water ice into frozen molecular hydrogen. The Sun's rays then released that gas, giving the comet an energetic boost that caused it to accelerate.



A Long Covid patient gets treatment at a U.K. clinic. The number of such patients is still rising, but the risk of contracting the syndrome seems to be declining.

COVID-19

New Long Covid cases decline with Omicron

Virus biology, widespread vaccination may be driving down risk of persistent symptoms

By **Jennifer Couzin-Frankel**

Ever since the COVID-19 pandemic unfurled across the United Kingdom, hematologist John Willan has worried about the disease's toll on his patients. In March 2020, Willan, who works at the University of Oxford and Wexham Park Hospital, began to track the hospital's COVID-19 cases among people with leukemias, lymphomas, and other blood diseases. He counted not just the dozens of deaths, but also persistent and disabling symptoms collectively called Long Covid, which have plagued millions over the past 3 years.

These days, Willan is less anxious. After Omicron began spreading in late 2021, COVID-19 deaths became a rarity even among his frail and immunocompromised patients, he says. And infections now carry a lower threat of lingering complications. "These patients with Omicron, they're much less likely to get Long Covid," says Willan, whose patients are overwhelmingly vaccinated. Earlier this month, he reported in the *British Journal of Haematology* that his patients' risk of Long Covid symptoms 3 months after infection had dropped from 46% with the original coronavirus strain and another called Alpha, to 35% with the Delta variant, to 14% with Omicron.

"My patients were so terrified … when COVID came out," and rightfully so, Willan says. Although the number with protracted symptoms is still higher than he'd like, "I want to try and get a message to those people to say, 'This is the actual risk to you now.'"

The trend appears in both vulnerable and healthy people. A group in the United Kingdom, Spain, and Italy reported this month in *The Lancet Oncology* that the risk of Long Covid among cancer patients fell from about 17% in 2021 to 6% more recently, as cases shifted to Omicron. Another just-published study of healthy Swiss hospital workers describes a similar pattern.

"The risk of Long Covid is not comparable between these variants," says Philipp Kohler, an infectious disease specialist at St. Gallen Cantonal Hospital, who co-led the Swiss study. Vaccination, Omicron's tendency to cause milder disease, and its distinct biology may all play a role, though the degree to which different factors blunt risk is a mystery.

Claire Steves, a geriatrician and epidemiologist at King's College London, was the first to rigorously compare Long Covid rates after Omicron versus after Delta, which struck in mid-2021. She drew on data from the U.K. COVID Symptom Study, in which tens of thousands type information into an app. Data from 97,000 vaccinated people revealed a 4.5% risk of symptoms persisting 4 weeks after an Omicron infection versus 10.8% following a Delta infection, the group reported in *The Lancet* in June 2022.

Since then, several studies have shown a decline in risk, although they disagree about the absolute numbers. The definition of Long Covid is still in flux, study designs differ, and the frequency with which Long Covid symptoms such as brain fog and intense fatigue also strike uninfected people isn't known, making it tougher to glean the prevalence of Long Covid today.

In the Swiss study this month in *Clinical Infectious Diseases*, Kohler and his colleagues, including infectious disease specialists Carol Strahm and Christian Kahlert, both also at St. Gallen, tried to pin down Long Covid risks in a cohort of Swiss health care workers. The team sorted participants—mostly female and young or middle-aged—by the variant they were likely infected with, based on the timing of their illness. Other volunteers, without a positive COVID-19 test and without antibodies to the virus, were assigned to a never-infected control group.

A survey given in June 2022 asked about Long Covid symptoms. "We decided this is not a yes or no question," Kohler says, so among nearly 3000 respondents, the team counted how many of 18 typical Long Covid symptoms—such as headache, cough, joint pain, and brain fog—they had. Because many people in the general population have at least

PHOTO: KIRSTY WIGGLESWORTH/AP

some of those symptoms, the team compared their frequency across different groups, including controls.

In the Omicron cohort, the average number of chronic symptoms was 0.52—below the other variants, but a touch above the control group's 0.39. Although this suggests Omicron infection carries a chance of Long Covid, it pales compared with the original strain: The health care workers infected early on were still averaging more than one ongoing symptom, despite having been hit far earlier. They also continued to report more missed days from work than those who caught Omicron.

In some ways, these numbers aren't surprising. During acute illness, Omicron is much less likely to land patients in the hospital due to severe disease, which researchers know is a major risk factor for Long Covid. But Steves says her data show lowered Long Covid risk "is not just about severity." Her group analyzed data on only nonhospitalized individuals and found the same gap. "I think it's highly likely that [Omicron] is acting as a different virus," she says.

Steves's study "suggests there may be an intrinsic property of Omicron that reduces the conversion to Long Covid," says Akiko Iwasaki, an immunologist at Yale School of Medicine. Iwasaki and Steves speculate that how different viral variants infiltrate the body could be key. Earlier variants seem to spread to vital organs more often than Omicron does. Such spread might not always produce symptoms in acute infection, Iwasaki theorizes, but it might make someone more likely to wind up with Long Covid.

Though shifting variants are likely driving down Long Covid risk, vaccination is probably playing a role, too, although untangling its potency can be tricky. In Kohler's study, outcomes after Omicron didn't appear affected by vaccination, but other studies see a link.

Scientists also wonder how reinfections might fuel Long Covid cases. Kohler's group has preliminary data suggesting that a person infected by the original COVID-19 strain and then by Omicron didn't have a higher risk of Long Covid than those infected only by the original strains. Daniel Ayoubkhani, a principal statistician at the Office for National Statistics who analyzes Long Covid data, notes that the U.K. COVID-19 Infection Survey reported last month that 2.4% of participants described ongoing symptoms after a second infection versus 4% after a first; most of the infections were likely Omicron.

Still, Iwasaki notes that even a small risk of Long Covid means a lot of affected people. Given how disabling the syndrome can be, she hasn't stopped worrying about the public—and herself. "I definitely don't want to get the virus," she says. ■

COVID-19

New clues to pandemic's origin surface, causing uproar

Genetic sequences from Wuhan market may point to animal that spread SARS-CoV-2, but data remain hidden

By **Jon Cohen**

A growing perception that the search for the origin of COVID-19 had hit a dead end was dramatically undercut last week by raccoon dogs and a French evolutionary biologist. The fox relative, little known outside of Asia, was thrust into the spotlight when the scientist and her colleagues found previously undisclosed genetic sequences from the early days of the pandemic. The data placed raccoon dogs and other animals susceptible to SARS-CoV-2 in stalls contaminated with the virus at the market in Wuhan, China, where many of the first COVID-19 cases surfaced.

Whether those data bolster the idea that infected raccoon dogs or other animals brought the coronavirus to the market and sparked COVID-19 has now become the latest flashpoint in the polarized debate over the pandemic's origin. Those who believe SARS-CoV-2 leaked from a virology lab in Wuhan have fiercely disputed any suggestion that the sequences weaken their position. Acrimony has also flared over why the Chinese team that collected the sequences from the market in 2020 did not release them earlier to the World Health Organization (WHO) and other scientists.

"These data could have—and should have—been shared 3 years ago," WHO Director-General Tedros Adhanom Ghebreyesus lamented at a press conference on 17 March, the day after media reports revealed the discovery of the market sequences. Maria Van Kerkhove, an infectious disease specialist who oversees the contentious origin issue for WHO, told *Science* the withholding of the data is "inexcusable."

As *Science* went to press, the sequences had again been hidden from view in the virology database GISAID, apparently at the request of their Chinese submitters. "Because the data have been removed from GISAID, we cannot share them. But I wish that other scientists could explore these data, which are very rich," says Florence Débarre of CNRS, the French national research agency, who first noticed the genetic sequences a few weeks ago. "The more people work on these data, the more we can make them speak."

In a report released this week, Débarre and 18 other researchers conclude that the data from the Huanan Seafood Wholesale Market "contribute to and underscore the large body of evidence supporting a natural origin of SARS-CoV-2." The group analyzed genetic sequences in 49 "environmental" samples that contained SARS-CoV-2's RNA and found they also had mitochondrial DNA (mtDNA) of raccoon dog, Amur hedgehog, Malayan porcupine, hoary bamboo rat, Himalayan marmot, masked palm civet, Siberian weasel, and hog badger. The team's report, posted on the open repository Zenodo, singles out the raccoon dog because its mtDNA was more abundant than that of other species in the SARS-CoV-2–laden samples and because it is known to shed the virus at high quantities. But its authors acknowledge that the other species could have transmitted the virus, too.

> **"We know that there's more information that is out there."**
> **Maria Van Kerkhove**, World Health Organization

Van Kerkhove convened a virtual meeting last week of the WHO panel exploring COVID-19's origin to discuss the findings with the report's authors and the Chinese researchers. "We know that there's more information that is out there," Van Kerkhove says, adding that she suspects it might help trace how the virus arrived at the market.

For Van Kerkhove, the uncovered sequences clearly bolster the marketplace scenario for the origin of the pandemic but are not conclusive. "Looking at all available data … it's much more likely that we have a zoonotic origin," she says. "The challenge is we cannot take the other hypotheses off the table without having evidence to do so."

Several scientists who remain unconvinced of the zoonotic scenario discounted the significance of the sequences, noting that they do not prove the virus reached the market in animals. "It does not influence the likelihood of different hypotheses in my mind," Akiko Iwasaki, an immunologist at Yale School of Medicine, told *Science*. But, she stressed, "Any and all relevant data from the market, and the

some of those symptoms, the team compared their frequency across different groups, including controls.

In the Omicron cohort, the average number of chronic symptoms was 0.52—below the other variants, but a touch above the control group's 0.39. Although this suggests Omicron infection carries a chance of Long Covid, it pales compared with the original strain: The health care workers infected early on were still averaging more than one ongoing symptom, despite having been hit far earlier. They also continued to report more missed days from work than those who caught Omicron.

In some ways, these numbers aren't surprising. During acute illness, Omicron is much less likely to land patients in the hospital due to severe disease, which researchers know is a major risk factor for Long Covid. But Steves says her data show lowered Long Covid risk "is not just about severity." Her group analyzed data on only nonhospitalized individuals and found the same gap. "I think it's highly likely that [Omicron] is acting as a different virus," she says.

Steves's study "suggests there may be an intrinsic property of Omicron that reduces the conversion to Long Covid," says Akiko Iwasaki, an immunologist at Yale School of Medicine. Iwasaki and Steves speculate that how different viral variants infiltrate the body could be key. Earlier variants seem to spread to vital organs more often than Omicron does. Such spread might not always produce symptoms in acute infection, Iwasaki theorizes, but it might make someone more likely to wind up with Long Covid.

Though shifting variants are likely driving down Long Covid risk, vaccination is probably playing a role, too, although untangling its potency can be tricky. In Kohler's study, outcomes after Omicron didn't appear affected by vaccination, but other studies see a link.

Scientists also wonder how reinfections might fuel Long Covid cases. Kohler's group has preliminary data suggesting that a person infected by the original COVID-19 strain and then by Omicron didn't have a higher risk of Long Covid than those infected only by the original strains. Daniel Ayoubkhani, a principal statistician at the Office for National Statistics who analyzes Long Covid data, notes that the U.K. COVID-19 Infection Survey reported last month that 2.4% of participants described ongoing symptoms after a second infection versus 4% after a first; most of the infections were likely Omicron.

Still, Iwasaki notes that even a small risk of Long Covid means a lot of affected people. Given how disabling the syndrome can be, she hasn't stopped worrying about the public—and herself. "I definitely don't want to get the virus," she says. ■

COVID-19

New clues to pandemic's origin surface, causing uproar

Genetic sequences from Wuhan market may point to animal that spread SARS-CoV-2, but data remain hidden

By **Jon Cohen**

A growing perception that the search for the origin of COVID-19 had hit a dead end was dramatically undercut last week by raccoon dogs and a French evolutionary biologist. The fox relative, little known outside of Asia, was thrust into the spotlight when the scientist and her colleagues found previously undisclosed genetic sequences from the early days of the pandemic. The data placed raccoon dogs and other animals susceptible to SARS-CoV-2 in stalls contaminated with the virus at the market in Wuhan, China, where many of the first COVID-19 cases surfaced.

Whether those data bolster the idea that infected raccoon dogs or other animals brought the coronavirus to the market and sparked COVID-19 has now become the latest flashpoint in the polarized debate over the pandemic's origin. Those who believe SARS-CoV-2 leaked from a virology lab in Wuhan have fiercely disputed any suggestion that the sequences weaken their position. Acrimony has also flared over why the Chinese team that collected the sequences from the market in 2020 did not release them earlier to the World Health Organization (WHO) and other scientists.

"These data could have—and should have—been shared 3 years ago," WHO Director-General Tedros Adhanom Ghebreyesus lamented at a press conference on 17 March, the day after media reports revealed the discovery of the market sequences. Maria Van Kerkhove, an infectious disease specialist who oversees the contentious origin issue for WHO, told *Science* the withholding of the data is "inexcusable."

As *Science* went to press, the sequences had again been hidden from view in the virology database GISAID, apparently at the request of their Chinese submitters. "Because the data have been removed from GISAID, we cannot share them. But I wish that other scientists could explore these data, which are very rich," says Florence Débarre of CNRS, the French national research agency, who first noticed the genetic sequences a few weeks ago. "The more people work on these data, the more we can make them speak."

In a report released this week, Débarre and 18 other researchers conclude that the data from the Huanan Seafood Wholesale Market "contribute to and underscore the large body of evidence supporting a natural origin of SARS-CoV-2." The group analyzed genetic sequences in 49 "environmental" samples that contained SARS-CoV-2's RNA and found they also had mitochondrial DNA (mtDNA) of raccoon dog, Amur hedgehog, Malayan porcupine, hoary bamboo rat, Himalayan marmot, masked palm civet, Siberian weasel, and hog badger. The team's report, posted on the open repository Zenodo, singles out the raccoon dog because its mtDNA was more abundant than that of other species in the SARS-CoV-2–laden samples and because it is known to shed the virus at high quantities. But its authors acknowledge that the other species could have transmitted the virus, too.

> **"We know that there's more information that is out there."**
> **Maria Van Kerkhove**, World Health Organization

Van Kerkhove convened a virtual meeting last week of the WHO panel exploring COVID-19's origin to discuss the findings with the report's authors and the Chinese researchers. "We know that there's more information that is out there," Van Kerkhove says, adding that she suspects it might help trace how the virus arrived at the market.

For Van Kerkhove, the uncovered sequences clearly bolster the marketplace scenario for the origin of the pandemic but are not conclusive. "Looking at all available data … it's much more likely that we have a zoonotic origin," she says. "The challenge is we cannot take the other hypotheses off the table without having evidence to do so."

Several scientists who remain unconvinced of the zoonotic scenario discounted the significance of the sequences, noting that they do not prove the virus reached the market in animals. "It does not influence the likelihood of different hypotheses in my mind," Akiko Iwasaki, an immunologist at Yale School of Medicine, told *Science*. But, she stressed, "Any and all relevant data from the market, and the

surrounding areas—including the virology laboratories—should be made public."

The sequence data took an odd journey to the spotlight. In early 2020, when the Wuhan market was closed after a cluster of COVID-19 cases arose there, a research group led by George Gao, then-head of China's Center for Disease Control and Prevention, took 923 samples from "containers," drains, and surfaces at specific stalls. In February 2022, the team posted a preprint reporting the presence of SARS-CoV-2 in 73 of the samples and human genetic material in some of those—leading the researchers to conclude that infected people brought the virus to the market, where it spread widely. But they didn't disclose what, if any, other animal sequences the market samples harbored, as some outside researchers highlighted to *Science* at the time.

having "deviated from its stated mission" of speeding the sharing of virological data. For its part, GISAID has said the researchers violated access agreements and has cut them off from the database.

Contacted by *Science* last week, Gao said the sequences are "[n]othing new. It had been known there was illegal animal dealing and this is why the market was immediately shut down." He would not explain the sequence of events that led GISAID last week to make the data invisible.

In the Zenodo report, Débarre and colleagues state their analysis is "not intended for publication in a journal" or meant to scoop the Gao team's own paper, which is under review by the *Nature* family of journals. "As scientists, we can work together on this," says Kristian Andersen, an evolutionary biologist at Scripps Research who is one of



Samples from a Wuhan market show susceptible animals were present at locations contaminated with SARS-CoV-2.

Four months after its preprint, Gao's team deposited some of those missing sequence data in GISAID. The information was made accessible to other users of the database only in January—perhaps to allow reviewers of the group's paper to examine it. On 4 March, Débarre stumbled on some of the genetic sequences in GISAID. But it wasn't until 5 days later that she realized how much data existed and began to collaborate with various evolutionary biologists who have become persuaded that SARS-CoV-2 spread from animals at the market to humans.

That group reached out to a member of Gao's team, who told them "that we could conduct an independent analysis," according to the Zenodo report, The next day, they found evidence of animals in the samples and notified the same researcher. By the following day, 11 March, the data became invisible on GISAID. In their report, Débarre and her co-authors sharply criticize GISAID for

the report's co-authors. Still, the report states the group went public with its analysis because the scientists feel an "unreasonable" amount of time has passed without the sequences becoming available.

To some fervent lab-leak proponents, the new report's authors are hopelessly biased. Several contributed to two 2022 *Science* papers that analyzed other evidence from Wuhan and concluded the pandemic probably emerged from infected animals at the market. But even if the new findings do not shift the battle lines, many agree on the need for China to disclose all pertinent data. David Relman, a Stanford University microbiologist who has argued that the lab-leak scenario deserves more attention, calls the market animal sequences, if verified, "helpful." But, he adds, "I think there are likely to be lots of relevant data and other information that have not yet seen the light of day—of relevance to both major hypotheses." ■

PARTICLE PHYSICS

A call for change at storied physics lab

Energy department opens new competition to run struggling Fermilab

By **Adrian Cho**

In an unusual move, the U.S. Department of Energy (DOE) has quietly begun a new competition for the contract to run the United States's sole dedicated particle physics laboratory. Announced in January, the rebid comes 1 year after Fermi National Accelerator Laboratory (Fermilab), which is managed in part by the University of Chicago (UChicago), failed an annual DOE performance review and 9 months after it named a new director. DOE would not comment, but observers say its frustrations include cost increases and delays in a gargantuan new neutrino experiment.

"I don't think it's surprising at all given the department's evaluation of [Fermilab's] performance," says James Decker, a physicist and consultant with Decker, Garman, Sullivan & Associates, LLC, who served as principal deputy director of DOE's Office of Science from 1973 to 2007. Although Fermilab passed its 2022 performance evaluation, the one for fiscal year 2021 was "one of the most scathing I have seen," Decker says.

DOE hires other parties to run its 17 national labs on 5-year contracts that can be renewed annually for another 15 years or more. Only rarely does DOE seek a new contractor because of performance problems. Since 2007, UChicago has run Fermilab with the Universities Research Association (URA), a consortium of research universities, in a partnership called the Fermi Research Alliance (FRA). The university also runs Argonne National Laboratory.

DOE has already solicited letters of interest and will issue a request for formal proposals this summer. It intends to award the new contract by the end of the next fiscal year, 30 September 2024, and transfer control of the lab, which employs 2100 staff and has an annual budget of $614 million, on

PHOTO: NOEL CELIS/AFP VIA GETTY IMAGES

some of those symptoms, the team compared their frequency across different groups, including controls.

In the Omicron cohort, the average number of chronic symptoms was 0.52—below the other variants, but a touch above the control group's 0.39. Although this suggests Omicron infection carries a chance of Long Covid, it pales compared with the original strain: The health care workers infected early on were still averaging more than one ongoing symptom, despite having been hit far earlier. They also continued to report more missed days from work than those who caught Omicron.

In some ways, these numbers aren't surprising. During acute illness, Omicron is much less likely to land patients in the hospital due to severe disease, which researchers know is a major risk factor for Long Covid. But Steves says her data show lowered Long Covid risk "is not just about severity." Her group analyzed data on only nonhospitalized individuals and found the same gap. "I think it's highly likely that [Omicron] is acting as a different virus," she says.

Steves's study "suggests there may be an intrinsic property of Omicron that reduces the conversion to Long Covid," says Akiko Iwasaki, an immunologist at Yale School of Medicine. Iwasaki and Steves speculate that how different viral variants infiltrate the body could be key. Earlier variants seem to spread to vital organs more often than Omicron does. Such spread might not always produce symptoms in acute infection, Iwasaki theorizes, but it might make someone more likely to wind up with Long Covid.

Though shifting variants are likely driving down Long Covid risk, vaccination is probably playing a role, too, although untangling its potency can be tricky. In Kohler's study, outcomes after Omicron didn't appear affected by vaccination, but other studies see a link.

Scientists also wonder how reinfections might fuel Long Covid cases. Kohler's group has preliminary data suggesting that a person infected by the original COVID-19 strain and then by Omicron didn't have a higher risk of Long Covid than those infected only by the original strains. Daniel Ayoubkhani, a principal statistician at the Office for National Statistics who analyzes Long Covid data, notes that the U.K. COVID-19 Infection Survey reported last month that 2.4% of participants described ongoing symptoms after a second infection versus 4% after a first; most of the infections were likely Omicron.

Still, Iwasaki notes that even a small risk of Long Covid means a lot of affected people. Given how disabling the syndrome can be, she hasn't stopped worrying about the public—and herself. "I definitely don't want to get the virus," she says. ■

COVID-19

New clues to pandemic's origin surface, causing uproar

Genetic sequences from Wuhan market may point to animal that spread SARS-CoV-2, but data remain hidden

By **Jon Cohen**

A growing perception that the search for the origin of COVID-19 had hit a dead end was dramatically undercut last week by raccoon dogs and a French evolutionary biologist. The fox relative, little known outside of Asia, was thrust into the spotlight when the scientist and her colleagues found previously undisclosed genetic sequences from the early days of the pandemic. The data placed raccoon dogs and other animals susceptible to SARS-CoV-2 in stalls contaminated with the virus at the market in Wuhan, China, where many of the first COVID-19 cases surfaced.

Whether those data bolster the idea that infected raccoon dogs or other animals brought the coronavirus to the market and sparked COVID-19 has now become the latest flashpoint in the polarized debate over the pandemic's origin. Those who believe SARS-CoV-2 leaked from a virology lab in Wuhan have fiercely disputed any suggestion that the sequences weaken their position. Acrimony has also flared over why the Chinese team that collected the sequences from the market in 2020 did not release them earlier to the World Health Organization (WHO) and other scientists.

"These data could have—and should have—been shared 3 years ago," WHO Director-General Tedros Adhanom Ghebreyesus lamented at a press conference on 17 March, the day after media reports revealed the discovery of the market sequences. Maria Van Kerkhove, an infectious disease specialist who oversees the contentious origin issue for WHO, told *Science* the withholding of the data is "inexcusable."

As *Science* went to press, the sequences had again been hidden from view in the virology database GISAID, apparently at the request of their Chinese submitters. "Because the data have been removed from GISAID, we cannot share them. But I wish that other scientists could explore these data, which are very rich," says Florence Débarre of CNRS, the French national research agency, who first noticed the genetic sequences a few weeks ago. "The more people work on these data, the more we can make them speak."

In a report released this week, Débarre and 18 other researchers conclude that the data from the Huanan Seafood Wholesale Market "contribute to and underscore the large body of evidence supporting a natural origin of SARS-CoV-2." The group analyzed genetic sequences in 49 "environmental" samples that contained SARS-CoV-2's RNA and found they also had mitochondrial DNA (mtDNA) of raccoon dog, Amur hedgehog, Malayan porcupine, hoary bamboo rat, Himalayan marmot, masked palm civet, Siberian weasel, and hog badger. The team's report, posted on the open repository Zenodo, singles out the raccoon dog because its mtDNA was more abundant than that of other species in the SARS-CoV-2–laden samples and because it is known to shed the virus at high quantities. But its authors acknowledge that the other species could have transmitted the virus, too.

> **"We know that there's more information that is out there."**
> **Maria Van Kerkhove**, World Health Organization

Van Kerkhove convened a virtual meeting last week of the WHO panel exploring COVID-19's origin to discuss the findings with the report's authors and the Chinese researchers. "We know that there's more information that is out there," Van Kerkhove says, adding that she suspects it might help trace how the virus arrived at the market.

For Van Kerkhove, the uncovered sequences clearly bolster the marketplace scenario for the origin of the pandemic but are not conclusive. "Looking at all available data … it's much more likely that we have a zoonotic origin," she says. "The challenge is we cannot take the other hypotheses off the table without having evidence to do so."

Several scientists who remain unconvinced of the zoonotic scenario discounted the significance of the sequences, noting that they do not prove the virus reached the market in animals. "It does not influence the likelihood of different hypotheses in my mind," Akiko Iwasaki, an immunologist at Yale School of Medicine, told *Science*. But, she stressed, "Any and all relevant data from the market, and the

surrounding areas—including the virology laboratories—should be made public."

The sequence data took an odd journey to the spotlight. In early 2020, when the Wuhan market was closed after a cluster of COVID-19 cases arose there, a research group led by George Gao, then-head of China's Center for Disease Control and Prevention, took 923 samples from "containers," drains, and surfaces at specific stalls. In February 2022, the team posted a preprint reporting the presence of SARS-CoV-2 in 73 of the samples and human genetic material in some of those—leading the researchers to conclude that infected people brought the virus to the market, where it spread widely. But they didn't disclose what, if any, other animal sequences the market samples harbored, as some outside researchers highlighted to *Science* at the time.

having "deviated from its stated mission" of speeding the sharing of virological data. For its part, GISAID has said the researchers violated access agreements and has cut them off from the database.

Contacted by *Science* last week, Gao said the sequences are "[n]othing new. It had been known there was illegal animal dealing and this is why the market was immediately shut down." He would not explain the sequence of events that led GISAID last week to make the data invisible.

In the Zenodo report, Débarre and colleagues state their analysis is "not intended for publication in a journal" or meant to scoop the Gao team's own paper, which is under review by the *Nature* family of journals. "As scientists, we can work together on this," says Kristian Andersen, an evolutionary biologist at Scripps Research who is one of



Samples from a Wuhan market show susceptible animals were present at locations contaminated with SARS-CoV-2.

PHOTO: NOEL CELIS/AFP VIA GETTY IMAGES

Four months after its preprint, Gao's team deposited some of those missing sequence data in GISAID. The information was made accessible to other users of the database only in January—perhaps to allow reviewers of the group's paper to examine it. On 4 March, Débarre stumbled on some of the genetic sequences in GISAID. But it wasn't until 5 days later that she realized how much data existed and began to collaborate with various evolutionary biologists who have become persuaded that SARS-CoV-2 spread from animals at the market to humans.

That group reached out to a member of Gao's team, who told them "that we could conduct an independent analysis," according to the Zenodo report, The next day, they found evidence of animals in the samples and notified the same researcher. By the following day, 11 March, the data became invisible on GISAID. In their report, Débarre and her co-authors sharply criticize GISAID for

the report's co-authors. Still, the report states the group went public with its analysis because the scientists feel an "unreasonable" amount of time has passed without the sequences becoming available.

To some fervent lab-leak proponents, the new report's authors are hopelessly biased. Several contributed to two 2022 *Science* papers that analyzed other evidence from Wuhan and concluded the pandemic probably emerged from infected animals at the market. But even if the new findings do not shift the battle lines, many agree on the need for China to disclose all pertinent data. David Relman, a Stanford University microbiologist who has argued that the lab-leak scenario deserves more attention, calls the market animal sequences, if verified, "helpful." But, he adds, "I think there are likely to be lots of relevant data and other information that have not yet seen the light of day—of relevance to both major hypotheses." ■

PARTICLE PHYSICS

A call for change at storied physics lab

Energy department opens new competition to run struggling Fermilab

By **Adrian Cho**

In an unusual move, the U.S. Department of Energy (DOE) has quietly begun a new competition for the contract to run the United States's sole dedicated particle physics laboratory. Announced in January, the rebid comes 1 year after Fermi National Accelerator Laboratory (Fermilab), which is managed in part by the University of Chicago (UChicago), failed an annual DOE performance review and 9 months after it named a new director. DOE would not comment, but observers say its frustrations include cost increases and delays in a gargantuan new neutrino experiment.

"I don't think it's surprising at all given the department's evaluation of [Fermilab's] performance," says James Decker, a physicist and consultant with Decker, Garman, Sullivan & Associates, LLC, who served as principal deputy director of DOE's Office of Science from 1973 to 2007. Although Fermilab passed its 2022 performance evaluation, the one for fiscal year 2021 was "one of the most scathing I have seen," Decker says.

DOE hires other parties to run its 17 national labs on 5-year contracts that can be renewed annually for another 15 years or more. Only rarely does DOE seek a new contractor because of performance problems. Since 2007, UChicago has run Fermilab with the Universities Research Association (URA), a consortium of research universities, in a partnership called the Fermi Research Alliance (FRA). The university also runs Argonne National Laboratory.

DOE has already solicited letters of interest and will issue a request for formal proposals this summer. It intends to award the new contract by the end of the next fiscal year, 30 September 2024, and transfer control of the lab, which employs 2100 staff and has an annual budget of $614 million, on

surrounding areas—including the virology laboratories—should be made public."

The sequence data took an odd journey to the spotlight. In early 2020, when the Wuhan market was closed after a cluster of COVID-19 cases arose there, a research group led by George Gao, then-head of China's Center for Disease Control and Prevention, took 923 samples from "containers," drains, and surfaces at specific stalls. In February 2022, the team posted a preprint reporting the presence of SARS-CoV-2 in 73 of the samples and human genetic material in some of those—leading the researchers to conclude that infected people brought the virus to the market, where it spread widely. But they didn't disclose what, if any, other animal sequences the market samples harbored, as some outside researchers highlighted to *Science* at the time.

having "deviated from its stated mission" of speeding the sharing of virological data. For its part, GISAID has said the researchers violated access agreements and has cut them off from the database.

Contacted by *Science* last week, Gao said the sequences are "[n]othing new. It had been known there was illegal animal dealing and this is why the market was immediately shut down." He would not explain the sequence of events that led GISAID last week to make the data invisible.

In the Zenodo report, Débarre and colleagues state their analysis is "not intended for publication in a journal" or meant to scoop the Gao team's own paper, which is under review by the *Nature* family of journals. "As scientists, we can work together on this," says Kristian Andersen, an evolutionary biologist at Scripps Research who is one of



Samples from a Wuhan market show susceptible animals were present at locations contaminated with SARS-CoV-2.

Four months after its preprint, Gao's team deposited some of those missing sequence data in GISAID. The information was made accessible to other users of the database only in January—perhaps to allow reviewers of the group's paper to examine it. On 4 March, Débarre stumbled on some of the genetic sequences in GISAID. But it wasn't until 5 days later that she realized how much data existed and began to collaborate with various evolutionary biologists who have become persuaded that SARS-CoV-2 spread from animals at the market to humans.

That group reached out to a member of Gao's team, who told them "that we could conduct an independent analysis," according to the Zenodo report, The next day, they found evidence of animals in the samples and notified the same researcher. By the following day, 11 March, the data became invisible on GISAID. In their report, Débarre and her co-authors sharply criticize GISAID for

the report's co-authors. Still, the report states the group went public with its analysis because the scientists feel an "unreasonable" amount of time has passed without the sequences becoming available.

To some fervent lab-leak proponents, the new report's authors are hopelessly biased. Several contributed to two 2022 *Science* papers that analyzed other evidence from Wuhan and concluded the pandemic probably emerged from infected animals at the market. But even if the new findings do not shift the battle lines, many agree on the need for China to disclose all pertinent data. David Relman, a Stanford University microbiologist who has argued that the lab-leak scenario deserves more attention, calls the market animal sequences, if verified, "helpful." But, he adds, "I think there are likely to be lots of relevant data and other information that have not yet seen the light of day—of relevance to both major hypotheses." ■

PARTICLE PHYSICS

A call for change at storied physics lab

Energy department opens new competition to run struggling Fermilab

By **Adrian Cho**

In an unusual move, the U.S. Department of Energy (DOE) has quietly begun a new competition for the contract to run the United States's sole dedicated particle physics laboratory. Announced in January, the rebid comes 1 year after Fermi National Accelerator Laboratory (Fermilab), which is managed in part by the University of Chicago (UChicago), failed an annual DOE performance review and 9 months after it named a new director. DOE would not comment, but observers say its frustrations include cost increases and delays in a gargantuan new neutrino experiment.

"I don't think it's surprising at all given the department's evaluation of [Fermilab's] performance," says James Decker, a physicist and consultant with Decker, Garman, Sullivan & Associates, LLC, who served as principal deputy director of DOE's Office of Science from 1973 to 2007. Although Fermilab passed its 2022 performance evaluation, the one for fiscal year 2021 was "one of the most scathing I have seen," Decker says.

DOE hires other parties to run its 17 national labs on 5-year contracts that can be renewed annually for another 15 years or more. Only rarely does DOE seek a new contractor because of performance problems. Since 2007, UChicago has run Fermilab with the Universities Research Association (URA), a consortium of research universities, in a partnership called the Fermi Research Alliance (FRA). The university also runs Argonne National Laboratory.

DOE has already solicited letters of interest and will issue a request for formal proposals this summer. It intends to award the new contract by the end of the next fiscal year, 30 September 2024, and transfer control of the lab, which employs 2100 staff and has an annual budget of $614 million, on

PHOTO: NOEL CELIS/AFP VIA GETTY IMAGES

eppendorf
& Science
PRIZE FOR
NEURO
BIOLOGY



Tell the World About Your Work!

応募締め切り
2023 年 6 月 15 日

Eppendorf & Science 神経生物学賞
Eppendorf & Science 神経生物学賞は、分子生物学や細胞生物学に基づく神経生物学研究において、卓越した貢献のあった若手科学者に毎年贈られる国際賞です。選出者は、*Science* 誌編集主任 Dr. Peter Stern をはじめとする科学者からなる独立委員会によって選出されます。年齢が35歳以下で、素晴らしい研究に従事していらっしゃる方なら、今こそこの賞に挑戦する時です。

受賞者には下記の賞が授与されます：
> 賞金 25,000 US ドル
> *Science* 誌に研究内容を掲載
> 米神経科学学会年次総会に伴って開催される授賞式への参加を全面サポート
> 10 年間の AAAS 会員資格および *Science* 誌オンライン購読権
> 1,000 US ドル相当のエッペンドルフ製品
> ドイツ ハンブルクのエッペンドルフ本社にご招待

応募は簡単です！あなたの研究について 1,000 語のエッセーを書いてください。

詳しくはこちらをご覧ください： **eppendorf.com/prize**

eppendorf Science AAAS

AAAS® and Science® are registered trademarks of the American Association for the Advancement of Science, USA. Eppendorf® and the Eppendorf Brand Design are registered trademarks of Eppendorf SE, Germany.
All rights reserved, including graphics and images. Copyright © 2023 by Eppendorf SE. Photography: Saverio Truglia.

eppendorf
& Science
PRIZE FOR
NEURO
BIOLOGY



申请截止日期
2023年6月15日

将您的工作公之于众!

Eppendorf & Science 神经生物学奖

一年一度的 Eppendorf & Science 神经生物学奖是一项国际奖项，授予用分子与细胞生物学方法在神经生物学领域取得非凡成果的青年科学家。获奖者及入围候选人均是由《Science》杂志高级编辑 Peter Stern 博士领衔的独立科学家所组成的委员会评出。如果您年龄不满35岁，并且正在从事出色的研究，现在是时候参选了。

您可能就是下一位获奖者并获得：

> $25,000 美元奖金
> 获奖论文发表在《Science》杂志上
> 获得全额资助参加美国神经科学协会年会和颁奖仪式
> 10 年 AAAS 会员和《Science》在线订阅
> 赠送价值 $1,000 美元的 Eppendorf 产品
> 获邀参观 Eppendorf 位于德国汉堡的总部

申请非常容易！只需写一份 1,000 字的文章，并告诉大家您所做的研究工作。

要了解更多信息，请登陆：

eppendorf.com/prize

eppendorf Science AAAS

AAAS® and Science® are registered trademarks of the American Association for the Advancement of Science, USA. Eppendorf® and the Eppendorf Brand Design are registered trademarks of Eppendorf SE, Germany. All rights reserved, including graphics and images. Copyright © 2023 by Eppendorf SE. Photography: Saverio Truglia.

1 January 2025. UChicago hopes to win the contract again, says Paul Alivisatos, president of the university, who is also chair of FRA's board of directors and a former director of DOE's Lawrence Berkeley National Laboratory. "We absolutely will be bidding to continue."

In 2021, DOE gave Fermilab's performance a B, whereas a B+ is needed to pass. In five of eight main subcategories, the lab earned failing marks, including a C on science and technology program management and a B- in business systems. In particular, DOE reviewers lamented Fermilab's poor management of the largest project the 56-year-old laboratory has ever undertaken: "The laboratory's biggest initiative is struggling."



Fermi National Accelerator Laboratory, outside Chicago, is the United States's only dedicated particle physics laboratory. It is building a giant neutrino experiment that is billions overbudget and years behind schedule.

PHOTO: RYAN POSTEL/FERMILAB

Physicists are preparing to shoot a beam of elusive particles called neutrinos from the lab in Batavia, Illinois, to a gigantic underground detector 1300 kilometers away in an abandoned gold mine in Lead, South Dakota. The experiment—known as the Long Baseline Neutrino Facility (LBNF) and the Deep Underground Neutrino Experiment (DUNE)—aims to be the definitive test of neutrino properties and could help explain why the infant universe generated more matter than antimatter. In 2015, DOE estimated the project would cost $1.5 billion and start to generate data in 2025. By late 2021, the cost estimate had more than doubled to $3.1 billion and the schedule had slipped 4 years.

Scientists say Fermilab has had trouble overseeing construction work at the mine. "We did not write a very good contract for the excavation," says a former Fermilab physicist who requested anonymity because he works at another DOE lab. "There were all kinds of loopholes in it, and the excavation company made an awful lot of money off of us."

The problems reveal a fundamental weakness of both FRA and URA, says Marvin Marshak, a neutrino physicist at the University of Minnesota, Twin Cities. They are ad hoc corporations devised to manage national labs, so they lack the resources of an industrial company, he says. "They're shells," Marshak says. "They don't have enough people and they have no assets."

FRA officials acknowledge that Fermilab was not adequately prepared to run a huge construction project. In 2019, the lab was managing about $150 million annually dedicated to big projects, says Juan de Pablo, vice president for national labs at UChicago and a member of the FRA board. Now, that number approaches $700 million, he says. "There were all sorts of things that the lab did not have the capacity, the size, the scale to be able to take on so quickly."

However, Fermilab may not deserve all the blame, says a theoretical physicist who requested anonymity to protect relations with DOE. For example, he says, after the lab finally hammered out an excavation contract with Thyssen Mining, months passed before DOE approved it. "I'm not sure whether it's really the lab that has a problem, or if it's DOE that has a problem and is blaming the lab."

The contracts are in place and excavation in South Dakota is 60% complete, De Pablo says, so the costs are now under better control. Still, DOE's budget request for fiscal year 2024, released last week, now estimates that LBNF/DUNE will cost $3.3 billion.

Many physicists say the lab also has problems beyond the neutrino experiment. Fermilab often lags in disbursing funding to collaborators at universities, multiple sources say. Even gaining entry to the lab site has become an ordeal as it tries to tighten security, physicists say. The lab requires occasional users to apply for site access 4 weeks in advance and repeat security training for each visit, the theorist says.

Opinions vary on how Fermilab wound up in turmoil. The former Fermilab physicist says the lab's previous director, Nigel Lockyer, dismissed many longtime managers and replaced them with poorly suited newcomers. "I could see things falling apart, but I wasn't empowered to help," the physicist says. Others say the exploding demands of LBNF/DUNE forced Lockyer to slash other smaller projects, which alienated the physicists who worked on them. "Nigel was in a terrible position," says a physicist who collaborates on a different Fermilab experiment. "And he didn't have a knack of presenting these difficult decisions as being in everybody's best interest." Lockyer did not respond to a request for comment.

The task of righting the ship now lies with Lia Merminga, who became the lab's director in April 2022. Merminga recently led development of a $978 million proton accelerator under construction at Fermilab. The lab's 2022 performance review commends her "for demonstrating a good understanding of [DOE's] concerns." But if the Fermilab contract changes hands, Merminga could lose the post. "I have every confidence in Lia," says the physicist who collaborates at Fermilab. "I just don't know whether she'll have the time."

How many parties will bid on the contract remains unclear. Managing the lab requires very specific technical expertise but pays $5 million per year, at most. "I don't think that there are too many organizations that could really compete for this contract," Decker says. If just UChicago or URA bid on the new contract, they'll need a new partner, multiple observers say, perhaps one with expertise in huge construction projects. DOE is sure to insist that something changes. ■

CHINA

China's research enterprise undergoes shake-up

Revamp aims to respond to U.S. challenge and promote "self-reliance" in science

By **Dennis Normile**

Facing tighter restrictions on access to key technologies and an increasingly competitive global scientific landscape, China has launched a major shake-up of its research organizations, seeking "self-reliance" in science and technology.

The National People's Congress earlier this month approved a plan to refocus China's Ministry of Science and Technology (MOST) on meeting top national priorities. It also creates a powerful Central Science and Technology Commission to enforce consistent policies across government agencies—and hold them accountable for achieving their objectives.

The revamp is "the most radical change to [China's] innovation system since the end of the Mao era," says Richard Suttmeier, a political scientist retired from the University of Oregon. The goal, says Denis Simon, a science policy expert at the University of North Carolina, Chapel Hill, is to get China "producing usable, desirable, needed technology that can be put into application sooner rather than later." But the plan does not slight basic research, which has enjoyed a surge in funding.



Beijing residents watch Chinese President Xi Jinping speak at a March congress.

PHOTO: JADE GAO/AFP VIA GETTY IMAGES

In part, the moves represent a response to recent decisions by the United States to restrict sales of advanced computer chips and semiconductor manufacturing equipment to China. U.S. officials are pushing Japan and the Netherlands to adopt similar bans. This led Chinese President Xi Jinping to bluntly tell business executives at a 6 March meeting that China is facing a U.S.-led strategy of "containment, encirclement, and suppression" that poses "severe challenges for China's development," according to Xinhua, the state news agency.

The self-sufficiency drive "seems like a natural response from Chinese leadership," says Emily Weinstein, an analyst at Georgetown University's Center for Security and Emerging Technology. And many Chinese scientists agree. "China indeed has to become more self-reliant because of these restrictions," says neuroscientist Mu-ming Poo, head of the Chinese Academy of Sciences's Institute of Neuroscience.

The reorganization also aims to address deeper problems in China's research environment, says Simon, a former executive vice chancellor at Duke Kunshan University in China. Over the years, officials gave MOST, a sprawling agency that oversees numerous research efforts, increased responsibility and resources "to build an innovation economy." But according to Simon, "Leadership has not been impressed by the results."

One problem has been that although MOST set priorities, allocated money, and evaluated projects, it had limited control over how other ministries conducted research. That contributed to lackluster results, analysts have said.

The new central commission will set governmentwide policies and evaluate results. It will sit at the loftiest political levels of China's government, directly under the Communist Party of China (CPC). The commission's size and composition remain uncertain, but it will "most likely [have] Xi as the chair," says Cong Cao, a science policy scholar at the University of Nottingham's campus in Ningbo, China. The CPC's involvement signals that "science and technology has become one of the [nation's] most critical issues," Cao says.

MOST is likely to retain an important role in executing the commission's policy directives, Suttmeier says. Notably, MOST will still manage China's National Natural Science Foundation, which provides grants to small groups of researchers working on fundamental topics. "China has not been quiet about its struggles to improve in more basic and foundational science," Weinstein says.

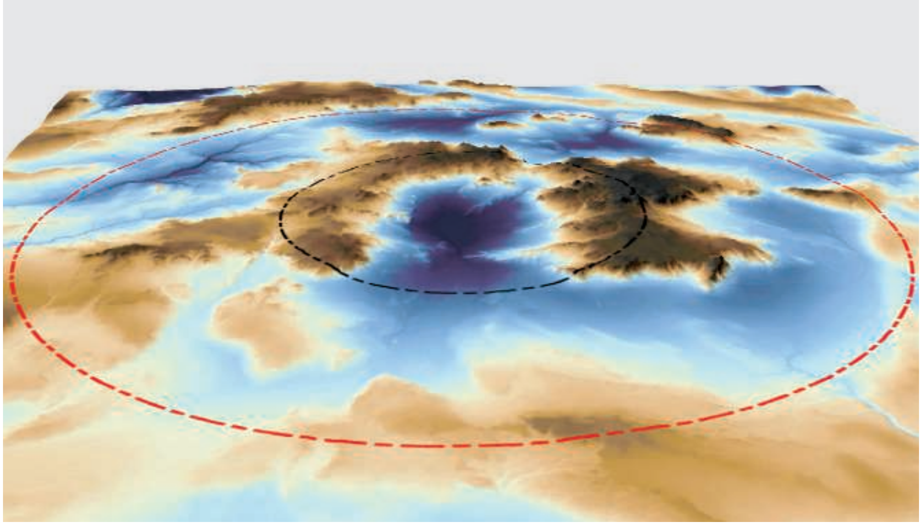
China has been increasing basic research funding, and Xi has signaled that he will continue that trend. Spending on basic science has doubled in 5 years and now accounts for 6.3% of total R&D money. China wants that share to rise to 8% by 2025, says economist Xuemei Xie of Tongji University. Even then China would trail the United States, which in 2019 spent 17% of R&D funding on basic science.

Some see the reorganization as a chance for China's panoply of research institutes to push for more autonomy. "I am calling [on the government] to give more money to institutions like the Institute of High Energy Physics [IHEP] so that *we* can decide what to do," says Yifang Wang, IHEP director. He also predicts that despite the emphasis on self-reliance, "international collaboration will not be affected." Groups from other countries helped design IHEP's proposed Circular Electron Positron Collider, and Wang says IHEP will soon resume international workshops that were suspended during the COVID-19 pandemic.

Despite its political backing, the reorganization is likely to face challenges. Individual ministries will still have some power to set their own agendas, potentially fragmenting research efforts. And private investment in basic research remains anemic, which could weaken efforts to commercialize discoveries.

Still, Simon believes the effort will help focus resources, improve cooperation between national labs and industry, and create better evaluation mechanisms. What remains to be seen, he says, is whether the shake-up can produce "a better scorecard when [China] places big bets in the race for greater technological self-reliance." ■

With reporting by Bian Huihui.



If Zhamanshin crater in Kazakhstan is 30 kilometers wide (red ring) instead of the accepted 13 kilometers (black ring), the impact that made it would have been far more fierce.

PLANETARY SCIENCE

Earth may face higher risk of catastrophic asteroid strikes

Sizes of geologically recent impact craters revised upward with sharper satellite imagery

By **Paul Voosen**, *in the Woodlands, Texas*

At a basic level, humanity's survival comes down to one thing: the chances of a giant space rock slamming into the planet and sending us the way of the dinosaurs. One way to calibrate that hazard is to look at Earth's recent large impact craters. And a provocative new study suggests they are bigger than previously thought—meaning Earth is more at risk of getting hit hard, says James Garvin, chief scientist of NASA's Goddard Space Flight Center, who presented the work last week here at the Lunar and Planetary Science Conference. "It would be in the range of serious crap happening."

Using a new catalog of high-resolution satellite imagery, Garvin and his colleagues identified large rings around three impact craters and one probable one that are 1 million years old or younger. To Garvin, the rings imply the craters are tens of kilometers wider, and record far more violent events, than researchers had thought.

If Garvin is right—no sure bet—each impact resulted in an explosion some 10 times more violent than the largest nuclear bomb in history, enough to blow part of the planet's atmosphere into space. Although not as destructive as the impact that killed off the dinosaurs, the strikes would have perturbed the global climate and caused local extinctions.

It's an extraordinary claim, as Garvin himself admits. "We haven't proven anything," he says. Without fieldwork to back up the conclusions, impact researchers are wary of the circles Garvin and his colleagues have drawn on maps—especially because they defy other estimates of impact rates. "I'm skeptical," says Bill Bottke, a planetary dynamicist at the Southwest Research Institute in Boulder, Colorado. "I want to see a lot more before I believe it."

Because water and wind quickly erase most impact craters on Earth, researchers estimate impact rates by tallying crater sizes and ages on the Moon. They also study the size of asteroids in orbit near Earth—potential future impactors. Based on those two methods, researchers estimate that an asteroid or comet 1 kilometer wide or larger hits the planet every 600,000 to 700,000 years.

The new study, however, suggests that in the past million years alone, four kilometer-size objects pummeled the continents—and, given that two-thirds of the planet is covered by water, that could mean up to a dozen struck Earth in total, Bottke says. Anna Łosiak, a crater researcher at the Polish Academy of Sciences, doubts the ring-like features identified by Garvin's team are truly crater rims. If they somehow are, she says, "that would be very scary because it would mean we really don't understand what's going on at all—and that there are a lot of space rocks that may come and make a mess."

The work stems from a database of high-resolution satellite imagery from the company Planet. Garvin and his collaborators used thousands of stereo overlapping images to create 3D maps of the four craters. Adding data from two height-measuring lasers that NASA operates in orbit, including one capable of penetrating tree cover, gave them maps with 4-meter resolution.

They removed features from the maps that were obviously unrelated to the impact. Then they applied an algorithm Garvin had first developed for Mars that searches for circular patterns in the topography. For simple, small craters, it invariably identified the obvious crater rim. But in thousands of runs on the four larger craters, the algorithm frequently identified a rimlike structure much farther out than the accepted rim. For example, Pantasma, an 800,000-year-old crater in Nicaragua, grew from 14.8 kilometers to 35.2 kilometers in diameter.

Experienced crater scientists don't see the new rims. "Those features are so subtle that I don't think they say 'big structural rim,'" says Gordon Osinski, a planetary scientist at Western University. They could instead be rings of debris ejected by the impacts, adds Brandon Johnson, a planetary scientist at Purdue University.

Garvin, however, doesn't think a mere ridge of debris would be visible after 1 million years of erosion. The rings imply that large craters on Earth have more variable structures than elsewhere in the Solar System because of high erosion rates, he says. "On Earth, things get messy, particularly when you throw a lot of energy at it."

For the results to gain credence, Johnson says the team will need to gather more evidence. First, the climate upheaval triggered by impacts as big as Garvin claims should have left its mark in ice cores or ocean or lake sediments. Second, researchers need to visit the sites of the rings to look for the deformed rocks and gravitational variations that would indicate a true crater rim.

Given the stakes, this is one hypothesis that can't afford to go untested, Johnson says. "We've got to go there, check out the geology, and get more detail." ■

IMAGE: J. GARVIN, C. TUCKER, C. ANDERSON, D. SLAYBACK, AND D. MCCLAIN/NASA GODDARD SPACE FLIGHT CENTER; AXAR WORLDVIEW; EARTHDEM; NASA PLANETARY DEFENSE COORDINATION OFFICE

FEATURES



ILLUSTRATION: JASON LYON

PALL OF SUSPICION

The National Institutes of Health's "China initiative" has upended hundreds of lives and destroyed scores of academic careers *By* **Jeffrey Mervis**

For decades, Chinese-born U.S. faculty members were applauded for working with colleagues in China, and their universities cited the rich payoff from closer ties to the emerging scientific giant. But those institutions did an about-face after they began to receive emails in late 2018 from the U.S. National Institutes of Health (NIH).

The emails asked some 100 institutions to investigate allegations that one or more of their faculty had violated NIH policies designed to ensure federal funds were being spent properly. Most commonly, NIH claimed a researcher was using part of a grant to do work in China through an undisclosed affiliation with a Chinese institution. Four years later, 103 of those scientists—some 42% of the 246 targeted in the letters, most of them tenured faculty members—had lost their jobs.

In contrast to the very public criminal prosecutions of academic scientists under the China Initiative launched in 2018 by then-President Donald Trump to thwart Chinese espionage, NIH's version has been conducted behind closed doors. Michael Lauer, head of NIH's extramural research, says that



ILLUSTRATION: A. MASTIN/*SCIENCE*

secrecy is necessary to protect the privacy of individual scientists, who are not government employees. Universities consider the NIH-prompted investigations to be a personnel matter, and thus off-limits to queries from reporters. And the targeted scientists have been extremely reticent to talk about their ordeal.

Only one of the five scientists whose cases are described in this article has previously gone public with their story. And only one has pushed back successfully, winning a large settlement against her university for terminating her.

But a running tally kept by the agency shows the staggering human toll of NIH's campaign. Besides the dismissals and forced retirements, more than one in five of the 246 scientists targeted were banned from applying for new NIH funding for as long as 4 years—a career-ending setback for most academic researchers. And almost two-thirds were removed from existing NIH grants.

NIH's data also make clear who has been most affected. Some 81% of the scientists cited in the NIH letters identify as Asian, and 91% of the collaborations under scrutiny were with colleagues in China.

In only 14 of the 246 cases—a scant 6%—did the institution fail to find any evidence to back up NIH's suspicions. Lauer, who oversees NIH's $30 billion grants portfolio, regards that high success rate as proof NIH only contacted institutions when there were compelling reasons to believe the targeted scientists were guilty of "scientific, budgetary, or commitment overlap" with NIH-funded projects.

"The fact that more than 60% of these cases have resulted in an employment separation, or a university taking the step of excluding a scientist from [seeking an NIH grant] for a significant period of time, means that something really, really serious has occurred," Lauer told *Science*.

But others, including some of the scientists targeted and the university administrators involved in investigating them, say the tremendous power differential between NIH and its grantees may be a better explanation for why so many scientists have been axed.

NIH is by far the largest funder of academic biomedical research in the United States, and some medical centers receive hundreds of millions of dollars annually from the agency. So when senior administrators heard Lauer say a targeted scientist "was not welcome in the NIH ecosystem," they understood immediately what he meant—and that he was expecting action.

"If NIH says there's a conflict, then there's a conflict, because NIH is always right," says David Brenner, who was vice chancellor for health sciences at the University of California, San Diego (UCSD), in November 2018 when the institution received a letter from Lauer asking it to investigate five medical school faculty members, all born in China. "We were told we have a problem and that it was up to us to fix it."

THERE WAS A NOTE OF URGENCY in the first email that Wuyuan Lu, a tenured professor at University of Maryland's Institute of Human Virology (IHV), got from a senior university research administrator.

"We have received an official communication from the National Institutes of Health," Dennis Paffrath wrote to Lu on 20 December 2018. "It concerns the failure by you and the University to disclose outside research support, relevant affiliations and foreign components" of Lu's existing NIH grants.

The NIH letter listed Lu's ties to Xi'an Jiaotong University and Fudan University, including grants NIH said Lu had received from Chinese research agencies. The letter also alleged that his NIH grant had supported work done in China. "I need to know if [this] is true," Paffrath wrote to Lu. "If not, we will need to work with NIH to help them understand that this is not the case."

Lu replied the next day, confident that his explanation would clear up what he assumed was a simple misunderstanding. Some of NIH's allegations, he wrote, appeared to be based on the acknowledgement section of papers with Chinese co-authors in which Lu noted their contributions to the research and the Chinese institutions that had funded them. But those references were a courtesy, Lu explained, and didn't mean his NIH grants were supporting any of their efforts.



103
jobs lost
42% of **246** targeted scientists were terminated by their institution or resigned.

In fact, he wrote, the opposite was true: His Chinese collaborations multiplied the payoff from the research that NIH had funded at IHV for more than 2 decades. Lu highlighted the intellectual property his lab generated for the university, telling Paffrath that "none of it would have been possible without" the talented Chinese students working at IHV through these collaborations. IHV had not only approved his interactions with Xi'an Jiaotong University, Lu added, but had touted them in its newsletters.

Lu accepted some blame. "It can be argued that I should have done a better job disclosing these past activities," he wrote to Paffrath. "But the truth of the matter is that I did not think they presented any conflict of interest."

Nor was it clear what he could have done differently, Lu continued. "Even if I had thought [those interactions] should be disclosed," he wrote, "I wouldn't have known where, how, and what to disclose due to lack of clear guidelines."

Lu expected his letter to allay NIH's concerns and allow him to continue research that contributed to the institute's search for new therapies to treat cancer and infectious diseases. His boss, renowned virologist Robert

Gallo, told *Science* a prominent colleague once called Lu "the most gifted protein chemist in America," and Gallo says Lu was a valued member of his management team.

But after hearing nothing for 15 months, Lu was told that NIH wanted more information. In his next reply, Lu included lengthy descriptions of each of his research projects with Chinese collaborators and explanations of how they did not conflict or overlap with his NIH funding.

That response was also insufficient, Paffrath told Lu in his next email. NIH wanted still more documents, Paffrath wrote, "and as quickly as possible." A few weeks later came what Lu interpreted as "a veiled threat" from NIH. "NIH will not continue to be patient in receiving these documents," Paffrath wrote, "and may pursue other remedies if we do not comply with their request."

By then Lu's patience was also wearing thin. For example, NIH had requested English and Mandarin copies of any contracts that Lu had signed with Chinese institutions. "I can't generate something that doesn't exist," Lu wrote Paffrath regarding an affiliation with Fudan that Lu says was "purely honorary … and with no contractual obligations."

Lu says he had recurring thoughts of returning to China to care for aging parents. Each time, Gallo told him he could do more to help the world by staying at IHV. But the increasingly bitter exchanges with NIH pushed him over the edge. In August 2020, Lu resigned his tenured position. He is now a professor at Fudan's medical school in Shanghai.

"NIH was acting like a bully," he tells *Science*, "and I decided that I'm not going to waste any more time on this witch hunt."

Lu doesn't blame the university, which through a spokesperson declined comment on the case, for his forced relocation. "The university never judged me, never put any pressure on me," he says. "They were simply the middleman, the messenger."

LU AND OTHER TARGETED SCIENTISTS interviewed say they had no idea their jobs were on the line when university officials first contacted them. None retained a lawyer at that point. After their initial replies, they often heard nothing for months. And once that silence was broken, most were told their only option was to resign or be fired.

Senior university administrators say they were surprised by the tone of the NIH letters. "It came out of nowhere, and the accusations were pretty ugly," says Robin Cyr, who was responsible for research compliance at the University of North Carolina, Chapel Hill (UNC), when the institution received its email in December 2018. "A Lauer letter meant that somebody at NIH thinks your faculty has wrongfully and willfully divulged intellectual property."



53
banned

21% of **246** targeted scientists were banned from applying for National Institutes of Health grants.

UCSD officials were so alarmed by the accusations in the NIH email they received that they circumvented a committee Brenner created years earlier to work with faculty members to avoid conflicts of commitment. (Research universities, including UCSD, typically allow their faculty to spend 1 day a week on outside activities, including foreign collaborations.) Instead, Brenner says, "the matter went straight to the chancellor's office."

The letters also forced administrators to recalibrate their understanding of what types of collaborations needed to be disclosed. "This is the way it works in academia; you collaborate with people," Brenner explains. "The money [a faculty member] received from NIH was always used in their lab, and then they would collaborate with other people using other funds. And we always thought that was a good thing until we were re-educated and told that it wasn't."

NIH'S SUDDEN SHIFT also surprised UNC biochemist Yue Xiong, who had assumed his ties to China benefited all parties, including NIH. Xiong, who studies protein degradation, had come to the United States in 1983 thanks to a prestigious state-backed graduate scholarship program that allowed China's most promising young scientists to finish their training in the West. A decade later, he landed at UNC and quickly established himself as a rising star.

"Yue is one of our most important scientists, a rock star, and a model of what we want our faculty to be," says Brian Strahl, chair of the medical school's department of biochemistry and biophysics, where Xiong spent 27 years on the faculty.

In 2003, Xiong set up a joint lab at Fudan with a friend and fellow alumnus of that scholarship program: biochemist Kun-Liang Guan, then a professor at the University of Michigan (UM), Ann Arbor. Fudan had reached out to Guan to seek his help in building up its graduate program in the life sciences, and Guan asked Xiong to join him so the work didn't interfere with his duties at UM.

Guan says the duo made sure the research it carried out in China was different from the work NIH was funding, and they hoped the Fudan students might wind up as postdocs in their U.S. labs. (Xiong declined to talk with *Science* but gave approval for colleagues to speak about his case.)

NIH contended Xiong's NIH grant had been comingled—in what Lauer calls "overlap"—with funding from Chinese entities. "NIH considers the work that was inappropriately disclosed [from foreign sources] to be part of their ecosystem, that is, work that they had funded," says Cyr, now executive vice chancellor for research at Northeastern University. "So the university had to disprove that, or we had to say it's inconclusive."

Cyr says NIH would not accept the latter response. "They just kept saying that we needed to dig deeper," she recalls. "But the faculty's stories didn't change. The narrative was what it was."

Another sticking point was whether Xiong had a contract with Fudan and had not disclosed it. Strahl and Leslie Parise, his department chair when the investigation was launched, say they were told the alleged contract contained language about intellectual property rights that UNC would never have accepted. But Xiong "kept saying he didn't remember signing any contract," recalls Parise, now dean of the University of Vermont's college of agriculture and life sciences.

Strahl says he was told repeatedly that UNC's entire portfolio of NIH grants—which was approaching $1 billion—was at risk if Xiong wasn't removed and that anything short of termination wasn't an option. Cyr also felt that pressure.

"When you have Mike Lauer saying that certain individuals are not welcomed in the NIH ecosystem, that's a powerful message," Cyr says. "I get that Congress holds NIH accountable and that NIH felt it was in the hot seat. But in dealing with the problem, you shouldn't compromise human beings."

Xiong never saw a list of specific allegations, nor did UNC ever give him any report of its findings. Instead, on 27 May 2020, Xiong was told at a face-to-face meeting with the medical school's head of human resources that he had 48 hours to decide whether to resign or be fired.

"He wasn't given any other options," recalls Strahl, who attended the meeting as Xiong's new boss. "If you want to resign, that would be fine," Strahl recalls Xiong being told. "But if you fight this, things won't end well for you."

They were both in shock, Strahl says. "All I could say was, 'I'm so sorry.' [Xiong] never

ILLUSTRATION: A. MASTIN/*SCIENCE*

expected to be let go. He thought that the truth would prevail."

Several of Xiong's colleagues tried to intervene. "We all wrote letters to the chancellor asking him to reverse the decision, but we never even got an answer," says biochemist William Marzluff, who had recruited Xiong to UNC. A UNC spokesperson declined to comment on the case.

Xiong retired quietly from UNC in July 2020 and is now chief scientific officer of Cullgene, a biotech startup in San Diego he co-founded fueled by some of his work at UNC. Six months after his retirement, a university press release touted a paper Xiong and others had published in a leading journal—but did not mention his departure.

LI WANG IS THE ONLY RESEARCHER *Science* spoke with who was able to overturn her termination, thanks to her union's collective bargaining agreement. But that isn't to say she emerged unscathed.

Within a week of receiving an email from Lauer on 6 November 2018, University of Connecticut (UConn), Storrs, officials had removed Wang, a tenured professor of physiology and neurobiology, from her NIH grant and denied her access to the mice she used to study liver metabolism.

But senior administrators soon decided NIH's claims that Wang held a position at Wenzhou Medical University and had received a grant from the National Natural Science Foundation of China did not hold up. "There is sufficient evidence to show that Dr. Wang is not formally affiliated" with Wenzhou, UConn's then–vice president for research, Radenka Maric, wrote Lauer on 21 November, and that the grant "was in fact awarded to a different Li Wang."

Lauer wasn't willing to accept those results, according to emails obtained by *Science* from UConn through a Freedom of Information Act (FOIA) request. On 28 November, Lauer wrote Maric, now UConn's president, that there were "at least four publications" that listed "Dr. Wang-UConn as affiliated with Wenzhou" and reminded Maric "to consider those publications as part of your ongoing reviews." Lauer also told Maric that "NIH thought a reasonable person would consider it more likely than not that Dr. Wang-UConn received financial support for her research" from the Chinese grant.



156 removed

63% of **246** targeted scientists were taken off their NIH grants.

91% China

For **225** of the cases China was the country of concern.

85% male

199 of the targeted scientists are men.

81% Asian

182 of the targeted scientists self-reported as Asian.

ILLUSTRATION: A. MASTIN/*SCIENCE*

Lauer suggested UConn officials contact the FBI, and in a subsequent email Maric told Lauer it had given UConn "additional information regarding Chinese talent programs, foreign affiliations, and key search terms." UConn used FBI techniques to search Wang's emails, she told Lauer, and obtained "a forensic image of [Wang's] laptop … that appear to contradict her denials."

UConn then changed its mind about Wang's innocence. "We cannot certify Dr. Wang as being honest, trustworthy and forthright," Maric told Lauer on 19 February 2019.

One month later, UConn banned Wang, who at one point held five NIH grants, from applying for NIH funding for 3 years, and in July the university decided to fire her. Wang resigned on 19 September 2019, 1 day before her termination went into effect.

Wang had already filed a grievance, which was rejected. But she had another way to fight back: A collective bargaining agreement gives UConn faculty the right to seek outside, binding arbitration in employment disputes.

Wang took advantage of that mechanism, in which an independent arbitrator conducts its own inquiry and issues a ruling that both parties have agreed to accept. The quasi-judicial process, which includes testimony from both sides, was conducted by the American Arbitration Association (AAA), and in November 2021 its arbitrator ruled in Wang's favor. In a 56-page decision, AAA's Peter Adomeit ordered UConn to pay Wang $1.4 million in compensation for being suspended and terminated "without just cause."

Wang declined to speak with *Science*, and her lawyer said a nondisclosure agreement prevents him or Wang from discussing the case. UConn officials also declined comment.

Adomeit's ruling, which *Science* obtained from UConn through its FOIA request, excoriated UConn officials for an investigation it characterized as deeply flawed.

"[Interim Provost John] Elliott's claim that the University 'has lost confidence' in Dr. Wang is true," Adomeit wrote. "But it was their fault, not hers. They relied on false evidence. [Wang] tried to correct them, but they wouldn't listen."

"They 'lost confidence' because they only listened to one side of the story," the decision continued. "Their minds were closed. They had no interest in contrary evidence."

Adomeit found the university's use of the results from its audit of Wang's computer to be especially egregious, criticizing lead investigator Michelle Williams's analysis. "Dr. Williams reached her conclusions without conducting metadata analysis on whether Dr. Wang wrote, modified, or accessed the computer data," Adomeit wrote. Williams, he explained, "became convinced, after visually inspecting the forensic image of Dr. Wang's computer, that Dr. Wang was lying, despite website evidence to the contrary."

BESIDES CONDUCTING flawed investigations, some universities seem to have cracked down even harder than NIH demanded. That was the case for UCSD neuroscientist Xiang-Dong Fu.

Fu, who studies neurodegenerative diseases including Parkinson's, was hired by UCSD in 1992 and earned tenure in 1998. That was also the year colleagues at Wuhan University, where Fu did his undergraduate studies, solicited his help in building up their research programs.

"You are already coming [to Wuhan] to visit your parents, so maybe you can provide some advice to our young faculty and work with their students?" Fu recalls being asked at dinner during one of those visits home. "If you have someone with similar research interests and some students, then I'd be happy to help out," he says he replied.

Five years later such an opportunity arose, and Fu began to tack on 2 or 3 days at Wuhan every few months after spending a weekend with his parents. In 2005 his hosts formalized his role by naming him a visiting professor, and over the next 3 years he was paid $1000 a month for 2 months' work with funds from a government program for domestic scholars.

From 2012 to 2016, Fu was again supported by Wuhan through China's Thousand Talents program, which was created to lure back Chinese-born scientists working abroad. Those who agreed to spend at least 9 months a year in China received generous salaries and lavish research funding. Given his full-time faculty position at UCSD, Fu chose the much less lucrative second tier,

which came with a modest monthly stipend. In return, he spent several weeks a year at Wuhan and the Institute for Biophysics at Peking University, where one of his former Wuhan students was now a faculty member.

Although Fu says his superiors knew about and had approved his activities, UCSD officials concluded that Fu had violated NIH's disclosure rules. In February 2020, UCSD banned him from applying for NIH funding for 4 years.

"They said that I did not follow certain procedures. OK, that's fair," Fu says. "I probably failed in many different ways." A UCSD spokesperson says the university "will not comment" on his case.

Such a ban would have been professionally fatal for most academic biomedical researchers. But a $9 million grant from a philanthropic initiative, Aligning Science Across Parkinson's, and patient donations allowed Fu to keep his lab going.

NIH told UCSD it regarded Fu's penalty to be sufficient punishment, according to multiple sources. *Science* has also learned that Brenner, now head of the neighboring Sanford Burnham Prebys research institute, told top UCSD officials he opposed any further sanctions. But UCSD continued to investigate Fu's ties to China. In a May 2021 report it concluded Fu had repeatedly violated UCSD's code of conduct for faculty pertaining to conflicts of commitment.

Fu didn't learn about the second investigation until July 2021 and didn't receive a copy of it until 6 months after that. In the interim he was invited to reply to the report, sight unseen, but told he "could not dispute the investigator's findings."

In January 2022, Fu was given the choice of either resigning or accepting a 4-year, unpaid suspension from the university that would ban him from campus and his lab. In March Executive Vice Chancellor Elizabeth Simmons submitted an official request that Fu be terminated, and in late April a faculty disciplinary committee recommended he be suspended without pay for 2 years.

"I probably failed in many different ways. ... But I still have a dream to chase."
Xiang-Dong Fu, Westlake University

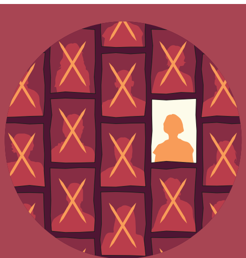


Fu filed a grievance, contending that many of the report's findings were incorrect and that the university had failed to follow its own procedures. More than 100 UCSD faculty members petitioned to lighten Fu's penalty, saying the continued prosecution of Fu "appeared rigged to assure the University lawyers would win their case rather than have justice be served."

UCSD officials never replied, says Christopher Glass, a professor of cellular medicine at UCSD who organized the petition, nor did Fu get a response to his grievance. On 5 December 2022, Fu "reluctantly resigned" after being told his 2-year campus suspension would go into effect on 1 January 2023.

Last month he accepted a position with the fledgling Westlake University, China's first private research university. There he hopes to spend the next few years refining a technique to convert brain cells called astrocytes into new neurons. His goal is to validate the controversial approach and use it to develop possible treatments for neurodegenerative diseases. "I don't need a huge lab, and I don't need 10 years," 66-year-old Fu says. "But I still have a dream to chase."

His move to China represents a huge loss for U.S. science, says Glass, who occupied an office next to Fu for 30 years. "He's an amazing scientist, incredibly productive," Glass says. "You couldn't ask for a better next-door neighbor."



14
no violations
In **6%** of **246** cases, the National Institutes of Health agreed with institutions that NIH policies had not been violated.

EVEN FOR SCIENTISTS who keep their U.S. jobs after surviving NIH scrutiny, the experience can take a heavy toll. Guan had rocketed up the academic ladder after joining UM's biological chemistry department in 1992. A 1999 profile in its alumni magazine that marked his MacArthur genius award the previous year called him "one of the great scientific minds of his generation."

His success in elucidating the cell signaling pathways involved in organ development and cancer attracted Fudan's attention, leading to the joint lab he set up with Xiong. The collaboration was no secret.

"My [then-]dean even offered to install a video conference link so it would be easier for me to communicate with people at Fudan," Guan recalls. And when Guan joined the UCSD faculty in 2007, he says his new bosses "were fully aware and very supportive of the collaboration."

Once Lauer's letter arrived in late 2018, Guan says, he cooperated fully with UCSD's investigation. "Whatever they asked for, I gave it to them," he says. "Passwords. My passport. All my travel records. I had a contract with Fudan University, and I gave them a copy of that." He also relinquished his existing NIH grants.

In 2019, the university concluded he had violated its code of conduct by failing to disclose research support from foreign sources and banned him from applying for NIH funding for 2 years. Guan says his work in China "was totally irrelevant" to what NIH was funding him to do, although he acknowledges he was "inconsistent" in reporting income from Fudan.

Guan says he never received a letter describing the allegations he was facing or a report on the outcome of the university's investigation. But, "UCSD did what it could" to keep his lab afloat, he says, and he was able to win new NIH awards once the suspension ended in 2021. Even so, his lab has shrunk dramatically, and he's no longer taking on new graduate students for fear that he won't be able to support them for the duration of their training.

His love of science has also suffered.

"I used to work very hard," he says. "Now, sometimes, I wonder what was the point of all the effort I made."

"And I'm one of the lucky ones," he continues. "I don't know how many people that NIH wanted to stop are able to start again. Maybe none." ■

This story was supported by the *Science* Fund for Investigative Reporting.

CREDITS: (PHOTO) XIANG-DONG FU; (ILLUSTRATION) A. MASTIN/*SCIENCE*

INSIGHTS

PERSPECTIVES



PHOTO: RUI OLIVEIRA

NEUROSCIENCE

The spread of fear in an empathetic fish

An evolutionarily ancient signaling pathway mediates emotional contagion

By **Ross S. DeAngelis** *and* **Hans A. Hofmann**

Empathy, the capacity to recognize the emotional state of others, is a hallmark of highly social mammals, such as primates, elephants, and dolphins (*1*). However, evidence from studies in rodents (*2*), fish (*3*), and birds (*4*) suggests that the capacity for empathy is widespread across vertebrates (*5*). In some species, an individual's emotional state can spread through a social group; yet, the prevalence of this emotional contagion is unclear (*1*). Although few studies have examined the neural basis of empathy and emotional contagion, research in mammals implicates the oxytocin system in striatal and septal circuits connecting to the amygdala (*6–10*). These brain regions are critical nodes of a conserved social decision-making network (SDMN) that enables vertebrates to produce context-appropriate behavior (*11*). On page 1232 of this issue, Akinrinade *et al.* (*12*) report that the evolutionarily ancient oxytocin system is a necessary component in the behavioral transmission of fear contagion in zebrafish (*Danio rerio*).

Akinrinade *et al.* demonstrate that wild-type individuals observing the erratic behavior of distressed conspecifics display freezing behavior—a proxy for fear across vertebrates. They show that mutant lines that lacked genes encoding the oxytocin ligand (*oxt*) or one of its two receptors (*oxtr* and *oxtrl*) did not exhibit this response, although administering exogenous oxytocin rescued the fear contagion. To uncover the neural basis of this fear contagion, the authors measured neural activity across nodes of the SDMN (*11*) in fish that observed a distressed shoal. They observed increased activity in the putative homologs of the mammalian lateral septum and striatum of the mutants. This suggests that these two brain regions, when active, inhibit freezing behavior and thus prevent fear contagion.

To demonstrate that the spread of fear contagion is an empathetic response and not simply behavioral copying, Akinrinade *et al.* allowed the focal fish to simultaneously observe videos of a distressed and a relaxed individual. During the observation phase, there were no differences between wild-type and mutant lines as both directed their attention toward the distressed fish. However, during the test phase, when a

Department of Integrative Biology and Institute for Neuroscience, The University of Texas at Austin, Austin, TX, USA. Email: hans@utexas.edu

Zebrafish adjust their behavior depending on the emotional state of other members of a shoal, even when observing other zebrafish in a video (as shown).

choice was provided between two relaxed fish, wild-type fish appeared empathetic and "consoled" previously distressed fish by preferentially associating with them, whereas mutant lines lacked this response.

The vertebrate nonapeptide system—which is comprised of both the oxytocin and arginine vasopressin pathways—is evolutionarily ancient, as are the brain regions implicated by Akinrinade *et al.* in zebrafish fear contagion. Notably, oxytocin also regulates empathy and consolation behavior in mice and prairie voles (*7*, *8*). Studies in both humans and rodents found that inhibition of oxytocin-sensitive neurons in the lateral septum and striatum reduces empathy (*9*, *10*), which could be a direct effect of oxytocin signaling or could be through the interaction of oxytocin with other important neuromodulators, such as dopamine. Indeed, oxytocin influences the synthesis and release of dopamine in reward-related brain areas in response to experiences of positive as well as negative salience and, as such, plays a role in regulating pro- and antisocial behavior (*13*).

> "...wild-type fish appeared empathetic and 'consoled' previously distressed fish..."

The apparent concordance between mammals and fish of how oxytocin regulates empathetic behavior raises the intriguing possibility that the mechanisms underlying empathy and some forms of emotional contagion may have been conserved since fish and mammals last shared a common ancestor, ~450 million years ago. To test this hypothesis, experiments like those reported by Akinrinade *et al.* need to be conducted in diverse species across all major lineages of vertebrates.

Such comparative research may have seemed a distant dream just a few years ago, but technological advances (such as CRISPR) have made nontraditional model systems increasingly amenable to targeted transgenic approaches. In addition, sophisticated automated behavioral tracking systems provide insight into animal behavior at unprecedented detail. Comparative studies that use similar experimental paradigms, genetic manipulations, and behavioral end points can be powerful for uncovering the extent to which the neural mechanisms underlying empathy and emotional contagion are species specific or are a conserved feature of vertebrate neural organization. Comparative transcriptomics within a phylogenetic framework provides a complementary opportunity to test the extent to which variation in brain region–specific gene expression patterns correlates with different aspects of social behavior while simultaneously discovering molecular pathways—other than the oxytocin system—that have not yet been implicated in these processes. For example, one such study discovered evidence for a conserved transcriptomic signature—including genes involved in cognition and neural plasticity—underlying social monogamy, which evolved independently numerous times in vertebrates (*14*). Given that empathetic behavior and maybe even emotional contagion have been described in diverse vertebrate taxa (*2*–*5*), using comparative transcriptomics to test whether the underlying neural and molecular substrates are similar and possibly conserved is promising.

A highly contentious debate, especially regarding fishes and invertebrates, is which animals have the capacity for subjective experiences, such as pain and pleasure, and therefore should be considered "sentient" (*15*). The discovery that the mechanisms underlying empathetic behavior, and even emotional contagion, are similar and possibly even evolutionarily conserved between fishes and mammals will certainly invigorate the debate on animal sentience. It seems likely that other fish species, as well as birds and some reptiles, also have the neuromolecular apparatus necessary for generating and experiencing emotions and for recognizing and acting upon conspecifics in distress. Comparative and evolutionary social neuroscience has much to contribute toward an understanding of the roots of human feelings and emotions. ■

REFERENCES AND NOTES

1. S. D. Preston, F. B. M. de Waal, *Behav. Brain Sci*. **25**, 1 (2002).
2. S.-W. Kim *et al*., *Neuron* **111**, 418 (2023).
3. S. Satoh *et al*., *Nat. Commun*. **12**, 1775 (2021).
4. J. E. C. Adriaense, J. S. Martin, M. Schiestl, C. Lamm, T. Bugnyar, *Proc. Natl. Acad. Sci. U.S.A.* **116**, 11547 (2019).
5. A. Pérez-Manrique, A. Gomila, *WIREs Cogn. Sci*. **13**, e1560 (2022).
6. E. Paradiso, V. Gazzola, C. Keysers, *Curr. Opin. Neurobiol*. **68**, 107 (2021).
7. M. T. Pisansky, L. R. Hanson, I. I. Gottesman, J. C. Gewirtz, *Nat. Commun*. **8**, 2102 (2017).
8. J. P. Burkett *et al*., *Science* **351**, 375 (2016).
9. R. Menon *et al*., *Curr. Biol*. **28**, 1066 (2018).
10. J. Lieberz *et al*., *Neuropsychopharmacology* **45**, 1134 (2020).
11. L. A. O'Connell, H. A. Hofmann, *J. Comp. Neurol*. **519**, 3599 (2011).
12. I. Akinrinade *et al*., *Science* **379**, 1232 (2023).
13. S. G. Shamay-Tsoory, A. Abu-Akel, *Biol. Psychiatry* **79**, 194 (2016).
14. R. L. Young *et al*., *Proc. Natl. Acad. Sci. U.S.A.* **116**, 1331 (2019).
15. H. Browning, J. Birch, *Philos. Compass* **17**, e12822 (2022).

10.1126/science.adh0769

BIOCHEMISTRY

A booster for vaccines from plants

Reconstituting a plant biosynthetic pathway enables a sustainable supply of vaccine adjuvants

By **Helena H. Chubatsu Nunes** and **Thu-Thuy T. Dang**

The vital role of immunization in public health has been displayed in full view during the COVID-19 pandemic with the race to develop and mass-produce vaccines using viruses and various antigen-generating technologies (*1*). Despite not often being in the spotlight, vaccine adjuvants are critical in modulating immune responses (*2*). Effective adjuvants are thus indispensable in the fight against current and emerging diseases. On page 1252 of this issue, Reed *et al*. (*3*) report a pipeline to produce QS-7, a promising vaccine adjuvant derived from the rare Chilean soapbark tree (*Quillaja saponaria*). By elucidating the biosynthesis of QS-7 in the native plant and reconstituting this pathway in the tobacco relative *Nicotiana benthamiana*, the authors obtained milligram amounts of QS-7, paving the way for industrial-scale production of this valuable adjuvant and its derivatives.

Endemic to difficult-to-access regions of Chile, Peru, and Bolivia, the Chilean soapbark tree has been traditionally used for medicine and soap, whereas industry has for years relied on its bark extracts to produce food additives and foaming agents (*4*). More recently, the tree has received attention owing to its ability to produce important vaccine adjuvants in its inner bark such as QS-21, QS-7, and QS-17 (*3*). These adjuvants are added to vaccines and they promote a more highly activated and longer-lasting immune response (*2*). Although their mechanism of action is still being studied, adjuvants are important to generating the vaccine immune response (*2*). For example, QS-21 has been used in the human vaccine against

Department of Chemistry, Irving K. Barber Faculty of Science, University of British Columbia, Kelowna, BC, Canada. Email: thuy.dang@ubc.ca

Zebrafish adjust their behavior depending on the emotional state of other members of a shoal, even when observing other zebrafish in a video (as shown).

choice was provided between two relaxed fish, wild-type fish appeared empathetic and "consoled" previously distressed fish by preferentially associating with them, whereas mutant lines lacked this response.

The vertebrate nonapeptide system—which is comprised of both the oxytocin and arginine vasopressin pathways—is evolutionarily ancient, as are the brain regions implicated by Akinrinade *et al.* in zebrafish fear contagion. Notably, oxytocin also regulates empathy and consolation behavior in mice and prairie voles (*7*, *8*). Studies in both humans and rodents found that inhibition of oxytocin-sensitive neurons in the lateral septum and striatum reduces empathy (*9*, *10*), which could be a direct effect of oxytocin signaling or could be through the interaction of oxytocin with other important neuromodulators, such as dopamine. Indeed, oxytocin influences the synthesis and release of dopamine in reward-related brain areas in response to experiences of positive as well as negative salience and, as such, plays a role in regulating pro- and antisocial behavior (*13*).

The apparent concordance between mammals and fish of how oxytocin regulates empathetic behavior raises the intriguing possibility that the mechanisms underlying empathy and some forms of emotional contagion may have been conserved since fish and mammals last shared a common ancestor, ~450 million years ago. To test this hypothesis, experiments like those reported by Akinrinade *et al.* need to be conducted in diverse species across all major lineages of vertebrates.

Such comparative research may have seemed a distant dream just a few years ago, but technological advances (such as CRISPR) have made nontraditional model systems increasingly amenable to targeted transgenic approaches. In addition, sophisticated automated behavioral tracking systems provide insight into animal behavior at unprecedented detail. Comparative studies that use similar experimental paradigms, genetic manipulations, and behavioral end points can be powerful for uncovering the extent to which the neural mechanisms underlying empathy and emotional contagion are species specific or are a conserved feature of vertebrate neural organization. Comparative transcriptomics within a phylogenetic framework provides a complementary opportunity to test the extent to which variation in brain region–specific gene expression patterns correlates with different aspects of social behavior while simultaneously discovering molecular pathways—other than the oxytocin system—that have not yet been implicated in these processes. For example, one such study discovered evidence for a conserved transcriptomic signature—including genes involved in cognition and neural plasticity—underlying social monogamy, which evolved independently numerous times in vertebrates (*14*). Given that empathetic behavior and maybe even emotional contagion have been described in diverse vertebrate taxa (*2*–*5*), using comparative transcriptomics to test whether the underlying neural and molecular substrates are similar and possibly conserved is promising.

A highly contentious debate, especially regarding fishes and invertebrates, is which animals have the capacity for subjective experiences, such as pain and pleasure, and therefore should be considered "sentient" (*15*). The discovery that the mechanisms underlying empathetic behavior, and even emotional contagion, are similar and possibly even evolutionarily conserved between fishes and mammals will certainly invigorate the debate on animal sentience. It seems likely that other fish species, as well as birds and some reptiles, also have the neuromolecular apparatus necessary for generating and experiencing emotions and for recognizing and acting upon conspecifics in distress. Comparative and evolutionary social neuroscience has much to contribute toward an understanding of the roots of human feelings and emotions. ■

"…wild-type fish appeared empathetic and 'consoled' previously distressed fish…"

REFERENCES AND NOTES

1. S. D. Preston, F. B. M. de Waal, *Behav. Brain Sci*. **25**, 1 (2002).
2. S.-W. Kim *et al*., *Neuron* **111**, 418 (2023).
3. S. Satoh *et al*., *Nat. Commun*. **12**, 1775 (2021).
4. J. E. C. Adriaense, J. S. Martin, M. Schiestl, C. Lamm, T. Bugnyar, *Proc. Natl. Acad. Sci. U.S.A*. **116**, 11547 (2019).
5. A. Pérez-Manrique, A. Gomila, *WIREs Cogn. Sci*. **13**, e1560 (2022).
6. E. Paradiso, V. Gazzola, C. Keysers, *Curr. Opin. Neurobiol*. **68**, 107 (2021).
7. M. T. Pisansky, L. R. Hanson, I. I. Gottesman, J. C. Gewirtz, *Nat. Commun*. **8**, 2102 (2017).
8. J. P. Burkett *et al*., *Science* **351**, 375 (2016).
9. R. Menon *et al*., *Curr. Biol*. **28**, 1066 (2018).
10. J. Lieberz *et al*., *Neuropsychopharmacology* **45**, 1134 (2020).
11. L. A. O'Connell, H. A. Hofmann, *J. Comp. Neurol*. **519**, 3599 (2011).
12. I. Akinrinade *et al*., *Science* **379**, 1232 (2023).
13. S. G. Shamay-Tsoory, A. Abu-Akel, *Biol. Psychiatry* **79**, 194 (2016).
14. R. L. Young *et al*., *Proc. Natl. Acad. Sci. U.S.A*. **116**, 1331 (2019).
15. H. Browning, J. Birch, *Philos. Compass* **17**, e12822 (2022).

10.1126/science.adh0769

BIOCHEMISTRY

A booster for vaccines from plants

Reconstituting a plant biosynthetic pathway enables a sustainable supply of vaccine adjuvants

By **Helena H. Chubatsu Nunes** *and* **Thu-Thuy T. Dang**

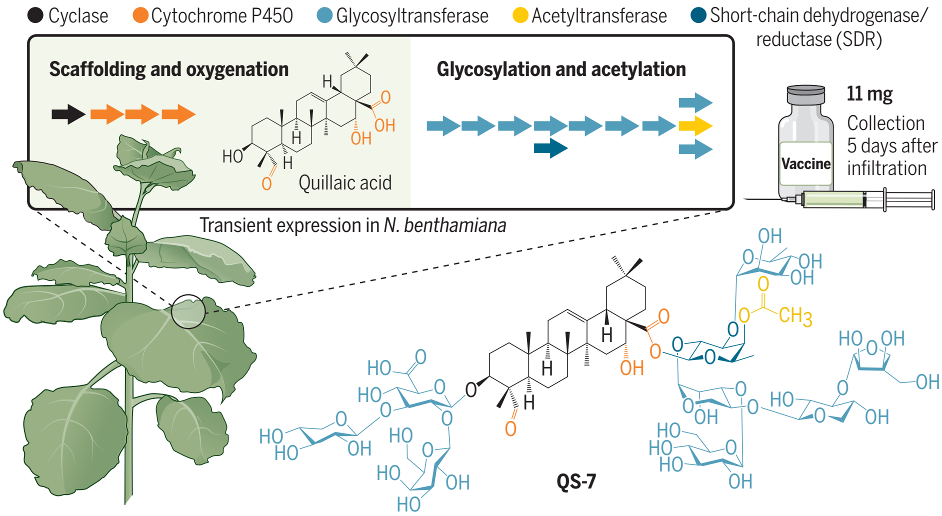
The vital role of immunization in public health has been displayed in full view during the COVID-19 pandemic with the race to develop and mass-produce vaccines using viruses and various antigen-generating technologies (*1*). Despite not often being in the spotlight, vaccine adjuvants are critical in modulating immune responses (*2*). Effective adjuvants are thus indispensable in the fight against current and emerging diseases. On page 1252 of this issue, Reed *et al*. (*3*) report a pipeline to produce QS-7, a promising vaccine adjuvant derived from the rare Chilean soapbark tree (*Quillaja saponaria*). By elucidating the biosynthesis of QS-7 in the native plant and reconstituting this pathway in the tobacco relative *Nicotiana benthamiana*, the authors obtained milligram amounts of QS-7, paving the way for industrial-scale production of this valuable adjuvant and its derivatives.

Endemic to difficult-to-access regions of Chile, Peru, and Bolivia, the Chilean soapbark tree has been traditionally used for medicine and soap, whereas industry has for years relied on its bark extracts to produce food additives and foaming agents (*4*). More recently, the tree has received attention owing to its ability to produce important vaccine adjuvants in its inner bark such as QS-21, QS-7, and QS-17 (*3*). These adjuvants are added to vaccines and they promote a more highly activated and longer-lasting immune response (*2*). Although their mechanism of action is still being studied, adjuvants are important to generating the vaccine immune response (*2*). For example, QS-21 has been used in the human vaccine against

Department of Chemistry, Irving K. Barber Faculty of Science, University of British Columbia, Kelowna, BC, Canada. Email: thuy.dang@ubc.ca

Biosynthesis of the vaccine adjuvant QS-7

In the Chilean soapbark tree (*Quillaja saponaria*), the formation of QS-7 relies on the action of a triterpenoid scaffolding cyclase followed by cytochrome P450 enzymes to form the main quillaic acid scaffold from the precursor 2,3-oxidosqualene. Glycosyltransferases and an acetyltransferase perform a series of modifications to produce the final vaccine adjuvant. Assembling the entire pathway in *Nicotiana benthamiana* enables scalable and sustainable production of the vaccine adjuvant.



shingles, and QS-7 and QS-17 are present in some COVID-19 vaccine candidates. Despite their potent therapeutic value, the current global supply of QS adjuvants is enough to make only ~6 million vaccine doses because mature trees of 10 years or older are required for adjuvant isolation (*5*). Moreover, because the complexity of the QS structures has challenged traditional chemical synthesis, understanding QS biosynthesis in the native tree presents an opportunity to sustainably obtain these pharmaceuticals.

The QS adjuvants belong to a group of secondary metabolites called triterpenoid glycosides or saponins. These compounds are characterized by the presence of a pentacyclic triterpene scaffold that is variously glycosylated; recognizable representatives include the anti-inflammatory ginsenosides from ginseng and the antimicrobial avenacins from oat (*6*). Although the biosynthesis of saponins has been studied extensively, Reed *et al.* achieved the feat of discovering and reconstituting a series of 16 enzymes, resulting in the complete biosynthesis of QS-7 from 2,3-oxodosqualene, the ubiquitous precursor of triterpenoids. The discovery of a scaffolding cyclase followed by the tailoring cytochrome P450 enzymes and glycosyltransferases that selectively perform nine consecutive glycosylation reactions was mostly powered by genome assembly, gene coexpression analysis, and biosynthetic gene cluster prediction tools such as plantiSMASH. Each enzyme was then transiently expressed in *N. benthamiana* and subjected to activity tests, accompanied by robust analyses of glycosylated intermediates. Finally, a total of 11 enzymatic steps with 14 enzymes were assembled in *N. benthamiana* through gene transformation by *Agrobacterium* inoculation, resulting in an impressive final QS-7 yield of 7.9 µg per gram of leaf (dry weight) for a total of 11 mg from 410 plants within 5 days (see the figure).

Reconstitution of plant biosynthetic pathways to produce natural products in heterologous systems is a promising alternative to traditional chemical synthesis and extractions from native plants (*7*). The *N. benthamiana* platform has become increasingly common for pathway assembly owing to its low maintenance cost and versatility in tolerating the coexpression of many heterologous enzymes. Recent examples include the biosynthesis of the pesticide strychnine and the flavoring and bioinsecticidal limonoids (*8*, *9*). With the production of QS-7 and its analogs, Reed *et al.* showcase *N. benthamiana* as a platform that can expand both the production capabilities and chemical space of natural products.

The study of Reed *et al.* reveals the combination of various types of enzymes that are involved in scaffolding and modifying complex structures of plant chemicals. Intriguingly, although glycosylation is usually catalyzed by a single glycosyltransferase, the D-fucosylation of the C-28 sugar chain in the QS-7 scaffold requires an additional short-chain dehydrogenase/reductase (SDR) "helper" enzyme. The clustering of genes that encode this glycosyltransferase–SDR pair in the genome of the Chilean soapbark tree suggests a plausible regulatory role and highlights the possibility of assessing gene clusters to speed up pathway discovery. Further physiological and mechanistic studies are required to fully characterize the SDR helper. Nevertheless, this work illustrates the complexity of plant biosynthetic pathways, underlining how the arrangement of biosynthetic genes in the genome, enzymes in the catalytic cascade, and auxiliary elements work in unison to synthesize complex phytochemicals. The discovery of the SDR helper and other enzymes in the biosynthesis of QS-7 also expands the catalytic toolbox for diversifying natural products and designing new-to-nature molecules.

Multistep biosynthetic pathways with few or no known intermediates and difficult-to-express enzymes challenge the investigation of specialized metabolism in plants (*7*). The study of Reed *et al.* adds QS-7 to the limited number of plant natural products that have a completely elucidated biosynthesis pathway and an even shorter list of compounds whose pathways are reconstituted in heterologous systems for scalable production. Large-scale biosynthesis of QS-7 will require further optimization of the *N. benthamiana* system to minimize unwanted by-products and metabolic bottlenecks. Nevertheless, this study illustrates how combinatorial sequencing-based genome reconstruction and gene expression analysis with pathway reconstitution accelerate the study and engineering of plant metabolism. In parallel with the advancement of sequencing technologies, more computational tools, such as artificial intelligence platforms, machine learning, and retrobiosynthesis, are expected to be at the frontier of creating new databases and tools for gene mining and pathway identification (*10*). For now, Reed *et al.* provide an avenue to access much-needed vaccine adjuvants and one more example of why plant biosynthetic prowess and the associated genomic features merit our attention. ■

REFERENCES AND NOTES

1. N. Pardi, M. J. Hogan, F. W. Porter, D. Weissman, *Nat. Rev. Drug Discov.* **17**, 261 (2018).
2. B. Pulendran, P. S. Arunachalam, D. T. O'Hagan, *Nat. Rev. Drug Discov.* **20**, 454 (2021).
3. J. Reed *et al.*, *Science* **379**, 1252 (2023).
4. J. D. Fleck *et al.*, *Molecules* **24**, 171 (2019).
5. G. Ragupathi, J. R. Gardner, P. O. Livingston, D. Y. Gin, *Expert Rev. Vaccines* **10**, 463 (2011).
6. S. T. Mugford *et al.*, *Plant Cell* **25**, 1078 (2013).
7. B. D. Kwan, B. Seligmann, T.-D. Nguyen, J. Franke, T.-T. T. Dang, *Curr. Opin. Plant Biol.* **71**, 102330 (2023).
8. B. Hong *et al.*, *Nature* **607**, 617 (2022).
9. R. De La Peña *et al.*, *Science* **379**, 361 (2023).
10. W. Finnigan, L. J. Hepworth, S. L. Flitsch, N. J. Turner, *Nat. Catal.* **4**, 98 (2021).

ACKNOWLEDGMENTS

The authors thank T.-D. Nguyen for insightful discussions.

10.1126/science.adg8823

GRAPHIC: N. CARY/SCIENCE

MATERIALS SCIENCE

A direct and clean route to MXenes

New, scalable methods synthesize two-dimensional carbide and nitride materials

By **Daniel D. Robertson** *and* **Sarah H. Tolbert**

Materials with layered crystal structures are an emerging class of compounds with desirable properties for numerous applications. In particular, the family of two-dimensional (2D) transition-metal carbides and nitrides (*1*) known as MXenes [where M is a transition metal and X is carbon (C) or nitrogen (N)] have shown exciting prospects for use in energy storage (*2*), electromagnetic interference shielding (*3*), transparent conductors (*4*), and more (*5*, *6*). However, MXenes have only been synthesized from MAX phases [where A is typically aluminum (Al) but can sometimes be other elements] by chemically removing A atoms with harsh solutions (*7*). Because this method generates large amounts of waste, it limits the scale of manufacturing for MXenes and hinders their utility. On page 1242 of this issue, Wang *et al.* (*8*) report the direct synthesis of MXenes by use of direct, scalable synthetic methods. These approaches also open pathways to produce new morphologies and phases of MXenes that have not been accessible by the typical route.

MXenes have seen considerable interest because of their properties as 2D metallic conductors. Like many layered materials, their bulk crystal form can be separated (or exfoliated) into individual sheets (*9*). The sheets can then be readily assembled into freestanding films while retaining their high electronic conductivity. The resulting material is essentially a conductive version of a standard exfoliated aluminosilicate clay and is a natural fit for devices for which thin sheets of conductor are needed. For example, MXene clays can be used in supercapacitors to store charge very quickly with their high surface area and facile electron conduction (*10*). Alternatively, films of MXene can shield devices from external electromagnetic radiation because the highly mobile electrons in the MXene can oscillate freely to cancel out the incoming waves (*3*).

[1]Department of Chemistry and Biochemistry, University of California, Los Angeles (UCLA), Los Angeles, CA 90095-1569, USA. [2]Department of Materials Science and Engineering, UCLA, Los Angeles, CA 90095-1595, USA. [3]The California NanoSystems Institute, UCLA, Los Angeles, CA 90095, USA. Email: tolbert@chem.ucla.edu

Single-MXene sheets also show exciting promise. Single-layer graphene was first isolated from graphite two decades ago (*11*). Since then, however, the incorporation of graphene and other single-layer materials into practical devices has presented challenges (*12*). Although graphene exhibits a wealth of exceptional properties, including record-high electron mobilities (*13*), its poor processability makes it difficult for some applications. As a sheet of sp^2-hybridized carbon, graphene has very little polarity and thus does not stay in solution when suspended. To address this problem, oxygen can be incorporated to form graphene oxide, but doing so decreases the material's conductivity, making it less useful (*14*). By contrast, MXenes are naturally hydrophilic and can be dispersed easily in water and polar solvents without compromising their high electronic conductivity. This combination of properties may make MXenes useful in situations in which graphene has not yet proved practical.

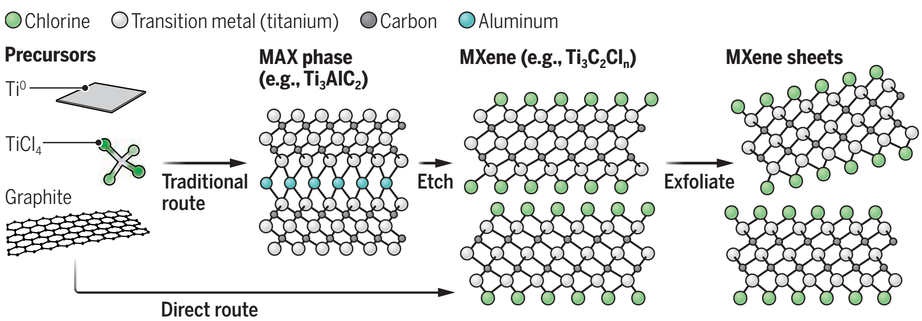
> **"…direct synthetic methods expand the boundaries for MXene use by making new phases and morphologies accessible."**

MXenes, however, cannot yet be made in the large amounts needed for widespread use. Translating from a laboratory scale to an industrial one requires processing and materials costs to meet strict requirements for a product to be competitive. On both fronts, MXenes show promise because the best-performing MXenes are derived from abundant, inexpensive elements such as titanium (Ti), C, and chlorine (Cl), and once formed, the MXenes can be processed readily. A key factor currently limiting their scalability is the etching step needed to produce MXenes from their parent MAX phases. Etching typically involves soaking a MAX material in hydrofluoric acid or other highly reactive solutions for up to 24 hours (*7*). This process of chemically removing A atoms is time consuming and generates large amounts of hazardous waste, both of which add cost and complexity to scaling the manufacturing of these materials (*15*).

Wang *et al.* report two direct ways to make MXenes without the need for etching from a MAX phase (see the figure). One involves traditional solid-state synthesis, in which a stoichiometric mix of solid precursors is heated until it forms the desired phase. The other uses chemical vapor deposition, in which gaseous precursors flow over a heated substrate to produce a film of material. In either case, the authors used a mix of Ti, C, and Cl to access one of the most prominent MXenes, Ti_2CCl_2, as well as others. These methods offer a clear proof of concept for direct synthesis to the MXene

Making MXenes directly

Two-dimensional carbides and nitrides (MXenes; M is a transition metal, X is carbon or nitrogen) are produced by etching MAX phases (A is typically aluminum), a time-consuming process that generates hazardous waste. Direct synthesis routes circumvent the etching process.



Precursors of the desired elements are heated together to produce a MAX phase.

Once synthesized, the MAX phase is treated with hydrofluoric acid or another etchant to remove A atoms and produce a layered MXene phase.

The bulk MXene material can then be exfoliated into individual sheets for applications.

GRAPHIC: A. MASTIN/*SCIENCE*

phase without the need to make and etch a MAX phase. The new routes save time and avoid hazardous waste production that is associated with an etching step. These benefits should improve the efficiency of scaling the production of MXenes and expedite the process of translating them to industrial-scale applications.

The study of Wang *et al.* further highlights how direct synthetic methods expand the boundaries for MXene use by making new phases and morphologies accessible. The chemical vapor deposition method, for example, produces a "carpet-like" film in which sheets of MXenes protrude perpendicular to the substrate. When precursors are added further, porous microspheres of the MXenes form and eventually detach from the substrate as a powder. These interconnected, yet porous, networks of MXenes represent ideal architectures for supercapacitor electrodes because they allow for electrolyte infiltration without compromising pathways for electron transport. The authors also report several new phases of MXenes that have not been previously prepared, including 2D Cl- and bromine (Br)–passivated zirconium carbides (Zr_2CCl_2 and Zr_2CBr_2) and 2D Cl-passivated titanium nitride (Ti_2NCl_2). Ti_2NCl_2 notably represents the first Cl-terminated nitride MXene and is one of only a handful of nitride MXenes that have been reported.

Wang *et al.* open up new opportunities in the synthesis of new MXenes, especially for cases in which the corresponding MAX phases are not stable. Considering the extensive possible combinations of elemental stoichiometries in this family of materials, the use of direct synthetic routes could substantially expand the possible MXenes and properties available. In the meantime, the improved scalability for existing MXenes from direct synthesis will likely facilitate their use in a number of applications. ■

REFERENCES AND NOTES

1. M. Naguib *et al.*, *Adv. Mater.* **23**, 4248 (2011).
2. B. Anasori, M. R. Lukatskaya, Y. Gogotsi, *Nat. Rev. Mater.* **2**, 16098 (2017).
3. F. Shahzad *et al.*, *Science* **353**, 1137 (2016).
4. J. Halim *et al.*, *Chem. Mater.* **26**, 2374 (2014).
5. V. Kamysbayev *et al.*, *Science* **369**, 979 (2020).
6. Y. R. Luo *et al.*, *Joule* **3**, 279 (2019).
7. M. Alhabeb *et al.*, *Chem. Mater.* **29**, 7633 (2017).
8. D. Wang *et al.*, *Science* **379**, 1242 (2023).
9. J. N. Coleman *et al.*, *Science* **331**, 568 (2011).
10. M. Ghidiu, M. R. Lukatskaya, M. Q. Zhao, Y. Gogotsi, M. W. Barsoum, *Nature* **516**, 78 (2014).
11. K. S. Novoselov *et al.*, *Science* **306**, 666 (2004).
12. G. R. Bhimanapati *et al.*, *ACS Nano* **9**, 11509 (2015).
13. A. H. Castro Neto, F. Guinea, N. M. R. Peres, K. S. Novoselov, A. K. Geim, *Rev. Mod. Phys.* **81**, 109 (2009).
14. D. R. Dreyer, S. Park, C. W. Bielawski, R. S. Ruoff, *Chem. Soc. Rev.* **39**, 228 (2010).
15. Y. Li *et al.*, *Nat. Mater.* **19**, 894 (2020).

10.1126/science.ade9914

OPTICS

Four-dimensional optics using time-varying metamaterials

Optical platforms using material parameters that change with time have diverse applications

By **Nader Engheta**

For optics, like semiconductor heterostructures, the interfaces and inhomogeneities in materials can manipulate optical waves and fields. Numerous photonic devices and components—for example, waveguides, lenses, and cavities—function owing to the presence of such interfaces and material spatial variations. Such parameter inhomogeneity is generally in three dimensions of space (spatial inhomogeneities). But what if the dimension of "time" could be introduced into material parameters? This would mean that parameters can change with time in addition to (or instead of) their variation in three-dimensional (3D) space. Such 4D material platforms for optics (or for any other wave and field phenomena) offer additional degrees of freedom in manipulating light–matter interaction, providing exciting opportunities such as in new approaches to frequency manipulation, signal amplification, and beam forming.

> **"Merging spatial and temporal interfaces may open a new horizon in four-dimensional optics, in which some of the features of both interfaces can be exploited."**

Research on time-dependent electromagnetic and electrical platforms dates back to the 1950s (*1*, *2*). Examples of time-varying platforms include time-varying electric circuits, in which the values of circuit components change in time; amplitude and frequency modulations (AM and FM), where the amplitude and the frequency of signals change owing to time-varying circuit elements; and mobile communication channels, where transmitters and receivers may move around. However, recent developments in the field of metamaterials and metasurfaces have resurrected growing interest in light–matter interaction in 4D metamaterials.

Department of Electrical and Systems Engineering, University of Pennsylvania, Philadelphia, PA, USA. Email: engheta@seas.upenn.edu

A "temporal interface," which is the temporal analog of a well-known spatial interface, occurs when a material parameter is changed in time rapidly while the optical wave is present in the material (see the figure). There are similarities between temporal and spatial interfaces, but there are also interesting differences. For example, when a wave impinges on a spatial interface between two materials with different parameters, reflected and transmitted waves are generated. Analogously, when the temporal interface occurs in the presence of a wave in the material, forward (FW) and backward (BW) waves—that is, waves that propagate along the same and the opposite directions of the original wave—result (*2*). However, in the spatial interface, the wavelength of the transmitted light would be different from that of the incident and reflected waves while their frequencies are the same (for linear materials). Conversely, for the temporal interface, the wavelength (and the wave number) for the FW and BW waves are the same as that of the original wave, but their frequency is changed owing to the change in wave velocity. The presence of the BW wave for such temporal interfaces has been used in a method for time reversal, which is elegantly shown for waves on the surface of water in a tank when a diverging wave is changed into a converging wave using a temporal interface (*3*). This work has shown how such a method can reverse the direction of a wave, leading to reconstruction of the original disturbance on the water surface (*3*).

Another interesting difference between spatial and temporal interfaces is that for the spatial interface, the electromagnetic energy is conserved (the sum of reflected and transmitted energies is the same as the incident energy, when materials are loss free), whereas in the temporal interface,

phase without the need to make and etch a MAX phase. The new routes save time and avoid hazardous waste production that is associated with an etching step. These benefits should improve the efficiency of scaling the production of MXenes and expedite the process of translating them to industrial-scale applications.

The study of Wang *et al.* further highlights how direct synthetic methods expand the boundaries for MXene use by making new phases and morphologies accessible. The chemical vapor deposition method, for example, produces a "carpet-like" film in which sheets of MXenes protrude perpendicular to the substrate. When precursors are added further, porous microspheres of the MXenes form and eventually detach from the substrate as a powder. These interconnected, yet porous, networks of MXenes represent ideal architectures for supercapacitor electrodes because they allow for electrolyte infiltration without compromising pathways for electron transport. The authors also report several new phases of MXenes that have not been previously prepared, including 2D Cl- and bromine (Br)–passivated zirconium carbides (Zr_2CCl_2 and Zr_2CBr_2) and 2D Cl-passivated titanium nitride (Ti_2NCl_2). Ti_2NCl_2 notably represents the first Cl-terminated nitride MXene and is one of only a handful of nitride MXenes that have been reported.

Wang *et al.* open up new opportunities in the synthesis of new MXenes, especially for cases in which the corresponding MAX phases are not stable. Considering the extensive possible combinations of elemental stoichiometries in this family of materials, the use of direct synthetic routes could substantially expand the possible MXenes and properties available. In the meantime, the improved scalability for existing MXenes from direct synthesis will likely facilitate their use in a number of applications. ■

REFERENCES AND NOTES

1. M. Naguib *et al.*, *Adv. Mater.* **23**, 4248 (2011).
2. B. Anasori, M. R. Lukatskaya, Y. Gogotsi, *Nat. Rev. Mater.* **2**, 16098 (2017).
3. F. Shahzad *et al.*, *Science* **353**, 1137 (2016).
4. J. Halim *et al.*, *Chem. Mater.* **26**, 2374 (2014).
5. V. Kamysbayev *et al.*, *Science* **369**, 979 (2020).
6. Y. R. Luo *et al.*, *Joule* **3**, 279 (2019).
7. M. Alhabeb *et al.*, *Chem. Mater.* **29**, 7633 (2017).
8. D. Wang *et al.*, *Science* **379**, 1242 (2023).
9. J. N. Coleman *et al.*, *Science* **331**, 568 (2011).
10. M. Ghidiu, M. R. Lukatskaya, M. Q. Zhao, Y. Gogotsi, M. W. Barsoum, *Nature* **516**, 78 (2014).
11. K. S. Novoselov *et al.*, *Science* **306**, 666 (2004).
12. G. R. Bhimanapati *et al.*, *ACS Nano* **9**, 11509 (2015).
13. A. H. Castro Neto, F. Guinea, N. M. R. Peres, K. S. Novoselov, A. K. Geim, *Rev. Mod. Phys.* **81**, 109 (2009).
14. D. R. Dreyer, S. Park, C. W. Bielawski, R. S. Ruoff, *Chem. Soc. Rev.* **39**, 228 (2010).
15. Y. Li *et al.*, *Nat. Mater.* **19**, 894 (2020).

10.1126/science.ade9914

OPTICS

Four-dimensional optics using time-varying metamaterials

Optical platforms using material parameters that change with time have diverse applications

By **Nader Engheta**

For optics, like semiconductor heterostructures, the interfaces and inhomogeneities in materials can manipulate optical waves and fields. Numerous photonic devices and components—for example, waveguides, lenses, and cavities—function owing to the presence of such interfaces and material spatial variations. Such parameter inhomogeneity is generally in three dimensions of space (spatial inhomogeneities). But what if the dimension of "time" could be introduced into material parameters? This would mean that parameters can change with time in addition to (or instead of) their variation in three-dimensional (3D) space. Such 4D material platforms for optics (or for any other wave and field phenomena) offer additional degrees of freedom in manipulating light–matter interaction, providing exciting opportunities such as in new approaches to frequency manipulation, signal amplification, and beam forming.

> **"Merging spatial and temporal interfaces may open a new horizon in four-dimensional optics, in which some of the features of both interfaces can be exploited."**

Research on time-dependent electromagnetic and electrical platforms dates back to the 1950s (*1*, *2*). Examples of time-varying platforms include time-varying electric circuits, in which the values of circuit components change in time; amplitude and frequency modulations (AM and FM), where the amplitude and the frequency of signals change owing to time-varying circuit elements; and mobile communication channels, where transmitters and receivers may move around. However, recent developments in the field of metamaterials and metasurfaces have resurrected growing interest in light–matter interaction in 4D metamaterials.

A "temporal interface," which is the temporal analog of a well-known spatial interface, occurs when a material parameter is changed in time rapidly while the optical wave is present in the material (see the figure). There are similarities between temporal and spatial interfaces, but there are also interesting differences. For example, when a wave impinges on a spatial interface between two materials with different parameters, reflected and transmitted waves are generated. Analogously, when the temporal interface occurs in the presence of a wave in the material, forward (FW) and backward (BW) waves—that is, waves that propagate along the same and the opposite directions of the original wave—result (*2*). However, in the spatial interface, the wavelength of the transmitted light would be different from that of the incident and reflected waves while their frequencies are the same (for linear materials). Conversely, for the temporal interface, the wavelength (and the wave number) for the FW and BW waves are the same as that of the original wave, but their frequency is changed owing to the change in wave velocity. The presence of the BW wave for such temporal interfaces has been used in a method for time reversal, which is elegantly shown for waves on the surface of water in a tank when a diverging wave is changed into a converging wave using a temporal interface (*3*). This work has shown how such a method can reverse the direction of a wave, leading to reconstruction of the original disturbance on the water surface (*3*).

Another interesting difference between spatial and temporal interfaces is that for the spatial interface, the electromagnetic energy is conserved (the sum of reflected and transmitted energies is the same as the incident energy, when materials are loss free), whereas in the temporal interface,

Department of Electrical and Systems Engineering, University of Pennsylvania, Philadelphia, PA, USA. Email: engheta@seas.upenn.edu

Cold Spring Harbor Laboratory 2023 Meetings & Courses



Symposium meeting social at the CSHL beach

87th CSHL Symposium

Stem Cells

May 31 - June 4, 2023

Poster Abstracts Due: **April 21**

Organizers - **Terri Grodzicker**, **David Stewart** & **Bruce Stillman,** Cold Spring Harbor Laboratory

Topics

Germ Cells

Embryonic & Trophoblast Stem Cells

Early Embryo Including Retrotransposons

Differentiation & Reprogramming

Epigenetics

Organ Stem Cells

Hematopoietic/Immune System

Neural Stem Cells

Adult Stem Cells/Regeneration

Cancer Stem Cells

Induced Pluripotent Stem Cells

Organoids & Multicellular Organoids

Disease Models

Clinical Therapies

meetings.cshl.edu

2023 Meetings

Telomeres & Telomerase May 2 - 6

The Biology of Genomes May 9 - 13

Mechanisms of Metabolic Signaling May 16 - 20

Retroviruses May 22 - 27

Genome Engineering: CRISPR Frontiers August 16 - 20

Eukaryotic mRNA Processing August 22 - 26

Mechanisms of Eukaryotic Transcription August 29 - September 2

Eukaryotic DNA Replication & Genome Maintenance
September 5 - 9

Microbial Pathogenesis & Host Response
September 11 - 15

Biology of Cancer: Microenvironment & Metastasis
September 19 - 23

Recombinant DNA: Fifty Years of Discovery & Debates
September 27 - 30

Neurobiology of *Drosophila* October 3 - 7

Cell State Conversions October 10 - 14

Single Cell Analyses November 8 - 11

Zebrafish Neurobiology November 15 - 18

Plant Genomes, Systems Biology & Engineering
November 29 - December 2

Genome Informatics December 6 - 9

Cold Spring Harbor Laboratory - Meetings & Courses Program - Cold Spring Harbor, New York

Advertorial



Aerial view of campus buildings and university hospital with the city of Nagoya in the distance.

Leading Japan in translational medical research

From bench to bedside and back again, Fujita Health University is building a foundational bridge between basic and clinical research.

Located near the automotive capital of the country in Aichi prefecture, Fujita Health University (FHU) is marking Japan's global lead in a different industry. Recognized as the third-best private university in the country[1] and having established a wide international academic network, FHU is a model for the future of medical research and medical education.

FHU's commitment to these two areas has existed since its founding in 1968 by Keisuke Fujita, a medical doctor and biochemist who envisioned the university as a leader in both basic research and clinical work. More than 50 years later, this balance remains a prerequisite for the university's faculty and its students.

"Many of our medical students are interested in basic research. Of course, they must be good medical doctors, but they must also have a research mind," says FHU Vice President Nakao Iwata.

It is not uncommon for students to gradually lose motivation in research, with a large number finding graduate school an unpleasant experience.[2] In Japan, many medical doctors eventually abandon their research to focus entirely on clinical work.[3] FHU, on the other hand, has dedicated itself to an educational environment that maintains if not raises a student's commitment to the bench.

This is because, compared with other academic leaders in the country, FHU is a small university, with just over 3,000 students but almost 1,000 faculty. This low student–faculty ratio provides an intimacy that allows the university to introduce students to research projects that match their interests and skills.

"I know every scientist and student at the university. I know what they are doing and what they want to do," notes Iwata.

Adaptation as a key to success

From the early days of 2020, the world was anticipating a new infectious disease, but the severity would not be known for several months. China and its neighboring countries were the first to go into lockdown. Japan would make the news early, well before COVID-19 was a pandemic, by refusing to disembark passengers and crew from the cruise ship Diamond Princess, which sat in Yokohama Bay that February. Unsure of the health risks, the Japanese government turned to its leading medical institutions for assistance. Among them was FHU, which took responsibility for over 100 passengers, testing for the virus and accumulating invaluable patient data about the disease, thus putting it at the forefront of infection-prevention measures.

As the pandemic grew, FHU realized it would not only have to adopt new measures for patient care—the education of its students would be affected greatly. It therefore became one of the first universities to transition to online lectures.

"It immediately happened," says International Relations Manager Ayako Masaki about the implementation. "That spirit reflects all our activities—research, clinical, and patient safety. Everything moves fast."

Online lectures also allowed the university to continue pursuing its international student cohort while the borders were closed to all non-residents. Since implementing an aggressive push to expand its international network 10 years ago, FHU now offers English-only degree programs and is growing its collaborations with foreign universities to jointly develop new medical technologies. It has also set up

PHOTO: COURTESY OF FUJITA HEALTH UNIVERSITY

exchange programs with several universities around the world, inviting students to earn credits while doing clinical fellowships at the partner's facilities.

An international collaboration with Johns Hopkins University in the United States has led to knowledge sharing in rehabilitation medicine, including swallowing disorders (dysphagia), a major problem in stroke patients. The two universities have a strong partnership researching imaging modalities, such as computed tomography (CT), magnetic resonance imaging (MRI), and videofluoroscopy, for the diagnosis and management of dysphagia.[4]

Emphasis on translation

These international efforts are part of expanding the university's translational research. Iwata is also the director of a new office, the Translation Research Headquarters, which was founded in 2022 and is responsible for translational research, clinical trials, and industry partnerships. It has already hired nearly 100 staff.





Left: Fujita Health University Vice President Nakao Iwata; **Right:** Fujita Health University President Yukio Yuzawa

Overall, the university is investing greatly in infrastructure for translation. A major focus is the development of chimeric antigen receptor (CAR) T-cell therapies. These therapies have shown extraordinary promise for incurable leukemias and are expected to perform similarly against other cancers. Like many universities across the country, FHU has established its own cell processing center (CPC) to prepare these and other cells for regenerative medicine. However, only FHU's CPC has both positive and negative pressure facilities, which allows FHU to concentrate viral vectors on-site. This independence from commercial sites both expedites and initiates the development of new experimental therapies.

As with many countries, Japan has a serious shortage of surgeons in rural areas. Moreover, these same areas generally have older populations who cannot travel to major metropolises. It is not a surprise then that patient outcomes correlate with geographical residence, but this relationship is expected to weaken with telesurgery. Although some telesurgery is approved in Japan, a critical limitation is the time lag in the signal between the surgeon in one location and the operating room in another, which can be dozens if not hundreds of kilometers away. FHU was the first to apply a new surgical robotics system to gastroenterology in Japan, with the surgeon located at one of its four medical centers and the surgery conducted at a second.[5] Complementing this robotics research is the application of deep learning for cancer diagnostics. FHU has worked with several companies in this sector to enhance the image quality while shortening the imaging time for organs and tissues.[6] Other industry partnerships are leading to spinoffs like Genonyxs, which offers genetic testing in a secure platform that protects the patient's data and identity.

PHOTOS: COURTESY OF FUJITA HEALTH UNIVERSITY

Smart Health

That protection is crucial for an even larger project. Despite Japan's reputation in electronics and technology, many medical records are kept in hard copy, and it is not unusual to see a fax machine beside the coffee maker. FHU is working with several companies to move these records to the cloud for the creation of a "Smart City." Medical records will be accessible by medical centers, pharmacies, and other relevant bodies all while maintaining the anonymity and security of the patient. In a super-aging society like Japan, healthcare workers cannot assume their patients have the cognizance to reliably provide all details of their health history and medication. In addition, the metadata from this project will contribute to disease modeling and recommendations for behavioral changes, such as diet and physical activity.

Its rich research environment and advanced infrastructure are two reasons companies and government organizations prefer FHU. Iwata adds that another reason concerns FHU's dynamic and flexible operations.

"We have a very fast decision-making process. When we make a decision, we expect to act on it the next day," he says.

Although a relatively young and small university, FHU has the largest number of beds at a teaching hospital in the country, according to FHU President Yukio Yuzawa. He adds that it is also leading the transformation of Japan's healthcare, making FHU one of the best places in Japan to make a difference in medicine for the country and worldwide: "We aim to create new medical care based on education and research using the philosophy cultivated under the principle of 'Our Creativity for the People.'"

References:

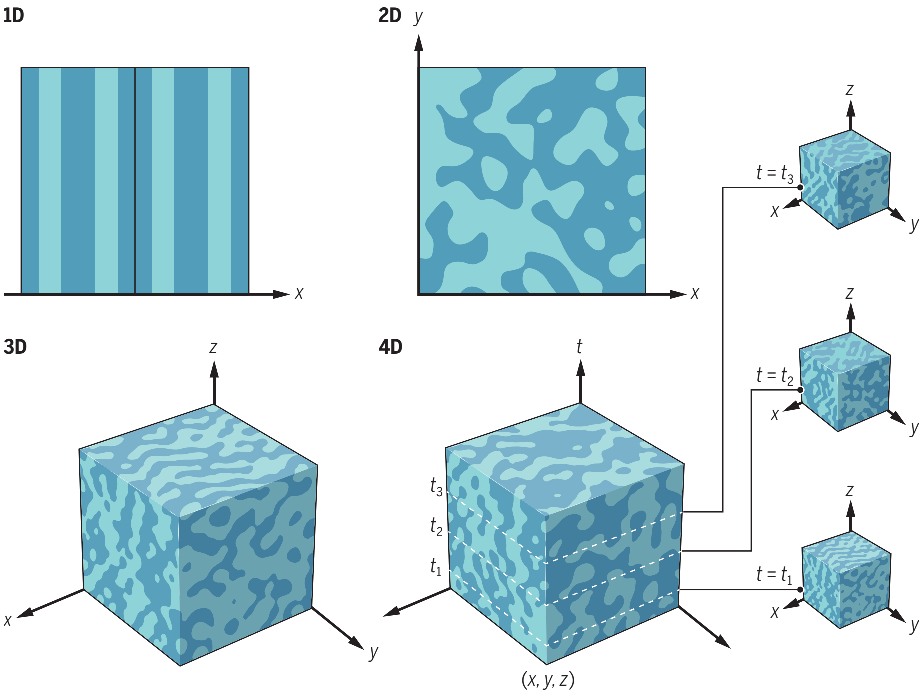
1. https://www.timeshighereducation.com/world-university-rankings/fujita-health-university
2. https://www.nature.com/articles/d41586-019-03459-7
3. https://www.mdpi.com/1660-4601/17/14/5221
4. https://link.springer.com/article/10.1007/s00455-021-10288-2
5. https://link.springer.com/article/10.1007/s00423-022-02710-6
6. https://link.springer.com/article/10.1007/s00330-022-08877-2

Sponsored by

FUJITA HEALTH UNIVERSITY

Material platform for optics

One-dimensional (1D), two-dimensional (2D), three-dimensional (3D), and four-dimensional (4D) variation of parameters in material structures can alter optical waves in different ways. 1D, 2D, and 3D platforms involve time-invariant material variation in space (*x, y, z*), whereas 4D materials change with time (t_1, t_2, or t_3) and vary in space (*x, y, z*). The boundaries between the different colors are examples of spatial interfaces, whereas the white dashed lines are examples of temporal interfaces.



GRAPHIC: A. FISHER/*SCIENCE* BASED ON N. ENGHETA

the energy required to change the material can affect the electromagnetic wave energy, causing the wave energy to increase or decrease. This feature underlies the mechanism behind phenomena such as the Faraday instability (*4*), which was recently used for the phase conjugation in water waves to refocus a diverging wave to its original source (*4*), and the parametric amplification. The latter relates to the recent proposal on light amplification in photonic time crystals, where the emission from a source inside such structures is enhanced owing to the temporal modulation of the material parameter (*5*).

It is important to note that although various wave features related to space and time have certain symmetries in electrodynamics, the ones resulting from temporal interfaces must follow the causality and can break the time-reversal symmetry. Consequently, time-varying platforms can provide mechanisms for breaking reciprocity, leading to methods for designing magnet-free nonreciprocal structures (*6*). Spatiotemporal materials can also become a test bed for exploring some of the relativistic phenomena, such as the Fresnel drag (*7*), superluminal and subluminal features (*8*), and the Doppler cloaks (*9*).

Four-dimensional metamaterials have already shown promising applications, such as time reversal (*3*), nonreciprocity (*6*), temporal aiming, and antireflection temporal coating (*10*), but the future may bring even more exciting directions. Merging spatial and temporal interfaces may open a new horizon in 4D optics, in which some of the features of both interfaces can be exploited. Mixing amplitude and frequency modulations can be considered in such scenarios. Another possible direction may be to bring synthetic dimensions (*11*) into 4D metamaterials. Synthetic dimensions offer additional dimensionalities beyond the conventional (3D) geometrical dimensionality in physical structures (*11*). Photonic structures with such synthetic dimensions, when combined with 4D metamaterials, may result in even higher (N)–dimensional photonics (ND optics), which may lead to interesting research directions for exploring possible bandgap features in higher (synthetic)–dimensional structures.

Metasurfaces, which are the 2D version of metamaterials, have undergone substantial recent development in terms of scalable nanofabrication and various applications in imaging and sensing. This is partly because metasurfaces can be constructed with available nanofabrication technology. Therefore, one spatial dimension was sacrificed in favor of technological development in manufacturing. A similar trend for 4D optics has already started: Spatiotemporal metasurfaces are being developed in which one spatial dimension has been removed in favor of getting access to the 2D surfaces in which the material parameters can be changed in time (*12*, *13*). A higher degree of freedom can be achieved when the temporal interface involves changing material parameters from an isotropic to an anisotropic scenario (*10*). This leads to interesting phenomena such as the inverse prism (*14*), in which a monochromatic signal propagating in various directions can, upon interaction with a temporal interface, become a signal whose frequency depends on its direction of propagation. Expanding the idea of transformation optics, in which spatial inhomogeneity and anisotropy can tailor electromagnetic fields and waves in desirable fashion, into four dimensions will likely open doors to richer light–matter interaction.

Perhaps in the future, 4D optics may also be exploited for connection to 4D imaging of transient structures with electron microscopy (*15*). Furthermore, the temporal interface could also become the basis for new devices and components, which could be further enhanced when hybrid combinations of spatial and temporal interfaces are considered. ■

REFERENCES AND NOTES

1. L. A. Zadeh, *Proc. IRE* **38**, 291 (1950).
2. F. Morgenthaler, *IRE Trans. Microw. Theory Tech*. **6**, 167 (1958).
3. V. Bacot, M. Labousse, A. Eddi, M. Fink, E. Fort, *Nat. Phys*. **12**, 972 (2016).
4. V. Bacot, G. Durey, A. Eddi, M. Fink, E. Fort, *Proc. Natl. Acad. Sci. U.S.A*. **116**, 8809 (2019).
5. M. Lyubarov *et al*., *Science* **377**, 425 (2022).
6. D. Sounas, A. Alu, *Nat. Photonics* **11**, 774 (2017).
7. P. A. Huidobro, E. Galiffi, S. Guenneau, R. V. Craster, J. B. Pendry, *Proc. Natl. Acad. Sci. U.S.A*. **116**, 24943 (2019).
8. P. A. Huidobro, M. G. Silveirinha, E. Galiffi, J. B. Pendry, *Phys. Rev. Appl*. **16**, 014044 (2021).
9. D. Ramaccia, D. L. Sounas, A. Alù, A. Toscano, F. Bilotti, *Phys. Rev. B* **95**, 075113 (2017).
10. V. Pacheco- Peña, D. M. Solís, N. Engheta, *Opt. Mater. Express* **12**, 3829 (2022).
11. L. Yuan, Q. Lin, M. Xiao, S. Fan, *Optica* **5**, 1396 (2018).
12. Y. Hadad, D. L. Sounas, A. Alu, *Phys. Rev. B Condens. Matter Mater. Phys*. **92**, 100304 (2015).
13. A. Shaltout, A. Kildishev, V. Shalaev, *Opt. Mater. Express* **5**, 2459 (2015).
14. A. Akbarzadeh, N. Chamanara, C. Caloz, *Opt. Lett*. **43**, 3297 (2018).
15. B. Barwick, H. S. Park, O.-H. Kwon, J. S. Baskin, A. H. Zewail, *Science* **322**, 1227 (2008).

ACKNOWLEDGMENTS

Thanks to D. Tzarouchis for assistance with the figure. N. E. acknowledges partial support from the Simons Foundation/Collaboration on Symmetry-Driven Extreme Wave Phenomena (grant 733684). N.E. is a strategic scientific adviser and consultant to Meta Materials, Inc.

10.1126/science.adf1094

POLICY FORUM

NATURAL HISTORY

A global approach for natural history museum collections

Integration of the world's natural history collections can provide a resource for decision-makers

By Kirk R. Johnson[1], Ian F. P. Owens[2], the Global Collection Group

Over the past three centuries, people have collected objects and specimens and placed them in natural history museums throughout the world. Taken as a whole, this global collection is the physical basis for our understanding of the natural world and our place in it, an unparalleled source of information that is directly relevant to issues as diverse as wildlife conservation, climate change, pandemic preparedness, food security, invasive species, rare minerals, and the bioeconomy (*1*). Strategic coordination and use of the global collection has the potential to focus future collecting and guide decisions that are relevant to the future of humanity and biodiversity. To begin to map the aggregate holdings of the global collection, we describe here a simple and fast method to assess the contents of any natural history museum, and report results based on our assessment of 73 of the world's largest natural history museums and herbaria from 28 countries.

Today, more than a thousand natural history museums exist, with the largest ones located in Europe and North America. The world's natural history collections provide a window into the planet's past and present, and they are increasingly being used to make actionable predictions relative to climate change, biodiversity loss, and infectious disease. For example, natural history museum data are the fundamental source of primary biodiversity knowledge underlying major policy frameworks. The 2018 Intergovernmental Panel on Climate Change (IPCC) Special Report on Global Warming of 1.5°C used over 385 million species occurrence records, aggregated and tracked by the Global Biodiversity Information Facility (GBIF), from 5432 data providers, mostly natural history museums (*2, 3*), to show species movement in response to climate change [see supplementary materials (SM) for additional case studies].

Yet despite their enormous potential value to society, the information embedded in the collections housed in these museums is largely inaccessible. Fortunately, advances in digital, isotopic, imaging, and genomic technologies, as well as machine learning and artificial intelligence, are transforming and amplifying how natural history collections can be accessed and used (*1*). These innovations are substantially broadening the range of possible applications to include human health, cultural revitalization, and environmental monitoring. Increasingly, Indigenous interlocuters are joining these conversations and enriching them (*4, 5*).

In the past few decades, several networks have increased cooperation between biodiversity-based institutions around the world. In addition to GBIF, the Taxonomic Databases Working Group (TDWG), the Global Genome Biodiversity Network (GGBN), the Catalogue of Life (COL), the Earth BioGenome Project (EBP), the International Barcode of Life (iBOL), and the Biodiversity Heritage Library (BHL) have provided global leadership for integrating specimen data, taxonomic observations, genomes, and published literature on the natural world. Guiding principles for governing such data have emerged for traditional [e.g., FAIR (*6*)] and nontraditional users [e.g., CARE (*4*)]. Atlas of Living Australia (ALA) and Integrated Digitized Biocollections (iDigBio) in the United States represent successful national programs that develop innovative solutions to support collection digitization, data integration, and mobilization. They have fostered integration among stakeholders by making large datasets readily accessible. Other successful initiatives include the South African National Biodiversity Institute (SANBI) network, speciesLink (CRIA) in Brazil, and the National Commission for the Knowledge and Use of Biodiversity (CONABIO) in Mexico.

Although these institutions and efforts are playing vital roles in aggregating data, they do not create the collections and fill gaps therein. It is the natural history museums that actively curate and expand the collections. Thus, it falls on the museums to lead the way to deploy strategic collecting in service of future collection and policy outcomes. It will not be possible to do this unless museums understand the present scope of the global collection and thus its gaps. Yet natural history museums have generally operated independently, and no interoperable data structure exists to provide open access to their collective holdings. Because most natural history museum data are not digitally discoverable, the networks of data aggregators have not been able to access these "dark data" (*7*), the majority of museum specimens and objects that are the physical basis of natural history and cultural knowledge.

As the first step toward building a global network, we worked with the directors and lead science and collection staff of 73 of the world's largest natural history museums and herbaria from 28 countries to design and complete a simple and rapid survey of their collective holdings (see the first figure). Until now, it has been difficult to enumerate or compare the complete contents of large museums because their collections are not fully digitized, and the terminology used to describe subcollections is variable. Each of the 73 museums did report a total specimen count, and the sum of these counts was 1,147,934,687. We then subdivided this aggregate collection by creating a shared vocabulary for collection types and their geographic source areas. The result is a grid of 19 collection types by 16 geographic regions, such that any collection object from anywhere in the world would fall into only one of the resulting 304 cells (e.g., African insects; see the second figure). For this effort, the term "collection unit" represents a single museum's holdings within a single cell.

We then worked with expert staff from each museum to estimate the number of objects in each collection unit to the nearest order of magnitude (see the second figure). Because it is based on curatorial knowledge of each collection rather than catalog records, this approach is very rapid (<2 weeks for most museums). The value of this coarse-grained approach is that it allows museums to identify their largest collection units and define the strengths of their collections relative to those at other museums.

Heat mapping of collection units demonstrates the aggregated effort of the sampled museums and highlights regional and taxonomic focal areas and gaps (see the second figure). Most of the collection information that we surveyed is not digitally accessible: Only 16% of the objects have digitally discoverable records, and only 0.2% of biological

[1]National Museum of Natural History (NMNH), Smithsonian Institution, Washington, DC, USA. [2]Cornell Laboratory of Ornithology, Cornell University, Ithaca, NY, USA. The Global Collection Group members and affiliations are listed in the supplementary materials. Email: johnsonkr@si.edu

collections have accessible genomic records.

We also surveyed the size and age distribution of the museum workforce that studies and cares for collections and that makes them available to the global community of users and found that the collections at the 73 museums and herbaria were tended by over 4500 science staff and nearly 4000 volunteers. See SM for further details on methods and data.

ACTIVATING THE GLOBAL COLLECTION

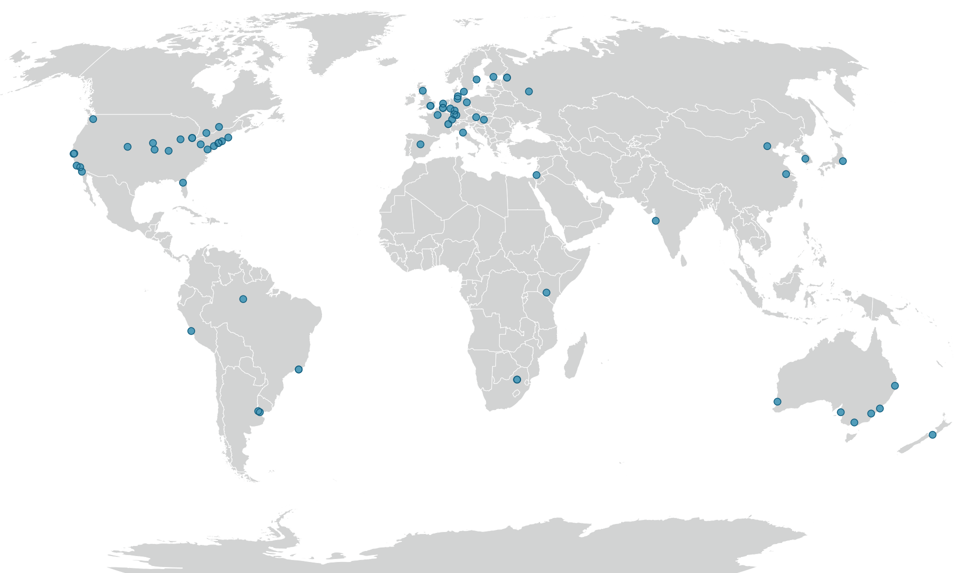
Our assessment allowed us to begin to map the aggregate holdings of the global collection, including the source areas and present locations of >1 billion objects (see the second figure and figs. S1 and S2). At the same time, it revealed many gaps, challenges, and opportunities. Work now needs to happen at a pace and magnitude that will meet the urgency of the Anthropocene and with the understanding that there are more species at risk of extinction than are currently known to science. Yet despite their potential value, natural history collections are at risk. Fires, natural disasters, and human conflicts can damage and destroy collections. Less pronounced degradation and destruction occur because of long-term underinvestment in infrastructure and expertise (*1*). We must invest in protecting and preserving these collections, and in expanding and integrating them, and associated expertise, with focused collecting efforts and new technologies such as genomics, environmental DNA, and artificial intelligence.

The concentration of the largest collections in European and North American cities remains a major barrier to connecting much of the world with its natural heritage, exacerbating the societal wrongs of colonial history in museum science. The same is true for museum expertise, where there is underinvestment relative to the potential of the collections and opportunities for training (fig. S3). Such support and coordination will be essential to overcome imbalances in information, expertise, and cultural differences.

Looking forward, we make the following recommendations [in line with those articulated in (*1, 8, 9*)] as a roadmap for museums, funders, governments, and industry to accelerate and coordinate their efforts while there is a window of opportunity in the next few decades to alter the trajectories of climate change and biodiversity loss.

Locations of participating natural history museums

These 73 museums (●) collectively hold more than 1.1 billion objects.



Collecting in a rapidly changing planet

In the year 2100, scientists and policy-makers will look back to the collections made in the 21st century to inform their decisions about the 22nd century. Natural history museums must thus focus on the future. For example, the recent Global Biodiversity Framework (*10*) bridges the Convention on Biological Diversity, the Intergovernmental Panel on Biodiversity and Ecosystem Services, and other efforts by goal-setting 2030 as the time frame for changing trends in biodiversity loss. This is an opportunity to integrate museum datasets with conservation efforts. Yet even now, many regions of the world and many biological groups remain insufficiently studied and documented. Further analysis of the global collection will refine our understanding of the gaps and provide a roadmap for future collecting efforts. Toward that end, it is our intention to work with GBIF to make our data available to all natural history museums by integrating it with the Global Registry of Scientific Collections (GRSciColl).

For example, although our data show that the scale of the global collection is vast, it also highlights conspicuous gaps with respect to tropical and polar regions, marine systems, and undiscovered arthropod and microbial diversity. Also, our study does not address the hundreds of smaller museums, their collections, and their staffs, which comprise the rest of the global collection; these are especially valuable because of their regional holdings and the specificity of their expertise (*8*). Further, many current data aggregation efforts have largely focused on biodiversity and have been less inclusive of data from Earth and planetary sciences and anthropology—two fields that are traditionally major components of natural history collections.

New roles for old institutions

The collections that natural history museums acquired over the past three centuries carry data that cannot be replicated but can be used as baselines for efforts to regenerate ecosystems and revitalize communities. To facilitate efforts to preserve, protect, and expand collections, natural history museums must coordinate with initiatives such as GBIF, ALA, iDigBio, Distributed System of Scientific Collections (DiSSCo), and Biodiversity Collections Network (BCoN) to accelerate data practices, data sharing, and data stewardship in common knowledge platforms that provide an open informatics infrastructure to build a network of extended digital specimens (*9*). This step will happen through (i) digitization, which is ongoing and should be accelerated through high-throughput pipelines (e.g., conveyor belts capable of imaging >6000 herbarium sheets per day) and by prioritizing collections that have the greatest potential to mitigate global crises; (ii) genomic collections (including collections of frozen gametes and stem cells), which can be coordinated with the EBP and GGBN to facilitate sequencing of genomes across the tree of life; (iii) informatics, which can illuminate and interlink collections, making their information available for societal benefit; and (iv) training and capacity building, which can deliver reciprocal benefits, expertise, and the democratization of access to technologies.

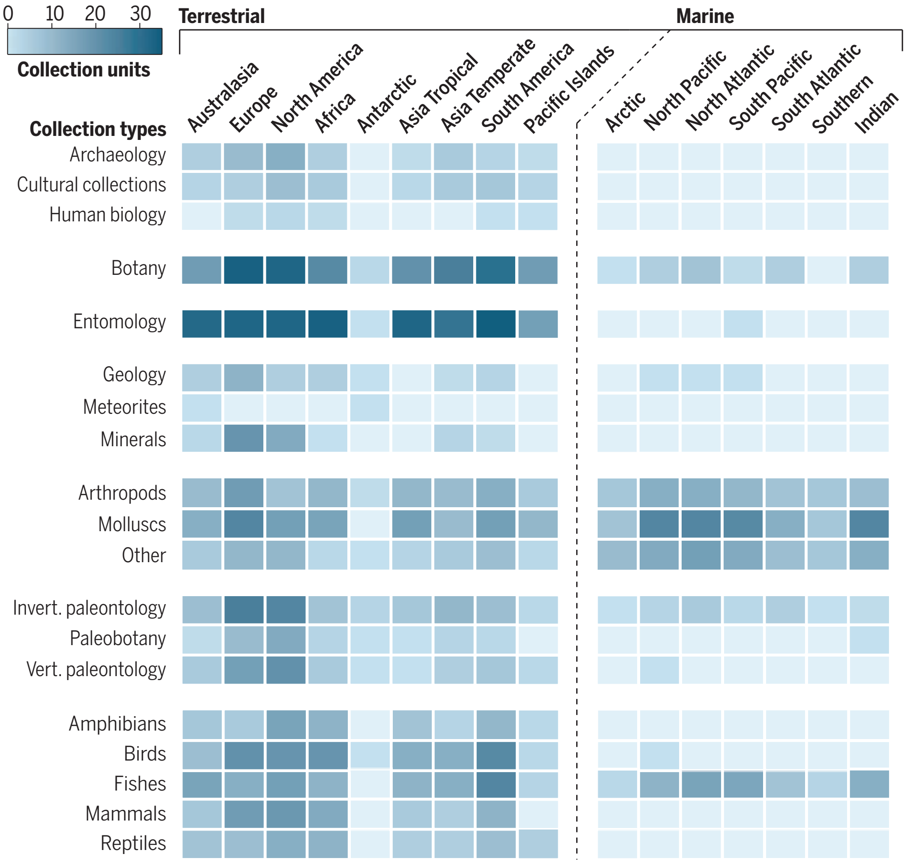
Evolving ethics

Many historical practices used to acquire collections do not meet today's values and

GRAPHIC: D. AN-PHAM/*SCIENCE*

Heatmap of global collection units

Any collection object in any museum can be categorized into only one of the 304 cells (19 collection types by 16 geographic regions). A "collection unit" is a single museum's holdings within a single cell. For 73 museums, there are 22,192 possible collection units. The heatmap shows the 1957 collection units with more than 10,000 objects. See supplementary materials for details and for a heatmap of the 242 collection units with more than 1 million objects.



GRAPHIC: D. AN-PHAM/*SCIENCE*

ethical standards for social and environmental justice. Many collections hold objects that may have been collected without prior consent, without permission from source communities, or without full recognition of contributors and cultural sensitivities (*4, 5, 11*). To redress past injustices, museums must engage with source communities to understand their perspectives and needs regarding objects and their associated metadata that may include sensitive cultural or ecological knowledge (*4, 12*). Ethical collecting in the 21st century requires local community engagement and benefit sharing that will also inspire and train the next generation of global scientists. There has been progress in this arena through national and international return efforts, which are largely focused on human remains and cultural artifacts (*13*), and there is increasing willingness to scrutinize the provenance of nonanthropological collections. The concept of shared stewardship is emerging as an opportunity to forge new partnerships around collection items where there are opportunities for mutual benefit. Growth and use of museum collections will be delayed or derailed unless there is real progress in this realm.

INTEGRATING INFRASTRUCTURE

The natural history museums of the world all hold portions of the global collection, a fact that argues for a new age of networked museums whose goal is to exceed the sum of their parts by strategic use of existing collections and thoughtful coordination of future collecting efforts. Yet despite several country-level initiatives to digitize specimens, most museum specimen information remains dark data (*7*). There is no single shared portal covering the breadth of life, Earth, and anthropological specimens in natural history collections, nor a way for researchers to link these data with other sources of information. We envision a coordinated strategy for the global collection that is based on strategic collecting, increased digitization, new technologies, and enhanced networking and coordination of museums. This strategy must embrace smaller regional collections, which bridge global gaps and provide critical insights and local context with source communities and geographies. Integrating this global infrastructure will also improve long-standing inequities in training and career opportunities and elevate marginalized voices.

Natural history collections are a form of science infrastructure that is necessary to support society-wide solutions. We hope to catalyze collaborative collection-based efforts to support future global sustainability, biodiversity, and climate frameworks (*10*, *11*) and identify critical gaps that might preclude such impact. Such collection-based efforts are typically not high-level institutional priorities; thus, the involvement of museum leadership, such as in our effort, is critical, particularly for mobilizing resources and coordinating efforts to strategically fill gaps in collections. ■

REFERENCES AND NOTES

1. Committee on Biological Collections, Their Past, Present, and Future Contributions and Options for Sustaining Them, Board on Life Sciences, Division on Earth and Life Studies, National Academies of Sciences, Engineering, and Medicine, *Biological Collections: Ensuring Critical Research and Education for the 21st Century* (National Academies Press, 2020); https://www.nap.edu/catalog/25592.
2. R. Warren, J. Price, E. Graham, N. Forstenhaeusler, J. VanDerWal, *Science* **360**, 791 (2018).
3. IPCC, "Summary for Policymakers. Global Warming of 1.5°C: IPCC Special Report on impacts of global warming of 1.5°C above pre-industrial levels in context of strengthening response to climate change, sustainable development, and efforts to eradicate poverty" (Cambridge Univ. Press, 2018).
4. S. R. Carroll *et al.*, *Data Sci. J.* **19**, 43 (2020).
5. L. Liggins, M. Hudson, J. Anderson, *Mol. Ecol.* **30**, 2477 (2021).
6. M. D. Wilkinson *et al.*, *Sci. Data* **3**, 160018 (2016).
7. C. R. Marshall *et al.*, *Biol. Lett.* **14**, 20180431 (2018).
8. A. K. Monfils *et al.*, *Bioscience* **70**, 1045 (2020).
9. M. Webster, J. Buschbom, A. Hardisty, A. Bentley, *Biodivers. Inf. Sci. Stand.* **5**, e75736 (2021).
10. UNEP Press Release, "COP15: Nations Adopt Four Goals, 23 Targets for 2030 in Landmark UN Biodiversity Agreement"; https://www.cbd.int/article/cop15-cbd-press-release-final-19dec2022.
11. Secretariat of the Convention on Biological Diversity United Nations Environmental Programme, *Nagoya Protocol on Access to Genetic Resources and the Fair and Equitable Sharing of Benefits Arising from their Utilization to the Convention on Biological Diversity* (2011).
12. M. Hudson *et al.*, *Nat. Rev. Genet.* **21**, 377 (2020).
13. L. Wade, *Science* **373**, 148 (2021).

ACKNOWLEDGMENTS

The authors thank the collections staff from participating institutions for providing data from their collections. We thank GBIF, GGBN, Consortium of European Taxonomic Facilities (CETAF), and iDigBio for assistance with access to information. We thank C. Butler, R. Corrigan N. Drew, H. Little, C. A. Meyer, and R. Snyder at the NMNH and staff at the Natural History Museum (NHM), London, for their technical assistance with data collation and C. Baldwin, J. Bell, C. Dove, S. Miller, E. Stofan, I. Krupnik, and E. Strong for comments and advice. We thank G. Mérite for information design and data illustration of the figures. Funding was provided by NMNH, NHM London, and the American Museum of Natural History. Data for the global collections survey have been published under an open license (Creative Commons Attribution 4.0 International), and can be persistently accessed at https://doi.org/10.5281/zenodo.6985399. Any personally identifiable information was redacted from the dataset prior to publication. A visualization dashboard of these data can be accessed at https://rebrand.ly/global-collections.

SUPPLEMENTARY MATERIALS

science.org/doi/10.1126/science.adf6434

10.1126/science.adf6434



Working together, universities and the towns in which they reside can bring new energy to a community.

PHOTO: JACK LOONEY/ISTOCK

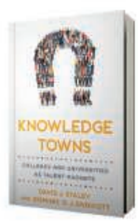
ACADEMIA

College towns as talent hubs

Communities can leverage institutions of higher education to lure knowledge workers to new regions

By **Jonathan Wai**

If you build it, they might come. That is the premise of *Knowledge Towns: Colleges and Universities as Talent Magnets* by historian David Staley and entrepreneur Dominic Endicott, which argues that US colleges and universities can be leveraged to attract white-collar workers recently released from on-site workplaces to new geographical regions, especially with buy-in from the communities in which these institutions are situated. The book is structured into four chapters, with each chapter introducing a core idea and then describing scenarios in which the idea might be applied.



Knowledge Towns
David J. Staley and Dominic D. J. Endicott
Johns Hopkins University Press, 2023. 256 pp.

In the introduction and chapter 1, Staley and Endicott introduce readers to their definition of "talent magnets"—describing them as towns or locations that have many qualities that make them attractive to talented people. They then outline how to create a talent magnet using 12 foundational principles. One example, "act local but harness the cloud," encourages communities to invest and hire locally but to also seek out remote workers looking to move to regions with a better cost of living than the one in which they currently reside. Another principle, "support the bionic worker," encourages communities to consider emerging technologies that seek to enhance productive partnerships between human workers and machines.

Next, the authors explore what they call "the knowledge enterprise," discussing how each of the principles introduced in the first chapter can be successfully applied by an academic institution. To "encourage lives of purpose, not of possessions," the authors suggest that the arts and humanities should be emphasized. To "harness the economic potential of the community," emphasis should be placed on reinforcing relationships among people who live and work in a particular community. For example, a university agricultural economist's knowledge and expertise might be fruitfully paired with that of local farmers.

Chapter 3 explores the simultaneous codevelopment of talent magnets and knowledge enterprises. Here, the authors describe how a community in which there is no college or university might start from scratch, outlining how an effective "town and gown" collaboration might be forged and how it might evolve across an entire state or region.

The authors then explore how different principles might be used in particular contexts. Here, they discuss a handful of possible futures, including so-called microcolleges, "echoing recent growth in microbreweries, microfactories, charter schools, and pod schools." These smaller, leaner institutions could bring new energy and experimentation to an underdeveloped region, they argue. In the book's final chapter, the authors bring all these ideas together, placing particular emphasis on the movement toward remote work and on the many changes currently underway at existing academic institutions.

Missing from this book is any real consideration of the core talent that already resides at institutions of higher education—the faculty that conduct the research that forms the stature of the university (*1*). In *The New Geography of Jobs*, economist Enrico Moretti explains that it is not the infrastructure that brings talent, it is talent that will build out the infrastructure (*2*).

Mobility has always been an expectation of becoming an academic. The journey often begins when one seeks admission to graduate school, and it continues as one proceeds to a postdoctoral fellowship and then on to a faculty position. In an increasingly competitive job market, the expectation that prospective employees will be able to relocate continues to affect who is able to rise through the ranks in the academic hierarchy. And yet the authors fail to discuss the benefits that a university and its surrounding community might derive from removing barriers to remote faculty appointments.

Also missing is a research-based definition of "talent" or even a reference to other recent treatments on the topic (*3*). Readers seeking a broader perspective on the current state of higher education may wish to consider the differing opinions of sociologists of education Steven Brint and David Labaree (*4*, *5*).

Despite these limitations, *Knowledge Towns* has many ideas that university administrators may find useful. This will likely prove especially true for those seeking to build a future where institutions and the communities in which they reside are better connected. ■

The reviewer is at the Department of Education Reform and Department of Psychology, University of Arkansas, Fayetteville, AR 72701, USA. Email: jwai@uark.edu

REFERENCES AND NOTES

1. Faculty Affairs Committee, Report to the Columbia Univ. Senate, 24 February 2017; http://senate.columbia.edu/archives/plenary/16-17/plenary_documents_16-17/fac_letter_to_bollinger_20170224.pdf.
2. E. Moretti, *The New Geography of Jobs* (Harper Business, 2013).
3. T. Cowen, D. Gross, *Talent* (St. Martin's Press, 2022).
4. S. Brint, *Two Cheers for Higher Education* (Princeton Univ. Press, 2019).
5. D. F. Labaree, *A Perfect Mess* (Univ. of Chicago Press, 2017).

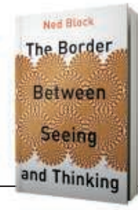
10.1126/science.adg8109

COGNITIVE SCIENCE

Seeing fast and thinking slow

A philosopher explores perception and cognition

The Border Between Seeing and Thinking
Ned Block
Oxford University Press, 2023. 560 pp.



By **Chaz Firestone** *and* **Ian Phillips**

Seeing is not believing, contrary to what popular idioms might claim. But what exactly is the difference? This question is the focus of *The Border Between Seeing and Thinking*, the long-awaited monograph by philosopher Ned Block.

The book's central theme is on display even before the first page: The cover features Akiyoshi Kitaoka's "rotating snakes" illusion—a psychedelic array of circles that appear to be moving, even though you know they cannot be. What you think about the circles differs from how you see them.

Precisely characterizing this difference is notoriously difficult, however. Imagine picking up your child from school. Light reflects off their face into your eyes. Their smile is broad, their eyebrows raised; you get the impression that they are happy. Why? Eventually, you work it out—they got their grades today and must have done well. But where did seeing end and thinking begin? Did you see your child's face as happy? Or did you only see their facial features and then infer what emotion they expressed? (Knowing which of your brain regions were active will not be enough to answer this question. That would require first establishing which activations counted as sight and which as thought, which turns on the very distinction at issue.)

Block proposes that we seek empirical "signatures" distinctive of seeing to adjudicate tricky cases. For example, seeing (unlike thinking) is extraordinarily fast: Open your eyes, and immediately you see your surroundings. By contrast, a scientist tasked with inferring your environment from your retinal input would need days.

Another signature is "pop-out": A lone red flower is easy to spot in a field of blues. But what about a single prime number in an array of nonprimes? Block doubts there is cognitive pop-out for the prime.



Do we "see" a face as happy or sad? Or do we see facial features and then "know" the person is happy or sad?

PHOTO: NISERIN/ISTOCKPHOTO

Block argues that the most important signature is adaptation. Stare at a blue surface for a minute, and what you see next looks yellower (blue's "opponent" color). Likewise, watching rightward motion makes stationary objects seem to move leftward. Block contends that adaptation is unique to perception: Thinking about blue does not somehow bias later thoughts yellow-ward.

Can this signature decide the tricky case of facial emotions? In Block's hands, the question becomes: Do happy faces cause adaptation? The remarkable answer is yes—staring at happy faces makes neutral faces look angry (*1*). Voilà: A scientifically grounded method to distinguish seeing and thinking (assuming that no cases of "cognitive adaptation" emerge to complicate matters).

Another puzzle Block pursues is whether we must be able to think about something in order to see it—a philosophical position known as conceptualism. Here, Block makes creative use of developmental psychology. Infants can see colors, as revealed by their tendency to look at an odd color out in an otherwise uniform array. But Block argues that the ability to conceptualize color only arises later. Infants who see colors just fine do not learn regularities about colors nor do they notice if objects magically change color (*2*). Block concludes that they cannot think about the colors they see; seeing is "nonconceptual." Of course, it is possible that infants can think about colors but just don't; and it is perhaps risky to generalize from infant color vision to vision tout court. But this is a fruitful inroad to a vexed philosophical issue.

Central to Block's project is an account of perception's underlying nature, explaining its distinctive signatures and content. For Block, perception fundamentally differs from thought in format. Consider how the same idea can be represented in different ways: A cat on a mat can be represented linguistically ("Fluffy is sitting on our Persian rug") or pictorially (a photograph of Fluffy atop the rug in question). Block argues that perception's format is exclusively picturelike, or iconic.

This allows perception to be rich and detailed. But a certain expressive power is absent from perception. For example, whereas language can represent disjunctions ("Fluffy is either on the rug or in the yard"), one cannot depict disjunctive scenarios. However, we should distinguish between vision using iconic representations and always being iconic. There is evidence that we perceive causal relations, high-level categories, and even possibilities (*3*); it is not obvious how iconic formats can accommodate this.

The great virtue of Block's discussion is its blending of philosophy and science, instigating an exciting empirical agenda to test his claims. Does cognition never adapt? Do all perceptual properties adapt? Do Block's signatures generalize to nonhuman animals, artificial systems, or other senses? Can iconicity account for the full breadth of visual representation? Whatever the answers, Block's approach offers deep insight into two fundamentally different aspects of mind. ■

The reviewers are at the Department of Psychological and Brain Sciences and Department of Philosophy, Johns Hopkins University, Baltimore, MD 21218, USA. Email: chaz@jhu.edu; ianbphillips@jhu.edu

REFERENCES AND NOTES

1. A. Butler *et al.*, *Brain Res.* **1191**, 116 (2008).
2. T. Wilcox, *Cognition* **72**, 125 (1999).
3. A. Hafri, C. Firestone, *Trends Cogn. Sci.* **25**, 475 (2021).

10.1126/science.adg8153

LETTERS



New South Wales, Australia needs policies to protect all koalas, not just those on public lands.

Edited by Jennifer Sills

Beyond protected areas for koala conservation

Australia recently declared the koala (*Phascolarctos cinereus*) an endangered species in Queensland, the Australian Capital Territory, and New South Wales (NSW) because of its stark population decline (*1*, *2*). In the state of NSW, koala conservation has become a key topic of discussion in the lead-up to the 25 March state election (*3*). However, the debate has focused on the expansion of protected areas and overlooked the importance of private land conservation and regulation.

The primary cause of the koala's decline—in addition to climate change, wildfire, disease, and encounters with vehicles and dogs—is the loss and degradation of suitable habitat (*1*). In response, the NSW Government has expanded publicly protected areas in the state. Over the past 20 years—about three koala generations (*1*, *2*)—NSW has designated an additional 1.5 million ha of protected land (*4*), some of which is high-quality koala habitat [e.g., (*5*)].

However, across Queensland, the Australian Capital Territory, and NSW, 77% of the koala's range is located on land that is owned or leased by private citizens or businesses (*6*), where degradation continues. Between 2003 and 2020, agriculture, forestry, and infrastructure development have led to the deforestation of 760,500 ha in NSW (*7*), including in regions such as the Cumberland Plain (*8*) and Liverpool Plains (*9*), where koalas are known to live. Such development has counteracted the gains made through new protected areas.

An effective koala conservation strategy must include private protected areas and other area-based conservation mechanisms, such as payments for ecosystem services (*9*–*11*), in addition to publicly protected areas. The current NSW Koala Strategy (*12*) acknowledges the importance of private lands, but its activities are limited largely to nonregulatory mechanisms. This approach leaves much of koala habitat conservation to the discretion of private landowners, leaseholders, and industry. Post-election agendas must enhance private land conservation as well as strengthen regulatory protection of koala habitat.

Brooke A. Williams*, Courtney Morgans, Jonathan R. Rhodes
School of Earth and Environmental Sciences and Centre for Biodiversity and Conservation Science, The University of Queensland, St. Lucia, QLD, Australia.
*Corresponding author.
Email: brooke.williams@uq.edu.au

REFERENCES AND NOTES

1. Australian Government Department of Agriculture, Water, and Environment, "Conservation Advice for *Phascolarctos cinereus* (Koala) combined populations of Queensland, New South Wales and the Australian Capital Territory" (2022); https://www.environment.gov.au/biodiversity/threatened/species/pubs/85104-conservation-advice-12022022.pdf.
2. C. Adams-Hosking *et al.*, *Divers. Distrib.* **22**, 249 (2016).
3. "Is a mega-sanctuary the answer to saving koalas?," *ABC News* (2023); https://www.abc.net.au/news/2023-01-20/is-a-mega-sanctuary-the-answer-to-saving-koalas/101875214.
4. NSW National Parks and Wildlife Service (NPWS) Estate (2022); https://datasets.seed.nsw.gov.au/dataset/nsw-national-parks-and-wildlife-service-npws-estate3f9e7. To find the total area of protected land added since 2003, click "Dataset Packages," and then download the zip file by clicking the download icon to the right of "Download Package (Dissolved Internal Boundaries)." Click "Extract all" to access the files in the zip file. Then open NPWS_Estate.dbf in Excel. Sort by the column titled GAZ_DATE to find reserves added since 2003. For the 324 rows dated 2003 or later, find the sum of the areas listed in the GAZ_AREA column (1,507,791.224 ha).
5. NSW Government, "New koala country national park" (2020); https://www.nsw.gov.au/media-releases/new-koala-country-national-park.
6. S. G. Kearney *et al.*, *Conserv. Sci. Pract*. **4**, e617 (2022).
7. NSW Government, Statewide Landcover and Tree Study (SLATS)–Landcover Science (2022); https://www.environment.nsw.gov.au/topics/animals-and-plants/native-vegetation/landcover-science. To find the total deforestation for each year since 2003, click "Results woody vegetation change SLATS 2020 (XLSX 594KB)" (found under "Monitoring and reporting," "Vegetation change," in the "Statewide" tab) to download the Excel spreadsheet. Go to the tab labeled "Tab 1 – Statewide Rates." Find the total vegetation loss for years 2009 to 2020 in row 6 (516,300 ha). Add the total of years 2003 to 2008 in row 12 (244,200 ha) to get the total of 760,500 ha.
8. "Plan for 'sea of roofs' will destroy last koala habitat in western Sydney, critics say," *The Guardian* (2022).
9. J. R. Dargan *et al.*, *Anim. Conserv*. **22**, 543 (2019).
10. D. Lunney, A. Matthews, C. Moon, J. Turbill, *Ecol. Manage. Restor.* **3**, 90 (2002).
11. CBD, "First draft of the post-2020 Global Biodiversity Framework" (2021); https://www.cbd.int/doc/c/abb5/591f/2e46096d3f0330b08ce87a45/wg2020-03-03-en.pdf.
12. NSW Government, "NSW Koala Strategy—Towards doubling the number of koalas in New South Wales by 2050" (2022); https://www.environment.nsw.gov.au/-/media/OEH/Corporate-Site/Documents/Animals-and-plants/Threatened-species/koala-strategy-2022-220075.pdf.

COMPETING INTERESTS

J.R.R. is a member of the New South Wales Government's Koala Expert Panel.

Published online 16 March 2023
10.1126/science.adh4128

PHOTO: COURTNEY MORGANS

Storylistening's role in policy advice

In their Policy Forum, "'Storylistening' in the science policy ecosystem" (13 January, p. 134), C. Craig and S. Dillon explain how the expert evaluation of narratives can facilitate the delivery of humanistic and social science advice for public policy on a range of issues, including those to which scientific advice is also pertinent. Choices about which problems scientists prioritize and which solutions policymakers select are infused with public values (*1*). Capturing these values can be as challenging as doing the science itself, so any process that makes decision-making more systematic and transparent, as storylistening is supposed to do, is welcome. However, as Craig and Dillon acknowledge, stories often do not tell the truth. In addition, stories do not always reflect universal values. Therefore, caution should be exercised when using the storylistening approach in policy advisory systems.

Science delivers options, not solutions. Analysis of narratives that relate to the policy area can be an important way of informing these choices. However, because stories are not bound by truth, the storylistening approach should be used to provide context rather than to design policies. For example, in biodiversity management, there are, rightly, increasing calls for the integration of Indigenous peoples into the policy-forming process (*2*). Indigenous peoples' long history of experience and spiritual values should help identify protection goals. But only evidence collected through the scientific process can determine how to save a valued species from overexploitation or exposure to pollutants.

The storylistening approach also requires an analysis of whether the values of those telling the stories match the values of those affected by the policies. For example, some stories related to biodiversity protection will reflect post-colonial values, whereas others will reflect values of Indigenous populations (*2*). The values of those doing the science or analyzing the narratives might differ from one or both. Which should prevail? In representative democracies, decisions are often made for us by elected officials and their technical advisers. But that has led to frustrations, especially when there is a sense of technocratic elitism (*3*). To make the process more open and inclusive, some embrace more informed and deliberative democracies (*4*), which involve citizen forums (*5*, *6*). I agree with Craig and Dillon that storylistening is a way to make the outcome of such discussions more transparent and rigorous.

Developing a system of science advice in public policy that satisfies most or all of those affected remains a challenge. Surely, the humanities have a part to play, as Craig and Dillon explain. However, these techniques should not be "embedded" in the policy advisory system. Stories should not be treated as evidence, and whose perspectives and preferences stories communicate must be clear. Used with caution, storylistening can complement rather than undermine the process of delivering solutions that work.

Peter Calow
Humphrey School of Public Affairs, University of Minnesota, Minneapolis, MN 55455, USA. Email: pcalow@umn.edu

REFERENCES AND NOTES

1. R. A. Pielke, *The Honest Broker* (Cambridge University Press, Cambridge, UK, 2007).
2. A. Antonelli, *Nature* **613**, 239 (2023).
3. P. Calow, *Integrated Environ. Assess. Manage.* **16**, 8 (2020).
4. *Nature* **588**, 370 (2020).
5. J. Fishkin, A. Siu, L. Diamond, N. Bradburn, *Am. Polit. Sci. Rev.* **115**, 1 (2021).
6. A. Taeihagh, *Pol. Sci.* **50**, 629 (2017).

10.1126/science.adg8025

Response

We agree with Calow that caution should be exercised when using storylistening in policy advisory systems. The same is true of all forms of evidence. Effective advisory systems that incorporate the natural, physical, and life sciences use mechanisms carefully calibrated to identify, synthesize, authenticate, challenge, and review such evidence. We advocate extending these mechanisms to the humanities and, in the case of storylistening, to the creation and use of narrative evidence.

Calow focuses on the relationship between stories and values. Stories can indeed provide insight into ethics and worldviews, but storylistening's role is to gather evidence, not to adjudicate the politics of value negotiation or value alignment in final decision-making. Moreover, stories are useful to public reasoning beyond the insight into judgments or principles they might offer. For example, the UK Ministry of Defence has deployed "useful fiction," in the form of commissioned short stories, to anticipate the military, political, social, and economic impacts of future transformative technologies such as quantum technology, artificial intelligence, cyberpsychology, drones, and human enhancement (*1*). Stories that are not true can contain truths and useful information.

In Calow's example of biodiversity management and Indigenous knowledge, stories—including, but not exclusively, those of Indigenous peoples—can contribute to more than goal setting. Narrative evidence can be used to inform decisions on how to frame the system, to understand the collective identities in play, to extend the range of models for potential policy options, and to anticipate outcomes. For example, narrative evidence might help inform what types of scientific evidence to collect, identify gaps in scientific models, and challenge the understanding of what systems should be considered. Knowledge gained from stories can also play a part in developing and potentially testing solutions, always alongside the science. Recent collaborations between scientists and Indigenous populations demonstrate how Indigenous knowledge (often narrative in form) can provide evidence to coproduce knowledge to inform environmental decision-making (*2*).

Storylistening is not about better framing of the science (that's storytelling), nor a form of or contribution to science communication (also storytelling). It is about recognizing that the knowledge stories contain and provide gives them worth—i.e, cognitive value—and that narrative evidence can indeed form part of a pluralistic evidence base. The rigorous structures of advisory systems, extended to storylistening, serve to guarantee the robustness of evidence, including narrative evidence, gathered. Embedding storylistening in such systems, as well as encouraging widespread narrative literacy so that people better understand how stories function and their effects at individual and collective levels, can ensure that the cognitive value of stories is properly accessed. Narratives are too important and convey too much information about the world to be excluded from public reasoning.

Claire Craig[1]* and Sarah Dillon[2]
[1]The Queen's College, University of Oxford, Oxford, UK. [2]Faculty of English, University of Cambridge, Cambridge, UK.
*Corresponding author.
Email: claire.craig@queens.ox.ac.uk

REFERENCES AND NOTES

1. P. W. Singer, A. Cole, "Stories from tomorrow: Exploring new technology through useful fiction" (UK Ministry of Defence, 2021); https://assets.publishing.service.gov.uk/government/uploads/system/uploads/attachment_data/file/1138973/Stories_From_Tomorrow_FINAL-web_issue.pdf.
2. R. Bronen *et al.*, *Pol. Geogr.* **43**, 188 (2019).

10.1126/science.adh4233

RESEARCH

IN *SCIENCE* JOURNALS

Edited by **Michael Funk**



CLIMATE ADAPTATION

Mismatch fix

A wide array of mammal species have adapted seasonal coat color change, shifting from brownish summer coats to white-ish winter coats to match their environment. Climate change has already begun to affect the extent and timing of snow cover, leaving many individuals and populations now mismatched to their backgrounds for part of the year. Ferreira *et al*. looked at the genetics underlying these coat color changes and their variation across populations in white-tailed jack rabbits. Patterns of variation at three specific genes drove coat color change and differed across populations. Models suggest that standing variation across these genes and populations may allow for rapid adaptation to reduced snow cover and browner coats in this species. —SNV

Science, ade3984, this issue p. 1238

Populations of white-tailed jack rabbits, such as the one pictured above in Montana, are under selective pressure to better match coat color to reduced snow cover.

PHOTO: DONALD M. JONES/MINDEN PICTURES

KONDO INSULATORS

Metallic puddles in an insulator

Certain properties of metals can oscillate as a function of applied magnetic fields, a phenomenon known as quantum oscillations. This process should not happen in insulators, which is what made the observation of quantum oscillations in the Kondo insulator samarium hexaboride so surprising. Multiple mechanisms, both intrinsic and extrinsic, have been proposed to explain these findings. Pirie *et al*. used scanning tunneling microscopy to study the vicinity of defects, including substitutions and vacancies. They found that the defects caused the formation of localized metallic puddles, which could explain the previously observed metal-like properties of this insulator. —JS

Science, abq5375, this issue p. 1214

MOLECULAR BIOLOGY

Chromatin retention of Pol V

A plant atypical RNA polymerase, Pol V, specifically synthesizes the scaffold long noncoding RNA for recruiting downstream effectors to chromatin to mediate DNA methylation. Xie *et al*. report the structure of a cauliflower Pol V in elongation conformation. Distinct from Pol II, the second subunit of Pol V, NRPE2, specifically stacks with the upcoming double-stranded DNA branch to attenuate transcription and captures the nontemplate DNA strand of the transcription bubble to enhance the backtracking, suggesting a chromatin retention mechanism underlying the scaffold function of Pol V. —DJ

Science, adf8231, this issue p. 1209

3D POROUS MATERIALS

Rational inverse design of 3D shapes

Nature has a wide range of tools for making cellular microstructures, such as those found in flowers, leaves, and other biological tissues. Despite advances in printing techniques, patterning porous curved surfaces can be challenging. Cheng *et al*. developed an inverse design method to achieve complex three-dimensional (3D) surfaces through a subset of 2D films that are bonded together. Analytic modeling and computations to inverse

design the 2D patterns allow for control of the final porosity. A wide range of examples is provided, including changes in the sign of the curvature. These structures can be fabricated from silicon, metals, chitosan, and polymers. —MSL

Science, adf3824, this issue p. 1225

3D PRINTING

Overcoming challenges with silicone

Silicone elastomers are used in a wide range of applications because of their resistance to heat, moisture, and chemical agents. However, three-dimensional (3D) printing with silicone is challenging because of the interfacial behavior of the precursors. Duraivel *et al*. present a method to 3D print precise, free-standing, highly detailed objects out of silicone-based materials by using densely packed emulsions surrounded by a silicone oil continuous phase as the support material. This technique allows for precise control over the interfacial tension between the support material and the printing fluid. The authors demonstrated that they could print features as small as four micrometers, as well as mechanically robust, thin-walled, accurate models of human vasculature. —MSL

Science, ade4441, this issue p. 1248

NEUROIMMUNOLOGY

Anaphylaxis brings on a chill

A prominent symptom of immunoglobulin E (IgE)–induced anaphylaxis in rodents is a profound drop in the core body temperature. Bao *et al*. used mouse models to explore the role of neural pathways in connecting antigen-induced cross-linking of IgE receptors on mast cells and subsequent mast cell degranulation in the development of hypothermia. They discovered that chymase, a mast cell–derived protease, activated heat-sensitive TRPV1$^+$ neurons through the PAR1 receptor, triggering a neural circuit that rapidly led to reduced heat generation by brown adipose tissue. These findings identify heat-sensing neurons as key contributors to the manifestations of anaphylaxis and suggest potential therapeutic targets for additional treatments aimed at reversing life-threatening symptoms associated with anaphylaxis. —IRW

Sci. Immunol. **8**, eadc9417 (2023).

FERROELECTRICS

A polarizing thin film

Shrinking the footprint of electronics may require coming up with ferroelectrics that retain their properties down to nanometer-thickness films. Yang *et al*. add to a growing list of materials that retain ferroelectricity at these small length scales. The authors found a ferroelectric bismuth oxide structure that they stabilized with a small amount of samarium substitution. When coated on a substrate, the ferroelectric behavior persists down to one nanometer. The relatively high polarization makes these films good candidates for a variety of applications. —BG

Science, abm5134, this issue p. 1218

VENUS

Signs of volcanic activity on Venus

Numerous volcanoes have been identified on the surface of Venus, but none has been observed to erupt, so it has been unclear whether volcanic activity has ceased. Herrick and Hensley examined locations on Venus that were observed two or three times by the radar instrument on the Magellan spacecraft when it was searching for changes between the images caused by ongoing volcanic activity. The authors identified a volcanic vent that enlarged and changed shape in the 8-month gap between two radar images and a possible lava flow running downhill from the vent. The results are interpreted as active volcanism on Venus. —KTS

Science, abm7735, this issue p. 1205

IN OTHER JOURNALS

Edited by **Caroline Ash** *and* **Jesse Smith**



PHOTO: ISAAC LICHTER-MARCK

ECOLOGY

Growing in a glacier's wake

Glaciers are retreating worldwide, leaving behind inorganic sediments that support new, rapidly changing ecosystems. These glacial forelands are constantly eroded by water and wind until they are eventually stabilized by vegetation. Eichel *et al.* compared patterns of disturbance and vegetation across two glacial forelands in New Zealand and Switzerland. In both locations, the intensity of disturbances decreased substantially when plant cover reached about 40%, a point at which increasing growth of shrubs stabilizes the soil. Similar plant traits allow species to establish and stabilize glacial substrates in the two disparate locations, which indicates that plant succession in postglacial ecosystems follows predictable patterns. —BEL

Ecosphere (2023) 10.1002/ecs2.4404.

IMMUNOLOGY

Monocytes fade fast?

Changes in diet can affect where immune cells are distributed in the body. This, in turn, can substantially influence how the immune system responds to pathogens and cancer. Janssen *et al.* report that when mice are made to fast for 24 hours, immune cells called monocytes transit from the circulation back to the bone marrow. Fasting prompts the release of corticosterone by the hypothalamic–pituitary–adrenal (HPA) axis, which causes monocytes to up-regulate the chemokine receptor CXCR4 and leave the blood. When mice refeed, the previously sequestered monocytes from the bone marrow

ALSO IN *SCIENCE* JOURNALS

Edited by **Michael Funk**

NANOMATERIALS

MXenes without MAX phases

Two-dimensional metal carbides and nitrides, or MXenes, have several potential applications in energy storage and electronics. They are usually made by delamination of a layered parent compound, a MAX phase, in a harsh etching step. Wang *et al*. synthesized one of the most widely used MXenes, Ti_2CCl_2, as well as MXenes not available from MAX phases, using chemical vapor deposition (see the Perspective by Robertson and Tolbert). The reaction of methane and titanium tetrachloride on a titanium surface led to the growth of Ti_2CCl_2 sheets perpendicular to the metal. Under some growth conditions, the sheets could buckle off the surface to form vesicles.—PDS

Science, add9204, this issue p. 1242; see also ade9914, p. 1189

NEUROLOGICAL DISEASE

ASOs for Angelman syndrome

Angelman syndrome is a neurodevelopmental disorder caused by mutations in the maternally inherited allele of the ubiquitin-protein ligase E3A (*UBE3A*) gene. In the central nervous system, the paternal allele of *UBE3A* is imprinted by the *UBE3A* antisense (*UBE3A-AS*) transcript, and reactivation of paternal *UBE3A* expression has been suggested as a potential treatment for the disease. Dindot *et al.* developed antisense oligonucleotides (ASOs) that specifically target evolutionarily conserved sequences at the start of the *UBE3A-AS* transcript to repress transcription, leading to reactivation of the paternal *UBE3A* allele in vitro and in cynomolgus monkeys. Based on these findings, a clinical trial testing these ASOs in patients with Angelman syndrome is underway. —MN

Sci. Transl. Med. **15**, eabf4077 (2023).

IMMUNOLOGY

Glucocorticoids calm cytokine storms

T cell–stimulating therapies can inadvertently induce a cytokine storm, a rapid, systemic release of proinflammatory cytokines that can cause tissue damage and death. Guo *et al*. investigated mechanisms underlying lethal immunotherapy-induced cytokine storms. The systemic release of cytokines occurred in mice treated with CD3 antibodies However, mice unable to release glucocorticoids through the adrenal stress response failed to resolve cytokine production and showed increased mortality, which was rescued by the administration of low-dose glucocorticoids before antibody therapy. —LKF

Sci. Signal. **16**, eadd4900 (2023).

PLANT SCIENCE

Growth on alkaline soils

Alkaline soils limit the ability of plants to take in nutrients and manage salt stress. Zhang *et al*. have now identified a locus in sorghum that determines sensitivity to salty alkaline soils. The Alkali Tolerance 1 (AT1) locus encodes a guanine nucleotide–binding protein gamma subunit that regulates the phosphorylation of aquaporins, channels that can transport hydrogen peroxide to alleviate oxidative stress. Crops that could better manage growth on alkaline soils could open up agriculture to the millions of hectares of alkaline soils. —PJH

Science, ade8416, this issue p. 1204

COMPARATIVE EMOTION

Fundamentals of empathy

Emotional contagion, in which individuals display fear or distress behaviors in response to observations of the same in another, is considered a basal form of empathy and is known to occur in fishes. Akinrinade *et al*. have shown that the neuropeptide oxytocin is responsible for these behaviors in zebrafish, as it is in mammals (see the Perspective by DeAngelis and Hofmann). They also found that the same regions of the brain are involved in zebrafish and in mammals. Such homologies in emotional response mechanisms across fishes and mammals suggest that this most basal form of empathy could have evolved many, many millions of years ago. —SNV

Science, abq5158, this issue p. 1232; see also adh0769, p. 1186

PLANT SCIENCE

Adjuvants derived from the soapbark tree

Saponins, a type of plant-derived glycoside, are useful in formulations including soaps, medicines, and root beer foam. Reed *et al*. studied how the Chilean soapbark tree (*Quillaja saponaria*) makes its saponins, which lend immunostimulatory activity to vaccines against shingles, malaria, and COVID-19 (see the Perspective by Chubatsu Nunes and Dang). The saponins are currently extracted from the tree's bark. The identification of enzymes in the biosynthetic pathway opens doors to the more sustainable production of these useful adjuvants and opportunities to engineer new adjuvants. —PJH

Science, adf3727, this issue p. 1252; see also adg8823, p. 1187

design the 2D patterns allow for control of the final porosity. A wide range of examples is provided, including changes in the sign of the curvature. These structures can be fabricated from silicon, metals, chitosan, and polymers. —MSL

Science, adf3824, this issue p. 1225

3D PRINTING

Overcoming challenges with silicone

Silicone elastomers are used in a wide range of applications because of their resistance to heat, moisture, and chemical agents. However, three-dimensional (3D) printing with silicone is challenging because of the interfacial behavior of the precursors. Duraivel *et al*. present a method to 3D print precise, free-standing, highly detailed objects out of silicone-based materials by using densely packed emulsions surrounded by a silicone oil continuous phase as the support material. This technique allows for precise control over the interfacial tension between the support material and the printing fluid. The authors demonstrated that they could print features as small as four micrometers, as well as mechanically robust, thin-walled, accurate models of human vasculature. —MSL

Science, ade4441, this issue p. 1248

NEUROIMMUNOLOGY

Anaphylaxis brings on a chill

A prominent symptom of immunoglobulin E (IgE)–induced anaphylaxis in rodents is a profound drop in the core body temperature. Bao *et al*. used mouse models to explore the role of neural pathways in connecting antigen-induced cross-linking of IgE receptors on mast cells and subsequent mast cell degranulation in the development of hypothermia. They discovered that chymase, a mast cell–derived protease, activated heat-sensitive $TRPV1^+$ neurons through the PAR1 receptor, triggering a neural circuit that rapidly led to reduced heat generation by brown adipose tissue. These findings identify heat-sensing neurons as key contributors to the manifestations of anaphylaxis and suggest potential therapeutic targets for additional treatments aimed at reversing life-threatening symptoms associated with anaphylaxis. —IRW

Sci. Immunol. **8**, eadc9417 (2023).

FERROELECTRICS

A polarizing thin film

Shrinking the footprint of electronics may require coming up with ferroelectrics that retain their properties down to nanometer-thickness films. Yang *et al*. add to a growing list of materials that retain ferroelectricity at these small length scales. The authors found a ferroelectric bismuth oxide structure that they stabilized with a small amount of samarium substitution. When coated on a substrate, the ferroelectric behavior persists down to one nanometer. The relatively high polarization makes these films good candidates for a variety of applications. —BG

Science, abm5134, this issue p. 1218

VENUS

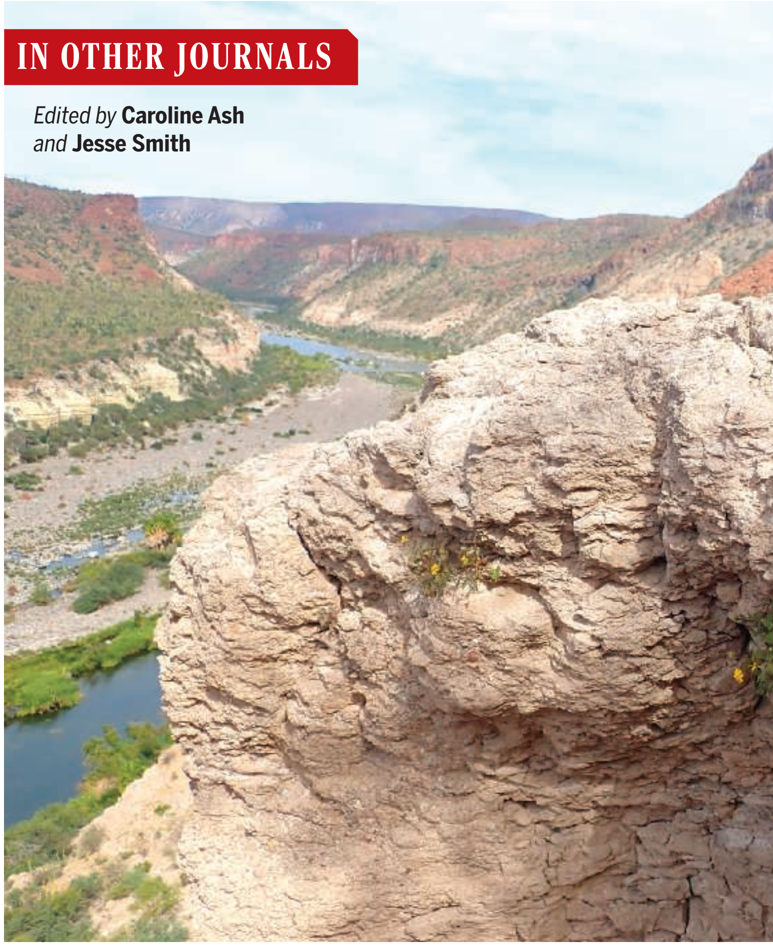
Signs of volcanic activity on Venus

Numerous volcanoes have been identified on the surface of Venus, but none has been observed to erupt, so it has been unclear whether volcanic activity has ceased. Herrick and Hensley examined locations on Venus that were observed two or three times by the radar instrument on the Magellan spacecraft when it was searching for changes between the images caused by ongoing volcanic activity. The authors identified a volcanic vent that enlarged and changed shape in the 8-month gap between two radar images and a possible lava flow running downhill from the vent. The results are interpreted as active volcanism on Venus. —KTS

Science, abm7735, this issue p. 1205

IN OTHER JOURNALS

Edited by **Caroline Ash** *and* **Jesse Smith**



ECOLOGY

Growing in a glacier's wake

Glaciers are retreating worldwide, leaving behind inorganic sediments that support new, rapidly changing ecosystems. These glacial forelands are constantly eroded by water and wind until they are eventually stabilized by vegetation. Eichel *et al.* compared patterns of disturbance and vegetation across two glacial forelands in New Zealand and Switzerland. In both locations, the intensity of disturbances decreased substantially when plant cover reached about 40%, a point at which increasing growth of shrubs stabilizes the soil. Similar plant traits allow species to establish and stabilize glacial substrates in the two disparate locations, which indicates that plant succession in postglacial ecosystems follows predictable patterns. —BEL

Ecosphere (2023) 10.1002/ecs2.4404.

IMMUNOLOGY

Monocytes fade fast?

Changes in diet can affect where immune cells are distributed in the body. This, in turn, can substantially influence how the immune system responds to pathogens and cancer. Janssen *et al.* report that when mice are made to fast for 24 hours, immune cells called monocytes transit from the circulation back to the bone marrow. Fasting prompts the release of corticosterone by the hypothalamic–pituitary–adrenal (HPA) axis, which causes monocytes to up-regulate the chemokine receptor CXCR4 and leave the blood. When mice refeed, the previously sequestered monocytes from the bone marrow

PHOTO: ISAAC LICHTER-MARCK



PLANT EVOLUTION

A study in daisies

Many deserts are geologically young. Studying organisms from these biomes can reveal whether species colonize new ecological niches because they are "pre-adapted" to similar environments or because they rapidly acquire new genetic capacities. Lichter-Marck and Baldwin captured DNA from 73 species of rock daisies (Perityleae), which are endemic to North American deserts, and performed phylogenetic analyses to find out when desert adaptations occurred. Many of these species had likely specialized to grow on desert-like microenvironments within other biomes, such as rocky outcrops in forests. Such characteristics apparently allow these species to survive desertification and therefore to adopt new niches without evolutionary modification. —CNS

Proc. Natl. Acad. Sci. U. S. A. (2023) 10.1073/pnas.2214729120.

Rock daisies prefer to colonize dry, rugged environments, even in forest biomes, which has allowed this tribe of plants to readily adapt to desert conditions.

SOCIAL LEARNING

Social learning in eusocial insects

The majority of eusocial female insects forgo reproduction to work in various supportive roles within the colony. This complexity of organization and behavior has generally been believed to be innate, meaning that it is genetically controlled and inherited rather than learned. However, eusocial insects can and do learn. For example, bumble bees learn to control and manipulate objects, and honeybees learn their classic waggle dance by watching others. Adding yet more complexity, Bridges *et al.* show that bumble bees learn to follow trained bees in opening a sugar-laden puzzle box. The bees' patterns of learning and preference for the demonstrator bees' methods are consistent with cultural transmission seen in primates and birds. —SNV

PLOS Biol. (2023) 10.1371/journal.pbio.3002019.

return to the circulation but are chronologically older and have a distinctive transcriptional footprint. Repeated bouts of fasting and refeeding enhance murine susceptibility to infection by *Pseudomonas aeruginosa*, indicating that the presence of this altered monocyte pool may have negative consequences for host defense. —STS

Immunity (2023) 10.1016/j.immuni.2023.01.024.

EDUCATION

Weeding out inequity

STEM has long been defined by large and academically challenging introductory courses, and these perceived "weed-out" courses are often a source of inequity. Hatfield *et al.* aimed to quantify these inequities by using a large, multi-institutional database to examine how students' race and ethnicity, sex, and number of D's, F's, and/or course withdrawals (DFWs) in introductory courses affected their path to a STEM degree. The association between DFWs in an introductory STEM class and failure to obtain a STEM degree was found to be stronger for historically marginalized students. As an example, the probability of obtaining a STEM degree for a white male student who received grades of C or better in all introductory courses was 48%. For an otherwise similar historically marginalized female student, the probability dropped to 35%. —MMc

PNAS Nexus (2022) 10.1093/pnasnexus/pgac167.

ELECTROCHEMISTRY

Lewis adducts at electrodes

The strength of Lewis adducts can be affected by redox conditions. Menachekanian *et al*. used Raman spectroscopy and density functional theory to explore the bonding between the N atom of the Lewis base mercaptopyridine adsorbed on a gold electrode with the B atom of Lewis base boron trifluoride (BF_3) with or without $LiBF_4$ in solution. The N–B bond was stable at positive potentials but cleaved at negative potentials (about –0.3 volts) without electron transfer current. This result was the opposite of that predicted for an electroinductive effect. However, it was consistent with the formation of ionic structures in which Li^+ stabilized the adduct at positive potentials but displaced BF_3 at negative potentials to form part of a halogen-bridged $[B_2F_7]^-$ complex. —PDS

J. Am. Chem. Soc. (2023) 10.1021/jacs.2c12370.

MATERIALS SCIENCE

Bulk, room-temperature, mixed conductors

It is challenging to develop materials that allow for efficient electronic and ionic conduction, particularly at room temperature, and there is a lack of understanding about how activating one mode of conduction might affect the other. Quill *et al.* combined an organic semiconductor with an ionic liquid to form a mixed conductor. The organic polymer crystallizes such that the backbone conducts electrons while the ordered side chains provide pathways for ionic conduction. They also used a combination of x-ray scattering and spectroscopy to track the behavior in situ and were thus able to observe how the addition of charge carriers modifies the side chain organization, thereby enhancing transport. —MSL

Nat. Mater. (2023) 10.1038/s41563-023-01476-6.

RESEARCH ARTICLE SUMMARY

PLANT SCIENCE

A Gγ protein regulates alkaline sensitivity in crops

Huili Zhang†, Feifei Yu†*, Peng Xie†, Shengyuan Sun†, Xinhua Qiao†, Sanyuan Tang, Chengxuan Chen, Sen Yang, Cuo Mei, Dekai Yang, Yaorong Wu, Ran Xia, Xu Li, Jun Lu, Yuxi Liu, Xiaowei Xie, Dongmei Ma, Xing Xu, Zhengwei Liang, Zhonghui Feng, Xiahe Huang, Hong Yu, Guifu Liu, Yingchun Wang, Jiayang Li, Qifa Zhang, Chang Chen, Yidan Ouyang*, Qi Xie*

INTRODUCTION: According to the Food and Agriculture Organization (FAO), there are currently >1 billion ha of land affected by salt. Among these, ~60% are classified as sodic soil areas. These have high pH and are dominated by sodium bicarbonate ($NaHCO_3$) and sodium carbonate (Na_2CO_3). The effects of global warming and a lack of fresh water will lead to >50% of arable land becoming affected by salt by 2050, thus severely affecting the world's food security. Identifying and/or engineering sodic-tolerant crops is imperative to solve this challenge. Although salinity tolerance has been studied extensively, alkalinity tolerance in plants has not been studied in depth.

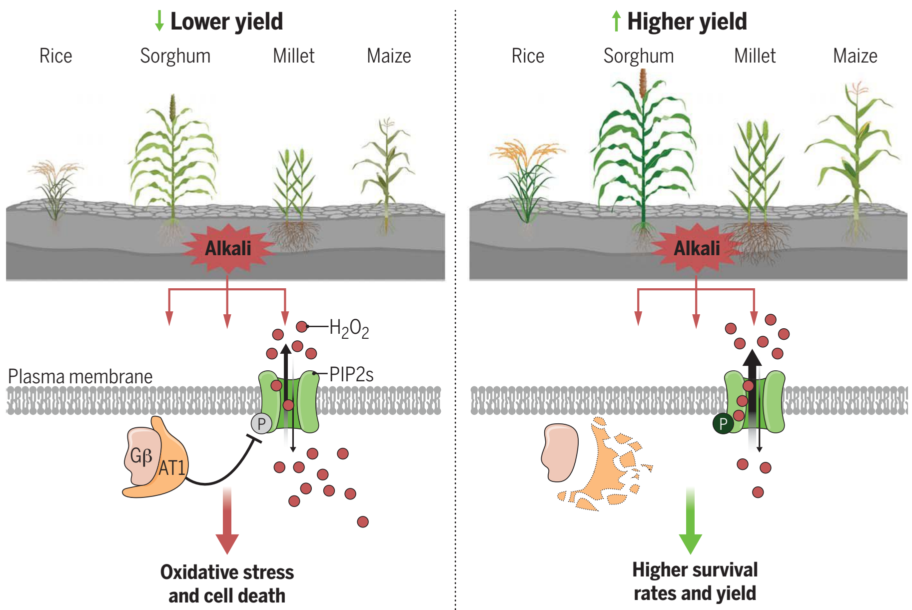
RATIONALE: Sorghum originates from Africa, where it can grow in harsh environments. As a result, sorghum has evolved greater tolerance to adapt to multiple abiotic stresses compared with other crops. Some sorghum varieties can survive in sodic soil with a pH as high as 10.0. A genome-wide association study (GWAS) analysis was performed with a large sorghum association panel consisting of 352 representative sorghum accessions. We detected a major locus, *Alkaline tolerance 1* (*AT1*), linked to alkaline tolerance. We found that *AT1*, encoding an atypical G protein γ subunit (a homolog to rice *GS3*), contributes to alkaline sensitivity by modulating the efflux of hydrogen peroxide (H_2O_2) under environmental stress.

RESULTS: On the basis of the results of the GWAS analysis, we sequenced the cDNA regions of *SbAT1* (*Sorghum bicolor AT1*) in 37 sorghum accessions with different degrees of alkaline sensitivity. Two typical haplotypes (Hap1 and Hap2) of *SbAT1* were identified according to the five leading variant sites associated with sorghum alkali sensitivity. Hap1 encodes an intact SbAT1. A frame shift mutation (from "G" to "GGTGGC") within Hap2 results in a premature stop codon probably encoding a truncated protein with only 136 amino acids at the N terminus (named *Sbat1*).

To confirm the function of the *AT1* locus, we generated a pair of near-isogenic lines (NILs) with two *AT1* haplotypes to assess the allelic effect of *AT1* on sorghum tolerance to alkali. We found that the *Sbat1* allele (Hap2), encoding a truncated form of SbAT1, increased plant alkaline sensitivity compared with wild-type full-length *SbAT1* (Hap1). Overexpression of *AT1/GS3* reduced alkaline tolerance in sorghum and rice, and overexpression of the C-terminal truncated AT1/GS3 showed a more severe alkaline sensitive response. This was confirmed in millet and rice, which suggests that *AT1/GS3* functions negatively in plant alkali tolerance. By contrast, knockout (ko) of *AT1/GS3* increased tolerance to alkaline stress in sorghum, millet, rice, and maize, which indicates a conserved pathway in monocot crops.

By immunoprecipitation in combination with mass spectrometry (IP-MS), we found that AT1/GS3 interacts with aquaporin PIP2s that are involved in reactive oxygen species (ROS) homeostasis. Genetic analysis showed that *OsPIP2;1^{ko}/2;2^{ko}* had lower alkaline tolerance than their wild-type control. The redox probe Cyto-roGFP2-Orp1 sensing H_2O_2 in the cytoplasm was applied. The results showed that, upon alkaline treatment, the relative H_2O_2 level increased in *OsPIP2;1^{ko}/2;2^{ko}* compared with wild-type plants. These results suggested that the phosphorylation of aquaporins could modulate the efflux of H_2O_2. Gγ negatively regulates the phosphorylation of PIP2;1, leading to elevated ROS levels in plants under alkaline stress. To assess the application of the *AT1/GS3* gene for crop production, field tests were carried out. We found that the nonfunctional mutant, either obtained from natural varieties or generated by gene editing in several monocots, including sorghum, millet, rice, and maize, can improve the field performance of crops in terms of biomass or grain production when cultivated on sodic lands.

CONCLUSION: We concluded that *SbAT1* encodes an atypical G protein γ subunit and inhibits the phosphorylation of aquaporins that may be used as H_2O_2 exporters under alkaline stress. With this knowledge, genetically engineered crops with knockouts of *AT1* homologs or use of natural nonfunctional alleles could greatly improve crop yield in sodic lands. This may contribute to maximizing the use of global sodic lands to ensure food security. ■



Genetic modification of AT1 enhances alkaline stress tolerance. The Gγ subunit, AT1, pairs with Gβ to negatively modulate the phosphorylation level of PIP2 aquaporins. Thus, AT1 reduces the H_2O_2 export activity of PIP2s, leading to the overaccumulation of H_2O_2 and resulting in alkaline stress sensitivity. By contrast, the artificial or natural knockouts of *AT1* homologs release the inhibition of PIP2s by AT1 in crops and have improved survival rates and yield under alkaline stress. [Figure created using BioRender]

The list of author affiliations is available in the full article online.
*Corresponding author. Email: qxie@genetics.ac.cn (Q.X.); ffyu@cau.edu.cn (F.Y.); diana1983941@mail.hzau.edu.cn (Y.O.)
†These authors contributed equally to this work.

Cite this article as H. Zhang *et al.*, *Science* **379**, eade8416 (2023). DOI: 10.1126/science.ade8416

READ THE FULL ARTICLE AT https://doi.org/10.1126/science.ade8416

RESEARCH ARTICLE

PLANT SCIENCE

A Gγ protein regulates alkaline sensitivity in crops

Huili Zhang[1,2]†, Feifei Yu[1,3]†*, Peng Xie[1]†, Shengyuan Sun[4,5]†, Xinhua Qiao[6]†, Sanyuan Tang[1], Chengxuan Chen[1], Sen Yang[1,7], Cuo Mei[1,7], Dekai Yang[1,7], Yaorong Wu[1], Ran Xia[1], Xu Li[4], Jun Lu[4], Yuxi Liu[4], Xiaowei Xie[2], Dongmei Ma[2], Xing Xu[2], Zhengwei Liang[8], Zhonghui Feng[7,8], Xiahe Huang[1], Hong Yu[1], Guifu Liu[1], Yingchun Wang[1,7], Jiayang Li[1,7], Qifa Zhang[4], Chang Chen[6,7], Yidan Ouyang[4]*, Qi Xie[1,7,9]*

The use of alkaline salt lands for crop production is hindered by a scarcity of knowledge and breeding efforts for plant alkaline tolerance. Through genome association analysis of sorghum, a naturally high-alkaline–tolerant crop, we detected a major locus, *Alkaline Tolerance 1* (*AT1*), specifically related to alkaline-salinity sensitivity. An *at1* allele with a carboxyl-terminal truncation increased sensitivity, whereas knockout of *AT1* increased tolerance to alkalinity in sorghum, millet, rice, and maize. *AT1* encodes an atypical G protein γ subunit that affects the phosphorylation of aquaporins to modulate the distribution of hydrogen peroxide (H_2O_2). These processes appear to protect plants against oxidative stress by alkali. Designing knockouts of *AT1* homologs or selecting its natural nonfunctional alleles could improve crop productivity in sodic lands.

Food security is affected by the growth of human populations worldwide and the potential negative impacts of climate change on agricultural production. Weather patterns resulting from global warming may limit fresh water availability. In the near future, saline soils are estimated to increase in ~50% of irrigated lands as a result of the application of chemical fertilizers (*1*). Consequently, soil salinity may become a global problem affecting plant growth and crop production. Use of these saline lands for crop production could help meet future food demands. Therefore, breeding more salinity-tolerant crops will likely be prioritized in the future of agriculture.

[1]State Key Laboratory of Plant Genomics, Institute of Genetics and Developmental Biology, The Innovative Academy of Seed Design, Chinese Academy of Sciences, Beijing 100101, China. [2]Breeding Base of State Key Laboratory of Land Degradation and Ecological Restoration of North Western China, School of Agriculture, Ningxia University, Yinchuan 750021, China. [3]College of Grassland Science and Technology, China Agricultural University, Beijing 100083, China. [4]National Key Laboratory of Crop Genetic Improvement and National Centre of Plant Gene Research (Wuhan), Hubei Hongshan Laboratory, Huazhong Agricultural University, Wuhan 430070, China. [5]Jiangsu Key Laboratory of Crop Genetics and Physiology and Co-Innovation Center for Modern Production Technology of Grain Crops, Key Laboratory of Plant Functional Genomics of the Ministry of Education, Yangzhou University, Yangzhou 225009, China. [6]National Laboratory of Biomacromolecules, CAS Center for Excellence in Biomacromolecules, Institute of Biophysics, Chinese Academy of Sciences, Beijing 100101, China. [7]University of Chinese Academy of Sciences, Beijing 100049, China. [8]Northeast Institute of Geography and Agroecology, Daan National Station for Agro-ecosystem Observation and Research, Chinese Academy of Sciences, Changchun 130102, China. [9]National Center of Technology Innovation for Maize, State Key Laboratory of Maize Germplasm Innovation and Molecular Breeding, Syngenta Group China, Beijing 102206, China.
***Corresponding author. Email: qxie@genetics.ac.cn (Q.X.); ffyu@cau.edu.cn (F.Y.); diana1983941@mail.hzau.edu.cn (Y.O.)**
†These authors contributed equally to this work.

On the basis of research by the Food and Agriculture Organization (FAO) of the United Nations (in 2015; https://www.fao.org/3/i5199e/i5199e.pdf), there are >1 billion ha of land affected by salt, and ~60% of the estimated area was classified as sodic [land with a high pH because of high alkali contents dominated by sodium bicarbonate ($NaHCO_3$) and sodium carbonate (Na_2CO_3)]. About 25 to 33% of the irrigated land worldwide is affected by secondary salinity (*2*). In analyzing publications from the past 20 years on Web of Science (https://www.webofscience.com/), we discovered that the number of published studies relevant to salt tolerance was up to 22,614 compared with only 457 for alkalinity tolerance. Because of insufficient knowledge about alkaline stress, technological development to increase crop production in saline-alkali soil has been limited. Different from neutral salinity (pH of ~7) with only ion toxicity, high pH in alkaline saline soil reduces the uptake rates of essential nutrients and sodium ion (Na^+) exclusion. This leads to more negative consequences on plant growth by inducing high cellular oxidative stress compared with salinity alone (*3*). Sorghum is currently the fifth main food crop in the world. It originates from Africa's harsh environments and has evolved a greater ability to adapt to some abiotic stresses compared with other crops. Thus, it is considered a useful resource for the discovery of mechanisms and genetic resources to improve crop responses to environmental stress, including alkaline stress (*4*).

High alkalinity boosts hydrogen peroxide (H_2O_2) levels in cells and causes oxidative damage to cellular proteins, lipids, and DNA, which results in apoptosis (*5*–*7*). Aquaporins (AQPs) are conserved from prokaryotes to eukaryotes. They are tetrameric, membrane-bound channels known to facilitate bidirectional transport of water and other small solutes across cell membranes. Researchers have reported that several members of the aquaporin superfamily in various organisms can also transport the redox signaling compound, H_2O_2, to facilitate the fine adjustment of H_2O_2 levels in the cytoplasm (*8*). Tong *et al.* (*9*) found that aquaporins from *Streptococcus* acted as peroxiporins for the efflux of intracellular H_2O_2 to alleviate oxidative stress. A study on the mammalian lens aquaporin, AQP5, showed that under hyperglycemic stress conditions with a higher level of intracellular H_2O_2, AQP5 facilitated H_2O_2 efflux from cells to maintain balance and homeostasis of H_2O_2 levels (*10*). In plants, aquaporins are involved in different stress defenses, and their phosphorylation plays an essential role in their transport activity (*11*, *12*). However, how crops sense alkaline stress and how the subsequent signaling affects H_2O_2 transport has yet to be explored.

Membrane-bound G proteins are conserved across the eukaryotic kingdom. They are heterotrimeric proteins bound to guanine nucleotides and consist of three subunits—G protein alpha (Gα), beta (Gβ), and gamma (Gγ). They play diverse roles in development and environmental interactions throughout an organism's life cycle. There are large numbers of diverse G protein γ subunits in plants with functions in different aspects of signal perception, transduction, and regulation of downstream effectors (*13*). Although G protein signaling pathways are well studied in mammals, the underlying mechanisms associated with G protein γ subunits in plants, especially in abiotic stress signaling, remain unclear.

In this work, we discovered *Alkaline Tolerance 1* (*AT1*, which encodes an atypical G protein γ subunit) showing alkaline tolerance in sorghum by genome-wide association study (GWAS) analysis. We reveal a conserved mechanism in which the G protein γ subunit modulates the phosphorylation of aquaporins to regulate reactive oxygen species (ROS) levels to maintain H_2O_2 homeostasis. This forms part of the plant protective response against oxidative stress caused by alkaline conditions. On the basis of this knowledge, we genetically edited the homologous gene of *AT1* in other crops to increase rice, maize, and millet alkaline tolerance in saline-alkali soils.

The AT1 locus is linked to alkaline tolerance

Sorghum has a specific tolerance to sodic soil, and some varieties can survive in a pH as high as 10.0 (*14*, *15*). To mimic the various saline-alkali conditions that may be found in saline-sodic soils in the field, we first tested different concentrations of mixtures of two alkali salts ($NaHCO_3$ and Na_2CO_3) and measured their effects on the survival rates of sorghum seedlings.

A mixture of alkali salts was used because it should produce a relatively stable pH range throughout various treatment periods. Different time periods of treatments were used on 16 selected sorghum accessions based on seed availability (table S1). Analysis of relative survival rates (a ratio of the survival rate under stress treatment to that without stress treatment) showed that after 21 days of treatment, the concentration of 75 mM mixed alkali salts (62.5 mM $NaHCO_3$ and 12.5 mM Na_2CO_3; pH = 9.2 to 9.4) showed the widest range in variation of rates and was the most reliable treatment to evaluate alkaline tolerance in sorghum (fig. S1, A to C). We then evaluated relative survival rates from a large sorghum association panel consisting of 352 representative sorghum accessions, and we observed that ~22% of the sorghum accessions exhibited high tolerance to alkali conditions with relative survival rates reaching >80%, whereas ~13% of sorghum accessions showed high sensitivity to alkalinity with relative survival rate no more than 20%. The frequency distribution in relative survival rate phenotypes of our sorghum population indicated that relative survival rate might be a useful index for genetic association analysis (fig. S1, D and E).

Using the above relative survival rate phenotypic data and a single-nucleotide polymorphism (SNP) genotype dataset for this panel, we performed a GWAS and identified two major loci ($P < 1.0 \times 10^{-5}$) linked with alkaline tolerance, both of which were located on the long arm of chromosome 1 (Fig. 1A and fig. S1F). We found a leading SNP (*S1_55779338*) located inside the annotated gene *Sobic.001G341700*, which was named *Alkaline Tolerance 1* (*SbAT1*) (Fig. 1B). *SbAT1* is predicted to encode an atypical G protein γ subunit of 198 amino acids in length, which includes a Gγ-like domain in the N terminus and a cysteine-rich domain in the C terminus. SbAT1 shares 55.56% protein sequence identity with OsGS3 in rice (*16*) and 82.30% protein sequence identity with ZmGS3 (*17*) in maize. To verify whether the sequence polymorphisms of *SbAT1* were correlated with alkaline tolerance in sorghum, we sequenced the cDNA region of *SbAT1* in 37 sorghum accessions with different degrees of alkaline stress tolerance. A total of 29 sequence variation sites were found, and five of them showed strong association signals ($P = 1.0 \times 10^{-3}$ to 1.0×10^{-5}) between the natural variations and relative survival rates in the 75 mM alkali treatment. Linkage disequilibrium (LD) analysis also indicated that the five leading association signals (positioned at +3863, +4151, +4157, +4438, and +4463) were attributable to high LD values [coefficient of determination (R^2) > 0.9] (Fig. 1C).

On the basis of sequence variations of the five leading sites, the selected 37 sorghum accessions from other stock (table S1) were

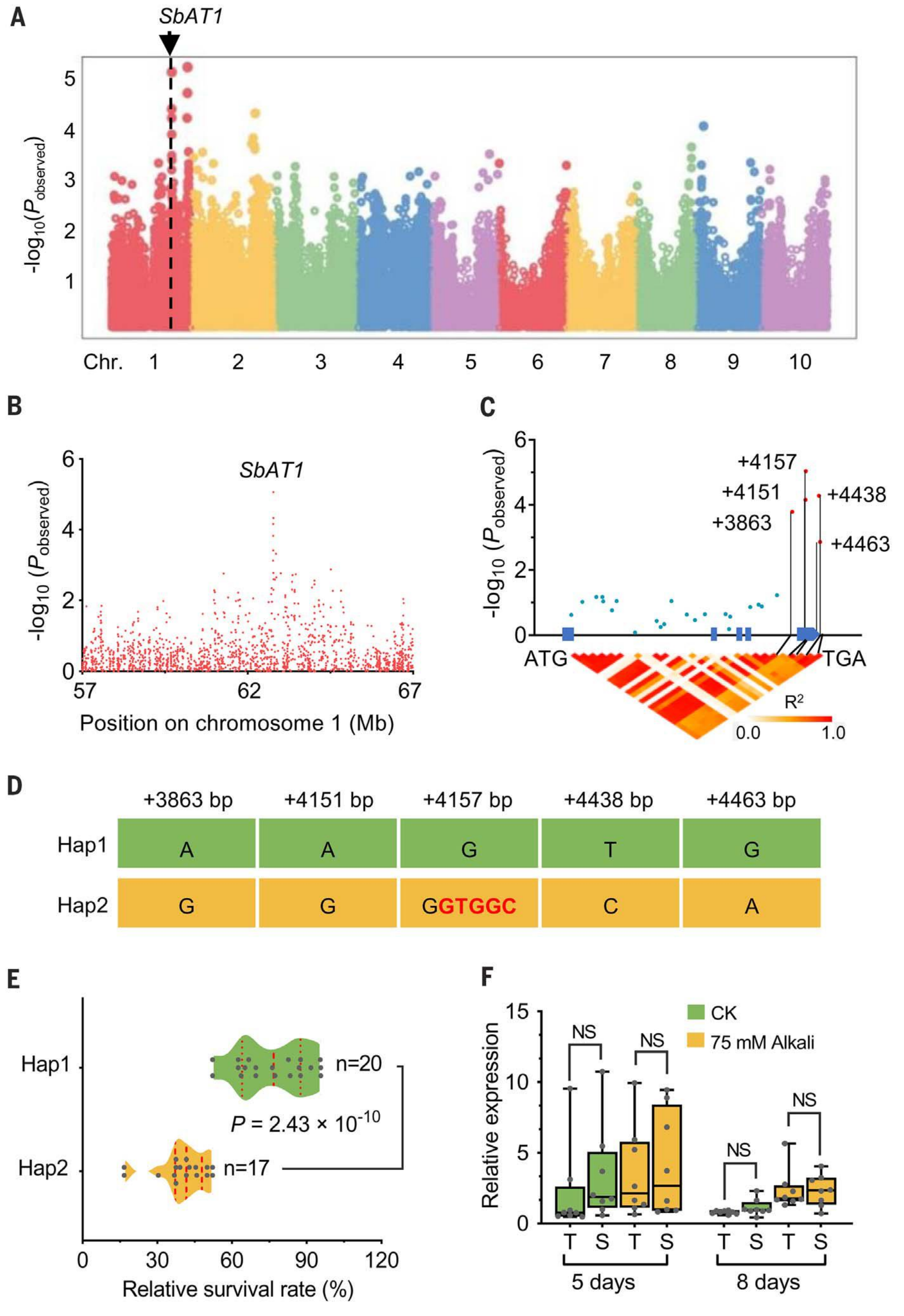


Fig. 1. Natural variation in *SbAT1* is associated with alkaline tolerance in sorghum. (**A**) Manhattan plot from a GWAS of alkaline tolerance in the natural sorghum association panel population. Relative survival rates were obtained from plants grown in conditions with (alkaline stress) or without (no-stress control) the addition of a 75 mM concentration of mixed alkali salts on the 21st day after seed sowing. The arrow identifies the major locus of *SbAT1*. (**B**) Scatter plot of the *SbAT1* locus flanked by an ~10-Mb genome region on chromosome 1. (**C**) *SbAT1*-based association mapping between the detected 29 sequence variations in the genic region of *SbAT1* and alkali tolerance among 37 sequenced sorghum accessions. LD analysis between the 29 causal sites indicates the linkage association signals. The five leading variant sites (red dots) show strong association signals with strong LD and are highlighted by black lines. (**D**) Two typical haplotypes (Hap1 and Hap2) of *SbAT1* were detected based on the five leading variant sites. A frame shift mutation (from "G" to "GGTGGC") within Hap2 is highlighted in red. (**E**) Relative survival rates of 20 sorghum accessions in Hap1 and 17 sorghum accessions in Hap2 subjected to alkaline stress (75 mM mixed alkali). Statistical *P* values were determined by two-tailed unpaired *t* test. (**F**) Relative expression levels of *AT1* in alkaline stress–tolerant (T) and –sensitive (S) lines (n = 8) after 5 and 8 days of stress in the 75 mM alkali treatment and the corresponding controls (CK). Statistical significance was determined by one-way ANOVA with Tukey's multiple comparisons test. NS, not significant.

classified into two typical haplotypes (Hap1 and Hap2) of *SbAT1*. Notably, compared with Hap1 [wild-type (WT)], we identified a frameshift mutation of a 5–base pair (bp) (GTGGC) insertion in the fifth exon of *SbAT1* (Fig. 1D), which resulted in a premature stop codon in Hap2 probably encoding a truncated protein with only 136 amino acids at the N terminus (named *Sbat1*). Furthermore, we observed that the sorghum accessions with Hap1 had much higher relative survival rates than those with Hap2 under the alkali treatment ($P = 2.43 \times 10^{-10}$) (Fig. 1E). Consistent with the finding that no strong association signals were found in the 5′ untranslated region (5′UTR) of *SbAT1*, we were able to confirm that haplotype-based variation was not associated with *SbAT1* expression levels on the basis of RNA levels obtained after 5 or 8 days of alkaline treatment (Fig. 1F). These data suggest that the alkali-sensitive and -tolerant phenotypes in the two *SbAT1* haplotypes are independent of the transcriptional levels of *SbAT1* and its variants but are instead due to the mutations leading to the protein changes inside the coding region.

The role of AT1 in alkaline tolerance

To assess the allelic effect of *AT1* on sorghum tolerance to alkali, we selected a pair of near-isogenic lines (NILs) with two *AT1* haplotypes in the F_{11} generation from our laboratory stock for breeding program (*18*). NILs were derived from a cross between two sorghum germplasms, SN010 and M-81E. SN010 was of the haplotype Hap1 (containing wild-type *SbAT1*) and showed higher alkaline tolerance than M-81E of the haplotype Hap2 (*Sbat1* mutant) according to our survival rate and plant height data (Fig. 2A and fig. S2, A to C). We treated the two NILs with 75 mM alkaline salt. NIL-*SbAT1* exhibited 56.1% higher relative survival rate and better growth than NIL-*Sbat1* under alkaline treatment, whereas the two NILs showed no significant difference when planted in neutral-pH soil (Fig. 2, B and C). The treatment with 75 mM mixed alkali salts imposed not only alkaline stress but also Na^+ stress on plants. To differentiate whether the *SbAT1*-related stress phenotype was caused by high pH or high Na^+ stress alone, we performed treatments similar to the alkaline treatments but with NaCl at 75-, 100-, 150-, and 200-mM concentrations and all soils at a neutral pH level. We found that both NILs were sensitive to high NaCl and there were only slight differences in stress responses between NIL-*SbAT1* and NIL1-*Sbat1* (fig. S2, D to F). This result indicates that the *SbAT1*- and *Sbat1*-related stress phenotype is more likely an alkaline-specific response rather than a salt-stress response.

To test this possibility, we generated additional transgenic sorghum plants in the Wheatland background (*Sb*WT) containing an intact wild-type *SbAT1* gene that was either overexpressed or knocked out using gene-editing technology. The overexpression or knockout (ko) was confirmed by quantitative reverse transcription polymerase chain reaction (RT-qPCR) or sequence analysis (fig. S2G) (*18*). Unexpectedly, we found that overexpression of *SbAT1* (*SbAT1-OE*) reduced tolerance, whereas plants with knockout of *SbAT1* (*SbAT1^{ko}*) showed greatly increased tolerance to alkalinity (Fig. 2, D to F, and fig. S2, H to J). *SbAT1*-overexpressing plants had a 13.95% lower survival rate than Wheatland plants under 75 mM alkaline stress, whereas *SbAT1^{ko}* plants had a 17.93% higher survival rate than *Sb*WT plants (Fig. 2F). The phenotype of the transgenic plants led us to reconsider the functionality of gene mutations in the *SbAT1* C terminus of natural varieties (Fig. 1, C and D) and to consider that a truncated protein may play a negative role in alkaline tolerance. To verify our speculation, we first transiently expressed the green fluorescent protein (GFP) fusion proteins SbAT1-GFP and Sbat1-GFP in plant cells and found that the protein accumulated to high levels (fig. S2K). This indicated that the mutated *Sbat1* gene could be translated (*18*).

To further investigate, we generated transgenic plants to create a stop codon at the same position as sorghum *at1* by gene editing in millet to mimic the production of a potential C-terminal truncated SiAT1^{102} protein. We also generated plants overexpressing SiAT1^{124} (*SiAT1^{124}-OE*) with a truncated C terminus and plants with *SiAT1* knockout (*SiAT1^{ko}*) (Fig. 3A and fig. S3, A and B). We used millet in this experiment for multiple reasons: (i) there is easier and faster plant transformation for millet compared with sorghum, (ii) millet is a close relative of sorghum with high genome similarity and similar environmental physiology, and (iii) the single copy of SiAT1 shares a 75.24% protein identity to SbAT1. Similar to the results with the transgenic sorghum, knockout of the *SiAT1* gene produced plants with greater tolerance to alkaline conditions, as observed in the higher survival rate compared with other genotypes (Fig. 3, B and C). By contrast, the transgenic millet with the

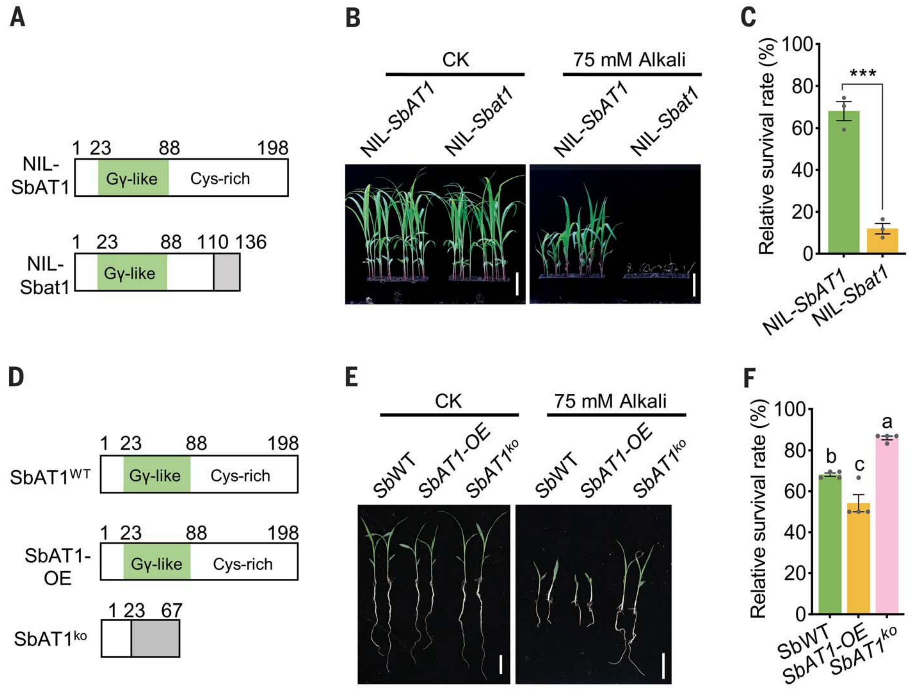


Fig. 2. *SbAT1* functions in alkaline tolerance in sorghum. (**A**) Schematic presentation of SbAT1 and its truncated protein Sbat1 in sorghum NIL-*SbAT1* and NIL-*Sbat1* plants. (**B**) Phenotypic analysis of sorghum NIL seedlings under alkaline stress. Seeds were sown in soil without (control, CK) or with 75 mM mixed alkali. Photographs were taken on the 14th day after seed sowing. Independent experiments were repeated three times. Scale bars, 5 cm. (**C**) Statistical analysis of the relative survival rates of seedlings in (B). Data are the means ± SEMs (n = 36 plants for each repeat) of three biological replicates. Statistical significance was determined by two-tailed unpaired t test. (**D**) Schematic presentation of SbAT1 and its nonfunctional version in *Sb*WT, *SbAT1-OE*, and *SbAT1^{ko}* plants. *Sb*WT is the Wheatland ecotype. (**E**) Representative seedlings of *Sb*WT, *SbAT1-OE*, and *SbAT1^{ko}* with or without 75 mM alkali stress treatment on the 14th day. Scale bars, 5 cm. (**F**) Statistical analysis of the relative survival rates of samples in (E). Data are the means ± SEMs (n = 16 plants for each repeat) of four biological replicates. Statistical significance was determined by ordinary one-way ANOVA with Tukey's multiple comparisons test.

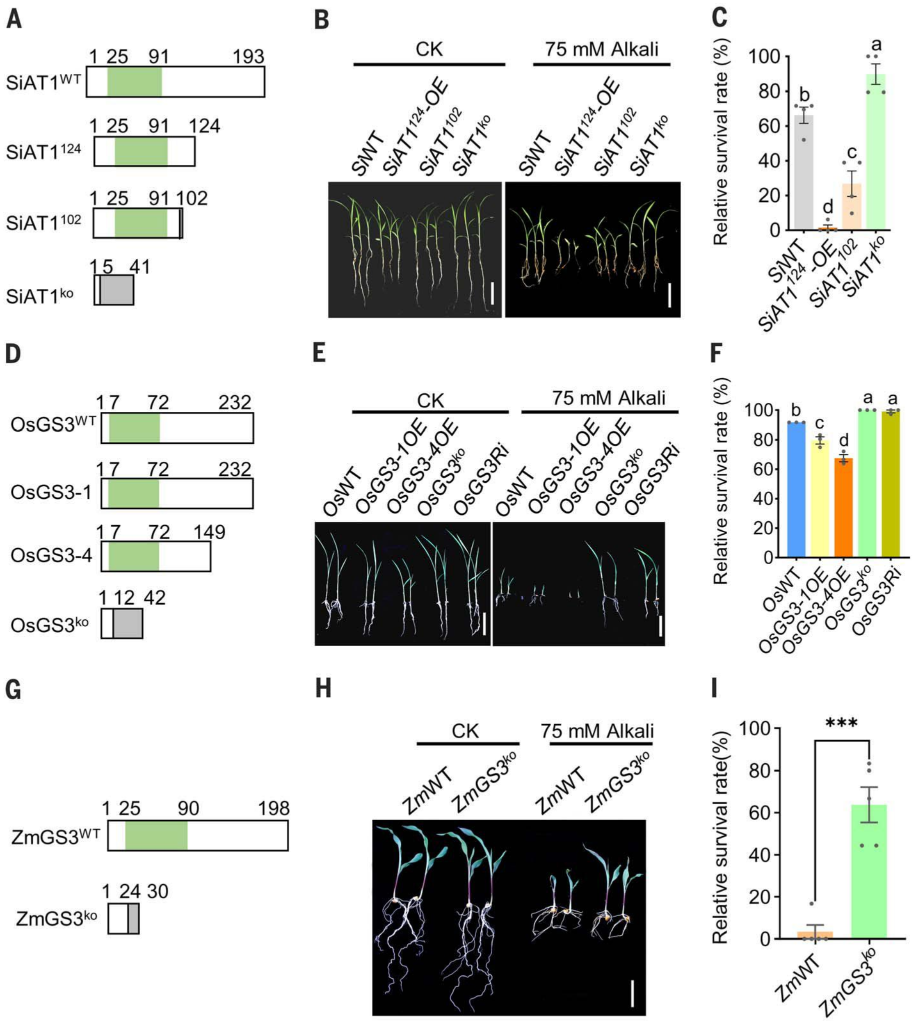


Fig. 3. The Gγ-like subunits of AT1 homologs have a conserved function in alkaline tolerance in millet, rice, and maize. (**A**) Schematic presentation of millet SiAT1 and its truncated or nonfunctional versions in *SiAT1* genetic plants. *Si*WT is the Ci846 ecotype. (**B**) Representative *SiAT1* genetic plants with or without 75 mM alkali stress on the 14th day. Scale bars, 5 cm. (**C**) Statistical analysis of the relative survival rates of millet lines in (B). Data are the means ± SEMs (n = 24 plants for each repeat) of three biological replicates. (**D**) Schematic presentation of rice OsGS3 and its truncated or nonfunctional versions in *OsGS3* genetic plants. *Os*WT is the ZH11 ecotype. (**E**) Representative seedlings of *OsGS3* genetic plants with or without 75 mM alkali stress on the 21st day after seed sowing. Scale bars, 5 cm. (**F**) Statistical analysis of the relative survival rate of rice lines in (E). Data are the means ± SEMs (n = 36 plants for each repeat) of three biological replicates. In (C) and (F), statistical significance was determined by ordinary one-way ANOVA with Tukey's multiple comparisons test. Different letters above the bars indicate significantly different groups. (**G**) Schematic presentation of wild-type ZmGS3 in *Zm*WT maize and its nonfunctional versions in *ZmGS3*^{ko} maize. *Zm*WT is the KN5585 ecotype. (**H**) Representative seedlings of *Zm*WT and *ZmGS3*^{ko} maize with or without 75 mM alkali stress treatment on the 14th day after seed sowing. Scale bar, 5 cm. (**I**) Statistical analysis of the relative survival rates of maize lines in (H) on the 50th day after seed sowing. Data are the means ± SEMs (n = 16 plants for each repeat) of four biological replicates. Significant differences were determined by two-tailed unpaired t test.

C terminus truncated (*SiAT1*^{102}) and the millet overexpressing the C terminus truncated SiAT1 (*SiAT1*^{124}*-OE*) showed reduced alkaline tolerance; *SiAT1*^{124}*-OE* plants exhibited the weakest growth in response to alkalinity (Fig. 3, B and C, and fig. S3C). This result suggests that the C-terminal truncated protein can be expressed in plants and that the increased amount of the C-terminal truncated protein had a negative effect on alkaline tolerance, whereas knockout of *AT1* could positively affect alkaline tolerance in plants. Together with the *AT1*-overexpression phenotype in sorghum, we conclude that AT1 plays a negative role, and at1 mutation enhances this role in alkaline tolerance in both sorghum and millet.

Similar roles of AT1 homologs in rice and maize

We further investigated the response of AT1 homologs in two other major monocot crops, rice and maize. The *AT1* ortholog in rice has been identified as *OsGS3*, a major quantitative trait locus (QTL) for grain size regulation (*16*, *19*). We found that in alkaline soils (75 mM alkaline salt; pH 9.0 to 9.2), overexpression of intact *OsGS3* (*OsGS3-1OE*) and a C-terminal truncated version (*OsGS3-4OE*) exhibited reduced alkaline tolerance, whereas rice with either a knockout (*OsGS3*^{ko}) or RNA interference of *OsGS3* (*OsGS3Ri*) showed greater tolerance in terms of relative survival rate, plant growth measured in relative plant height, and relative chlorophyll content compared with the ZH11 wild type (*Os*WT) (Fig. 3, D to F, and fig. S3, D to F). Among the transgenic plants, *OsGS3-1OE* and *OsGS3-4OE* exhibited 12.5 and 26.4% lower relative survival rates than *Os*WT, respectively, whereas *OsGS3*^{ko} and *OsGS3Ri* showed 8.3 and 7.4% higher relative survival rates than *Os*WT, respectively (Fig. 3F). These results demonstrated that inhibition of *OsGS3* function in rice could enhance alkaline tolerance and suggested a conserved function of the Gγ subunit. Moreover, by manipulating or selecting nonfunctioning alleles of *OsGS3*, we could enhance alkaline tolerance in rice.

The maize ortholog of *AT1* was previously identified as *ZmGS3* (*17*). We thus designate this gene as *AT1/GS3*, with a prefix to specify the species; *AT1* and *GS3* may also be separately or interchangeably used, depending on the context. We generated maize *ZmGS3* knockout (*ZmGS3*^{ko}) lines through gene editing in the maize line KN5585 (*Zm*WT). The maize *ZmGS3*^{ko} plants had a 34-bp deletion and a base mutation occurring in the first exon of *ZmGS3*. These mutations resulted in a frame shift and early translational termination of the predicted protein (fig. S3G). Upon alkaline treatment, the knockout plants appeared to have enhanced alkaline tolerance, as indicated by growth performance at day 14 of cultivation, compared with the wild type (Fig. 3, G and H, and fig. S3H). Differences in phenotypes were more marked after 50 days of treatment; almost all the wild-type seedlings died, whereas the *ZmAT1/GS3*^{ko} survived and continued to grow (Fig. 3I and fig. S3I). This evidence supports that *ZmAT1/GS3*^{ko} could also increase alkaline tolerance in maize, similar to what we observed in sorghum, millet, and rice.

AT1/GS3 cooperates with aquaporins

To further ascertain how AT1/GS3 regulates crop alkaline tolerance, we detected SbAT1-interacting proteins by immunoprecipitation in combination with mass spectrometry

(IP-MS). Glutathione S-transferase (GST)–SbAT1 was applied to bind proteins in alkaline-treated root samples, and then those bound proteins were released for further analysis. There were 386 proteins detected as candidates interacting with SbAT1 (table S2), including the guanine nucleotide–binding protein β subunit (Gβ subunit) (Fig. 4A), which supports the IP-MS result because it is well known that Gβ and Gγ function together in a complex to regulate a wide range of biological processes (*20*–*22*). A number of aquaporins, especially the PIP2;1/2;2 and PIP1;3/1;4 proteins, were found among the interacting proteins. Homologs of these aquaporins have been reported to be involved in stress biology by regulating ROS homeostasis in both plants and mammals (*12*, *23*). We confirmed the interactions of these proteins with both SbAT1 and Sbat1 by performing different assays. The luciferase complementation imaging (LCI) assay data together with the coimmunoprecipitation (Co-IP) assay and pull-down assay all demonstrated their interactions both in vivo and in vitro (Fig. 4, A and B, and fig. S4, B and C).

The rice aquaporin OsPIP2;1 shares high sequence similarity with its sorghum counterpart, and we also confirmed the interaction between OsPIP2;1 and OsGS3 (fig. S4D). We thus examined the function of OsPIP2 in the alkaline stress response. To investigate the roles of *OsPIP2;1* and its homolog *OsPIP2;2*, we generated a double knockout mutant of *OsPIP2;1* and *OsPIP2;2* using CRISPR-Cas9. Two independent T_2 homozygous lines with knockouts of both *OsPIP2;1* and *OsPIP2;2* (*OsPIP2;1^{ko}/2;2^{ko}*-8-3 and *OsPIP2;1^{ko}/2;2^{ko}*-9-8) were selected for further analysis (fig. S4, E and F). As shown in Fig. 4, C and D, *OsPIP2;1^{ko}/2;2^{ko}* had lower alkaline tolerance, as illustrated by their poorer relative survival rates and plant growth, compared with the respective control in rice. Because aquaporins are known to be involved in the homeostasis of ROS in cells across different life kingdoms (*12*, *24*) and plant root growth inhibition under alkaline stress is closely associated with ROS accumulation (*6*), we measured ROS accumulation by 2′,7′-dichlorodihydrofluorescein diacetate (H_2DCFDA) staining in rice roots. The fluorescent signal of H_2DCFDA staining reflects the ROS contents in plant tissues (*25*). The strong signal confirmed the higher ROS contents in plant roots of *OsPIP2;1^{ko}/2;2^{ko}* lines compared with the wild-type control line subjected to alkaline treatment (Fig. 4, E and F). These results suggest that aquaporins *PIP2;1/2;2* are involved in the regulation of alkaline tolerance by affecting the ROS status in plants. Because PIP2;1/2;2 interact with Gγ, we then measured the ROS accumulation of different transgenic lines of both sorghum and rice. Overexpression of *AT1/GS3* or the C-terminal truncated protein enhanced ROS accumulation in the roots of sorghum and rice compared with that of their respective controls, whereas knockout of *AT1/GS3* greatly reduced ROS accumulation (Fig. 4, G to J). The strong fluorescent signal staining also confirmed the higher ROS contents in plant roots of NIL-*Sbat1* compared with NIL-*SbAT1* after alkali treatment (fig. S5A).

We also analyzed ROS status in the leaves of transgenic sorghum, millet, rice, and maize that either overexpressed *AT1/GS3* or had a knocked out *AT1/GS3* together with sorghum NIL lines by 3,3′-diaminobenzidine (DAB) staining. DAB staining detected a brown precipitate in tissues, and the intensity of the staining was indicative of the amount of H_2O_2 accumulation. The DAB staining results in all

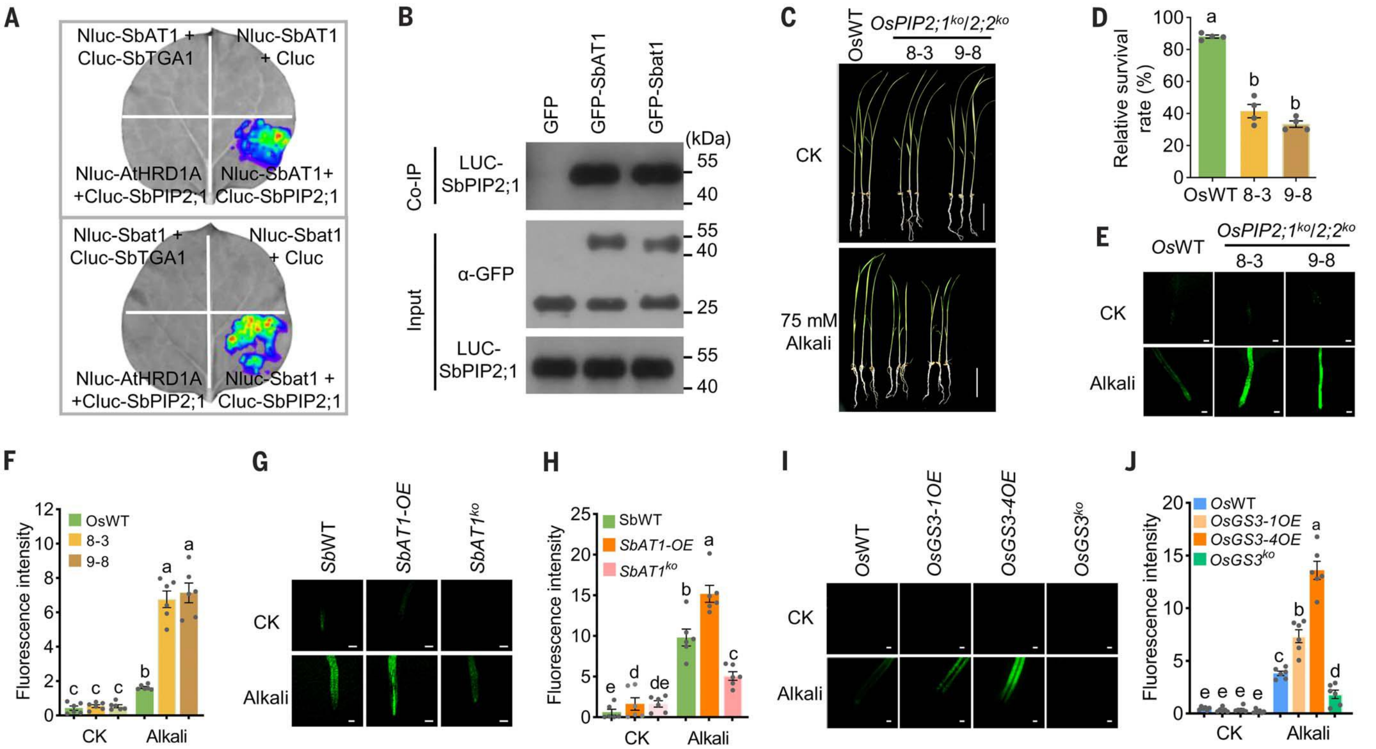


Fig. 4. The Gγ subunit AT1 interacts with aquaporin PIP2;1, which functions in plant alkaline tolerance. (**A**) LCI assay of both SbAT1 and Sbat1 with SbPIP2;1. Cluc-SbTGA1 and Nluc-AtHRD1A were used as the negative controls. (**B**) Co-IP assay of SbAT1 and Sbat1 with SbPIP2;1. (**C**) Phenotypic analysis of *OsPIP2;1^{ko}/2;2^{ko}* mutants under alkaline stress. Seeds of *Os*WT and two independent *OsPIP2;1^{ko}/2;2^{ko}* lines were sown in soil without (CK) or with 75 mM alkali. Photographs were taken on the 27th day after seed sowing. Scale bars, 5 cm. (**D**) Statistical analysis of the relative survival rates of plant materials, as in (C). Data are the means ± SEMs (n = 16 plants for each repeat) of four biological replicates in each treatment. (**E**, **G**, and **I**) H_2O_2 amount detection by an ROS detection probe (H_2DCFDA) in the root tips of *PIP2;1* and Gγ subunit–related genetic plants. Two-week-old sorghum and rice seedlings treated with or without 200 mM alkali for 48 hours were used for analysis. Scale bars, 100 μm. (**F**, **H**, and **J**) Statistical analysis of the H_2O_2 concentration in (E), (G), and (I). Data are the means ± SEMs (n = 6 plants). In (D), (F), (H), and (J), statistical significance was determined by ordinary one-way ANOVA with Tukey's multiple comparisons test.

four crops (fig. S5, B to F) confirmed the results of H_2DCFDA staining. It is well known that alkaline stress can cause ROS accumulation (*6*). Excessive amounts of ROS result in cellular oxidative stress, which causes cell death in plants and consequently reduces plant survival rates. The regulation of cellular ROS accumulation might explain why the truncated Gγ had lower survival rates and why the knockout of Gγ increased alkaline tolerance in these crops.

Gγ regulates PIP2 phosphorylation in ROS distribution

To further study how Gγ interacts with PIP2 aquaporins to affect ROS homeostasis in response to alkaline stress, we applied the redox probe Cyto-roGFP2-Orp1, which senses H_2O_2 in the cytoplasm (*26*–*28*). Fluorescence after excitation was observed at 405 and 488 nm but not in the no-plasmid control group (fig. S6A), which indicated that we successfully expressed the Cyto-roGFP2-Orp1 probe in rice protoplasts. We next analyzed the redox state of protoplasts overexpressing Cyto-roGFP2-Orp1 under different redox challenges. The morphology of the protoplast was complete, and fluorescence was not quenched under 100 μM dithiothreitol (DTT) or 100 μM H_2O_2. Protoplasts overexpressing Cyto-roGFP2-Orp1 responded well to reductive challenge and oxidative challenge, and the response range (ratio of oxidation:reduction) was 2.9 (Fig. 5, A and B), which is within the dynamic range of the roGFP2-Orp1 probe reported (*29*). These results showed that this system is suitable for the detection of redox in rice protoplasts.

Next, we performed the assay under alkaline treatment conditions. The standard pH for rice protoplasts is 5.4, and we found that the highest pH under which the protoplasts can still remain intact after a certain treatment time was 7.5. Then, we treated the wild-type protoplast with this alkaline condition for different time points and observed cell integrity. Imaging results showed that the protoplasts remained intact at pH 7.5 for 40 min, but rupture of the protoplast was observed after 60 min of alkali treatment (as shown by the blue arrow in fig. S6B, left panel). We also found that the H_2O_2 level at 40 min was markedly higher than that of the control but was not induced at 20 min under the alkali treatment compared with CK buffer (pH 5.4) treatment. Therefore, we selected the 40-min time point as the appropriate treatment condition (fig. S6B, right panel).

We then used this Cyto-roGFP2-Orp1 system and the treatment conditions to detect redox status in the protoplasts of *Os*WT, *OsGS3-4OE*, *OsGS3*^{ko}, and *OsPIP2;1*^{ko}*/2;2*^{ko} lines. The results showed that the relative H_2O_2 level increased upon alkaline treatment compared with their untreated controls, and representative cells are shown in fig. S6C based on $n > 30$ protoplasts analyzed in each group. To overcome the variation in individual protoplasts, we measured the redox states in large numbers of cells (with 1×10^5 protoplasts each repeat) of those same lines transfected with Cyto-roGFP2-Orp1 at 525 nm after excitation at 405 and 488 nm detected by a microplate reader. As shown in Fig. 5C, after alkaline treatment, the relative H_2O_2 levels were higher in the *OsGS3-4OE* group than in the *Os*WT. These results suggested that *OsGS3-4OE* performed negatively in the alkali response because of the production of high H_2O_2 in cells, whereas lower ROS accumulation in *OsGS3*^{ko} could be one of the reasons why *OsGS3*^{ko} is tolerant to alkaline treatment. We also observed that the relative H_2O_2 levels were significantly higher in *OsPIP2;1*^{ko}*/2;2*^{ko}-8-3 compared with *Os*WT under alkali treatment (Fig. 5D).

Previous studies on PIP2;1 in *Arabidopsis* have found that modifications in the phosphorylation of PIP2;1 affect its activity (*30*, *31*). Thus, we studied the function of SbPIP2;1 phosphorylation on ROS distribution under alkaline stress. First, we identified phosphorylation sites in SbPIP2;1 by liquid chromatography with tandem mass spectrometry (LC-MS/MS) in seedling samples treated or untreated with alkaline stress and detected two phosphorylation sites, S285 and S288 (fig. S6D). We found that overexpression of *SbAT1* could attenuate the phosphorylation of SbPIP2;1 (Fig. 5E). Using the anti-pS285/288 antibody, we quantified the phosphorylation levels of OsPIP2;1 in rice *OsGS3* transgenic lines grown in the control and alkali treatment conditions. The phosphorylation levels of OsPIP2;1 in both lines overexpressing the full-length *OsGS3* (*OsGS3-1OE*) and the short form of *OsGS3* (*OsGS3-4OE*) were lower than the level in the wild-type control, whereas the phosphorylation levels of OsPIP2;1 were higher in *OsGS3*^{ko} (Fig. 5F), which is similar to what we found in sorghum PIP2;1 (Fig. 5E). These results suggested that AT1/GS3 might modulate ROS homeostasis in plants by attenuating the phosphorylation of PIP2;1 when stressed by alkaline conditions.

To confirm our observation of the phosphorylation of PIP2;1 on the cellular ROS status in plant cells, we transiently expressed a fusion construct in the protoplast of the rice *OsPIP2;1*^{ko}*/2;2*^{ko} mutant by inserting a P2A self-cleaving peptide (*32*) in the region between different phosphorylation forms of OsPIP2;1 and the ROS probe (Cyto-roGFP2-Orp1), which could produce two equal molar proteins of OsPIP2;1 and the ROS probe (Fig. 5G). As shown in Fig. 5H, there was no significant difference in untreated cells, but the higher ROS production in cells was repressed by overexpression of *OsPIP2;1* in the *OsPIP2;1*^{ko}*/2;2*^{ko} mutant. Additionally, the phosphorylated form of OsPIP2;1(3SD) effectively attenuated the ROS level, whereas the dephosphorylated form of PIP2;1 (3SA) accumulated higher ROS levels in cells upon alkali treatment (Fig. 5H). These results indicate that Gγ negatively regulates the phosphorylation of PIP2;1, leading to elevated ROS levels in plants.

To further reveal how PIP2s and AT1/GS3 function in the control of cellular ROS levels under stress conditions, we detected and quantified the relative ROS content in both cytosol and apoplast in the root tissues of rice lines, such as wild-type ZH11, *OsGS3-4OE*, *OsGS3*^{ko}, and *OsPIP2;1*^{ko}*/2;2*^{ko}-8-3 lines, by staining with H_2DCFDA (cytosolic redox status) and OxyBURST Green H_2HFF BSA (apoplastic redox status) upon alkaline treatment. We found very little difference in the ROS content in all of these rice lines without alkaline treatment (Fig. 5, I to L). After alkali treatment, significantly increased cytosolic ROS accumulation was detected in *OsGS3-4OE*, whereas cytosolic ROS accumulation was reduced in *OsGS3*^{ko} compared with the wild-type control (Fig. 5, I and J). We also examined the apoplastic ROS level of the same lines. *OsGS3-4OE* showed relatively lower-apoplast ROS than *Os*WT, whereas high-apoplast ROS accumulation was detected in the roots of the *OsGS3*^{ko} line. Increased cytosolic ROS and reduced apoplastic ROS accumulation were also detected in *OsPIP2;1*^{ko}*/2;2*^{ko} compared with ZH11 (Fig. 5, I to L). These results revealed that the G protein γ subunit GS3/AT1 and aquaporin OsPIP2;1/2;2 could function in opposite ways to regulate the cytosolic/apoplast ROS ratios in response to alkaline stress in plant roots. Together with cytosol ROS detected by the ROS probe (Cyto-roGFP2-Orp1), these results suggest that GS3/AT1-mediated phosphorylation of OsPIP2 aquaporins might function to regulate intracellular ROS levels and avoid damage to plant roots under alkaline stress.

Enhanced field crop yield in highly sodic lands

To assess the usefulness of the *AT1/GS3* gene for crop production, we field tested sorghum, rice, maize, and millet with different natural alleles and genetically modified *AT1/GS3* genes in highly sodic lands containing natural alkali. The fields are located in two sites within sodic regions in China—the Daan region in Jilin Province (northern China) and the Pinglou region in Ningxia Province (northwestern China). These regions are among the main crop production areas in China but have large areas of sodic soils, which limit crop production.

KY^{NIL}(*GS3*) is the elite cultivar Kongyu131 carrying *OsGS3-2* (with an in-frame 3-bp insertion in the C terminus relative to *OsGS3-1*), which is functionally equivalent to *OsGS3-1*. KY^{NIL}(*gs3*$^{-}$) is in the background of Kongyu131 with an introgressed *OsGS3-3*, which is a complete loss-of-function allele. Before the field

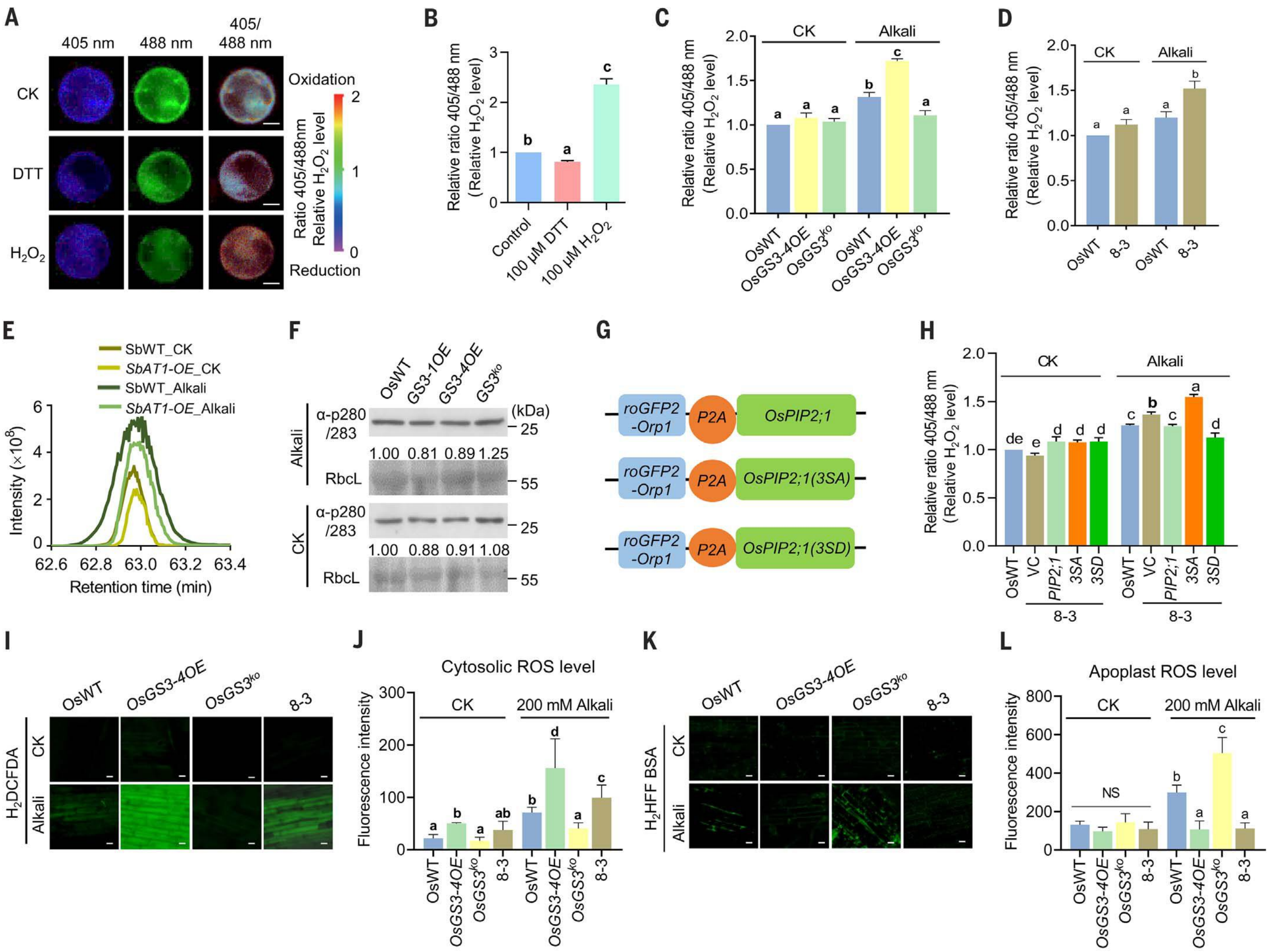


Fig. 5. The Gγ subunit of AT1 homologs regulates the plant alkali response through the H_2O_2 exporter PIP2;1. (**A**) Confocal imaging of Cyto-roGFP2-Orp1 in *Os*WT protoplasts treated with 100 μM DTT and 100 μM H_2O_2 separately. Scale bars, 5 μm. (**B**) The relative 405/488 nm ratio of Cyto-roGFP2-Orp1 in samples measured with a microplate reader. (**C** and **D**) Detection of cytosolic H_2O_2 accumulation in the Gγ subunit and *PIP2;1*-related genetic plants. The protoplasts transfected with Cyto-roGFP2-Orp1 were treated with standard W5 liquid (pH 5.54, CK) or W5 liquid by the addition of alkali to pH 7.5 (Alkali) for 40 min. 8-3, *OsPIP2;1^{ko}/2;2^{ko}*-8-3. (**E**) Relative abundance of the phosphopeptides, including S285 and S288 sites, by LC-MS/MS. *Sb*WT and *SbAT1-OE* plants were treated with or without 75 mM alkali. (**F**) OsGS3 affects the phosphorylation level of OsPIP2;1. Three-day-old rice plants treated with 200 mM alkali for 6 hours were subjected to phosphorylation analysis with an α-p280/283 antibody. The large subunit of ribulose-1,5-bisphosphate carboxylase/oxygenase (RbcL) was used as a loading control. (**G**) Schematic diagram of *roGFP2-Orp1-P2A-OsPIP2;1/OsPIP2;1 (3SA)/OsPIP2;1(3SD)* fusion genes used in (H). (**H**) Phosphorylation of OsPIP2;1 is essential for its function in modulating H_2O_2 accumulation in the cytosol. VC, vector control. *3SA*, *OsPIP2;1(3SA)*; *3SD*, *OsPIP2;1(3SD)*. In (B) to (D) and (H), data are the means ± SEMs (three replicates, ~1×10^5 cells of each line in each replicate). (**I** and **K**) Cytosol and apoplast ROS in situ detection of *Os*WT, *OsGS3-4OE*, *OsGS3^{ko}*, and *OsPIP2;1^{ko}/2;2^{ko}*-8-3 plants. Scale bars, 20 μm. (**J** and **L**) Statistical analysis of H_2O_2 accumulation in (I) and (K). Data are the means ± SEMs ($n \geq 8$). In (B) to (D), (H), (J), and (L), statistical significance was determined by ordinary one-way ANOVA with Tukey's multiple comparisons test.

trial, the alkaline tolerance of KY^{NIL}(*GS3*) was tested in comparison with KY^{NIL}(*gs3$^-$*). The test was carried out at the seedling stage in a greenhouse with 75 mM alkali. As expected, KY^{NIL}(*gs3$^-$*) showed much higher alkaline tolerance than Kongyu131 (fig. S7, A and B).

We then conducted an experiment to compare NILs in soils with two different pH values, 9.45 and 7.74 (control), using highly sodic soils from the same region mixed with nutrient soil. Except for the number of panicles per plant (fig. S7C), KY^{NIL}(*gs3$^-$*) showed significantly better performance than KY^{NIL}(*GS3*) in relative survival rate, the number of grains per panicle, grain weight, and grain yield (fig. S7C) under sodic soil with pH 9.45.

We also performed a field test with a designed plot experiment in Daan, where the soil pH was 9.17. The KY^{NIL}(*gs3$^-$*) line performed much better than KY^{NIL}(*GS3*) at both the seedling (fig. S7D) and harvest stages (Fig. 6A, left panel), indicating enhanced alkaline tolerance in KY^{NIL}(*gs3$^-$*). At the harvest stage, KY^{NIL}(*gs3$^-$*) rice produced larger panicles (fig. S7E) with a higher number of grains per panicle (Fig. 6A, third panel) and increased grain weight (Fig. 6A, fourth panel), resulting in a 29.3% increase in grain yield per clump (Fig. 6A, fifth panel). The grain yield was 27.8% higher for the KY^{NIL}(*gs3$^-$*) rice compared with the control (Fig. 6A, right panel).The same plantings were established in a field with a pH of 5.58, where the difference in yield per plant between

KY^{NIL}(*gs3*$^{-}$) and the control was only 10.3% (fig. S7F). The grain yield of the rice NILs in sodic soil and acidic soil was studied in the same location on the second year. There was a 22.4% yield increase in alkaline soil and a 6.64% increase in the control field (fig. S7, G and H), similar to results obtained previously. Furthermore, *OsGS3* knockout contributed to grain length in both sodic soil and neutral soil. We also found that *OsGS3* knockout contributed to width in sodic soil but not in neutral soil (fig. S7, I and J). These results show that the nonfunctional allele of *GS3* could achieve higher crop production in highly sodic soils.

Because of its good quality and high yield, the improved elite rice line Zhongkefa5 (ZKF5) has been planted in >0.1 million ha in northern China since 2018. ZKF5 has a nonfunctional allele of *GS3* (*OsGS3-3*), similar to that in KY^{NIL}(*gs3*$^{-}$). We tested ZKF5 field performance in relatively high-sodic soil (pH 8.5 to 8.7) and low-sodic soil (pH 7.4 to 7.6) in the summer of 2021. At the end of the growing season, field production data were obtained from >30 ha of land by the local farmer association. We found only a 7.8% reduction in yield production in the sodic field when compared with that in the neutral field (fig. S7K). These large-area field production data also indicate the potential for increasing crop production by using the *GS3-3* allele in rice production in sodic lands.

We also planted Zhonghua 11 (ZH11) rice and its *OsGS3* knockout line, *OsGS3*^{ko}, in soils of the same two pH levels—7.74 as the control and 9.45 as the sodic soil—in a greenhouse. Although we failed to harvest the seeds of ZH11 because of its photoperiod sensitivity when planted in Jilin Province, the greater relative survival rate observed in the *OsGS3*^{ko} line (fig. S7L) demonstrates its greater tolerance to sodic conditions.

Sorghum, maize, and millet were tested in the Pingluo region, which consists of dry lands with highly sodic soil in northwestern China. In this region, the pH naturally increases during the crop growing season because of changes in the underground water level (*2*). The Wheatland wild-type and *SbAT1*^{ko} lines of sorghum were planted in the same plot with a pH of 8.97 in the spring season that reached a pH of 9.27 at the flowering stage in August. The survival rate was >60% for the *SbAT1*^{ko} line and only 33% for the Wheatland wild-type control (Fig. 6B, first and second panels). Leaf burn, a symptom that usually occurs in monocotyledonous crops affected by high salt or sodic stress, was observed in most Wheatland wild-type plants but not in plants of the *SbAT1*^{ko} line (Fig. 6B, first panel). At the harvest stage, the grain yield of the *SbAT1*^{ko} line was 20.1% greater than that of the control (Fig. 6B, third panel) despite its lower numbers of tillers and panicles (Fig. 6B, fourth and fifth panels). Because whole sorghum plants are commonly used for silage, we measured the fresh weight of whole-plant biomass and found that the fresh weight of plants in the *SbAT1*^{ko} line was 30.5% higher than that of the control (Fig. 6B, right panel). Both the higher grain production and whole-plant biomass of the *SbAT1*^{ko} line compared with those of the wild type demonstrated greater field performance for sorghum grown in sodic land. In the same region, we also planted the NIL-*SbAT1* and NIL-*Sbat1* lines in the summer season. At the end of August, we found that NIL-*SbAT1* outperformed NIL-*Sbat1* (Fig. 6C), and the differences were similar to the results recorded from the greenhouse experiment (Fig. 2B).

The *SiAT1*^{ko} line and its control, Ci846, were also planted together with sorghum in the same region. The *SiAT1*^{ko} line at the seedling stage had a survival rate of nearly 100%, whereas the wild-type Ci846 had a survival rate of only 75% (Fig. 6D, left panel). Additionally, at the harvest stage, the panicle size of the knockout line was also larger than that of the control (Fig. 6D, middle panel), and the grain yield of *SiAT1*^{ko} was 19.5% higher than that of the control (Fig. 6D, right panel).

In the same field, we also planted maize with *ZmGS3* knocked out together with its control line KN5585 (*Zm*WT). At the seedling stage, the *ZmGS3*^{ko} line showed a relative survival rate of 42.5% compared with 18.5% of the wild-type control, as recorded 1 month after planting (Fig. 6E). After 3 months of growth, most individuals of the KN5585 line died, whereas 7.4% of individuals from the knockout line survived. Although none of these plants reached maturity to produce grains because of the inherent sensitivity of maize to alkaline conditions, knockout of *ZmGS3* showed enhanced alkaline tolerance. Altogether, we conclude that nonfunctional mutants, either obtained from natural variations or generated by gene editing, can improve the field performance of crops in terms of biomass or grain production when cultivated in sodic soils.

Discussion

In this study, we have identified and demonstrated that natural alleles of AT1, an atypical G protein γ subunit, contribute to alkaline tolerance in four different monocotyledonous crops. The N-terminal domain of AT1 and its homologs played negative roles in alkaline stress tolerance. Crops with a truncated protein were highly sensitive to alkaline stress. This might be because of the inhibitory role of the C-terminal domain, which is necessary for protein degradation in its rice homolog (*33*, *34*). Accordingly, overexpression of the entire protein results in higher sensitivity to alkaline stress due to higher amounts of the protein, and overexpression of the truncated protein leads to an even higher sensitivity to alkaline stress. By contrast, high tolerance to alkalinity was observed in the knockout or natural variants with nonfunctional alleles in all four crops because of a lack of the N-terminal domain (Fig. 6F).

SbAT1 and *OsGS3* play pleiotropic roles in agronomic trait regulation and stress response (*35*, *36*). Both *OsGS3* and *SbAT1/qTGW1a* are key determinants of grain size (*19*, *37*). *OsGS3* also participates in stigma exsertion (*38*). Additionally, we found that *SbAT1*, previously also named *GC1* (*Glume Coverage 1*) because of its role in regulating sorghum glume coverage (*18*), affects alkaline tolerance in monocot crops (sorghum, rice, maize, and millet). *OsGS3* is also involved in salinity and chilling stress with an unknown mechanism (*36*) and controls thermotolerance in rice through alteration of wax biosynthesis (*39*). Accordingly, SbAT1 and OsGS3 act as negative regulators of these traits, and the truncated proteins with only an N-terminal domain led to a reduced grain size and low glume coverage. Because G protein γ subunits play important roles at the early stages of cell signaling pathways, it is not a surprise that they have pleiotropic effects in different aspects of plant development and stress tolerance. Nevertheless, the identification of the downstream components of the G protein is an important aspect in plants. We also note the need to consider the probable negative effect of nonfunctional alleles of *SbAT1/GC1* for sorghum due to the production of longer glume sizes (*18*), which might be unfavorable for threshing. For rice, slightly higher plant height was observed in the knockout mutant and natural nonfunctional mutant of *OsGS3* (*33*), and this characteristic might not be favored by breeders.

Cells have developed different systems to protect themselves by activating metabolic pathways involving ROS or peroxiporins to facilitate H_2O_2 export from cells and maintain homeostasis. Aquaporins have no catalytic activity to convert oxidative species to less harmful molecules in cells, but aquaporins are known to be involved in bidirectional transport of oxidative species in cells. Most transport assays were performed with additions of excess amounts of extracellular H_2O_2 to demonstrate the ability of transporters to import H_2O_2 across the cell membrane. However, when genes encoding the H_2O_2-degrading enzyme glutathione peroxidase (GPX1) or catalase (CAT) are knocked out, the excess amount of H_2O_2 present in stressed cells can be exported with the assistance of certain aquaporins that function as peroxiporins to detoxify the cell (*9*). We found a similar function in plant aquaporins in the regulation of the ROS level under stress after we investigated mutants with a knockout of *OsPIP2;1* that overexpressed both sorghum and rice aquaporins. Overall, these results highlight the important

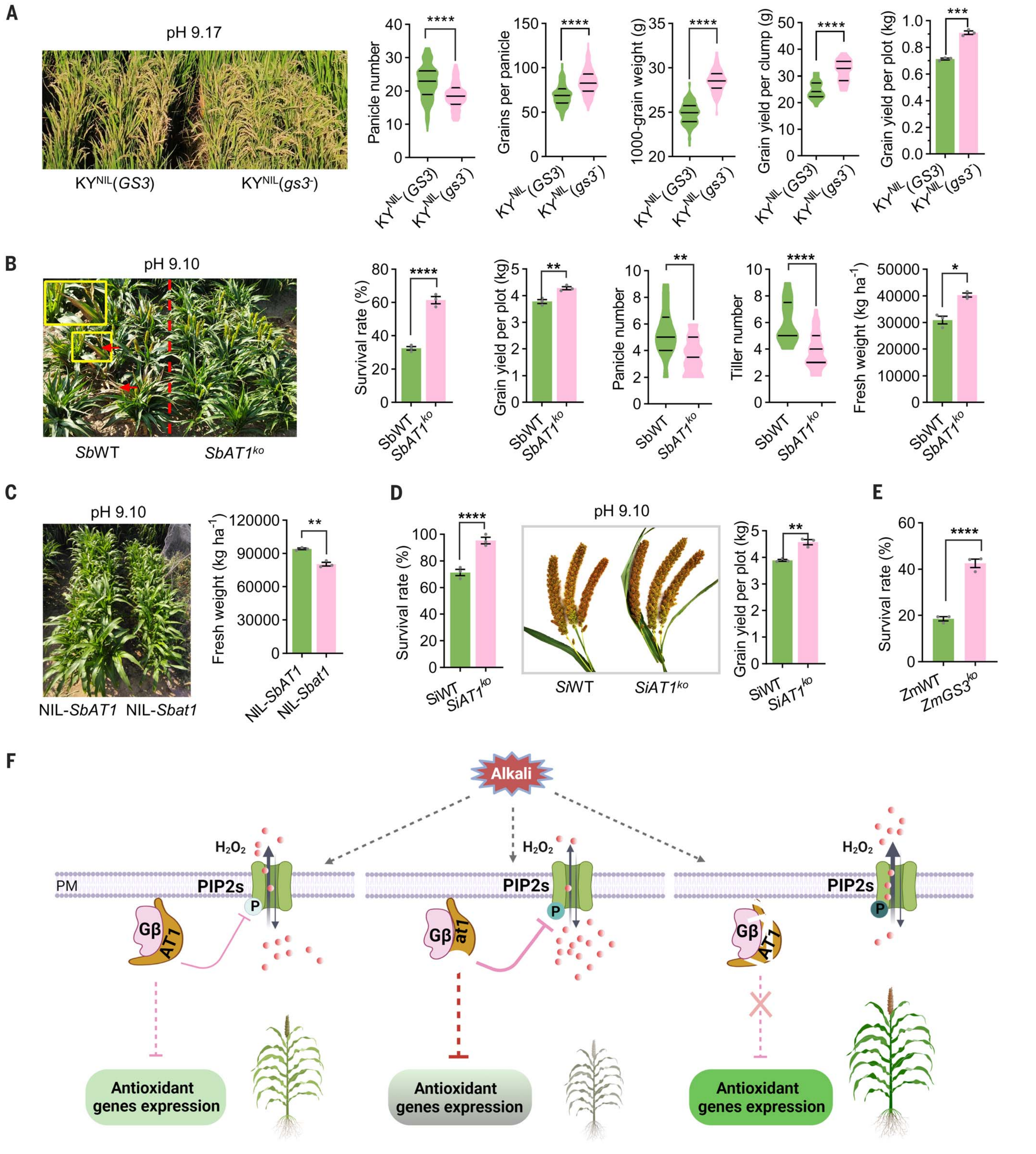


Fig. 6. *AT1/GS3* knockout and natural nonfunctional alleles enhance crop yield in saline-alkaline fields. (**A**) Phenotype and grain production of rice KY^{NIL}(*GS3*) and KY^{NIL}(*gs3*$^{-}$) from the alkali field (pH 9.17) in Jilin Province, China, in 2021. The first panel shows the phenotype of the rice plants at the reproductive stage (3 months after planting in the field). The panicle number indicates the number of panicles per plant. Data are the means ± SEMs (n = 3 plots). (**B**) Phenotype, survival rate, grain production, and whole biomass of *Sb*WT and *SbAT1*^{ko} grown in the alkali field (pH 9.10) of Ningxia Province, China, in 2021. Data are the means ± SEMs (n = 3 plots). (**C**) Phenotype and fresh weight of NIL-*SbAT1* and NIL-*Sbat1* seedlings grown in the alkali field (pH 9.10) of Ningxia Province, China, in 2021. (**D**) Phenotype, survival rate, and grain production of the millet lines grown in the alkaline field (pH 9.10) of Ningxia Province, China, in 2021. Data are the means ± SEMs (n = 3 plots). (**E**) Statistical analysis of the survival rates of *Zm*WT and *ZmGS3*^{ko} grown in the alkaline field (pH 9.10) of Ningxia in 2021. Data are the means ± SEMs (n = 3 plots). In (A) to (E), statistical significance was determined by two-tailed

unpaired *t* test. *P < 0.05; **P < 0.01; ***P < 0.001; ****P < 0.0001. (**F**) A proposed model of the Gγ subunit AT1-mediated response to alkaline stress in plants. Under alkaline stress, PIP2s function as H_2O_2 exporters. The Gγ subunit AT1 could pair with Gβ to negatively modulate the phosphorylation level of PIP2s and thus reduce their H_2O_2 export activity, leading to overaccumulation of H_2O_2 and resulting in plant sensitivity to alkaline stress. The truncated form of AT1, at1, further inhibited H_2O_2 export activity and led to plant hypersensitivity to stress. However, the knockout of AT1 homologs or their natural nonfunctional form releases the inhibition of PIP2s and efficiently improves the alkaline stress tolerance of crops.

roles of water-facilitator type aquaporins in contributing to H_2O_2 detoxification to protect cells against oxidative stress.

With the knowledge that AT1 plays a negative role in modulating the phosphorylation of aquaporins to regulate the ROS level under alkaline stress conditions (Fig. 6F), we might be able to design crops that tolerate high alkaline stress. We have successfully demonstrated the potential alkaline tolerance improvement in a number of monocot crops (sorghum, rice, maize, and millet) by modifying *AT1* through knockout of *AT1* orthologs or selecting for nonfunctional alleles in *AT1* crops. This strategy might have potential value in other cereal crops. Other options to explore are the genetic engineering of *AT1* in dicotyledonous crops, such as tomatoes, potatoes, and fruit trees. The results may be even more complex because the *GS3* homolog has been reported to play opposite roles between dicots and monocots (*33*).

Materials and methods

Plant materials

Sixteen selected sorghum accessions based on seed availability belonging to a sorghum association panel (SAP) used in the study (*40*, *41*) were first used to screen the suitable concentration of alkaline treatment. The SAP population was composed of 352 sorghum inbred lines and was used to evaluate relative survival rates for GWASs. Seeds of the SAP population and another 37 sorghum accessions were all obtained from the United States Department of Agriculture's Agricultural Research Service (USDA-ARS). SN010 (of the Hap1 haplotype) is a sorghum variety from China, whereas M-81E (of Hap2) is a sorghum improved inbred from the United States. The NILs $AT1^{SN010}$ and $AT1^{M\text{-}81E}$ are from our laboratory stocks, and they differ in a 58-kb interval from that of the F_{11} generation. The interval was flanked by two molecular markers, *MSR0069* and *MSN0013*.

The rice NILs KY^{NIL}(*GS3*) and KY^{NIL}($gs3^-$) used in field trials were developed in the Kongyu131 (KY131) variety. Two rice varieties, Kongyu 131 (KY131) and Minghui 63 (MH63), were used as the parents for the construction of NILs. KY131, with a functional *GS3* allele, was used as the recipient and is a *japonica* variety with the largest planting area in China (https://www.ricedata.cn/variety/). MH63, with a nonfunctional *GS3-3* allele, was used as the donor and is an elite *indica*-type restorer line with the largest planting area in China. The overall construction followed a recurrent backcross procedure including four generations of backcrosses and two generations of selfing. A cross was made between the recipient KY131 and the donor MH63. In backcrossing generations from BC_1F_1 to BC_4F_1, selected individuals heterozygous at *GS3* were backcrossed to KY131. Negative selections were carried out in BC_3F_1, BC_4F_1, BC_4F_2, and BC_4F_3. In BC_3F_1 and BC_4F_1, the recombinants heterozygous at *GS3* were subjected to background selection using whole-genome array GSR40K. Subsequently, the BC_4F_3 population was developed from an individual in BC_4F_1 with the highest proportion of genome recovery of the sequence of the recurrent parent by two rounds of recombination selection. The genotype of an NIL from BC_4F_4 was further confirmed by whole-genome array GSR40K.

Zhongkefa5 (ZKF5) was generated from a cross between the recipient KY131 and Jiahe212 (containing a nonfunctional $gs3^-$ allele, a C to A mutation at position +16733441 of chromosome 3, and obtained a premature termination). Then, an F_1 individual was used as the recipient, and the landrace rice Songgen88 was used as the donor for subsequent backcrossing and selection. The *GS3-3* allele was confirmed by sequencing.

The sorghum transgenic overexpression line *SbAT1-OE* and mutant $SbAT1^{ko}$ used in this study were constructed in the sorghum variety Wheatland background. The millet $SiAT1^{124}$ transgenic line and the $SiAT1^{ko}$ and $SiAT1^{102}$ mutants used in this study were constructed in the millet variety Ci846 background. The rice *OsGS3-1OE*, *OsGS3-4OE*, $OsGS3^{ko}$, and *OsGS3Ri* transgenic lines with the ZH11 background have been previously described (*34*). The maize mutant line $ZmGS3^{ko}$ used in this study was developed using the maize variety KN5585. Related primers are shown in table S3.

Plant growth conditions

Before sowing, all seeds for each line that were plump and of similar size were chosen for study. Seeds were sterilized in 70% EtOH for 30 s and washed three times with distilled water. Subsequently, seeds were shaken in 10% bleach solution for 30 min and washed with distilled water 8 to 10 times. The seedlings were grown in a controlled greenhouse under long-day conditions (16 hours light/8 hours dark) at 28°C. The illumination was 600 μmol m^{-2} s^{-1}, and the relative humidity was 60 to 80%.

Field trials of sorghum, maize, and millet NILs and/or transgenic T_1 homozygous lines were carried out from April 2021 to September 2021 in Huiwei Village, Pingluo County of Ningxia Hui Autonomous Region (38°57′29″ N, 106°32′39″ E; elevation 1090 m). All the field tests in this study were performed with three plots as three repeats. The plot dimensions were 3.6 m by 1.5 m with row spacing of 0.5 m, plant spacing of 0.2 m, and walkways of 1 m between plots. Our sowing method was single-hole sowing, and the sowing depth was ~3 cm.

Field trials of rice KY NILs grown in sodic soil with a high pH of 9.17 were carried out in Honggangzi town, Jilin Province (45°36′19″ N, 123°50′55″ E; elevation 130 m). A pH 5.58 soil control was established by planting rice KY NILs in the same season in Heilongjiang (47° 25′34″ N, 143°02′45″ E; elevation 80 m). One-month-old seedlings of each line cultivated in a greenhouse were selected and sown into the above paddy fields. The plot dimensions in the paddy fields were 1.5 m by 0.9 m, the row spacing was 0.3 m, and the plant spacing was 0.15 m. Three seedlings were transplanted per clump. Each plot had three replicates and was established based on a randomized block design. The field locations of ZKF5 plants grown in soils of pH 8.5 to 8.7 were 123°22′12″ to 124°54′ N and 45°23′24″ to 45°37′48″ E (composed of four plots, 7, 10, 8, and 8 ha separately), and those in soils of pH 7.4 to 7.6 were 122°48′36″ to 123°24′ N and 45°37′48″ to 45°39′36″ E (composed of two plots, 11 and 22 ha separately).

Phenotypic evaluation

The seeds used for phenotype evaluation were all harvested at the same time and stored under the same conditions. In an initial test, seeds of each of the 16 selected sorghum lines were sown uniformly in a nutrient soil with 50% vermiculite. Concentrations of 0, 25, 50, 75, 100, 125, and 150 mM mixed alkali ($NaHCO_3$:Na_2CO_3 with a molar ratio of 5:1) were used to immediately treat the soil. The 75 mM alkali treatment was selected as the most suitable concentration. The detailed working concentrations of $NaHCO_3$ and Na_2CO_3 in 75 mM alkali are 62.5 and 12.5 mM, respectively. It should be noted that the final concentration of mixed alkali is calculated based on the total volume of soil and absorbed water. Relative survival rate after plants spent 3 weeks under 75 mM alkali stress was recorded. The relative survival rate of a GWAS population was calculated by taking the numbers of survival plants under alkali stress and dividing it by the numbers of survival plants under standard conditions after 3 weeks of treatment. Thus,

the relative survival rate is contributed to by both the abilities of seed germination and seedling survival under alkali conditions. Three biological repeats for the phenotypic evaluation of the SAP population were performed. For transgenic and genome-edited plants, survival rates were recorded as the phenotypic data on the 14th day after the 75 mM mixed alkali stress treatment was applied. For phenotype evaluation of the field trials of sorghum, rice, maize, and millet plants, relative survival rates were calculated 1 month after sowing in the field, and other important agronomic traits, including biomass and grain yield, were recorded at maturity. The fresh weights of the aboveground materials of 10 seedlings from each line grown under the control and alkali treatments were also measured.

GWAS

Reference genome sequences of the sorghum variety BTx623 were obtained from a database of the Phytozome website (https://phytozome-next.jgi.doe.gov/) (*42*). SNP markers for the SAP population were obtained from the public community resource https://www.morrislab.org/data (*43*). SNPs with >20% missing data and minor allele frequencies (MAFs) below 0.05 were removed. A total of 82,430 SNPs for the SAP population were used for the GWAS and analyzed using a mixed linear model. The threshold for genome-wide significance was determined using Bonferroni correction, and significant differences were determined based on $P < 1 \times 10^{-5}$.

Bacterial strains and growth conditions

Escherichia coli strains XL1-Blue and DE3 were used for vector construction. XL1-Blue, separately transformed with each recombinant vector, was cultured in LB medium (1% tryptone, 0.5% yeast extract, and 1% NaCl) with an antibiotic (kanamycin or ampicillin) at 37°C overnight. *Agrobacterium tumefaciens* strains GV3101 and EHA105 harboring the corresponding recombinant vectors were liquid-cultured in the same LB medium with the appropriate antibiotics at 28°C overnight.

Plasmid construction and crop transformation

A *SbAT1* overexpression (*SbAT1-OE*) construct in sorghum was prepared by taking the full-length cDNAs of *SbAT1*$^{\mathrm{SN010}}$ and cloning them into the pCambia2300-Myc vector with a Myc tag located at the N-terminal and driven by the ubiquitin promoter. A *SbAT1*^{ko} mutant was constructed using a genome-editing system previously reported (*44*). A 20-bp–specific single-guide RNA (sgRNA) target sequence of Hap1 was synthesized and ligated to the pYLgRNA-*OsU6a* vector. The purified guide RNA (gRNA) expression cassette was subsequently inserted into the binary pYLCRISPR–Cas9-MB vector. *SbAT1-OE* and the recombinant pYLCRISPR–Cas9-MB plasmids were each introduced into the sorghum cultivar Wheatland (with the *SbAT1*$^{\mathrm{SN010}}$ allele) through *Agrobacterium*-mediated transformation (performed in a crop transformation platform led by Y. Sui at the Biotechnology Research Institute, China Academy of Agriculture Sciences). The positive transgenic plants of the T_0 generation were identified by PCR. Gene expression levels of *SbAT1* in transgenic overexpression plants were detected by qPCR. Homozygous mutants of the T_1 generation were confirmed in the sgRNA target sequence by PCR.

We synthesized a truncated G protein γ subunit version of SiAT1^{124}, which mimicked the truncated SbAT1$^{\mathrm{M\text{-}81E}}$. The *SiAT1*^{124} overexpression construct was generated in the same pCambia2300-Myc vector as described above. The same genome-editing system (described above) was used to construct the *SiAT1*^{ko} and *SiAT1*^{102} mutants by designing the sgRNA target sequences in the second exon and the fifth exon of *SiAT1*, respectively. Each corresponding gRNA expression cassette was inserted into the final pYLCRISPR–Cas9-MH vector. All these successful constructs were introduced into the millet inbred line Ci846 (with the *SiAT1* allele) by *Agrobacterium*-mediated transformation. Positive transgenic overexpression plants of the T_0 generation were verified by PCR and qPCR. Homozygous mutants of the T_1 generation were identified in the designed sgRNA target sites by PCR.

The rice *OsGS3-1OE*, *OsGS3-4OE*, *OsGS3*^{ko}, and *OsGS3Ri* transgenic plants used in this study have been described in detail in previous studies (*34*).

A single mutant of *ZmGS3*^{ko} (sgRNA designed in exon 1 and exon 2) with a 34-bp deletion was generated with the maize promoter *ZmU6* using the CRISPR-Cas9 system (*45*). The sgRNAs were designed using the website http://crispr.hzau.edu.cn/CRISPR2/. The vector confirmed by sequencing was introduced into *A. tumefaciens* EHA105 and transformed into the maize variety KN5585 by *Agrobacterium*-mediated transformation. Vector construction and plant transformation were performed by WIMI Biotechnology Co., Ltd. (China), as previously described (*45*). Mutations were confirmed by PCR sequencing samples from the T_0 and T_1 generations. All related primers are shown in table S3.

qPCR

Total RNA was extracted from fresh sorghum seedling roots by using a pure RNA extraction kit (Huayueyang, Beijing, China), with DNA digested by ribonuclease (RNase)–free Dnase I treatment. cDNA was obtained using a cDNA synthesis kit (TransGen, Beijing, China). qPCR was performed with the KOD SYBR qPCR Mix Kit (TransGen, Beijing, China) on an Applied Biosystems 7900HT Fast Real-Time PCR System. The relative expression of targeted genes was calculated by the relative quantification method ($2^{-\Delta\Delta CT}$). Three biological repeats were performed for each sample. The expression level of *SbEIF* was used to normalize all qPCR data. Related primers are shown in table S3.

Transient protein expression in *Nicotiana benthamiana*

Agrobacterium-mediated transient expression in *N. benthamiana* was performed according to a protocol described previously with some modifications (*46*). Approximately 1-month-old tobacco plants grown in a greenhouse under a 16-hours light/8-hours dark photoperiod were selected for infiltration. The *A. tumefaciens* strain EHA105 containing targeted gene vectors or the gene-silencing suppressor p19 was prepared. *Agrobacterium* colonies were inoculated into 5 ml of LB liquid medium with the appropriate antibiotics at 28°C and placed on a shaker overnight. Then, a 1/100 volume (50 μL) of the *Agrobacterium* culture was transferred into 5 ml of LB liquid medium with 40 μM acetosyringone (AS). After the OD_{600} (the optical density of a sample measured at a wavelength of 600 nm) reached ~3.0, bacteria were collected, and pellets were resuspended in 10 mM $MgCl_2$ to an OD_{600} of 1.5 for targeted genes and an OD_{600} of 1.0 for *p19*. Equal amounts of *Agrobacterium* transfected with targeted genes and *p19* were mixed. The mixed *Agrobacterium* solutions were kept still at room temperature for 2 to 5 hours and then infiltrated into the undersides of tobacco leaves. After 3 days, the leaf veins were removed, and the infiltrated tobacco leaves were collected for Western blot assays with the corresponding antibodies.

Protein expression in bacteria and purification

The plasmid for GST-AT1, GST-at1, or MBP-SbPIP2;1 protein expression was transformed into *E. coli* strain BL21 (DE3). A single colony was inoculated into 10 ml of liquid LB medium containing the ampicillin antibiotic and incubated at 37°C overnight. Then, the 10-ml culture was transferred into 300 ml of LB medium. When the OD_{600} reached 0.6 to 0.8, final concentrations of 0.8 mM isopropyl-β-D-thiogalactopyranoside (IPTG) and 0.2% glucose were added, and the bacteria were cultured at 18°C for 16 to 20 hours to induce fusion protein expression. The bacteria were lysed with a pressure machine (JNBIO), and glutathione Sepharose 4B beads (GE Healthcare) or amylase resin (NEB) was used for purification of the fusion proteins. The bound proteins were washed three times with 1× phosphate-buffered saline (PBS) buffer with 150 mM NaCl. MBP-PIP2;1 coated on the amylase resin was eluted by 10 mM maltose. The purified proteins GST-AT1 and GST-at1 coated on beads and eluted MBP-PIP2;1 were stored at −80°C until use.

LC-MS/MS assay

To obtain the interacting proteins of SbAT1, an LC-MS/MS assay was performed after a cell-free assay, which enriched the interacting proteins through incubation of the GST-SbAT1 protein with plant extracts. Seeds of the Wheatland sorghum were sown in soil supplemented with 75 mM alkali. Fourteen-day-old plants were collected and frozen in liquid nitrogen to be ground into fine powder. Native extraction buffer (50 mM Tris-MES at pH 8.0, 0.5 M sucrose, 1 mM $MgCl_2$, 10 mM EDTA, 5 mM DTT, 1 mM PMSF, Roche cOmplete Mini protease inhibitor cocktail tablets, and 0.2% NP40) was applied for total protein extraction. The plant extracts were centrifuged three times at 12,000 rpm for 10 min at 4°C, and the final protein supernatant was filtered with a 0.45-μm sterile membrane to remove the debris that could not be removed by centrifugation. GST-SbAT1 fusion proteins (200 ng) coated on beads were incubated with the above prepared plant protein extracts supplemented with MG132 (26S proteasome inhibitor) at 4°C for 3 hours, and then the beads were washed three times (for 10 min each time) with 1× PBS buffer along with 150 mM NaCl. The buffer was discarded completely after the last wash, and the beads were resuspended in 2× SDS protein loading buffer and heated at 95°C for 10 min. The sample was separated and purified by an SDS–polyacrylamide gel electrophoresis (SDS-PAGE) gel running for ~1 cm, and the gel was collected for in-gel digestion.

The gel sample containing GST-SbAT1 and its potential interacting proteins was cut into 2- to 3-mm^2 pieces in a dust-free environment. The destained gel pieces were treated with 10 mM DTT at 56°C for 1 hour and then with 55 mM iodoacetamide at room temperature in darkness for 45 min. Then, the proteins in the gel pieces were digested with trypsin (enzyme-to-substrate ratio 1:50) at 37°C overnight. The peptides were extracted from the gel pieces by sonication and freeze-dried in a SpeedVac concentrator. Finally, the peptides were redissolved in 0.1% formic acid and filtered through a 0.45-μm centrifugal filter before conducting the LC-MS/MS assay with a nanoLC-Q EXACTIVE mass spectrometer. The raw data were analyzed by Thermo Proteome Discoverer (1.4.0.288) and using the UniProt-proteome-*Sorghum bicolor* (*Sorghum vulgare*) database (strain: cv. BTx623) (20190715).

In the experiment identifying the phosphorylated sites in SbPIP2;1, the powder was lysed in a buffer containing 4% SDC and 100 mM Tris-HCl (pH 8.5). After sonication, the lysates were centrifuged for 10 min at 12,000 g to remove insoluble debris. Protein (~1200 μg) was reduced and alkylated by TCEP and CAA and digested with trypsin (1:50 w/w) at 37°C overnight. After digestion, the phosphopeptides were enriched using titanium dioxide beads (TiO_2; GL Sciences, 5010-21315). The phosphopeptides were analyzed by an Orbitrap Fusion Lumos Tribrid mass spectrometer (Thermo Scientific, Rockford, IL Waltham, MA) coupled online to an Easy-nLC 1000 in the data-dependent mode. Precursor ions were measured in the Orbitrap analyser at 240,000 resolution. The twenty most intense ions from each MS scan were isolated and fragmented by high-energy collisional dissociation. The database search was performed for all raw MS files using the software MaxQuant (version 1.6.3.4). The *S. bicolor* proteome sequence database was applied to search the data. Serine, threonine, and tyrosine phosphorylation; protein N-terminal acetylation; and methionine oxidation were included in the search as the variable modifications. Cysteine carbamidomethylation was set as a stable modification.

LCI assay

LCI assays were carried out following a method published previously (*29*). The coding sequences of targeted genes or a control gene were cloned into pCAMBIA1300-nLUC or pCAMBIA1300-cLUC, respectively. The constructs Nluc-SbAT1, Nluc-Sbat1, Nluc-OsGS3-1, Nluc-OsGS3-4, Cluc-SbPIP2;1, Cluc-OsPIP2;1, and Cluc-SbTGA1 were then transformed into *A. tumefaciens* strain GV3101. As described in the section on protein transient expression in tobacco leaves, equal amounts of bacteria harboring different constructs and *p19* were mixed and infiltrated into tobacco leaves. After 3 days, 1 mM luciferin substrate was spread evenly on the underside of leaves and allowed to react for 5 min in the dark. Subsequently, luciferase activity signals were detected with a cooled low-light charge-coupled device camera (Night OWL II LB 983).

Pull-down assay

To investigate the direct interaction of SbAT1 or Sbat1 with SbPIP2;1, the GST-SbAT1, GST-Sbat1, and MBP-SbPIP2;1 fusions were expressed in *E. coli* strain BL21 (DE3) and purified with glutathione Sepharose 4B beads or amylase resin (NEB), as described above. Equimolar amounts of GST, GST-SbAT1, and GST-Sbat1 proteins coated on beads were incubated with equal amounts of eluted MBP-SbPIP2;1 protein at 4°C for 2 hours. Then, the beads were washed five times with 1× PBS containing 150 mM NaCl. All the supernatant was removed and transferred into 2× SDS protein loading buffer before heating at 95°C for 10 min. The eluted proteins were examined by Western blot with an anti-MBP antibody.

Co-IP assay

GFP, GFP-SbAT1, GFP-Sbat1, and Cluc-SbPIP2;1 proteins were transiently expressed in tobacco leaves. The samples were ground into powder in liquid nitrogen, and the protein extracts were prepared with native extraction buffer supplemented with MG132. GFP, GFP-SbAT1, and GFP-Sbat1 protein extracts were enriched with magnetic beads coated with an anti-GFP antibody and then placed at 4°C for 2 hours. The beads were then washed three times with 1× PBS buffer. Equal amounts of Cluc-SbPIP2;1 protein extracts were added to the beads and incubated at 4°C for 2 hours. After washing three times with 1× PBS supplemented with 150 mM NaCl, the bead samples were placed into 2× SDS protein loading buffer and heated at 95°C for 10 min. Finally, the precipitates were analyzed by Western blotting with an anti-Luc antibody.

Detection of redox states in protoplasts by confocal microscopy and microplate reader

Redox states assays determined by Cyto-roGFP2-Orp1 were performed as described by Gutscher *et al.* (*29*). Briefly, genes encoding Cyto-roGFP2-Orp1 were cloned into the pGFP2 vector and to generate pGFP2-Cyto-roGFP2-Orp1. Protoplasts were prepared with 10-day-old rice seedlings grown in a sterile container. Protoplasts overexpressed the Cyto-roGFP2-Orp1 probe by the PEG transfection method. After 12 to 16 hours, the protoplasts were centrifuged gently at 100 g for 3 min, the supernatant was removed and the protoplasts were resuspended in W5 liquid buffer (154 mM NaCl, 125 mM $CaCl_2$, 5 mM KCl, 2 mM MES) with different pH for 40 min. Then the redox states of those rice protoplasts were analyzed by confocal microscopy and microplate reader. A total of 1×10^5 sample protoplasts were used for microplate reader analyzing in each sample repeat. For mircroscopy assay, transfected protoplasts were set on glass bottom dishes and analyzed using a laser scanning confocal microscopy system (LSM 710, Carl Zeiss) with a Plan-Apochromat 63× oil immersion lens (NA 1.4), and then the redox states of those rice protoplasts were analyzed using a laser scanning confocal microscopy system (LSM 710, Carl Zeiss). Fluorescence ratiometric intensity images (1024 × 1024 points, 16 bits) of protoplasts were acquired. A 405-nm diode and 488-nm argon lasers (or 458-nm diode) were used for excitation. The signal was detected with 510- to 550-nm filters. Images were analyzed using ImageJ (National Institutes of Health) and Zen (Carl Zeiss) softwares, and the ratio of 405/488 nm indicated the relative level of H_2O_2.

The redox states of protoplasts overexpressing Cyto-roGFP2-Orp1 were detected using a microplate reader (Thermo Scientific Varioskan LUX). We measured Cyto-roGFP2-Orp1 at 525 nm after excitation at 405 and 488 nm in a black plate reader. The background of the fluorescence value produced by untransfected protoplasts was subtracted, and the ratio of 405/488 nm indicated the relative level of H_2O_2. All the raw and non-normalized data were shown in table S4.

ROS, H_2O_2, and relative chlorophyll content detection

The formation of peroxides in the leaves was investigated by the 3,3′-diaminobenzidine (DAB) staining method (*47*). Seedling leaves of the control (CK) and alkali treatments were soaked in 10 ml of staining buffer (50 mM Na_2HPO_4 and DAB). After vacuuming, the samples were incubated overnight in the dark at room temperature. Samples were transferred to an eluent (anhydrous ethanol:glacial acetic acid:glycerol = 3:1:1) and boiled for 10 min to remove chlorophyll, and then the images of samples were taken under the same condition.

For the detection of cytosolic ROS levels in the root tips of *PIP2;1* and Gγ subunit-related genetic plants, the dye OxyBURST Green H_2DCFDA (Molecular Probes D-2935, Thermo Fisher Scientific) was used with staining method described before (*48*). Two-week-old sorghum and rice seedlings grown in soil culture under normal conditions treated with or without 200 mM alkali for 48 hours were used for analysis. Then, the lateral roots of the alkali-treated and control-treated seedlings were collected, cleanly rinsed, and gently transferred to 50-ml tubes. H_2DCFDA was primarily dissolved in dimethyl sulfoxide (DMSO) to 10 mM and then diluted with sample buffer (10 mM Tris-HCl, 50 mM KCl, pH 7.2) into a final concentration of 50 μM for use. Samples were soaked in 0.01% Tween 20 and vacuumed for 30 min, rinsed twice with distilled water, and then washed with washing buffer (10 mM Tris-HCl pH 7.2 and 50 mM KCl). Samples were subsequently incubated with 50 μM H_2DCFDA staining solution in the dark at room temperature for 10 min, and the excess dye was removed with distilled water twice. For the detection of apolast ROS accumulation, samples were prepared as the detection of cytosolic ROS above. Each sample was soaked with OxyBURST Green H_2HFF BSA (100 μg ml^{-1}) dissolved in 1× PBS buffer for 45 min in the dark, and then washed with distilled water to remove the excess dye. All the samples were examined using a Zeiss LSM 510 confocal microscope with 488-nm excitation and 530-nm emission. To compare the fluorescence intensity, all axes of parameters from different experimental conditions were fixed simultaneously and analyzed under the confocal microscope by using the same settings.

Five to 20 lateral roots of each sample were chosen, and one to three visual fields of each lateral root were selected for imaging. For quantification of the intracellular ROS accumulation at the single–root cell level, three representative root cells of each visual field were selected for statistical data. The average value of fluorescence intensity was recorded as one replicate. For quantification of extracellular ROS accumulation at the single–root cell level, one representative single cell was selected for each visual field. A typical root cell contains a rectangular contour, including two lengths and two widths. The sum of rectangular contour was recorded as the fluorescence intensity of each replicate. The final average value of all repetitions was taken as the fluorescence intensity of each sample.

A portable SPAD-502 handheld chlorophyll meter (Minolta, Osaka, Japan) was used to noninvasively measure the relative chlorophyll content of seedling leaves. Six biological repeats were performed.

Quantification and statistical analyses

For image quantification of H_2O_2 detection, six unsaturated confocal images were selected and analyzed with ImageJ software (https://imagej.nih.gov/ij/). All data plotting and statistical analyses were performed with GraphPad Prism 8.0 software (https://www.graphpad.com/). Details about the statistical parameters, such as the means ± SDs (standard deviations), SEs (standard errors), and 95% confidence intervals, are shown in the figure legends. A two-tailed Student's t test for two groups or a one-way analysis of variance (ANOVA) with Dunnett's or Tukey's multiple comparisons test for multiple groups were carried out. The number of samples is represented by n. Asterisks indicate statistical significance: $^*P < 0.05$; $^{**}P < 0.01$; $^{***}P < 0.001$; $^{****}P < 0.0001$; NS, not significant.

REFERENCES AND NOTES

1. A. Kumar, S. Singh, A. K. Gaurav, S. Srivastava, J. P. Verma, Plant growth-promoting bacteria: Biological tools for the mitigation of salinity stress in plants. *Front. Microbiol.* **11**, 1216 (2020). doi: 10.3389/fmicb.2020.01216; pmid: 32733391
2. B. P. Singh, A. L. Cowie, K. Y. Chan, Eds., *Soil Health and Climate Change*, vol. 29 of *Soil Biology* (Springer, 2011).
3. M. Javid, R. Ford, M. E. Nicolas, Tolerance responses of *Brassica juncea* to salinity, alkalinity and alkaline salinity. *Funct. Plant Biol.* **39**, 699–707 (2012). doi: 10.1071/FP12109; pmid: 32480821
4. G. K. S. Ananda *et al*., Wild sorghum as a promising resource for crop improvement. *Front. Plant Sci.* **11**, 1108 (2020). doi: 10.3389/fpls.2020.01108; pmid: 32765575
5. X. Sun *et al*., A *Glycine soja* methionine sulfoxide reductase B5a interacts with the Ca^{2+}/CAM-binding kinase GsCBRLK and activates ROS signaling under carbonate alkaline stress. *Plant J.* **86**, 514–529 (2016). doi: 10.1111/tpj.13187; pmid: 27121031
6. H. Zhang *et al*., Root damage under alkaline stress is associated with reactive oxygen species accumulation in rice (*Oryza sativa* L.). *Front. Plant Sci.* **8**, 1580 (2017). doi: 10.3389/fpls.2017.01580; pmid: 28943882
7. M. An *et al*., Application of compound material alleviates saline and alkaline stress in cotton leaves through regulation of the transcriptome. *BMC Plant Biol.* **20**, 462 (2020). doi: 10.1186/s12870-020-02649-0; pmid: 33032521
8. G. P. Bienert, F. Chaumont, Aquaporin-facilitated transmembrane diffusion of hydrogen peroxide. *Biochim. Biophys. Acta* **1840**, 1596–1604 (2014). doi: 10.1016/j.bbagen.2013.09.017; pmid: 24060746
9. H. Tong *et al*., A *Streptococcus* aquaporin acts as peroxiporin for efflux of cellular hydrogen peroxide and alleviation of oxidative stress. *J. Biol. Chem.* **294**, 4583–4595 (2019). doi: 10.1074/jbc.RA118.006877; pmid: 30705089
10. K. Varadaraj, S. S. Kumari, Lens aquaporins function as peroxiporins to facilitate membrane transport of hydrogen peroxide. *Biochem. Biophys. Res. Commun.* **524**, 1025–1029 (2020). doi: 10.1016/j.bbrc.2020.02.031; pmid: 32063362
11. Q. Chen *et al*., ERAD-related E2 and E3 enzymes modulate the drought response by regulating the stability of PIP2 aquaporins. *Plant Cell* **33**, 2883–2898 (2021). doi: 10.1093/plcell/koab141; pmid: 34015125
12. O. Rodrigues *et al*., Aquaporins facilitate hydrogen peroxide entry into guard cells to mediate ABA- and pathogen-triggered stomatal closure. *Proc. Natl. Acad. Sci. U.S.A.* **114**, 9200–9205 (2017). doi: 10.1073/pnas.1704754114; pmid: 28784763
13. S. Pandey, Heterotrimeric G-protein signaling in plants: Conserved and novel mechanisms. *Annu. Rev. Plant Biol.* **70**, 213–238 (2019). doi: 10.1146/annurev-arplant-050718-100231; pmid: 31035831
14. M. N. Haque *et al*., Characteristics of arsenic adsorption to sorghum biomass. *J. Hazard. Mater.* **145**, 30–35 (2007). doi: 10.1016/j.jhazmat.2006.10.080; pmid: 17241742
15. S. Griebel, A. Adedayo, M. R. Tuinstra, Genetic diversity for starch quality and alkali spreading value in sorghum. *Plant Genome* **14**, e20067 (2021). doi: 10.1002/tpg2.20067; pmid: 33259143
16. H. Mao *et al*., Linking differential domain functions of the GS3 protein to natural variation of grain size in rice. *Proc. Natl. Acad. Sci. U.S.A.* **107**, 19579–19584 (2010). doi: 10.1073/pnas.1014419107; pmid: 20974950
17. Q. Li *et al*., Cloning and characterization of a putative *GS3* ortholog involved in maize kernel development. *Theor. Appl. Genet.* **120**, 753–763 (2010). doi: 10.1007/s00122-009-1196-x; pmid: 19898828
18. P. Xie *et al*., Natural variation in *Glume Coverage 1* causes naked grains in sorghum. *Nat. Commun.* **13**, 1068 (2022). doi: 10.1038/s41467-022-28680-3; pmid: 35217660
19. C. Fan *et al*., *GS3*, a major QTL for grain length and weight and minor QTL for grain width and thickness in rice, encodes a putative transmembrane protein. *Theor. Appl. Genet.* **112**, 1164–1171 (2006). doi: 10.1007/s00122-006-0218-1; pmid: 16453132
20. S. M. Assmann, Heterotrimeric and unconventional GTP binding proteins in plant cell signaling. *Plant Cell* **14**, S355–S373 (2002). doi: 10.1105/tpc.001792; pmid: 12045288
21. B. R. Temple, A. M. Jones, The plant heterotrimeric G-protein complex. *Annu. Rev. Plant Biol.* **58**, 249–266 (2007). doi: 10.1146/annurev.arplant.58.032806.103827; pmid: 17201690
22. Y. Trusov, D. Chakravorty, J. R. Botella, Diversity of heterotrimeric G-protein γ subunits in plants. *BMC Res. Notes* **5**, 608 (2012). doi: 10.1186/1756-0500-5-608; pmid: 23113884
23. N. Smirnoff, D. Arnaud, Hydrogen peroxide metabolism and functions in plants. *New Phytol.* **221**, 1197–1214 (2019). doi: 10.1111/nph.15488; pmid: 30222198
24. S. Tian *et al*., Plant aquaporin AtPIP1;4 links apoplastic H_2O_2 induction to disease immunity pathways. *Plant Physiol.* **171**, 1635–1650 (2016). doi: 10.1104/pp.15.01237; pmid: 26945050
25. M. Oparka *et al*., Quantifying ROS levels using CM-H_2DCFDA and HyPer. *Methods* **109**, 3–11 (2016). doi: 10.1016/j.ymeth.2016.06.008; pmid: 27302663
26. B. Morgan, M. C. Sobotta, T. P. Dick, Measuring E_{GSH} and H_2O_2 with roGFP2-based redox probes. *Free Radic. Biol. Med.* **51**, 1943–1951 (2011). doi: 10.1016/j.freeradbiomed.2011.08.035; pmid: 21964034
27. A. V. Baranova, Y. L. Orlov, The papers presented at 7th Young Scientists School "Systems biology and bioinformatics" (SBB'15): Introductory note. *BMC Genet.* **17**, S20 (2016). doi: 10.1186/s12863-015-0326-5; pmid: 26822407
28. R. E. Carmichael, A. Boyce, C. Matthewman, N. J. Patron, An introduction to synthetic biology in plant systems. *New Phytol.* **208**, 20–22 (2015). doi: 10.1111/nph.13433; pmid: 26311282
29. M. Gutscher *et al*., Proximity-based protein thiol oxidation by H_2O_2-scavenging peroxidases. *J. Biol. Chem.* **284**, 31532–31540 (2009). doi: 10.1074/jbc.M109.059246; pmid: 19755417
30. C. J. Huang, X. H. Wang, J. Y. Huang, C. G. Zhang, Y. L. Chen, Phosphorylation of plasma membrane aquaporin PIP2;1 in C-terminal affects light-induced stomatal opening in *Arabidopsis*. *Plant Signal. Behav.* **15**, 1795394 (2020). doi: 10.1080/15592324.2020.1795394; pmid: 32693667
31. D. Qing *et al*., Quantitative and functional phosphoproteomic analysis reveals that ethylene regulates water transport via the C-terminal phosphorylation of aquaporin PIP2;1 in Arabidopsis. *Mol. Plant* **9**, 158–174 (2016). doi: 10.1016/j.molp.2015.10.001; pmid: 26476206
32. A. L. Szymczak *et al*., Correction of multi-gene deficiency *in vivo* using a single 'self-cleaving' 2A peptide–based retroviral

vector. *Nat. Biotechnol.* **22**, 589–594 (2004). doi: 10.1038/nbt957; pmid: 15064769
33. S. Sun *et al*., A G-protein pathway determines grain size in rice. *Nat. Commun.* **9**, 851 (2018). doi: 10.1038/s41467-018-03141-y; pmid: 29487318
34. W. Yang *et al*., The RING E3 ligase CLG1 targets GS3 for degradation via the endosome pathway to determine grain size in rice. *Mol. Plant* **14**, 1699–1713 (2021). doi: 10.1016/j.molp.2021.06.027; pmid: 34216830
35. Y. Tao *et al*., Large-scale GWAS in sorghum reveals common genetic control of grain size among cereals. *Plant Biotechnol. J.* **18**, 1093–1105 (2020). doi: 10.1111/pbi.13284 pmid: 31659829
36. Y. Cui, N. Jiang, Z. Xu, Q. Xu, Heterotrimeric G protein are involved in the regulation of multiple agronomic traits and stress tolerance in rice. *BMC Plant Biol.* **20**, 90 (2020). doi: 10.1186/s12870-020-2289-6; pmid: 32111163
37. G. Zou *et al*., Sorghum *qTGW1a* encodes a G-protein subunit and acts as a negative regulator of grain size. *J. Exp. Bot.* **71**, 5389–5401 (2020). doi: 10.1093/jxb/eraa277; pmid: 32497208
38. N. Takano-Kai, K. Doi, A. Yoshimura, *GS3* participates in stigma exsertion as well as seed length in rice. *Breed. Sci.* **61**, 244–250 (2011). doi: 10.1270/jsbbs.61.244
39. Y. Kan *et al*., *TT2* controls rice thermotolerance through SCT1-dependent alteration of wax biosynthesis. *Nat. Plants* **8**, 53–67 (2022). doi: 10.1038/s41477-021-01039-0; pmid: 34992240
40. G. P. Morris *et al*., Population genomic and genome-wide association studies of agroclimatic traits in sorghum. *Proc. Natl. Acad. Sci. U.S.A.* **110**, 453–458 (2013). doi: 10.1073/pnas.1215985110; pmid: 23267105
41. D. M. Goodstein *et al*., Phytozome: A comparative platform for green plant genomics. *Nucleic Acids Res.* **40**, D1178–D1186 (2012). doi: 10.1093/nar/gkr944; pmid: 22110026
42. M. Li, N. Yuyama, L. Luo, M. Hirata, H. Cai, In silico mapping of 1758 new SSR markers developed from public genomic sequences for sorghum. *Mol. Breed.* **24**, 41–47 (2009). doi: 10.1007/s11032-009-9270-2
43. X. Ma *et al*., A robust CRISPR/Cas9 system for convenient, high-efficiency multiplex genome editing in monocot and dicot plants. *Mol. Plant* **8**, 1274–1284 (2015). doi: 10.1016/j.molp.2015.04.007; pmid: 25917172
44. H. J. Liu *et al*., High-throughput CRISPR/Cas9 mutagenesis streamlines trait gene identification in Maize. *Plant Cell* **32**, 1397–1413 (2020). doi: 10.1105/tpc.19.00934; pmid: 32102844
45. L. Liu *et al*., An efficient system to detect protein ubiquitination by agroinfiltration in *Nicotiana benthamiana*. *Plant J.* **61**, 893–903 (2010). doi: 10.1111/j.1365-313X.2009.04109.x; pmid: 20015064
46. H. Chen *et al*., Firefly luciferase complementation imaging assay for protein-protein interactions in plants. *Plant Physiol.* **146**, 323–324 (2008). doi: 10.1104/pp.107.111740; pmid: 18065554
47. N. Jambunathan, in *Plant Stress Tolerance*, R. Sunkar, Ed., vol. 639 of *Methods in Molecular Biology* (Humana Press, 2010), pp. 291–297.
48. G. B. Monshausen, T. N. Bibikova, M. A. Messerli, C. Shi, S. Gilroy, Oscillations in extracellular pH and reactive oxygen species modulate tip growth of *Arabidopsis* root hairs. *Proc. Natl. Acad. Sci. U.S.A.* **104**, 20996–21001 (2007). doi: 10.1073/pnas.0708586104; pmid: 18079291

ACKNOWLEDGMENTS

We thank the US Department of Agriculture–Agricultural Research Service (USDA-ARS) for providing sorghum seeds for the sorghum association panel. We are grateful to N. Li from the Hong Kong University of Science and Technology for providing the anti-PIP2.1 (pS285/288) antibody and to C. Chu from Huanan Agriculture University for providing the genome sequence of the rice lines. **Funding:** This work was supported by National Natural Science Foundation of China grants U1906204 (to Q.X.) and 32222010 (to F.Y.), Strategic Priority Research Program of the Chinese Academy of Sciences grant XDA24010306 (to Q.X.), Agricultural Breeding Program in NingXia Province grant 2019NYYZ04 (to Q.X. and X.Xu), National Natural Science Foundation of China grant 31821005 (to Q.Z.), and Chinese Universities Scientific Fund grant 1201 −15052001 (to F.Y.). S.T. is supported by the Youth Innovation Promotion Association of the Chinese Academy of Sciences. **Author contributions:** Q.X. conceived the project. Q.X., F.Y., and Y.O. designed the research procedure. H.Z., F.Y., P.X., S.S., X.Q., S.T., C.M., D.Y., X.H., and Z.F. performed the experiments. Che.C., H.Y., J.Lu, Q.Z., Y.Wu, R.X., Y.Wa., and Cha.C. analyzed the data. S.Y., X.L., J.Li, Y.L., X.Xi., D.M., X.Xu, Z.L., G.L., J.Lu, and Q.Z. provided field tests and guidance. Q.X. and F.Y. wrote the manuscript with input from all authors. **Competing interests:** Patent applications related to this work have been submitted by Q.X., F.Y., H.Z., Y.O., and Q.Z. All other authors declare no competing interests. **Data and materials availability:** All data needed to evaluate the conclusions in the paper are present in the paper or the supplementary materials. Rice- and maize-related materials are available from Y.O. and sorghum- and millet-related materials are available from Q.X. under a material transfer agreement with the Institute of Genetics and Developmental Biology or Huazhong Agricultural University, respectively. **License information:** Copyright © 2023 the authors, some rights reserved; exclusive licensee American Association for the Advancement of Science. No claim to original US government works. https://www.science.org/about/science-licenses-journal-article-reuse

SUPPLEMENTARY MATERIALS

science.org/doi/10.1126/science.ade8416
Figs. S1 to S7
Tables S1 to S4
MDAR Reproducibility Checklist

View/request a protocol for this paper from *Bio-protocol*.

Submitted 16 September 2022; accepted 8 February 2023
10.1126/science.ade8416

RESEARCH ARTICLE

VENUS

Surface changes observed on a Venusian volcano during the Magellan mission

Robert R. Herrick[1]* and Scott Hensley[2]

Venus has a geologically young surface, but it is unknown whether it has ongoing active volcanism. From 1990 to 1992, the Magellan spacecraft imaged the planet's surface, using synthetic aperture radar. We examined volcanic areas on Venus that were imaged two or three times by Magellan and identified an ~2.2-square-kilometer volcanic vent that changed shape in the 8-month interval between two radar images. Additional volcanic flows downhill from the vent are visible in the second-epoch images, although we cannot rule out that they were present but invisible in the first epoch because of differences in imaging geometry. We interpret these results as evidence of ongoing volcanic activity on Venus.

Venus has nearly the same size and mass as Earth. Compositional constraints are consistent with Venus having an Earth-like abundance of radioactive elements, which release heat that might drive volcanic activity (*1*). The number of impact craters on Venus indicates a mean surface age of a few hundred million years (*2*). However, many of the craters have morphologies that appear to have been modified by volcanic processes; if so, it could mean that the average surface age of Venus is only tens of millions of years, as young as Earth's ocean basins (*3*). The vast majority of Earth's volcanism is associated with crust formation at mid-ocean ridges or volcanic arcs above subduction zones. Venus does not have current plate tectonics (*4*). Geodynamic models of Venus that match the geological and geophysical observations of the planet disagree on the expected current level of volcanism, variously predicting that it could be lower than, the same as, or many times higher than the level of hot spot volcanism on Earth (*5*–*9*).

On Earth, the Hawaiian volcanic hot spot erupts every few years (*10*, *11*). There are several dozen volcanoes on Venus with sizes (*12*) and gravity signatures indicative of underlying hot mantle plumes (*13*) larger than that of Hawaii's Big Island (*14*). It has been predicted (*15*) that multiple basaltic eruptions might occur over the course of a Venusian sidereal day (243 Earth days). Extending this analogy predicts lava-flow areas covering several tens of kilometers over the same period (*10*, *11*, *16*).

Magellan radar images

From 1990 to 1992, the Magellan spacecraft (*17*) imaged the surface of Venus using synthetic aperture radar (SAR) at a resolution of 100 to 300 m. Data were recorded in overlapping swaths taken on the descending passes of the spacecraft's highly elliptical orbit, such that a given surface location was imaged once per sidereal day as the planet rotated. Images were acquired over three sidereal days, referred to as cycles. During cycle 1, ~84% of the planet was observed with east-looking SAR images. During cycle 2, gaps from cycle 1 were filled, and second images were acquired for ~35% of the planet with west-looking SAR images. About 15% of Venus was imaged again during cycle 3, with east-looking images generally at an incidence angle (the angle from vertical with which the SAR beam intersects the surface) differing by ~20° from that used in cycle 1. Because ~8% of the planet was imaged in all three cycles, a total of ~42% of the global surface area was imaged two or more times.

The different imaging geometries used for each cycle are not conducive to automated methods of searching for changes due to volcanic activity. We therefore performed a manual search of areas previously identified as most likely to possess active volcanism (*18*–*20*) (table S1). The areas that we searched included large volcanoes identified in a published database (*12*) that also have geoid anomalies (a distortion of the planet's equipotential surface) greater than 15 m, topographic rises (*20*), coronae considered to be active in another database (*19*), and shield volcanoes that were evaluated as likely being active in (*18*). We restricted the search to areas that were imaged multiple times. Our goal was to identify volcanic constructs that appeared or were altered in the gap between the images, such as volcanic cones, vents, or lava flows.

We examined full-resolution Magellan images of each area of interest, looking for changes in geologic features that occurred between cycles (*21*). Whenever we interpreted a feature as

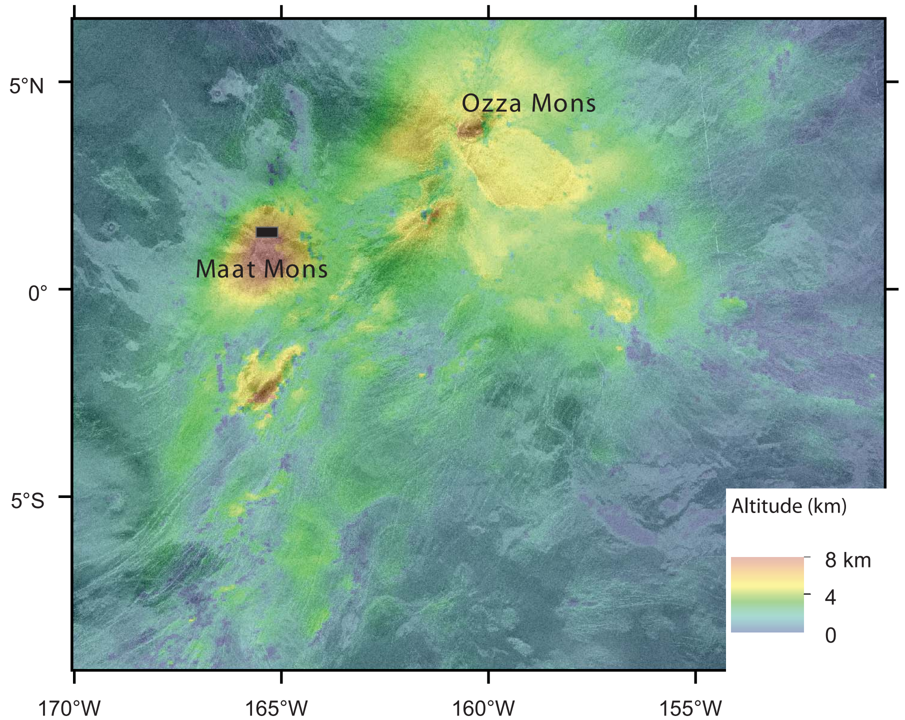


Fig. 1. Topography and SAR image of the study area on Venus. The colors indicate elevations, which are measured relative to the mean planetary radius from gridded Magellan altimetry. The *x* and *y* axes indicate planetary longitude and latitude, respectively. The background grayscale images are from cycle 1 east-looking SAR. The black rectangle indicates the area shown in Fig. 2.

[1]Geophysical Institute, University of Alaska Fairbanks, Fairbanks, AK 99775, USA. [2]Jet Propulsion Laboratory, California Institute of Technology, Pasadena, CA 91109, USA.
*Corresponding author. Email: rrherrick@alaska.edu

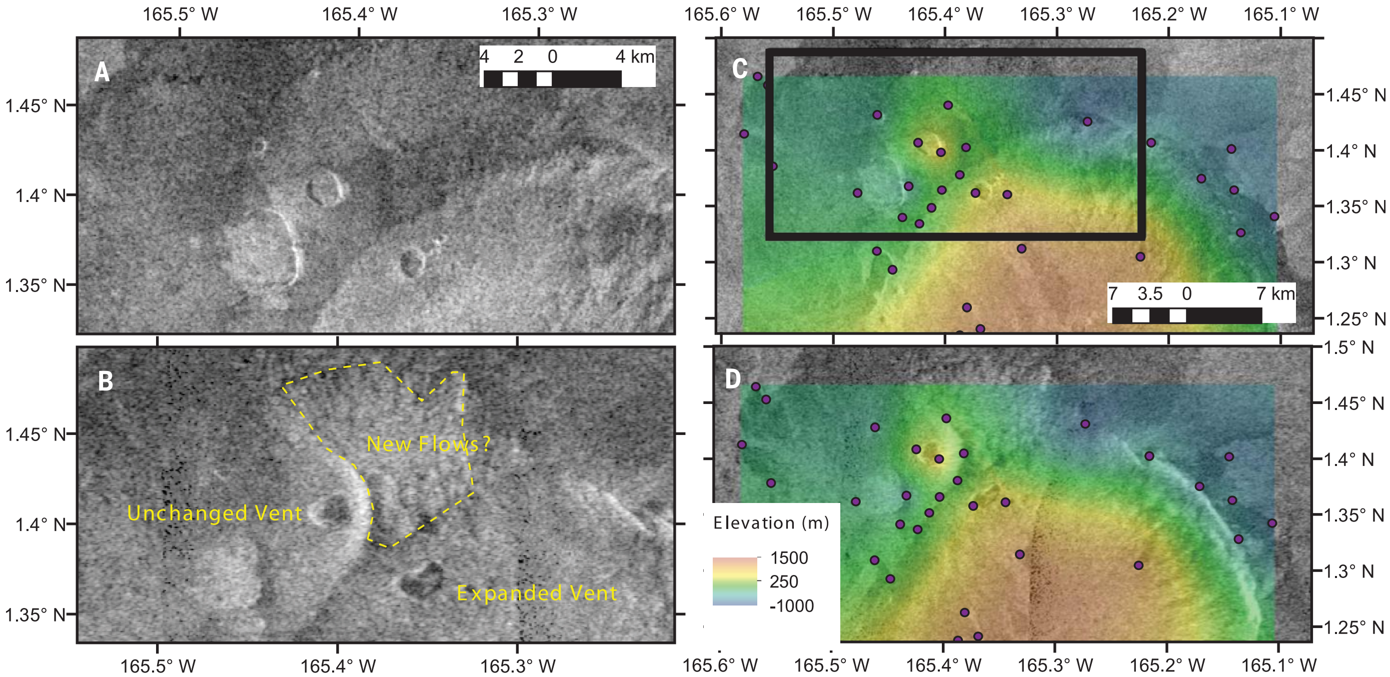


Fig. 2. Radar images of a vent that has changed shape. (**A**) East-looking cycle 1 image and (**B**) west-looking cycle 2 image of the changed vent and its surroundings. In the cycle 1 image, the vent appears nearly circular and deep with steep walls. In the cycle 2 image, the vent appears larger, irregular in outline, shallower, and nearly filled. The dashed yellow line outlines radar-bright lava flows visible in the cycle 2 image that were not apparent in the cycle 1 image. (**C** and **D**) The same images indicating the manually selected match points (purple dots) that were used to generate relative elevations (overlain in color) and to orthorectify the images. The black box in (C) indicates the extent of the unrectified images shown in (A) and (B). All images are shown in a sinusoidal projection with a projection longitude of 165.359°W.

having changed, we used stereo radargrammetry to produce a topographic model for the area surrounding the feature and to orthorectify the images (*21*). Stereo radargrammetry applies stereo photogrammetry techniques to SAR images; terrain variations in a scene cause changes in the relative position of features in images taken from two different perspectives, which are exploited to derive the topography. The original images were then altered to appear as if the viewpoint was directly overhead (orthorectification). We then used the stereo-derived topography and the orthorectified images to interpret the nature and potential cause of the observed change in appearance. We evaluated the viability of each interpretation with a simple geometric model of the feature, which we developed using forward modeling of the cycle 1 image (*21*). The model was used to simulate the appearance of the feature under the different viewing geometries (*21*), which were qualitatively compared to the cycle 2 and/or cycle 3 images.

An active vent in Atla Regio

Figure 1 shows gridded Magellan altimetry overlain on Magellan cycle 1 SAR images of an area in Atla Regio, Venus, which extends from 9°S, 170°W to 6.25°N, 151°W, covering ~3.2×10^6 km^2. This area contains two of the planet's largest volcanoes, Ozza Mons and Maat Mons, which have previously been hypothesized to be locations of active volcanism (*22–24*). Magellan observed this area with east-looking images in cycle 1 (incidence angle 45°) and west-looking images in cycle 2 (incidence angle 25°). This area has not been imaged by Earth-based radar, nor was it imaged during the earlier Venera 15 and Venera 16 missions to Venus.

We identified a volcanic vent at 1.363°N, 165.359°W that changed shape and expanded (Fig. 2) in the 8-month interval between the Magellan imaging in cycle 1 and 2 (February to October 1991). The vent is located on the north side of a domed shield volcano that is part of the larger Maat Mons volcano (*23*). In the east-looking cycle 1 image, the vent appears near-circular (1.5 × 1.8 km, area 2.2 km^2) with steep interior slopes. We speculate that it was a drained posteruptive vent. In the west-looking cycle 2 image, the vent has become larger (4.0 km^2) and irregular in shape. In cycle 2, the vent wall, identifiable as bright pixels on the vent's west side (an east-facing slope) and dark pixels on its east side (west-facing slope), is narrow, so the vent interior and exterior are separated by only a few pixels in the 75 m/pixel radar mosaic. We interpret this narrowness as being due to short vent walls, perhaps only tens of meters high, which implies that the vent is nearly filled to its rim in the cycle 2 image. We speculate that a lava lake formed in the vent interior during the 8-month gap between images.

To provide regional context, we identified matching points in the cycle 1 and 2 images and used them to generate relative elevations and to orthorectify the images (*21*) (Fig. 2, C and D). The cycle 2 image contains a set of radar-bright lava flows, downhill and to the north of the vent, that are not visible in the cycle 1 image. However, the topographic relief of the flows is not resolved by the Magellan data, and the two radar images were taken at different incidence angles. We therefore cannot exclude the possibility that the flows were present when the cycle 1 image was taken but were not apparent in the image, perhaps because the surface texture makes the flows more distinguishable at the smaller incidence angle used for the cycle 2 image. The surface area of the flows is 69 km^2, consistent with typical hot spot volcanism on Earth. By comparison, the 2018 Kīlauea Puna eruption in Hawaii covered an area of ~35 km^2 (*25*), and the associated caldera collapse atop Kīlauea (~500-m drop) had an area of ~5 km^2 (*26*).

A vent atop a volcano could expand because either (i) an influx of magma disrupts, fills, and expands the vent; or (ii) an underlying magma chamber drains, causing the vent to expand because of partial collapse. The lack of visible topographic features within the enlarged

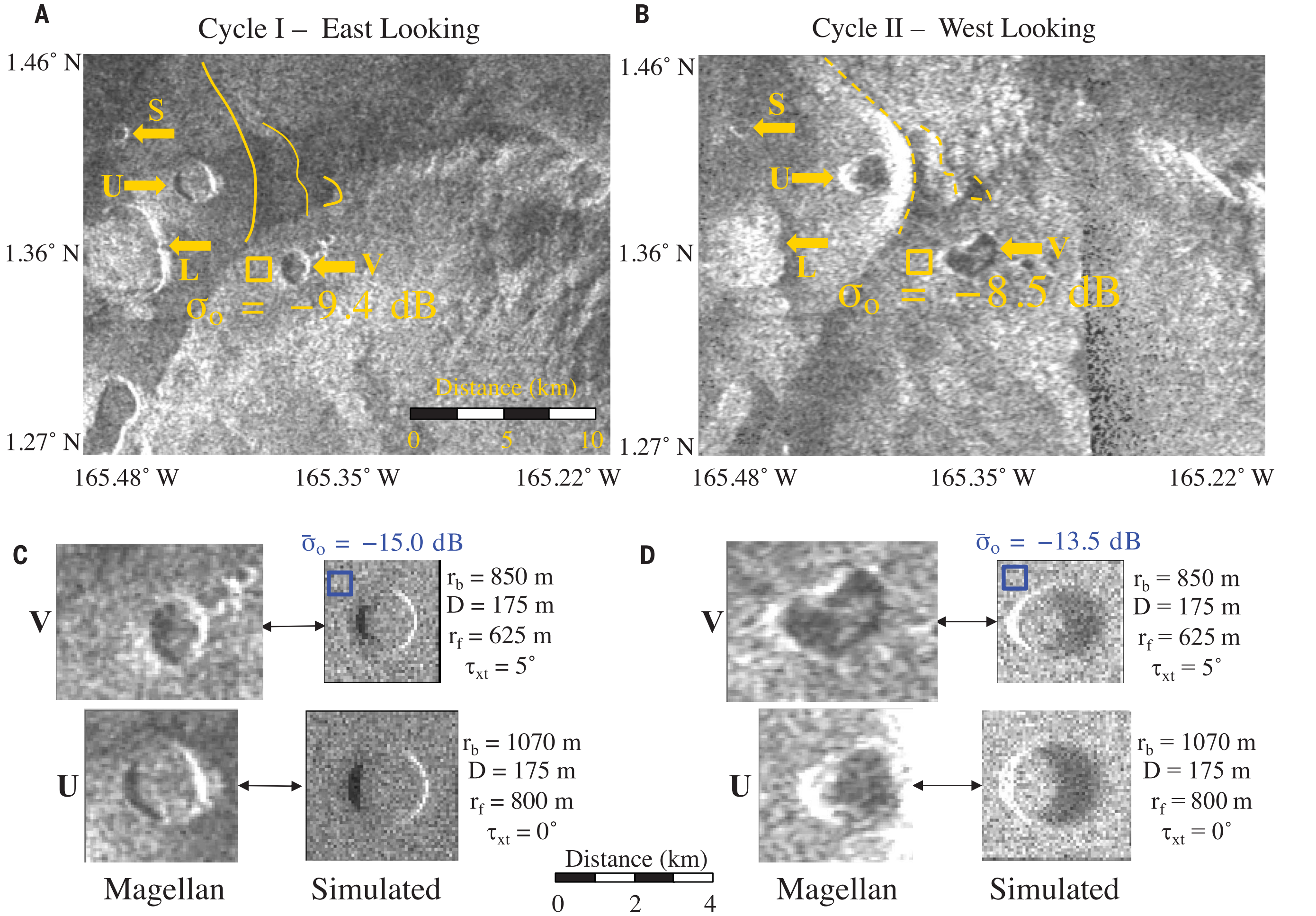


Fig. 3. Comparison between the observations and simulated appearances of model vents. Radar images acquired in (**A**) cycle 1 and (**B**) cycle 2, indicating the changed vent, V, and an unchanged vent, U. Also visible are a smaller vent, S, and ridge, L. The yellow lines are interpreted as breaks in topographic slope in the cycle 1 (solid lines) and cycle 2 (dotted lines) images, within the area of the potential lava flow. Yellow rectangles indicate the regions used to compute the mean backscatter level for the terrain surrounding vent V in the Magellan data; the resulting values are labeled. Scale bar in (A) also applies to (B). (**C**) Simulated appearances of model vents, with geometries selected to appear similarly to the two vents in the cycle 1 image, shown as zoomed cutouts from (A) for comparison. The mean backscatter in the simulated data was measured in the blue box, with the resulting value labeled. The parameters of each model are labeled. (**D**) The same models as they would appear in the cycle 2 images, compared to cutouts from (B). The simulated model is consistent with the observations of vent U but does not match vent V in either geometry or radiometry. Scale bar applies to (C) and (D).

vent in the cycle 2 image is consistent with a fluid (e.g., lava) having filled the vent to a hydrostatic level. However, the image resolution is insufficient to rule out the interior of the vent being filled with debris at the time of cycle 2 rather than by an active or cooled lava lake. It is possible that the increase in vent size was caused by collapse rather than by magmatism. If collapse occurred, it could have been caused by withdrawal of magma from a chamber below the vent, which flowed to feed a nearby eruption. The flows to the north might have been fed by an unresolved vent rather than directly from the vent that changed in size. Regardless of the cause, we definitively conclude that the vent has changed. We are not aware of an Earth analog for multikilometer changes to a volcanic vent occurring with no accompanying volcanism, but we cannot rule out the possibility for this Venusian vent.

No newly formed volcanic constructs, such as a small shield or a cinder cone, were identified in this study area or in regions that were previously surveyed (table S1).

Comparison with simulations

To check our interpretation, we constructed a simple model (*21*) of a vent as a circular, flat-floored, rimless pit, to match the vent observed in the cycle 1 imaging conditions. We then examined how the model pit would appear under cycle 2 observation conditions and compared the model to the observed cycle 2 image (Fig. 3). We applied the same modeling approach to another vent of similar size just to the north, which we interpreted as unchanged between the two observations (Fig. 3, vent U). The models of the changed vent (Fig. 3, vent V) and vent U had rim radii, r_b, of 850 and 1070 m, respectively, with varying depths and steepness of the walls. We used a simple analytic function (*21*) to describe smooth walls extending from the pit rim to a flat floor of radius r_f. We varied the vent depth, D, from 175 to 675 m in increments of 125 m for vent V and from 175 to 875 m in increments of 175 m for vent U. The different increment sizes were chosen to produce the same change in wall-slope angles, given the differing vent radii. We varied the steepness of the walls in the model by varying the floor radii from 400 to 625 m (shallowest

and steepest interior slopes, respectively) in increments of 75 m for the changed vent and from 500 to 800 m in increments of 100 m for vent U. We also simulated west–east terrain slopes, τ_{xt}, of 0°, 5°, 10°, and 25° (positive slope upward to the east). The simulation incorporated a variety of radar imaging effects associated with noise and terrain variation (*21*). The simulated appearances of all these models are shown in figs. S5 to S9. Varying the depths and slopes of the model vent changed the width and magnitude of shadowing, foreshortening, and layover. Varying the west–east slope caused the width of the pit rim to appear differently between opposite-look images and changed the apparent elongation in the west–east direction.

For the changed vent, the simulation that visually most resembles the cycle 1 image is a pit with depth 175 m and floor radius 625 m on a 5° west-facing slope (Fig. 3). This is consistent with the surrounding stereo-derived topography from manual match-point selection (Fig. 2) and provides some west–east elongation of the vent in the cycle 2 image. The visual indicators used to assess whether the model was similar to the observed cycle 1 image were the size and shape of the shadow region on the west side of the interior of the vent, the shape and magnitude of the layover region on the east side of the interior of the vent, and the ellipticity of the vent rim. The latter was quantified by using the ratio of north–south to east–west vent diameters. The cross-track slope was assessed by comparing mean image brightness between the cycle 1 and cycle 2 images. The simulated 5° west-facing slope is consistent with the mean image brightness difference observed between the cycle 1 and cycle 2 images in an area just to the west of the vent. The observed difference is 0.9 dB, whereas the simulated 5° west-facing slope has a 1.5-dB difference (*21*); the corresponding simulated values for 0° and 10° are 3 and 0 dB, respectively.

The observed cycle 2 image of vent V is substantially different from the simulation (Fig. 3). The observed cycle 2 image does not show elongated shadowing on the east side; the elongation of the simulated vent in the east–west direction is less than the observed elongation; the simulation has a prominent foreshortened bright western wall that is not present in the observed image; and the simulation cannot reproduce the vent's kidney shape as viewed from above. There is no large shadowed region associated with the vent's eastern wall in the observed cycle 2 image, which indicates that the vent became shallower than it was at the time of the cycle 1 image. By comparison, our model of vent U matches its appearance and mean backscatter in both imaging cycles, having a pit depth of 175 m, a rim radius of 1070 m, and a floor radius of 800 m on a west-facing slope of 0° (Fig. 3). The bright backscatter arc to the east of vent U (not included in the models) is due to an east-facing slope of 15° to 20°, inferred from the difference between cycle 1 and 2 backscatter values.

Implications for volcanism on Venus

On the basis of only one changed feature, we cannot determine how common currently active volcanism is on Venus. We draw a distinction between identifying recent volcanism on a planet (*23*, *27*, *28*) and demonstrating that it is currently volcanically active. For example, Mars has lava flows with estimated ages of less than a few million years (*29*, *30*), but no volcanic activity has been identified over multiple decades of continuous observation. Only one changed feature has been identified in our survey of the Magellan data, and none have been found in kilometer-scale radar observations from Earth that covered ~25% of Venus' surface (*31*). The low detection rate indicates that Venus is less volcanically active than Jupiter's moon Io, for which over 100 active spots have been imaged (*32*). We estimate that our search of the Magellan data has examined ~1.5% of Venus' surface area (table S1), accounting for missing and poor data. The changed vent is located in a region where volcanic activity was thought to be most likely (*22*, *23*). Our results indicate it to be unlikely that volcanism on Venus has dwindled to a small fraction of Earth's activity over the last few hundred million years (*5*, *7*), but there are a wide range of possible activity scenarios that are compatible with Hawaiian-like levels of volcanism in Atla Regio.

REFERENCES AND NOTES

1. V. L. Barsukov, A. T. Basilevsky, V. P. Volkov, V. N. Zharkov, *Venus Geology, Geochemistry, and Geophysics: Research Results from the USSR.* (Univ. of Arizona Press, 1992).
2. R. J. Phillips *et al.*, *J. Geophys. Res.* **97**, 15923–15948 (1992).
3. R. R. Herrick, M. E. Rumpf, *J. Geophys. Res. Planets* **116**, E02004 (2011).
4. S. C. Solomon *et al.*, *J. Geophys. Res.* **97**, 13199–13255 (1992).
5. R. G. Strom, G. G. Schaber, D. D. Dawson, *J. Geophys. Res.* **99**, 10899–10926 (1994).
6. P. K. Byrne *et al.*, *Proc. Natl. Acad. Sci. U.S.A.* **118**, e2025919118 (2021).
7. A. T. Basilevsky, J. W. Head, *Geology* **30**, 1015–1018 (2002).
8. V. S. Solomatov, L.-N. Moresi, *J. Geophys. Res.* **101**, 4737–4753 (1996).
9. J. E. Guest, E. R. Stofan, *Icarus* **139**, 55–66 (1999).
10. F. W. Klein, *J. Volcanol. Geotherm. Res.* **12**, 1–35 (1982).
11. R. I. Tilling, C. Heliker, D. A. Swanson, *Eruptions of Hawaiian Volcanoes: Past, Present, and Future* (US Geological Survey, 2010).
12. L. S. Crumpler *et al.*, in *Venus II: Geology, Geophysics, Atmosphere, and Solar Wind Environment*, S. W. Bougher, D. M. Hunten, R. J. Phillips, Eds. (Univ. of Arizona Press, 1997), pp. 697–756.
13. A. S. Konopliv, W. B. Banerdt, W. L. Sjogren, *Icarus* **139**, 3–18 (1999).
14. M. Monnereau, A. Cazenave, *J. Geophys. Res.* **95**, 15429–15438 (1990).
15. R. D. Lorenz, *Planet. Space Sci.* **117**, 356–361 (2015).
16. C. A. Neal *et al.*, *Science* **363**, 367–374 (2019).
17. R. S. Saunders *et al.*, *J. Geophys. Res.* **97**, 13067–13090 (1992).
18. R. R. Herrick, J. Dufek, P. J. McGovern, *J. Geophys. Res. Planets* **110**, E01002 (2005).
19. A. J. P. Gülcher, T. V. Gerya, L. G. J. Montési, J. Munch, *Nat. Geosci.* **13**, 547–554 (2020).
20. E. R. Stofan, S. E. Smrekar, in *Plates, Plumes, and Paradigms*, G. R. Foulger, J. H. Natland, D. C. Presnall, D. L. Anderson, Eds. (Geological Society of America, 2005), vol. 388, pp. 841–857.
21. Materials and methods are available as supplementary materials.
22. J. Brossier, M. S. Gilmore, K. Toner, A. J. Stein, *J. Geophys. Res. Planets* **126**, e2020JE006722 (2021).
23. C. A. Robinson, J. A. Wood, *Icarus* **102**, 26–39 (1993).
24. R. J. Phillips, *Icarus* **112**, 147–170 (1994).
25. P. Lundgren, M. Bagnardi, H. Dietterich, *Geophys. Res. Lett.* **46**, 9554–9562 (2019).
26. D. R. Shelly, W. A. Thelen, *Geophys. Res. Lett.* **46**, 14395–14403 (2019).
27. E. R. Stofan, S. E. Smrekar, N. Mueller, J. Helbert, *Icarus* **271**, 375–386 (2016).
28. S. E. Smrekar *et al.*, *Science* **328**, 605–608 (2010).
29. W. K. Hartmann, D. C. Berman, *J. Geophys. Res.* **105**, 15011–15025 (2000).
30. D. G. Horvath, P. Moitra, C. W. Hamilton, R. A. Craddock, J. C. Andrews-Hanna, *Icarus* **365**, 114499 (2021).
31. B. A. Campbell, D. B. Campbell, "The Earth-Based Radar Search for Volcanic Activity on Venus" in *52nd Lunar and Planetary Science Conference*, 15 to 19 March 2021 (LPSC, 2021), 2339.
32. P. E. Geissler, *Annu. Rev. Earth Planet. Sci.* **31**, 175–211 (2003).
33. S. Hensley, Model Code and Datasets for Science Magellan Surface Change Paper, version 1, Dataverse (2023); https://doi.org/10.48577/jpl.U5IBW5.

ACKNOWLEDGMENTS

We thank B. Grimm, J. Whitten, S. Smrekar, B. Campbell, and Z. Haddad for comments that improved the content, as did comments from three anonymous reviewers. **Funding:** S.H. was funded by NASA contract 80NM0020F0035. **Author contributions:** R.R.H. searched for changes in the Magellan images, generated the stereo-derived topography and orthorectified the images, and contributed the geologic interpretation. S.H. provided an independent check of the stereo-derived topography and performed the simulations. Both authors wrote sections of the paper. **Competing interests:** The authors declare that they have no competing interests. **Data and materials availability:** Four Magellan datasets were used, all available through NASA's Planetary Data System Annex: mosaic of the cycle 1 images: https://astrogeology.usgs.gov/search/map/Venus/Magellan/Venus_Magellan_LeftLook_mosaic_global_75m; cycle 2 mosaic: https://astrogeology.usgs.gov/search/map/Venus/Magellan/Venus_Magellan_RightLook_mosaic_global_75m; cycle 3 mosaic: https://astrogeology.usgs.gov/search/map/Venus/Magellan/Venus_Magellan_StereoLook_mosaic_global_75m; and a global mosaic of Magellan gridded altimetry: https://astrogeology.usgs.gov/search/map/Venus/Magellan/RadarProperties/Venus_Magellan_Topography_Global_4641m_v02. The modeling source code and output files are available through the Jet Propulsion Laboratory Dataverse (*33*).

License information: Copyright © 2023 the authors, some rights reserved; exclusive licensee American Association for the Advancement of Science. No claim to original US government works. https://www.science.org/about/science-licenses-journal-article-reuse

SUPPLEMENTARY MATERIALS

science.org/doi/10.1126/science.abm7735
Materials and Methods
Supplementary Text
Figs. S1 to S9
Table S1
References (*34*–*36*)

Submitted 11 October 2021; accepted 21 February 2023
Published online 15 March 2023
10.1126/science.abm7735

MOLECULAR BIOLOGY

Structure and mechanism of the plant RNA polymerase V

Guohui Xie[1]†, Xuan Du[2]†, Hongmiao Hu[1]†‡, Sisi Li[2], Xiaofeng Cao[3], Steven E. Jacobsen[4,5], Jiamu Du[1]*

In addition to the conserved RNA polymerases I to III (Pols I to III) in eukaryotes, two atypical polymerases, Pols IV and V, specifically produce noncoding RNA in the RNA-directed DNA methylation pathway in plants. Here, we report on the structures of cauliflower Pol V in the free and elongation conformations. A conserved tyrosine residue of NRPE2 stacks with a double-stranded DNA branch of the transcription bubble to potentially attenuate elongation by inducing transcription stalling. The nontemplate DNA strand is captured by NRPE2 to enhance backtracking, thereby increasing 3′-5′ cleavage, which likely underpins Pol V's high fidelity. The structures also illuminate the mechanism of Pol V transcription stalling and enhanced backtracking, which may be important for Pol V's retention on chromatin to serve its function in tethering downstream factors for RNA-directed DNA methylation.

Transcription by DNA-dependent RNA polymerases (DdRPs) transmits genetic information from DNA to RNA. Whereas RNA polymerases I to III (Pols I to III) are conserved in most eukaryotes (*1*), plants have two additional polymerases, Pols IV and V, that are involved in the plant-specific RNA-directed DNA methylation (RdDM) pathway (*2*–*7*). In RdDM, Pol IV transcripts are used by RNA-DEPENDENT RNA POLYMERASE 2 (RDR2) to produce double-stranded RNAs (dsRNAs), which are subsequently processed by DICER-LIKE 3 (DCL3) into small interfering RNAs (siRNAs) that are loaded into ARGONAUTE 4 (AGO4) (*8*–*19*). In a second downstream step, Pol V produces long noncoding RNA transcripts that serve as a scaffold to bind the AGO4-siRNA complex, which then recruits the DNA methyltransferase DOMAINS REARRANGED METHYLASE 2 (DRM2) to mediate DNA methylation and gene silencing (*20*–*24*). Therefore, Pol V serves the dual role of both producing transcripts and tethering other factors to chromatin. Despite having evolved from Pol II, the Pol IV-V–clade DdRPs have substitutions in multiple subunits and critical residues that are adapted to their distinctive functions (*25*–*27*). Pols IV and V were both reported to require RNA primers and to show weaker in vitro transcription activity as compared with Pol II (*12*). Pol IV is also more error-prone than Pol II, whereas Pol V was reported to have higher fidelity (*28*). Although structural studies have been essential for understanding the mechanism of Pols (*13*, *29*–*34*), determining a structure for Pol V has remained a challenge.

[1]Key Laboratory of Molecular Design for Plant Cell Factory of Guangdong Higher Education Institutes, Institute of Plant and Food Science, Department of Biology, School of Life Sciences, Southern University of Science and Technology, Shenzhen 518055, China. [2]Department of Biochemistry and Molecular Biology, International Cancer Center, Shenzhen University Medical School, Shenzhen 518060, China. [3]State Key Laboratory of Plant Genomics and National Center for Plant Gene Research, Institute of Genetics and Developmental Biology, Chinese Academy of Sciences, Beijing 100101, China. [4]Department of Molecular, Cell and Developmental Biology, University of California at Los Angeles, Los Angeles, CA 90095, USA. [5]Howard Hughes Medical Institute, University of California at Los Angeles, Los Angeles, CA 90095, USA.
*Corresponding author. Email: dujm@sustech.edu.cn
†These authors contributed equally to this work.
‡Present address: MRC Laboratory of Molecular Biology, Cambridge CB2 0QH, UK.

Structure determination of cauliflower Pol V

To investigate the Pol V transcription mechanism, we obtained a monoclonal antibody against a C-terminal peptide of cauliflower (*Brassica oleracea* var. *botrytis*) NRPE1, a distinctive Pol V subunit. We used this antibody to purify Pol V from cauliflower inflorescence (Fig. 1A and fig. S1, A and B), a tissue enriched in dividing cells and DdRPs (*35*, *36*). All 12 subunits of Pol V were confirmed in the purified material by mass spectroscopy (MS) (fig. S1, B and C). Although *Arabidopsis* Pol V was shown to only transcribe the bipartite scaffold of a template DNA (DNA_T) plus an RNA primer (*12*), the purified *B. oleracea* Pol V (*Bo*Pol V) showed substantial transcription activity toward both a bipartite scaffold and a transcription bubble (fig. S1, D and E). We determined the cryo–electron microscopy (cryo-EM) structures of *Bo*Pol V in both apo and transcription bubble–containing elongation complex (EC) conformations at 3.57- and 2.73-Å resolution, respectively (Fig. 1, figs. S2 to S4, and tables S1 and S2). Overall, the two structures were similar with a superimposition root mean square deviation of 0.8 Å. Despite being detected by MS, the NRPE4 and NRPE7 subunits could not be traced in the density, whereas the other 10 subunits could be traced and modeled in both states. In Pol II, the RPB4-RPB7 subcomplex interacts with the clamp domain of RPB2 and the C terminus of RPB1 (*37*). These two regions showed weak density in our Pol V structure, which suggests loose binding and/or flexible conformations of NRPE4-7, potentially explaining why they were missing in our structure.

Overall structure of *Bo*Pol V

Both Pols IV and V evolved from Pol II (*38*). In *Arabidopsis*, Pol V has distinctive subunits NRPE1, NRPE5, and NRPE7, whereas NRPE(D)2 and NRPE(D)4 are shared by Pols V and IV but are different from those in Pol II. All other small subunits are shared by Pols II, IV, and V (*27*). The overall structure of Pol V adopts the classic Pol architecture and resembles other Pols, especially Pol IV (fig. S5) (*13*, *30*, *31*, *33*). Like Pol IV, Pol V lacks the binding surface for Pol II transcription factors, such as the initiation-related factor TFIIB and cleavage-related factor TFIIS (fig. S6, A and B) (*39*, *40*). This is consistent with the lack of these factors in our MS data and indicates that Pol V acts via a distinctive regulatory mechanism compared with Pol II. Despite being encoded by different genes, NRPE5 resembles RPB5 of Pol II and NRPD5 of Pol IV (fig. S6C). By contrast, NRPE9, which is common to Pols II, IV, and V, displays notable structural differences in the different Pols. Although the NRPE9 N-terminal jaw domains of Pols II, IV, and V occupy similar positions, the C-terminal zinc ribbon domain of NRPE9 occupies a specific position to interact with NRPE1, which is different from that seen in Pol II, in which RPB9 interacts with RPB2 (fig. S6D) (*13*, *30*). Compared with Pol IV, the Pol V NRPE9 zinc ribbon domain resides in a similar position but has a ~40° rotation (fig. S6E) (*13*). The funnel domain of Pol V NRPE1 is ~50 residues shorter than that of Pol IV NRPD1, resulting in a reduced binding interface between NRPE1 and the NRPE9 zinc ribbon domain (figs. S6F and S7).

In the EC structure, the last 3′-end RNA nucleotide is linked to the RNA (fig. S4Q). It pairs with the DNA_T and occupies the +1 position (Fig. 2A), representing a pretranslocation conformation (*41*). In the active center of DdRPs, two Mg^{2+} ions, metals A and B, are involved in RNA substrate and incoming nucleoside triphosphate (NTP) binding and catalysis (fig. S8A) (*41*). Because we did not observe NTP binding in our structure, only one Mg^{2+} ion at the metal A binding site was observed to be coordinated by Asp^{449}, Asp^{451}, and Asp^{453} of NRPE1, forming the catalytic site, consistent with a previous biochemical and genetic study (*25*) (Fig. 2A and fig. S8B). Like other Pols, the active center of Pol V has two essential structural elements: the bridge helix (BH) and the trigger loop (TL) (Fig. 2A). The Pol V BH resembles the Pol II BH, despite multiple sequence variations (*29*, *41*) (Fig. 2B and fig. S7).

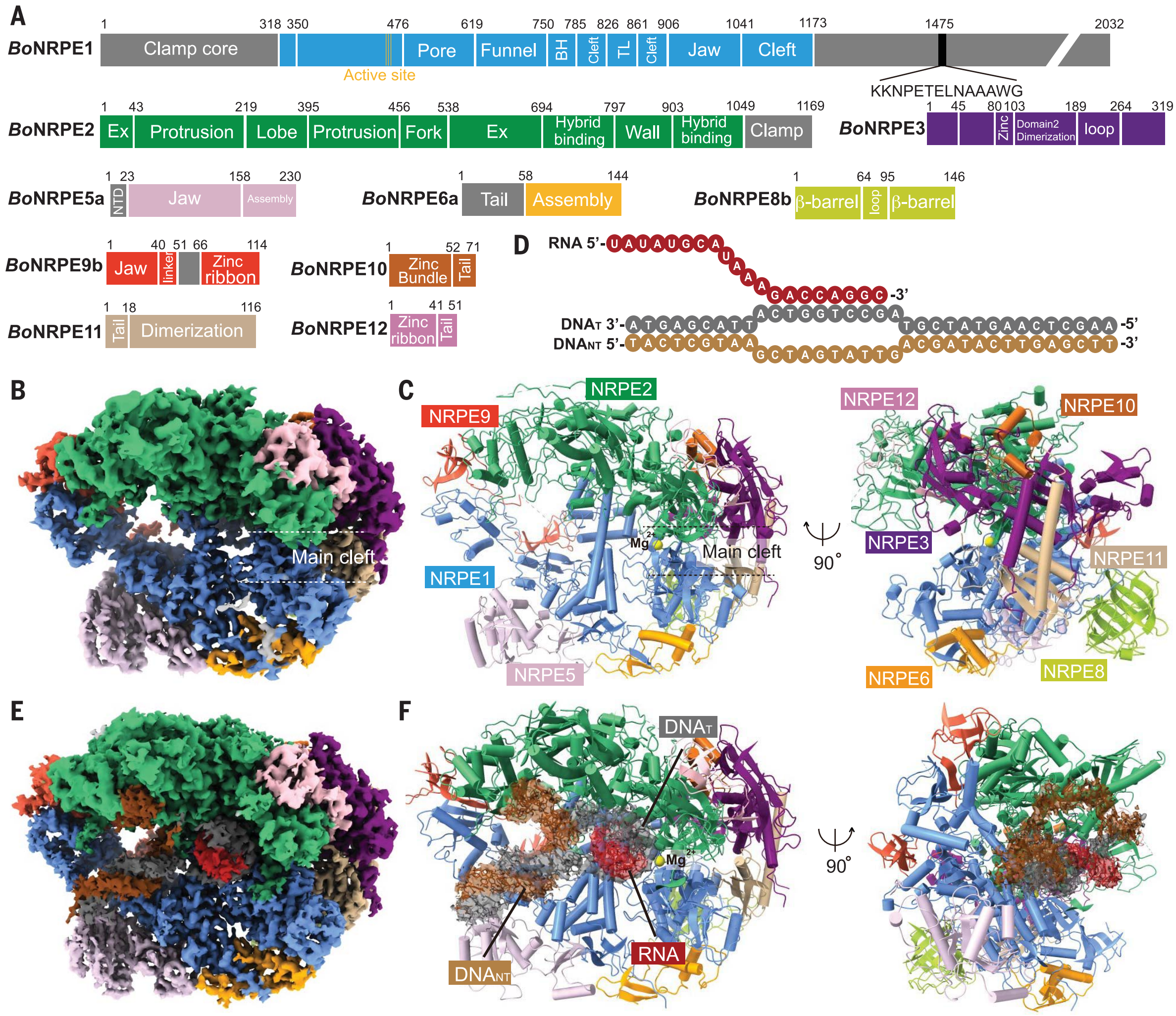


Fig. 1. Structures of *Bo*Pol V in apo and elongation conformations. (**A**) Domain architecture of *Bo*Pol V subunits. The sequence of NRPE1 C-terminal peptide for antibody production is listed. (**B**) Cryo-EM map of *Bo*Pol V in apo form. (**C**) Structure of *Bo*Pol V in the apo form. The subunits are colored as in (A). (**D**) Nucleic acid scaffold for EC formation. (**E**) Cryo-EM map of *Bo*Pol V in complex with a transcription bubble. (**F**) Structure of *Bo*Pol V in the elongation conformation.

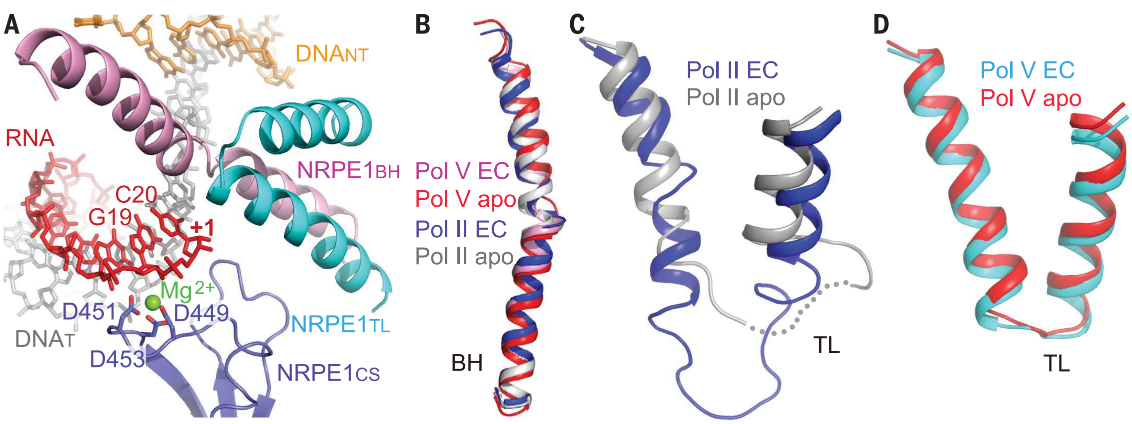


Fig. 2. Active-site conformation. (**A**) Active site of *Bo*Pol V. NRPE1$_{CS}$, catalytic site of NRPE1; NRPE1$_{BH}$, the bridge helix of NRPE1; NRPE1$_{TL}$, the trigger loop of NRPE1. (**B**) Superimposition of the BH of *Bo*Pol V in the apo and elongation states and yeast Pol II in the apo [Protein Data Bank (PDB) ID 1I50] and elongation (PDB ID 2E2H) states, which shows no appreciable conformational change. (**C** and **D**) Superimposition of the TL of yeast Pol II in the apo (PDB ID 1I50) and elongation (PDB ID 2E2H) states (C) and *Bo*Pol V in the apo and elongation states (D), which show that the TL of Pol II is more flexible, whereas Pol V TL is less flexible. D, Asp.

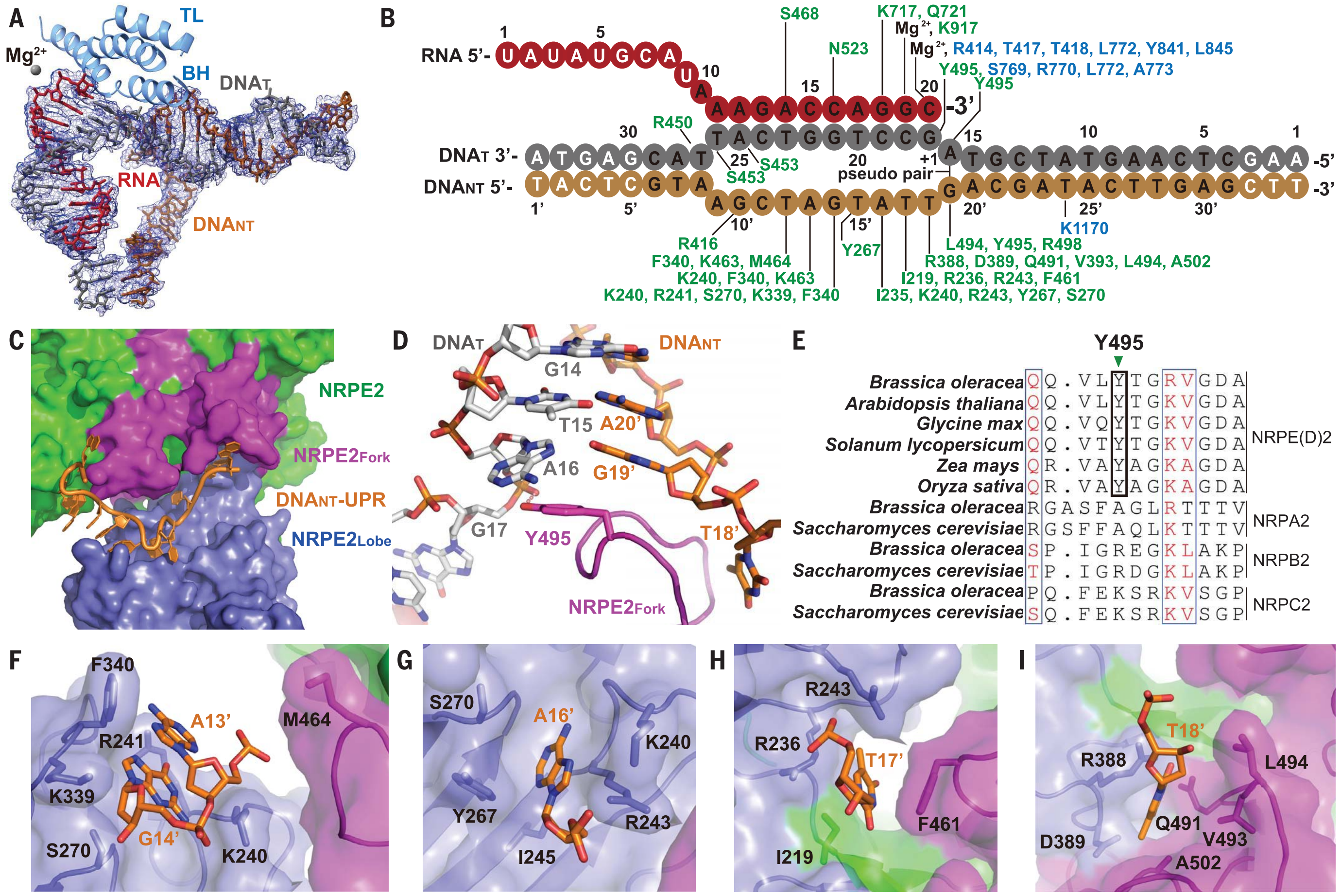


Fig. 3. The interaction between NRPE2 and the transcription bubble. (**A**) Cryo-EM map of the transcription bubble. (**B**) Schematic of the overall interactions between *Bo*Pol V and the transcription bubble. The nucleotides observed in the structure are colored in black and the unobserved ones in white. The residues of NRPE1 and NRPE2 are colored in blue and green, respectively. (**C**) DNA_{NT}-UPR is clamped between the NRPE2 fork ($NRPE2_{Fork}$) and lobe ($NRPE2_{Lobe}$) domains. Other regions of NRPE2 are colored in green. (**D**) $NRPE2_{Fork}$ residue Tyr^{495} stacks with the A16-G19′ pseudo-pair and hydrogen bonds with the phosphate group of G17. (**E**) Structure-based sequence alignment of the NRPE(D)2 from multiple species and NRPA2, NRPB2, and NRPC2 reveals that the Tyr^{495} is conserved only in the NRPE(D)2 clade but not in others. (**F** to **I**) DNA_{NT}-UPR bases G14′ (F), A16′ (G), T17′ (H), and T18′ (I) are accommodated by surface pockets of NRPE2. Single-letter abbreviations for the amino acid residues are as follows: A, Ala; C, Cys; D, Asp; E, Glu; F, Phe; G, Gly; H, His; I, Ile; K, Lys; L, Leu; M, Met; N, Asn; P, Pro; Q, Gln; R, Arg; S, Ser; T, Thr; V, Val; W, Trp; and Y, Tyr.

The Pol V TL is shorter than that in Pol II and also exhibits sequence variations (fig. S7). In contrast to the Pol II TL which shows conformational change in the transition from the apo form to the EC form (*29*, *41*) (Fig. 2C), the TL in both the Pol V apo and EC structures adopts a similar compacted conformation (Fig. 2D), which suggests less conformational flexibility of the Pol V TL. Compared with Pols I and III, although their BHs adopt conformations similar to that of Pol V (fig. S8, C and D), the TLs of Pols I and III are flexible such that they are partially disordered in both the apo and EC forms (fig. S8, E and F) (*31*, *33*, *42*). Given that the TL conformational dynamics is required for NTP substrate binding to promote the transcription reaction, the less-flexible Pol V TL may decrease the NTP incorporation, resulting in lower activity (*12*, *41*).

Interactions between NRPE2 and the transcription bubble

Except for some terminal nucleotides, the entire transcription bubble, including the unpaired region of the nontemplate DNA (DNA_{NT}-UPR), which is often disordered in Pol II structures (*43*, *44*), can be fully traced and modeled in our Pol V EC structure (Fig. 3, A and B). This is likely due to the extensive interactions between DNA_{NT}-UPR and NRPE2 (Fig. 3B), the shared second subunit of Pols IV and V. Overall, DNA_{NT}-UPR is clamped between the lobe and fork domains of NRPE2 (Fig. 3C). At the downstream double-stranded DNA (dsDNA) branching site of the transcription bubble, the first unpaired nucleotides, G19′ of the DNA_{NT} and A16 of the DNA_T, form a pseudo-pair (Fig. 3D), probably mimicking the last DNA base pair in natural transcription. The NRPE2 fork loop residue Tyr^{495}—which is conserved in NRPE(D)2 across multiple species, but not in the NRPA2, NRPB2, and NRPC2 clades (Fig. 3E)—specifically inserts to the DNA branching position to stack with the upcoming A16-G19′ pseudo-pair while also forming a hydrogen bond with the phosphate group of the DNA_T G17 (Fig. 3D). The specific stacking and hydrogen-bonding interactions by the bulky side chain of Tyr^{495} may help Pol V to stabilize the transcription bubble, potentially allowing Pol V pausing to help it serve as a scaffold to recruit downstream effectors, and not only to produce and release RNA transcripts. Moreover, bases G14′, A16′, T17′, and T18′ of DNA_{NT}-UPR are anchored, through extensive interactions, by a series of surface base-binding pockets on NRPE2 (Fig. 3, B and F to I), which stabilizes their relative positions and potentially slows down transcription. The Pol V–bound DNA_{NT}-UPR could be nicely modeled onto that of Pol IV but showed

CALL FOR PAPERS

SPJ SCIENCE PARTNER JOURNALS



Journal of Remote Sensing

The *Journal of Remote Sensing* is an online-only Open Access Science Partner Journal published in affiliation with **Aerospace Information Research Institute, Chinese Academy of Sciences (AIR-CAS)** and distributed by the **American Association for the Advancement of Science (AAAS)**. Like all partners participating in the Science Partner Journal program, the *Journal of Remote Sensing* is editorially independent from the *Science* family of journals and AIR-CAS is responsible for all content published in the journal. This journal covers multiple research areas that include theory, science, technology of remote sensing, and interdisciplinary research with earth science and information science. Particular topics of interest within the journal include radiative transfer modeling, biogeosciences remote sensing, remote sensing of energy, and more.

Submit your research to the *Journal of Remote Sensing* today!

Learn more at **spj.sciencemag.org/remotesensing**

The Science Partner Journal (SPJ) program was established by the American Association for the Advancement of Science (AAAS), the nonprofit publisher of the *Science* family of journals. The SPJ program features high-quality, online-only, Open Access publications produced in collaboration with international research institutions, foundations, funders and societies. Through these collaborations, AAAS furthers its mission to communicate science broadly and for the benefit of all people by providing top-tier international research organizations with the technology, visibility, and publishing expertise that AAAS is uniquely positioned to offer as the world's largest general science membership society.

Visit us at **spj.sciencemag.org**

@SPJournals **@SPJournals**

OPEN ACCESS

ARTICLE PROCESSING CHARGES WAIVED UNTIL JULY 2023

the steric clashes with Pol I and III and a loss of specific interactions upon modeling into Pol II (fig. S9) (*13*, *30*, *31*, *33*), suggesting that this is a feature specific to the Pol IV-V clade.

*Bo*Pol V attenuates transcription elongation

To investigate the biochemical relevance of our structures, we performed in vitro transcription assays using purified *Bo*Pol V and transcription bubble substrates with different gaps between the RNA primer 3′ end and the downstream dsDNA branching site, which are stacked by Tyr^{495} in our structure (Fig. 4A, scaffolds 2 to 5). Pol V showed substantial transcription activity, with an accumulation of transcript corresponding to the unpaired region of DNA_T (DNA_T-UPR) (Fig. 4B). By contrast, the bipartite substrate lacking the DNA_{NT} did not show accumulation of a specific transcript (Fig. 4B), which demonstrates transcription pausing at the downstream DNA branching site, consistent with NRPE2 Tyr^{495} obstructing Pol V translocation at this site. Low levels of longer transcripts were also observed with the transcription bubble substrates (Fig. 4B), which indicates that Pol V has a weak ability to open downstream paired DNA. By contrast, purified cauliflower Pol II (fig. S10) produced longer transcripts without an accumulation of DNA_T-UPR transcription product (Fig. 4C), suggesting that transcription pausing at the branch site is a specific feature of Pol V, or more generally of the Pol IV-V clade, consistent with Tyr^{495} being conserved in NRPE(D)2 but not in that of the other clades (Fig. 3E). Our results suggest that Pol V has relatively high transcriptional activity on the DNA_T-UPR but is less efficient in opening paired DNA, likely because of the conserved bulky Tyr^{495} stacking with, and blocking access to, downstream paired DNA. Because the natural template is always fully paired, Pol V may constitutively exhibit low transcription activity, plausibly contributing to transcriptional pausing and thereby enhancing Pol V retention on chromatin to support its function in tethering chromatin factors to promote RdDM.

NRPE2–DNA_{NT}-UPR interactions enhance backtracking

Transcription pausing is a key step in the induction of transcription backtracking and subsequent 3′-5′ cleavage for proofreading (*39*, *45*). Consistent with transcription pausing, abundant bands corresponding to the RNA-backtracked 3′-5′ cleavage product were observed in our Pol V activity assays (Fig. 4 and fig. S1, D and E). In the presence of Mg^{2+} and absence of NTP, Pol V almost exclusively showed RNA primer cleavage activity without transcription elongation (Fig. 4C). EDTA inhibited this cleavage, which confirmed a Mg^{2+}-dependent cleavage mechanism, similar to that of Pol II (Fig. 4C) (*39*). Addition of NTP and Mg^{2+} triggered *Bo*Pol V transcription elongation while maintaining strong cleavage (Fig. 4C). By contrast, under the same reaction conditions, *Bo*Pol II showed stronger transcription elongation and lower cleavage activity (*12*, *28*) (Fig. 4C). For the DdRP proofreading function to achieve high fidelity (*45*), 3′-5′ cleavage is required, which is consistent with the hypothesis that enhanced 3′-5′ cleavage activity underpins the higher fidelity of Pol V (*28*).

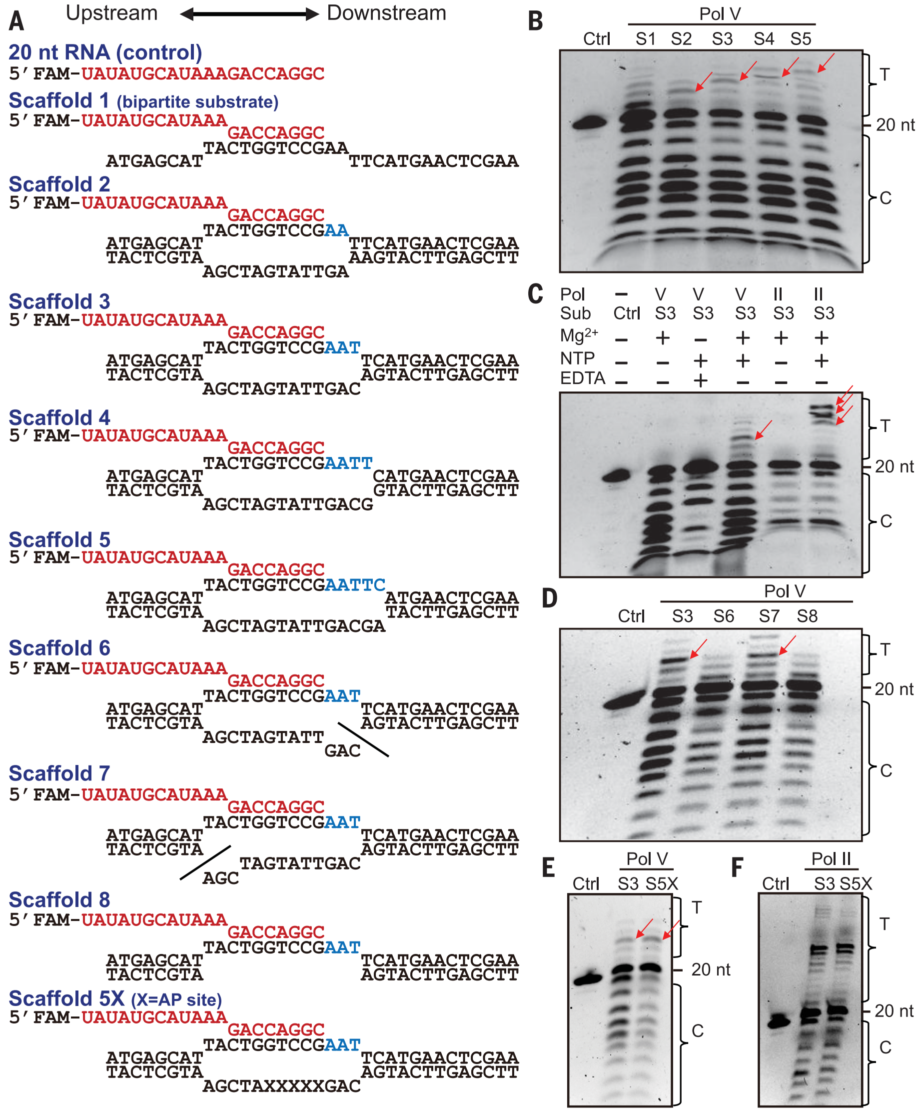


Fig. 4. In vitro biochemical assay. (**A**) Nucleic acid scaffold design. The RNA is 5′-labeled by fluorescein amidite (FAM) and highlighted in red, whereas the downstream DNA_T-UPR is highlighted in blue. In scaffolds 6 and 7, the oligos are disconnected at the lines. (**B**) Transcription assay using different substrate bubbles shows accumulation of transcription products of the downstream DNA_T-UPR, as highlighted by the red arrows. C, cleavage product; Ctrl, control; S1, scaffold 1; T, transcription product. (**C**) RNA primer 3′-5′ cleavage activity of Pol V is stimulated by Mg^{2+} and suppressed by EDTA, whereas transcription elongation requires NTP. Compared with Pol II, Pol V showed stronger 3′-5′ cleavage activity but weaker transcription activity. Sub, substrates. (**D**) Transcription assay using bubbles with different designs of the DNA_{NT} shows that the downstream DNA branching site and the DNA_{NT}-UPR are important for both the transcription and cleavage activities of Pol V. (**E** and **F**) Substitution of the NRPE2-interacting DNA_{NT}-UPR bases by AP sites reduced the 3′-5′ cleavage activity of Pol V (E) but not of Pol II (F), and these substitutions did not change transcription activity. The images shown in (B) to (F) are polyacrylamide gel electrophoresis (PAGE) results.

Excluding the A16-G19′ pseudo-pair, the Pol V transcription bubble contains a DNA_{NT}-UPR of 10 nucleotides (nt) with the downstream branching site–proximal bases T18′, T17′, A16′, and G14′ specifically captured by NRPE2 (Fig. 3, B and F to I), a Pol V–specific feature not observed in other Pols. To analyze the roles of the DNA_{NT}-UPR and the downstream branch in Pol V transcription, we designed a series of transcription bubbles. Compared with the

intact transcription bubble, breaking the DNA_{NT} at the downstream branch site or removing the DNA_{NT}-UPR (Fig. 4A, scaffolds 6 and 8) resulted in similar patterns that decreased both transcription and cleavage activities (Fig. 4D). This is likely because of the loss of interaction with the downstream reaction center in both cases. DNA_{NT} breakage at the upstream branch site (Fig. 4A, scaffold 7) resulted in almost full transcription activity and partial cleavage activity, relative to the intact bubble (Fig. 4D). Moreover, the shortening of DNA_{NT} while only keeping the downstream paired region decreased both the elongation and cleavage activities as well (fig. S11). Overall, these data suggest that the downstream branch and DNA_{NT}-UPR conformation both influence transcription and cleavage activity.

To investigate the NRPE2–DNA_{NT}-UPR interaction that is specific to Pol V (Fig. 3, B and F to I), we eliminated individual DNA_{NT}-UPR nucleotides by replacing them with an apurinic-apyrimidinic (AP) site while retaining DNA_{NT}-UPR integrity (fig. S12A). The loss of DNA_{NT}-UPR bases mildly reduced cleavage activity, with downstream bases having a greater effect than upstream ones (fig. S12B), which is consistent with downstream DNA_{NT}-UPR nucleotides having more interactions with NRPE2 (Fig. 3B). By contrast, all substitutions retained transcription activity similar to that of the unmodified substrate (fig. S12B). Nevertheless, all of the different individual substitutions only weakly affected cleavage activity. We also simultaneously substituted five contiguous downstream DNA_{NT}-UPR nucleotides with AP sites (Fig. 4A, scaffold 5X), which yielded a loss of cleavage activity but did not affect the elongation (Fig. 4E). By contrast, this multiple substitution showed no effect on either transcription or cleavage using *Bo*Pol II (Fig. 4F), which suggests that the importance of these base interactions is specific to Pol V, or likely the Pol IV-V clade. These results suggest that the interaction of the DNA_{NT}-UPR with NRPE2 is mainly responsible for enhancing Pol V cleavage activity. The 3′-5′ cleavage of all Pols requires transcription bubble backtracking to feed RNA into the active site on the largest subunit, that is, NRPE1 in Pol V. Therefore, the NRPE2–DNA_{NT}-UPR interaction promotes increased backtracking to feed RNA into NRPE1, resulting in enhanced Pol V 3′-5′ cleavage activity, a mechanism different from the intrinsic backtracking that is common in Pols.

Discussion

Distinct from Pols I to III, whose principal function is producing transcripts for release, Pols IV and V have evolved specialized transcription features adapted for RdDM. For example, Pol IV generates a single-stranded RNA 3′ end as a substrate for RDR2 through backtracking (*13*), and Pol V likely limits its transcription rate to prolong its chromatin occupancy, thereby providing a scaffolding function for the recruitment of chromatin factors. We speculate that the Pol IV-V–clade DdRPs evolved the shared NRPE(D)2 subunit so that they can stall transcription through the conserved NRPE(D)2 tyrosine residue and enhance backtracking through the NRPE(D)2–DNA_{NT}-UPR interactions. In the case of Pol V, the strong backtracking and transcription stalling may regulate the equilibrium between forward and backward steps, which delays termination and release of transcripts and thus leads to Pol V–long noncoding RNA complex retention on chromatin to promote its scaffolding function. This may also explain the short and relatively uniform length of Pol IV transcripts (35 to 50 nt) (*8*, *13*, *17*). Pol IV likely backtracks to feed RNA into RDR2 through an interpolymerase channel that likely bypasses cleavage (*13*), which may also explain its lower fidelity (*28*). Given NRPE(D)2-induced transcription stalling and high backtracking activity, Pol IV–RNA is unable to undergo long extension before backtracking. Pol IV–RNA may be captured by RDR2 once the nascent transcript is long enough to trigger the dsRNA synthesis by RDR2 and subsequent termination of Pol IV transcription (*13*).

REFERENCES AND NOTES

1. R. G. Roeder, W. J. Rutter, *Nature* **224**, 234–237 (1969).
2. J. R. Haag, C. S. Pikaard, *Nat. Rev. Mol. Cell Biol.* **12**, 483–492 (2011).
3. A. J. Herr, M. B. Jensen, T. Dalmay, D. C. Baulcombe, *Science* **308**, 118–120 (2005).
4. T. Kanno *et al.*, *Nat. Genet.* **37**, 761–765 (2005).
5. M. A. Matzke, R. A. Mosher, *Nat. Rev. Genet.* **15**, 394–408 (2014).
6. Y. Onodera *et al.*, *Cell* **120**, 613–622 (2005).
7. D. Pontier *et al.*, *Genes Dev.* **19**, 2030–2040 (2005).
8. T. Blevins *et al.*, *eLife* **4**, e09591 (2015).
9. X. Du *et al.*, *Plant Cell* **34**, 2140–2149 (2022).
10. A. Fukudome *et al.*, *Proc. Natl. Acad. Sci. U.S.A.* **118**, e2115899118 (2021).
11. V. Gasciolli, A. C. Mallory, D. P. Bartel, H. Vaucheret, *Curr. Biol.* **15**, 1494–1500 (2005).
12. J. R. Haag *et al.*, *Mol. Cell* **48**, 811–818 (2012).
13. K. Huang *et al.*, *Science* **374**, 1579–1586 (2021).
14. J. Singh, V. Mishra, F. Wang, H. Y. Huang, C. S. Pikaard, *Mol. Cell* **75**, 576–589.e5 (2019).
15. Q. Wang *et al.*, *Science* **374**, 1152–1157 (2021).
16. Z. Xie, E. Allen, A. Wilken, J. C. Carrington, *Proc. Natl. Acad. Sci. U.S.A.* **102**, 12984–12989 (2005).
17. J. Zhai *et al.*, *Cell* **163**, 445–455 (2015).
18. D. Zilberman, X. Cao, S. E. Jacobsen, *Science* **299**, 716–719 (2003).
19. D. Zilberman *et al.*, *Curr. Biol.* **14**, 1214–1220 (2004).
20. X. Cao, S. E. Jacobsen, *Curr. Biol.* **12**, 1138–1144 (2002).
21. X. Cao, S. E. Jacobsen, *Proc. Natl. Acad. Sci. U.S.A.* **99**, 16491–16498 (2002).
22. G. Moissiard *et al.*, *Science* **336**, 1448–1451 (2012).
23. A. T. Wierzbicki, T. S. Ream, J. R. Haag, C. S. Pikaard, *Nat. Genet.* **41**, 630–634 (2009).
24. X. Zhong *et al.*, *Cell* **157**, 1050–1060 (2014).
25. J. R. Haag, O. Pontes, C. S. Pikaard, *PLOS ONE* **4**, e4110 (2009).
26. R. Landick, *Structure* **17**, 323–325 (2009).
27. T. S. Ream *et al.*, *Mol. Cell* **33**, 192–203 (2009).
28. M. Marasco, W. Li, M. Lynch, C. S. Pikaard, *Nucleic Acids Res.* **45**, 11315–11326 (2017).
29. P. Cramer *et al.*, *Science* **288**, 640–649 (2000).
30. P. Cramer, D. A. Bushnell, R. D. Kornberg, *Science* **292**, 1863–1876 (2001).
31. N. A. Hoffmann *et al.*, *Nature* **528**, 231–236 (2015).
32. C. Engel, S. Sainsbury, A. C. Cheung, D. Kostrewa, P. Cramer, *Nature* **502**, 650–655 (2013).
33. C. Fernández-Tornero *et al.*, *Nature* **502**, 644–649 (2013).
34. M. Girbig, A. D. Misiaszek, C. W. Müller, *Nat. Rev. Mol. Cell Biol.* **23**, 603–622 (2022).
35. T. J. Guilfoyle, *Biochemistry* **19**, 5966–5972 (1980).
36. L. Huang *et al.*, *Nat. Struct. Mol. Biol.* **16**, 91–93 (2009).
37. K. J. Armache, S. Mitterweger, A. Meinhart, P. Cramer, *J. Biol. Chem.* **280**, 7131–7134 (2005).
38. S. L. Tucker, J. Reece, T. S. Ream, C. S. Pikaard, *Cold Spring Harb. Symp. Quant. Biol.* **75**, 285–297 (2010).
39. A. C. Cheung, P. Cramer, *Nature* **471**, 249–253 (2011).
40. S. Sainsbury, J. Niesser, P. Cramer, *Nature* **493**, 437–440 (2013).
41. D. Wang, D. A. Bushnell, K. D. Westover, C. D. Kaplan, R. D. Kornberg, *Cell* **127**, 941–954 (2006).
42. S. Neyer *et al.*, *Nature* **540**, 607–610 (2016).
43. C. Bernecky, F. Herzog, W. Baumeister, J. M. Plitzko, P. Cramer, *Nature* **529**, 551–554 (2016).
44. H. Kettenberger, K. J. Armache, P. Cramer, *Mol. Cell* **16**, 955–965 (2004).
45. E. Nudler, *Cell* **149**, 1438–1445 (2012).

ACKNOWLEDGMENTS

We thank P. Wang, J. Tan, S. Xu, and X. Ma at the Southern University of Science and Technology (SUSTech) Cryo-EM Center for data collection; the SUSTech Core Research Facilities for help with MS experiments; and G. Riddihough (Life Science Editors) for editing. **Funding:** This work was funded by the Shenzhen Science and Technology Program (grants JCYJ20200109110403829 and KQTD20190929173906742 to J.D.); the Key Laboratory of Molecular Design for Plant Cell Factory of Guangdong Higher Education Institutes (grant 2019KSYS006 to J.D.); the China Postdoctoral Science Foundation (grant 2022M712173 to X.D.); the National Natural Science Foundation of China (grant 31788103 to X.C.); the Chinese Academy of Sciences Strategic Priority Research Program (grant XDB27030201 to X.C.); and the National Institutes of Health (grant R35 GM130272 S.E.J.). S.E.J. is an investigator of the Howard Hughes Medical Institute. **Author contributions:** Conceptualization: G.X., H.H., and J.D.; Methodology: G.X., X.D., H.H., S.L., and X.C.; Investigation: G.X., X.D., and H.H.; Funding acquisition: X.D., X.C., S.E.J., and J.D.; Project administration: J.D.; Supervision: X.C., S.E.J., and J.D.; Writing – original draft: J.D.; Writing – review and editing: S.E.J. and J.D. **Competing interests:** The authors declare no competing interests. **Data and materials availability:** The structures have been deposited in the Protein Data Bank under accession codes 8HIL and 8HIM. The cryo-EM maps have been deposited in the Electron Microscopy Data Bank under accession codes EMD-34820 and EMD-34821. The biological material is available upon request to J.D. All data are available in the main text or the supplementary materials.

License information: Copyright © 2023 the authors, some rights reserved; exclusive licensee American Association for the Advancement of Science. No claim to original US government works. https://www.science.org/about/science-licenses-journal-article-reuse. This research was funded in whole or in part by the Howard Hughes Medical Institute, a cOAlition S organization. The author will make the Author Accepted Manuscript (AAM) version available under a CC BY public copyright license.

SUPPLEMENTARY MATERIALS

science.org/doi/10.1126/science.adf8231
Materials and Methods
Figs. S1 to S12
Tables S1 and S2
References (*46–58*)
MDAR Reproducibility Checklist

View/request a protocol for this paper from *Bio-protocol*.

Submitted 5 December 2022; accepted 25 February 2023
Published online 9 March 2023
10.1126/science.adf8231

KONDO INSULATORS

Visualizing the atomic-scale origin of metallic behavior in Kondo insulators

Harris Pirie[1,2], Eric Mascot[3], Christian E. Matt[1], Yu Liu[1], Pengcheng Chen[1], M. H. Hamidian[1], Shanta Saha[4], Xiangfeng Wang[4], Johnpierre Paglione[4], Graeme Luke[5], David Goldhaber-Gordon[6,7], Cyrus F. Hirjibehedin[8,9,10]†, J. C. Séamus Davis[2,11,12,13], Dirk K. Morr[3], Jennifer E. Hoffman[1]*

A Kondo lattice is often electrically insulating at low temperatures. However, several recent experiments have detected signatures of bulk metallicity within this Kondo insulating phase. In this study, we visualized the real-space charge landscape within a Kondo lattice with atomic resolution using a scanning tunneling microscope. We discovered nanometer-scale puddles of metallic conduction electrons centered around uranium-site substitutions in the heavy-fermion compound uranium ruthenium silicide (URu_2Si_2) and around samarium-site defects in the topological Kondo insulator samarium hexaboride (SmB_6). These defects disturbed the Kondo screening cloud, leaving behind a fingerprint of the metallic parent state. Our results suggest that the three-dimensional quantum oscillations measured in SmB_6 arise from Kondo-lattice defects, although we cannot exclude other explanations. Our imaging technique could enable the development of atomic-scale charge sensors using heavy-fermion probes.

When the electrons in a material interact strongly with one another, they often produce unexpected behavior. Above a characteristic temperature T_K, a lattice of local *f* moments within a conducting Fermi sea behaves like an ordinary magnetic metal, with a Curie-Weiss susceptibility. But below T_K, the competition between antiferromagnetic ordering of the local moments and their screening by conduction electrons leads to a rich phase diagram, exhibiting quantum criticality (*1*), unconventional superconductivity (*2*), and heavy fermions (*3*, *4*)—quasiparticles with *f*-electron character (Fig. 1A). A Kondo insulator forms if the spectral gap opened by hybridization between the conduction band and the renormalized *f* band spans the Fermi level. Mysteriously, some Kondo insulators seem to “remember” their metallic parent state long after this gap is fully developed. For example, the topological Kondo insulator samarium hexaboride (SmB_6) displays a sizable bulk optical conductivity at terahertz frequencies (*5*) and a finite electronic specific heat at low temperatures (*6*–*9*). A complete three-dimensional (3D) Fermi surface matching its high-temperature metallic state was reconstructed from quantum oscillation (*9*, *10*) and Compton scattering (*11*) measurements performed in the insulating regime. Notably, these metallic properties persist even as the bulk resistivity of SmB_6 increases by 10 orders of magnitude (*12*). This discrepancy led to several theoretical proposals: Some argue that the metallic behavior is intrinsic, either a consequence of the small hybridization gap in Kondo insulators (*13*) or arising from exotic charge-neutral quasiparticles (*14*, *15*). Others suggest an extrinsic origin (*16*–*19*), which implies the presence of microscopic metallic pockets.

Charge inhomogeneity is commonplace at nanometer length scales, especially in materials with strong electron interactions that promote competing orders (*20*). In a Kondo lattice, defects that substitute or remove the *f*-contributing moment, called Kondo holes, have a widespread impact on the nearby electronic structure (*21*–*23*). First, these defects locally untangle the hybridized wave function, leaving puddles of unhybridized conduction electrons behind (Fig. 1B). In theory, these charge puddles should have the same itinerant character as the metallic parent state (*22*), but they have not been imaged directly. Additionally, the excess conduction electrons released from hybridization adjust the strength of their interactions with the remaining *f* moments (*22*, *24*), leading to enhanced local magnetism (*25*) (Fig. 1C). For example, $Sm_{1-x}La_xB_6$ samples with nonmagnetic La dopants are known to display increased specific heat and magnetic susceptibility compared with undoped samples (*26*–*28*). More recently, the existence of local metallic puddles around Gd dopants in $Sm_{1-x}Gd_xB_6$ was inferred from electron spin-resonance measurements (*29*). Meanwhile, an increased concentration of Sm vacancies in $Sm_{1-x}B_6$ was shown to globally inhibit the development of the hybridization gap (*30*), eventually leading to bulk conduction (*12*, *31*). All of these findings suggest that Sm-site defects manifest as Kondo holes in SmB_6, yet their key signature—the accompanying charge oscillations relating to the parent metallic Fermi surface (*22*)—remains undetected by any microscopic probe.

Directly imaging the metallic puddles around Kondo holes is difficult, because the inherent screening strongly renormalizes the bare charge distribution. However, there are a few promising approaches (*32*–*34*). The most common is to decorate the tip of a Kelvin probe force microscope with a single atom or molecule (*35*, *36*). This technique was used to image the charge variations within an adsorbed molecule (*37*). However, it becomes inaccurate for small tip-sample separations, because of the influence of short-range forces (*38*, *39*), complicating further improvements to its spatial resolution (*40*). Meanwhile, a scanning tunneling microscope (STM) routinely achieves the subnanometer spatial resolution, cryogenic temperatures, and sub–milli–electron volt (sub-meV) energy resolution required to access atomic charge distributions, but existing methods to extract the electrostatic potential from the STM vacuum decay length contain substantial artifacts (*41*). Consequently, simultaneously achieving the high charge precision and high spatial resolution required to measure the charge environment around a Kondo hole is not possible using existing techniques.

We have developed a dedicated STM modality to image the charge environment within a Kondo lattice with sub-angstrom resolution. At temperatures below T_K, we image charge oscillations matching the parent Fermi surface centered around spinless thorium atoms in the Kondo metal uranium ruthenium silicide (URu_2Si_2) and around three separate Sm-site defects in the Kondo insulator SmB_6. The charge puddles we image in SmB_6 exhibit the same metallic wave vector seen in recent quantum oscillation experiments (*9*, *10*), suggesting that Kondo-lattice defects are the source of those oscillations.

Measuring local charge density in a Kondo lattice

To visualize the conduction-electron density $n_c(\mathbf{r})$ in a Kondo lattice [and hence the local charge $-en_c(\mathbf{r})$, where $-e$ is the electron charge], we first show theoretically that $n_c(\mathbf{r})$ determines the energy position of the Kondo resonance $\tilde{\varepsilon}_f(\mathbf{r})$, which forms near the Fermi level as the magnetic *f* moments are screened by conduction electrons. Then, we establish an experimental metric capable of detecting the sub-meV variations in $\tilde{\varepsilon}_f(\mathbf{r})$ around a Kondo hole. Our technique takes advantage of how the many-body Kondo resonance responds to local doping.

[1]Department of Physics, Harvard University, Cambridge, MA 02138, USA. [2]Clarendon Laboratory, University of Oxford, Oxford OX1 3PU, UK. [3]Department of Physics, University of Illinois at Chicago, Chicago, IL 60607, USA. [4]Maryland Quantum Materials Center, Department of Physics, University of Maryland, College Park, MD 20742, USA. [5]Department of Physics and Astronomy, McMaster University, Hamilton, ON L8S 4M1, Canada. [6]Department of Physics, Stanford University, Stanford, CA 94305, USA. [7]Stanford Institute for Materials and Energy Sciences, SLAC National Accelerator Laboratory, Menlo Park, CA 94025, USA. [8]London Centre for Nanotechnology, University College London (UCL), London WC1H 0AH, UK. [9]Department of Physics and Astronomy, UCL, London WC1E 6BT, UK [10]Department of Chemistry, UCL, London WC1H 0AJ, UK. [11]Department of Physics, University College Cork, Cork T12 R5C, Ireland. [12]Laboratory of Atomic and Solid State Physics, Department of Physics, Cornell University, Ithaca, NY 14850, USA. [13]Max Planck Institute for Chemical Physics of Solids, D-01187 Dresden, Germany.
*Corresponding author. Email: jhoffman@physics.harvard.edu
†Present address: Lincoln Laboratory, Massachusetts Institute of Technology, Lexington, MA 02421, USA.

In the Abrikosov fermion representation for local moments, $\tilde{\varepsilon}_f$ is the Lagrange multiplier that enforces uniform *f*-electron density, typically $n_f = 1$ at each site. As additional charge carriers Δn_c enter a uniform Kondo lattice, the hybridized Fermi surface reshapes to accommodate them, leading to a corresponding change in $\tilde{\varepsilon}_f$ in order to maintain $n_f = 1$ (Fig. 1D, black triangles, and fig. S2E). The magnitude and direction of the shift in $\tilde{\varepsilon}_f$ depend on the details of the band structure. But the relationship between n_c and $\tilde{\varepsilon}_f$ is linear over a wide range of band parameters and charge doping (fig. S2), implying that the charge density at position $\mathbf{r}$ can usually be inferred by measuring $\tilde{\varepsilon}_f(\mathbf{r})$. In fact, the linear dependence of $\tilde{\varepsilon}_f(\mathbf{r})$ on $n_c(\mathbf{r})$ was recently verified experimentally by micrometer-scale angle-resolved photoemission spectroscopy (ARPES) measurements in Eu-doped SmB_6 (*42*).

In STM measurements, the Kondo resonance normally appears as a peak-dip feature in the tunneling conductance dI/dV (*43*) (where I is the sample-to-tip tunneling current at applied sample bias V), because of the presence of multiple tunneling channels (*44*, *45*) (see calculation in Fig. 1D). In simple cases, $\tilde{\varepsilon}_f$ can be estimated by fitting dI/dV to a Fano-like model (*46*, *47*). However, the exact value of $\tilde{\varepsilon}_f$ depends on the model used, so this approach is not immediately suitable for detecting the small, sub-meV energy shifts in $\tilde{\varepsilon}_f(\mathbf{r})$ expected around a Kondo hole. Instead, we track the ratio of forward-to-backward tunneling current, that is, the local rectification $R(\mathbf{r},V) = |I(\mathbf{r},+V)/I(\mathbf{r},-V)|$. This ratio is insensitive to STM setup artifacts, and it was previously used to track charge inhomogeneity from the spectral weight transfer at high biases in hole-doped cuprates (*48*). We focus on low biases, typically $V \lesssim 10$ mV, where the small shifts in $\tilde{\varepsilon}_f(\mathbf{r})$ generate large variations in $R(\mathbf{r},V)$ owing to the energy asymmetry of dI/dV about the Fermi level at $V = 0$ (Fig. 1, D and E, and fig. S2). To demonstrate this effect locally, we self-consistently calculated $dI(\mathbf{r},V)/dV$, $n_c(\mathbf{r})$, and $R(\mathbf{r},V)$ around a Kondo hole in a metallic Kondo lattice, as shown in Fig. 1, F to H. The calculated $dI(\mathbf{r},V)/dV$ at $V = 0$ tracks the local Fermi-level density of states, so it reveals the hybridized Fermi surface of heavy fermions with a wave vector $2k_F^h$. In contrast, both $n_c(\mathbf{r})$ and $R(\mathbf{r},V)$ are dominated by static oscillations at the unhybridized wave vector $2k_F^c$, associated with the Friedel-like redistribution of the Kondo screening cloud. The correlation between $n_c(\mathbf{r})$ and $R(\mathbf{r},V)$ establishes $R(\mathbf{r},V)$ as a qualitative probe of local charge, except at very short distances from a Kondo hole ($|\mathbf{r}| \sim a$), likely because $n_f = 1$ is not enforced at that site.

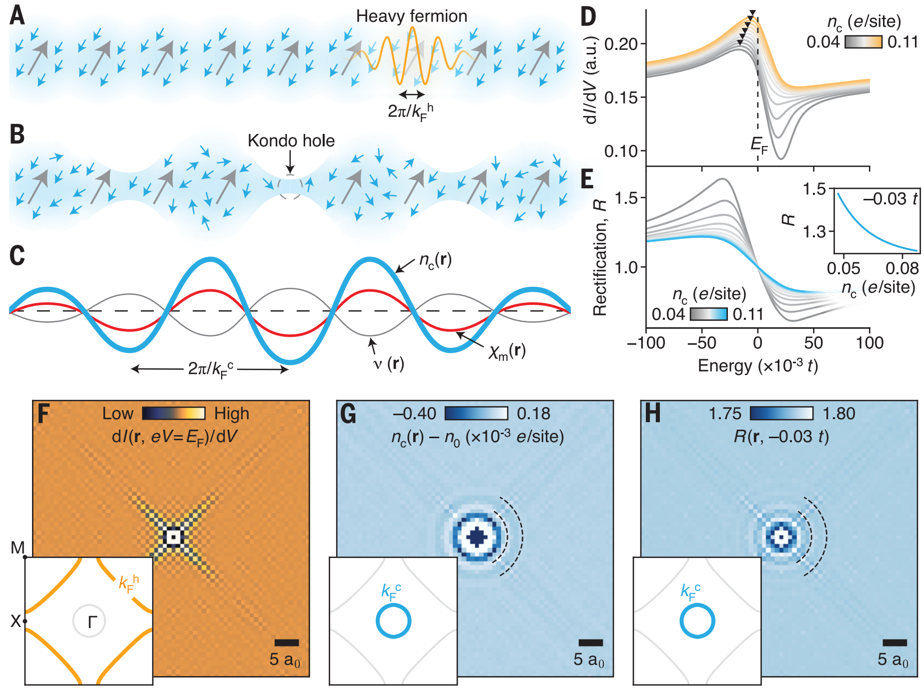


Fig. 1. Expected disruption of the screening cloud around Kondo holes. (**A**) In a uniform Kondo lattice, magnetic moments at each site (gray arrows) are coherently screened by itinerant conduction electrons (blue cloud) to form a spinless ground state of heavy fermions (orange line), characterized by the wave vector k_F^h. (**B**) If one moment is removed to create a Kondo hole, the conduction electrons previously screening it can redistribute themselves. (**C**) The redistributed screening cloud causes oscillations of the local conduction electron density $n_c(\mathbf{r})$, interaction strength $\nu(\mathbf{r})$, and magnetic susceptibility $\chi_m(\mathbf{r})$ at the conduction-band wave vector k_F^c, as shown schematically. (**D**) In a uniform Kondo lattice, the Kondo resonance creates a peak-dip feature in the calculated dI/dV, caused by the quantum interference between tunneling into the conduction band and the *f*-electron states with respective amplitudes t_c and t_f. The energy position of the peak (black triangles) shifts linearly according to the local conduction-electron density n_c. a.u., arbitrary units. (**E**) The calculated rectification $R(V) = |I(+V)/I(-V)|$ acquires a strong peak because dI/dV is asymmetric around the Fermi level E_F (which occurs at $V = 0$). The $R(V)$ peak amplitude depends on the dI/dV peak energy. These changes are almost linear over the small range of local doping expected around a Kondo hole (inset). (**F**) The calculated oscillations in $dI(\mathbf{r},V)/dV$ at the Fermi level around a Kondo hole match the hybridized Fermi surface (k_F^h, orange line in inset). (**G**) In contrast, the calculated $n_c(\mathbf{r})$ varies according to the circular wave vector of the unhybridized Fermi surface (k_F^c, blue line in inset), as it mainly reflects the disturbance to the screening cloud. (**H**) Calculated $R(\mathbf{r},V)$ is dominated by unhybridized electrons for biases within the hybridization gap. The calculations in (D) to (H) are based on a Kondo-Heisenberg model with nearest-neighbor hopping strength t, Kondo coupling $J = 2t$, antiferromagnetic exchange $I = 0.002t$, and tunneling amplitudes $t_f/t_c = -0.025$. In (D) and (E), the hybridization strength is fixed at $\nu = 0.1t$, and the antiferromagnetic correlation strength is fixed at $\chi = 0.0003t$. The Fermi wavelength is $\lambda_F^c = 8a_0$ in (F) to (H), where a_0 is the lattice spacing.

Kondo holes in URu_2Si_2

To test our technique, we first studied the Kondo metal URu_2Si_2 with 1% thorium dopants, which are known to induce Kondo-hole behavior (*24*, *49*). Previous STM measurements mapped a metal-like Fermi surface in URu_2Si_2 for temperatures above $T_o = 17.5$ K, consisting of a single conduction band with wave vector $k_F^c \approx 0.3\,\pi/a$, where a is the lattice constant (Fig. 2A) (*46*). The onset of coherent heavy fermion bands below T_o (*50*) is accompanied by the appearance of a peak-dip feature in dI/dV, that is, the Kondo-Fano resonance (Fig. 2B). Close to a thorium dopant, this feature shifts upward in energy, toward the Fermi level. This energy shift—and even the barely perceptible shifts 2 nm away from the dopant—are easily detected in the amplitude of $R(\mathbf{r},V)$ (Fig. 2C). For biases within the hybridization gap $|V| < \Delta/e \approx 5$ mV (where Δ is the gap magnitude), $R(\mathbf{r},V)$ displays widespread spatial oscillations emanating from thorium dopants, as shown in Fig. 2, D to F. Their wave vector of 0.29 ± 0.01 $(2\pi/a)$ agrees with the hybridization oscillations previously measured around Kondo holes in this compound (*24*). It matches the URu_2Si_2 parent metallic Fermi surface detected above T_o from our measured quasiparticle interference patterns in $dI(\mathbf{r},V)/dV$ at $V = 0$, but it is distinct from the heavy bands that we measured below T_o (Fig. 2G). As a final check, we independently extracted $\tilde{\varepsilon}_f(\mathbf{r})$ by fitting $dI(\mathbf{r},V)/dV$ curves to a Fano model (fig. S3).

The excellent agreement between $\tilde{\varepsilon}_f(\mathbf{r})$ and $R(\mathbf{r},V)$ corroborates the existence of charge oscillations at $2k_F^c$ in URu_2Si_2, indicating that some electrons retain their itinerant character around Kondo holes, even below T_o.

Metallic puddles in SmB_6

In our Kondo insulating SmB_6 samples, any atomic defect that replaces a Sm atom to alter the 4*f* moment could generate metallic puddles like those seen in URu_2Si_2. We searched for these puddles in flux-grown samples lightly doped with Fe, which contain two clear Sm-site defects: Sm vacancies and Fe substitutions (Fig. 3B). We focused on the (2×1) Sm termination, as its charge environment most closely represents that of the bulk (*51*). As in URu_2Si_2, we noticed that the dI/dV peak attributed to the Kondo resonance changes its energy position near candidate Kondo holes (Fig. 3C), strongly affecting the $R(\mathbf{r},V)$ peak amplitude (Fig. 3D). Similar shifts in dI/dV peak position were previously linked to the buildup of charge around boron clusters on the Sm (1×1) termination (*52*). For biases within the hybridization gap $|V| < \Delta/e \approx 10$ mV, $R(\mathbf{r},V)$ reveals prominent oscillations around Sm-site defects (Fig. 3, E and F). These oscillations create a sharp ellipse in the Fourier transform of $R(\mathbf{r},V)$, as shown in Fig. 3G. The wave vectors of the $R(\mathbf{q},V)$ ellipse are larger than those of the surface state detected by quasiparticle interference imaging (*53*), and they do not disperse

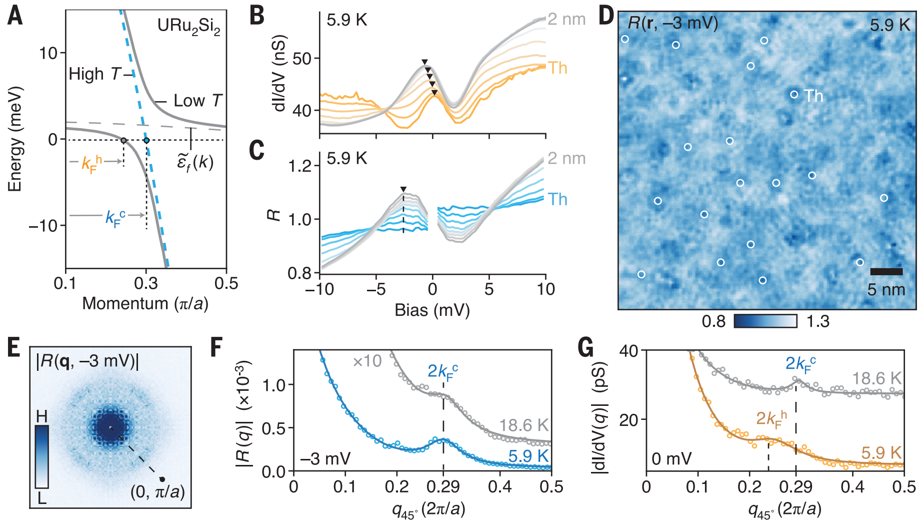


Fig. 2. Thorium dopants induce Kondo-hole behavior in URu_2Si_2. (**A**) Schematic band structure of URu_2Si_2 showing the onset of heavy fermion bands (gray solid lines) at temperatures below T_o = 17.5 K, as itinerant conduction electrons (blue dashed line) hybridize with a renormalized 5*f* level (gray dashed line), reducing the Fermi wave vector from k_F^c to k_F^h. (**B**) Experimental measurement of an asymmetric Fano line shape in the tunneling conductance at temperatures below T_o on the U termination (gray curve). This feature shifts toward the Fermi level near a thorium dopant (black triangles), consistent with an expected change in local charge density. (**C**) For a fixed bias, the $R(V)$ peak amplitude (black triangle) is highly sensitive to the dI/dV peak position. The spectra in (B) and (C) are averaged over the 18 well-isolated thorium dopants marked in (D). (**D**) The measured $R(\mathbf{r},V)$ exhibits clear oscillations that manifest as a ring in (**E**) the fourfold-symmetrized Fourier transform. H, high; L, low. (**F**) These oscillations match the high-temperature Fermi wave vector of $2k_F^c \approx 0.3\ (2\pi/a)$, both above and below T_o. (**G**) In contrast, a conventional dI/dV measurement couples to the temperature-dependent Fermi surface, which changes drastically from 18.6 K to 5.9 K. For clarity, the 18.6 K data have been scaled in (F) and offset in (G).

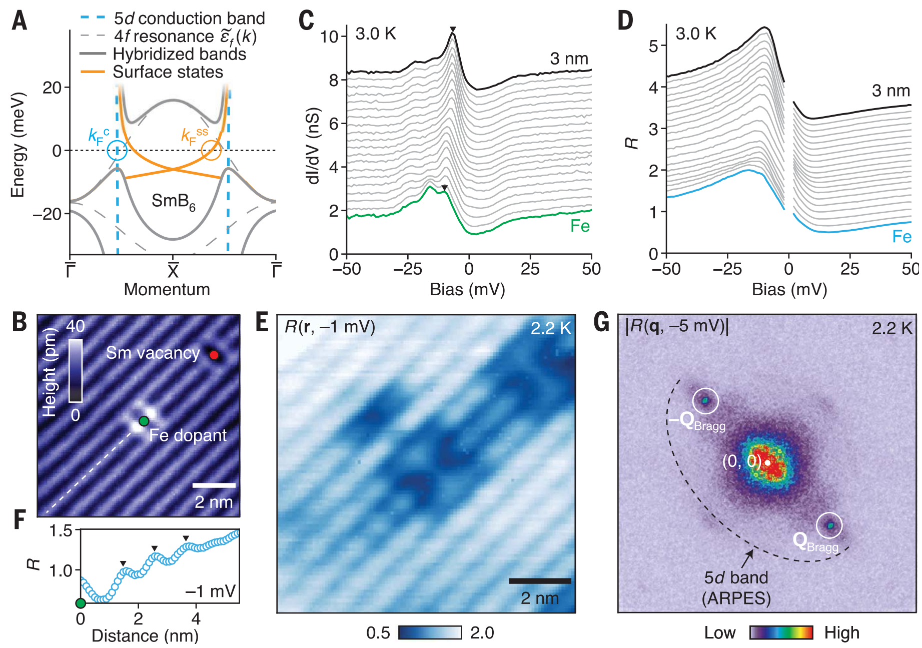


Fig. 3. Kondo holes nucleate metallic puddles in SmB_6. (**A**) Schematic band structure of SmB_6 showing the hybridization between conduction electrons (blue dashed line) and localized 4*f* moments (gray dashed line), which leads to an inverted band structure (gray solid line) hosting emergent heavy Dirac surface states with a reduced Fermi wave vector (orange). (**B**) STM topography of the (2×1)-reconstructed Sm surface of lightly Fe-doped SmB_6. Both the Fe dopant and Sm vacancy in this image are expected to act as Kondo holes because they each displace a 4*f* moment. (**C** and **D**) Near the Fe dopant, the measured dI/dV peak changes energy position (black triangles), leading to large variations in the $R(\mathbf{r},V)$ peak amplitude. The spectra in (C) and (D) have been offset for clarity. (**E**) $R(\mathbf{r},V)$ in the same area as shown in (B) contains clear oscillations around the two impurities. (**F**) Linecut of $R(\mathbf{r},V)$ along the white dashed line in (B). (**G**) $R(\mathbf{r},V)$ oscillations appear as a sharp ring in the twofold-symmetrized Fourier transform (taken from a larger 65 nm by 80 nm area for enhanced $\mathbf{q}$ resolution), which matches the unhybridized 5*d* Fermi surface inferred from ARPES experiments (dashed line) (*54*). The surface reconstruction creates a sharp peak in $R(\mathbf{r},V)$ at $\mathbf{Q}_{Bragg} = (0,\pi/a)$.

for biases within the hybridization gap, indicating a different origin (fig. S4). On the other hand, the size and shape of the ellipse matches the unhybridized *5d* band found by extrapolating ARPES data (*54*) to the Fermi level (i.e., it matches the SmB_6 metallic parent state), after accounting for band folding on the (2×1) surface (Fig. 2G and fig. S5). Our observation of this *5d* wave vector within the Kondo insulating gap is direct evidence of atomic-scale metallicity around Kondo holes. This metallicity is supported by the large residual dI/dV at V = 0 mV that we measured around Kondo holes (Fig. 3C, green curve), indicating a sizable Fermi-level density of states even when the metallic surface states are suppressed (*55*). We confirmed this discovery by checking for $R(\mathbf{r},V)$ oscillations around a third type of Kondo hole, Gd dopants, as detailed in fig. S6.

Magnetic fluctuations at Kondo holes in SmB_6

Our $R(\mathbf{r},V)$ maps show the real-space structure of the metallic puddles around Kondo holes in SmB_6. For these puddles to contribute to the measured de Haas–van Alphen oscillations in magnetization, they must have a finite magnetic susceptibility. Several Sm-site defects are already suspected to be locally magnetic from their impact on bulk susceptibility (*7*, *26*, *27*, *56*) and their influence on the topologically emergent surface states (*53*, *55*). In general, topological surface states can provide a test of local magnetism because they are protected against backscattering from nonmagnetic defects but not from magnetic defects that locally break time-reversal symmetry (*57*). This additional magnetic backscattering was previously imaged around Fe dopants in two Bi-based topological insulators (*58*, *59*). We visualized the intensity of magnetic fluctuations at Sm-site defects in SmB_6 by identifying spatial regions where its surface states backscatter. For biases within the hybridization gap, we measured large-area $dI(\mathbf{r},V)/dV$ maps that contain clear quasiparticle interference patterns at the backscattering wave vector $\mathbf{q} \equiv \mathbf{k}_f - \mathbf{k}_i = 2\mathbf{k}^{ss}$ (Fig. 4B), consistent with our previous report (*53*). We determined the spatial origin of this signal by Fourier-filtering $dI(\mathbf{r},V)/dV$ at the wave vector $2\mathbf{k}^{ss}$ to create an image of the local backscattering strength (Fig. 4C). Most of the peaks in this image align with the positions of Sm vacancies or Fe dopants, indicating that these Kondo holes harbor the necessary magnetic fluctuations to backscatter topological states.

Discussion and outlook

The charge puddles around Kondo holes present an alternative yet compelling origin for many of the strange observations of metallic behavior in SmB_6. First, the detection of de Haas–van Alphen (magnetic) oscillations without accompanying Shubnikov–de Haas (resistivity) oscillations (*8*–*10*) is expected for electrically isolated metallic puddles, provided that they do not meet the percolation threshold [which could be unreachable (*17*)]. Second, the large Fermi surface size and light effective mass extracted by bulk probes (*9*–*11*) is in excellent agreement with our observation of itinerant *5d* electrons. Third, the magnetic length of the high-frequency (large-k_F) quantum oscillations that onset above 35 T (*9*, *10*) is comparable to the $R(\mathbf{r})$ decay length of γ = 2.6 nm, such that a Landau orbit could fit inside a metallic puddle. Additionally, many of the metallic properties were detected in floating zone–grown samples (*5*, *6*, *9*–*11*), which are known to have higher concentrations of Sm vacancies than samples grown with an aluminum flux (*60*). Floating-zone samples also contain a higher concentration of dislocations (*31*), which may similarly disrupt the Kondo screening cloud and thus further enhance the quantum oscillation amplitude beyond that expected from Sm vacancies alone. In contrast, the quantum oscillations completely disappear in flux-grown samples once embedded aluminum is removed (*8*).

Atomic-scale charge inhomogeneity has a profound impact on many interacting quantum materials, but it has typically not been possible to measure. In Kondo-lattice systems, $R(\mathbf{r},V)$ provides a peek at the ground-state charge landscape, which is strongly perturbed by Kondo holes. These Kondo holes nucleate nanometer-scale metallic puddles that could explain many of the strange phenomena detected by bulk probes. More broadly, the sensitivity to local charge within a Kondo lattice may enable atomic-scale charge imaging using STM tips decorated with a Kondo impurity (*61*) or fabricated from heavy-fermion materials (*62*).

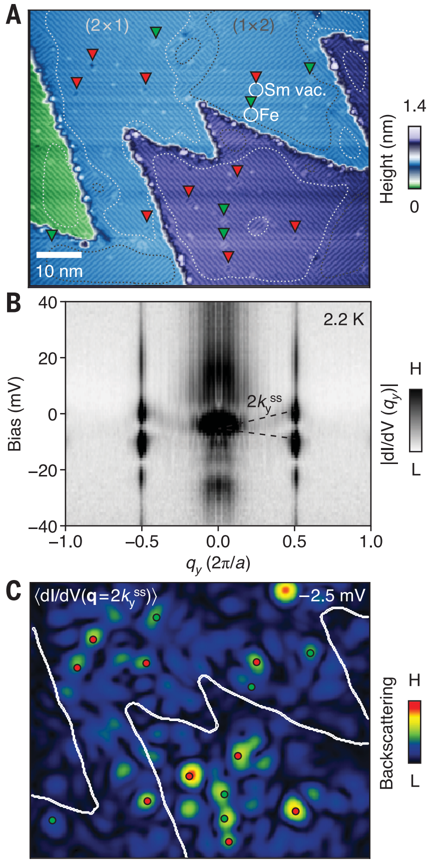


Fig. 4. Kondo holes backscatter heavy Dirac fermions. (**A**) Topography of an SmB_6 region that contains 15 well-isolated Kondo holes (position indicated by red and green triangles) on several (2×1)- or (1×2)-reconstructed domains (dotted lines). (**B**) For energies within the Kondo insulating gap, the Fourier-transformed dI/dV along q_y (perpendicular to Sm rows) contains a linearly dispersing signal (black dashed line) corresponding to quasiparticle interference from backscattered heavy Dirac fermions. The Fourier transform from the (1×2) domains was rotated by 90° before being averaged with that from the (2×1) domains. (**C**) The intensity of backscattering from topological states, calculated from Fourier-filtering dI/dV at the y component of the backscattering wave vector $q_y = 2k_y^{ss}$, is strongly peaked around each Kondo hole. This map is computed only for ordered patches of the sample, as marked in (A), and excludes step edges. H, high; L, low.

REFERENCES AND NOTES

1. S. Doniach, *Physica B+C* **91**, 231–234 (1977).
2. F. Steglich *et al*., *Phys. Rev. Lett.* **43**, 1892–1896 (1979).
3. K. Andres, J. E. Graebner, H. R. Ott, *Phys. Rev. Lett.* **35**, 1779–1782 (1975).
4. Z. Fisk, H. R. Ott, T. M. Rice, J. L. Smith, *Nature* **320**, 124–129 (1986).
5. N. J. Laurita *et al*., *Phys. Rev. B* **94**, 165154 (2016).
6. K. Flachbart *et al*., *Physica B* **378–380**, 610–611 (2006).
7. W. T. Fuhrman *et al*., *Nat. Commun.* **9**, 1539 (2018).
8. S. M. Thomas *et al*., *Phys. Rev. Lett.* **122**, 166401 (2019).
9. M. Hartstein *et al*., *Nat. Phys.* **14**, 166–172 (2018).
10. B. S. Tan *et al*., *Science* **349**, 287–290 (2015).
11. T. E. Millichamp *et al*., arXiv:2111.07727 [cond-mat.str-el] (2021).
12. Y. S. Eo *et al*., *Proc. Natl. Acad. Sci. U.S.A.* **116**, 12638–12641 (2019).
13. J. Knolle, N. R. Cooper, *Phys. Rev. Lett.* **115**, 146401 (2015).
14. G. Baskaran, arXiv:1507.03477 [cond-mat.str-el] (2015).
15. O. Erten, P.-Y. Chang, P. Coleman, A. M. Tsvelik, *Phys. Rev. Lett.* **119**, 057603 (2017).
16. H. Shen, L. Fu, *Phys. Rev. Lett.* **121**, 026403 (2018).
17. B. Skinner, *Phys. Rev. Mater.* **3**, 104601 (2019).
18. W. T. Fuhrman, P. Nikolić, *Phys. Rev. B* **101**, 245118 (2020).
19. M. Abele, X. Yuan, P. S. Riseborough, *Phys. Rev. B* **101**, 094101 (2020).
20. E. Dagotto, *Science* **309**, 257–262 (2005).
21. R. Sollie, P. Schlottmann, *J. Appl. Phys.* **70**, 5803–5805 (1991).
22. J. Figgins, D. K. Morr, *Phys. Rev. Lett.* **107**, 066401 (2011).
23. J. Figgins *et al*., *Nat. Commun.* **10**, 5588 (2019).
24. M. H. Hamidian *et al*., *Proc. Natl. Acad. Sci. U.S.A.* **108**, 18233–18237 (2011).
25. R. R. Urbano *et al*., *Phys. Rev. Lett.* **99**, 146402 (2007).
26. E. V. Nefedova *et al*., *J. Exp. Theor. Phys.* **88**, 565–573 (1999).
27. S. Gabáni *et al*., *Czech. J. Phys.* **52** (suppl. 1), A225–A228 (2002).
28. M. Orendáč *et al*., *Phys. Rev. B* **96**, 115101 (2017).
29. J. C. Souza *et al*., *Phys. Rev. Res.* **2**, 043181 (2020).
30. M. E. Valentine *et al*., *Phys. Rev. B* **94**, 075102 (2016).

31. Y. S. Eo *et al*., *Phys. Rev. Mater.* **5**, 055001 (2021).
32. B. Koslowski, C. Baur, *J. Appl. Phys.* **77**, 28–33 (1995).
33. C. Wagner *et al*., *Phys. Rev. Lett.* **115**, 026101 (2015).
34. P. Hapala *et al*., *Nat. Commun.* **7**, 11560 (2016).
35. M. Nonnenmacher, M. P. O'Boyle, H. K. Wickramasinghe, *Appl. Phys. Lett.* **58**, 2921–2923 (1991).
36. L. Gross, F. Mohn, N. Moll, P. Liljeroth, G. Meyer, *Science* **325**, 1110–1114 (2009).
37. F. Mohn, L. Gross, N. Moll, G. Meyer, *Nat. Nanotechnol.* **7**, 227–231 (2012).
38. U. Zerweck, C. Loppacher, T. Otto, S. Grafström, L. M. Eng, *Phys. Rev. B* **71**, 125424 (2005).
39. S. Sadewasser *et al*., *Phys. Rev. Lett.* **103**, 266103 (2009).
40. F. Albrecht *et al*., *Phys. Rev. Lett.* **115**, 076101 (2015).
41. F. Albrecht, M. Fleischmann, M. Scheer, L. Gross, J. Repp, *Phys. Rev. B* **92**, 235443 (2015).
42. E. Kotta *et al*., Research Square [Preprint] (2022). https://www.researchsquare.com/article/rs-1239795/v1.
43. V. Madhavan, W. Chen, T. Jamneala, M. F. Crommie, N. S. Wingreen, *Science* **280**, 567–569 (1998).
44. M. Maltseva, M. Dzero, P. Coleman, *Phys. Rev. Lett.* **103**, 206402 (2009).
45. J. Figgins, D. K. Morr, *Phys. Rev. Lett.* **104**, 187202 (2010).
46. A. R. Schmidt *et al*., *Nature* **465**, 570–576 (2010).
47. I. Giannakis *et al*., *Sci. Adv.* **5**, eaaw9061 (2019).
48. Y. Kohsaka *et al*., *Science* **315**, 1380–1385 (2007).
49. A. de la Torre, P. Visani, Y. Dalichaouch, B. Lee, M. Maple, *Physica B* **179**, 208–214 (1992).
50. A. F. Santander-Syro *et al*., *Nat. Phys.* **5**, 637–641 (2009).
51. C. E. Matt *et al*., *Phys. Rev. B* **101**, 085142 (2020).
52. Z. Sun *et al*., *Phys. Rev. B* **97**, 235107 (2018).
53. H. Pirie *et al*., *Nat. Phys.* **16**, 52–56 (2020).
54. J. Jiang *et al*., *Nat. Commun.* **4**, 3010 (2013).
55. L. Jiao *et al*., *Sci. Adv.* **4**, eaau4886 (2018).
56. K. Akintola *et al*., *Phys. Rev. B* **95**, 245107 (2017).
57. Q. Liu, C.-X. Liu, C. Xu, X.-L. Qi, S.-C. Zhang, *Phys. Rev. Lett.* **102**, 156603 (2009).
58. Y. Okada *et al*., *Phys. Rev. Lett.* **106**, 206805 (2011).
59. B. Jäck, Y. Xie, B. Andrei Bernevig, A. Yazdani, *Proc. Natl. Acad. Sci. U.S.A.* **117**, 16214–16218 (2020).
60. W. A. Phelan *et al*., *Sci. Rep.* **6**, 20860 (2016).
61. J. Bork *et al*., *Nat. Phys.* **7**, 901–906 (2011).
62. A. Aishwarya *et al*., *Science* **377**, 1218–1222 (2022).
63. H. Pirie *et al*., Dataset for visualizing the atomic-scale origin of metallic behavior in Kondo insulators, Zenodo (2023); https://doi.org/10.5281/zenodo.7510910.

ACKNOWLEDGMENTS

We thank A.-P. Li, B. Skinner, C. Wagner, F. Lüpke, S. Ulrich, Y. S. Eo, and Z. Fisk for helpful conversations. We thank A. Soumyanarayanan, M. Yee, and Y. He for their help measuring Gd-doped SmB_6. **Funding:** This project was supported by the Gordon and Betty Moore Foundation's EPiQS Initiative through grants GBMF4536, GBMF9071, and GBMF9457. The experiments at Harvard were supported by US National Science Foundation grant DMR-1410480. The data interpretation received support from AFOSR grant FA9550-21-1-0429. The work of E.M. and D.K.M. was supported by the US Department of Energy, Office of Science, Basic Energy Sciences, under award DE-FG02-05ER46225. C.E.M. is supported by the Swiss National Science Foundation under fellowship P400P2_183890. Work at the University of Maryland was supported by AFOSR FA9550-22-1-0023. Research at McMaster University was supported by the Natural Sciences and Engineering Research Council. J.C.S.D. acknowledges support from the Science Foundation of Ireland under award SFI 17/RP/5445, from the Royal Society under award R64897, and from the European Research Council under award DLV-788932. This project received funding from the European Union's Horizon 2020 research and innovation program under the Marie Skłodowska-Curie grant agreement 893097. **Author contributions:** H.P., C.E.M., Y.L., P.C., and M.H.H. carried out the STM experiments. S.S., X.W., J.P., and G.L. synthesized the samples. E.M. and D.K.M. developed the theoretical model. D.G.-G., C.F.H., and J.C.S.D. contributed to the understanding of the results. H.P. and J.E.H. analyzed the data and wrote the manuscript with contributions from E.M., C.F.H., J.C.S.D., and D.K.M. **Competing interests:** The authors have no competing interests. **Data and materials availability:** All data and analysis presented in this paper are deposited in Zenodo (*63*).

License information: Copyright © 2023 the authors, some rights reserved; exclusive licensee American Association for the Advancement of Science. No claim to original US government works. https://www.science.org/about/science-licenses-journal-article-reuse

SUPPLEMENTARY MATERIALS

science.org/doi/10.1126/science.abq5375
Materials and Methods
Supplementary Text
Figs. S1 to S7
Table S1
References (*64*–*69*)

Submitted 18 April 2022; accepted 28 February 2023
10.1126/science.abq5375

FERROELECTRICS

Ferroelectricity in layered bismuth oxide down to 1 nanometer

Qianqian Yang[1]†, Jingcong Hu[2]†, Yue-Wen Fang[3,4]†, Yueyang Jia[5], Rui Yang[5], Shiqing Deng[1], Yue Lu[2]*, Oswaldo Dieguez[6], Longlong Fan[7], Dongxing Zheng[8], Xixiang Zhang[8], Yongqi Dong[9], Zhenlin Luo[9], Zhen Wang[7], Huanhua Wang[7], Manling Sui[2], Xianran Xing[10], Jun Chen[11], Jianjun Tian[1]*, Linxing Zhang[1]*

Atomic-scale ferroelectrics are of great interest for high-density electronics, particularly field-effect transistors, low-power logic, and nonvolatile memories. We devised a film with a layered structure of bismuth oxide that can stabilize the ferroelectric state down to 1 nanometer through samarium bondage. This film can be grown on a variety of substrates with a cost-effective chemical solution deposition. We observed a standard ferroelectric hysteresis loop down to a thickness of ~1 nanometer. The thin films with thicknesses that range from 1 to 4.56 nanometers possess a relatively large remanent polarization from 17 to 50 microcoulombs per square centimeter. We verified the structure with first-principles calculations, which also pointed to the material being a lone pair–driven ferroelectric material. The structure design of the ultrathin ferroelectric films has great potential for the manufacturing of atomic-scale electronic devices.

Ultrathin ferroelectric film is a core material for the preparation of miniature and large-capacity nonvolatile memories (*1*, *2*). The urgent demand for ultrascaled devices has prompted the gradual exploration of atomic-scale ferroelectric thin films (*3*). In recent decades, it has been demonstrated that some traditional perovskite oxide systems (*4*–*8*), doped HfO_x ferroelectric systems (*9*, *10*), and two-dimensional layered ferroelectric systems [$CuInP_2S_6$ (*11*), α-In_2Se_3 (*12*, *13*), and so on] can keep their macroscopic ferroelectric properties while gradually approaching subnanometer size, but this is still far from atomic scale. The primary problem that hinders the continued research of nanoscale ferroelectric thin films is the critical size effect, whereby the huge depolarization field caused by the thickness reduction shields the ferroelectric effect, leading to the instability of the ferroelectric phase (*1*). For example, as the thickness decreases to tens of nanometers or a few nanometers, ferroelectric thin films of classical perovskites with ABO_3 structure [where *A* is a rare-earth or alkaline-earth metal and *B* is a transition metal; e.g., $BaTiO_3$ (*7*, *8*)] will change from the ferroelectric phase to the paraelectric phase and lose their ferroelectricity. However, recent studies suggest that the size effect can be suppressed in some materials. Many films with thicknesses of a nanometer or several unit cells have been reported to still be ferroelectric, such as three–unit cell freestanding $BiFeO_3$ films with giant polarization due to the release of the tensile strain given by the substrate (*14*), 1-nm-thick $Hf_{0.8}Zr_{0.2}O_2$ films with enhanced ferroelectricity due to imposed confinement strain (*9*), half–unit cell (~3 Å) hafnium oxide with localized dipoles induced by flat phonon bands (*15*), and subnanometer ZrO_2 films with emergent ferroelectricity obtained by reducing the dimension on silicon (*16*). However, the ferroelectric properties of the ultrathin films reported in these works have only been confirmed through cross-sectional high-angle annular dark-field scanning transmission electron microscopy (HAADF-STEM) images, piezoresponse force microscopy (PFM), theoretical calculations, or tunnel electroresistance hysteresis, rather than by using macroscopic ferroelectric hysteresis loops with polarization-electric field measurements, which can identify the ferroelectricity directly and is the prime determinant of the applications of ferroelectrics in electronic devices.

Layered bismuth oxides are one kind of classical ferroelectric materials that have a high Curie temperature (T_c) and great fatigue resistance (*17*, *18*). These systems of Bi_2WO_6 (*19*), $SrBi_2Ta_2O_9$ (*17*), $Bi_4Ti_3O_{12}$ (*4*), and so on, which have a distinctive Aurivillius structure, are the famous layered bismuth oxide ferroelectrics (*20*, *21*), which are composed of an intergrowth of $(Bi_2O_2)^{2+}$ sheets and *n* perovskite-like blocks that contain a layer of octahedral *B* sites. Several new Bi-based oxide ferroelectric films with a layered supercell structure have been reported recently, such as Bi_2AlMnO_6 (*22*) and Bi_2NiMnO_6 (*23*), which have a high degree of flexibility in their structure with the controlled bismuth layers. Some of them show great multiferroic properties. However, most of the above layered films exhibit in-plane ferroelectric properties, which limits their application in devices (*24*). The growth rate of the layered-structure film in the horizontal direction is higher than that in the vertical direction, which is conducive to the preparation of smooth and continuous atomic-level films (*25*, *26*). The excellent insulating property and high tolerance to the vacancy of layered bismuth oxide are also beneficial to the ferroelectric measurement of monolayer unit cells with low leakage (*27*). We have developed a type of layered bismuth oxide through Sm substitution [$Bi_{1.8}Sm_{0.2}O_3$ (BSO)]. We grew this thin film as a single phase on a (0001) Al_2O_3 (AO) or (001) $SrTiO_3$ (STO) substrate by the sol-gel method. At a thickness of 1 nm, the film can maintain extremely strong out-of-plane ferroelectricity and demonstrate the macroscopic ferroelectric hysteresis loop that other systems cannot achieve at such thicknesses. This work develops a new generation of ferroelectric films that are highly promising for creating miniaturized and high-quality electronic devices.

The design of the layered structure

The bismuth-based fluorite structure is a kind of classical material with a variable and flexible structure (*28*, *29*). We designed a structure based on the fluorite structure by removing a whole layer of bismuth, leading to a layered structure with a framework of bismuth oxide. Density functional theory (DFT) calculations (fig. S1) demonstrate that these layered structures with variable periods of different bismuth layers possess relatively high stability because of low formation energies of −1.086, −1.135, and −1.095 eV per atom for variable periods of three, five, and seven bismuth layers, respectively. We focused on the period of three bismuth layers, which can be stabilized in the film with a tetragonal-like (T-like) structure under the action of Sm substitution (Fig. 1A). If the oxygen is not removed in the fluorite structure that has one of four Bi layers missing, then the molecular formula is Bi_6O_{16}, which is not stable. Hence, we performed genetic-algorithm searches of the arrangements that lead to the lowest possible energy of each

[1]Beijing Advanced Innovation Center for Materials Genome Engineering, Institute for Advanced Materials and Technology, University of Science and Technology Beijing, Beijing 100083, China. [2]Beijing Key Laboratory of Microstructure and Properties of Solids, Faculty of Materials and Manufacturing, Beijing University of Technology, Beijing 100124, China. [3]Centro de Física de Materiales (CSIC-UPV/EHU), Manuel de Lardizabal Pasealekua 5, 20018 Donostia/San Sebastián, Spain. [4]Fisika Aplikatua Saila, Gipuzkoako Ingeniaritza Eskola, University of the Basque Country (UPV/EHU), Europa Plaza 1, 20018 Donostia/San Sebastián, Spain. [5]University of Michigan–Shanghai Jiao Tong University Joint Institute, Shanghai Jiao Tong University, Shanghai, China. [6]Department of Materials Science and Engineering, The Iby and Aladar Fleischman Faculty of Engineering, The Raymond and Beverly Sackler Center for Computational Molecular and Materials Science, Tel Aviv University, Tel Aviv, Israel. [7]Institute of High Energy Physics, University of Chinese Academy of Sciences, Chinese Academy of Sciences, Beijing 100049, China. [8]Physical Science and Engineering Division, King Abdullah University of Science and Technology (KAUST), Thuwal 23955-6900, Saudi Arabia. [9]National Synchrotron Radiation Laboratory, University of Science and Technology of China, Hefei 230026, China. [10]Institute of Solid State Chemistry, University of Science and Technology Beijing, Beijing 100083, China. [11]Department of Physical Chemistry, University of Science and Technology Beijing, Beijing 100083, China.
***Corresponding author. Email: linxingzhang@ustb.edu.cn (L.Z.); tianjianjun@mater.ustb.edu.cn (J.T.); luyue@bjut.edu.cn (Y.L.)**
†These authors contributed equally to this work.

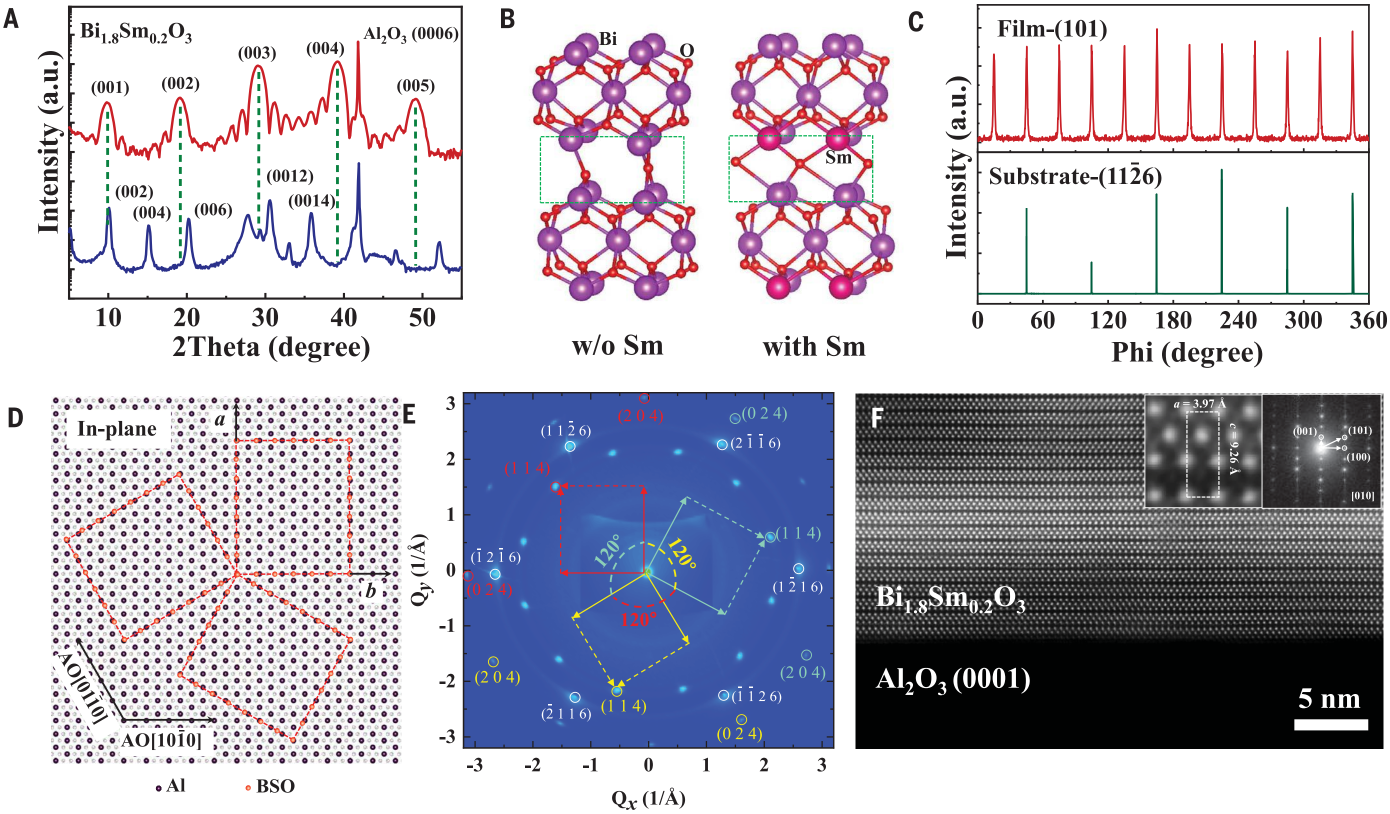


Fig. 1. Crystal structure characterization of layered bismuth oxide thin films grown on (0001) Al_2O_3 substrates. (**A**) Out-of-plane XRD diffraction of bismuth oxide films with (red) and without (blue) Sm substitution under the same conditions. The dashed green lines are used to guide the eye. a.u., arbitrary units. (**B**) The final structures of Bi_6O_9 and Bi_5SmO_9 that were simulated in ab initio molecular dynamics simulations at 300 K. The green dashed rectangles are used to guide the eyes. (**C**) XRD phi scanning reflections of (101) BSO film plane and (11$\bar{2}$6) Al_2O_3 substrate plane. (**D**) The matching diagram of the BSO film and the substrate. The red wire frames are six (or three) BSO unit cells by seven BSO unit cells. (**E**) The diffractive RSM images of film and substrate in the (Q_x, Q_y) plane at Q_z = 2.72 Å^{-1}, where the substrate diffraction peak is marked in white and the thin film diffraction peak is marked in red, blue, and yellow. The three different colors correspond to the three domain variants that have varied orientations and show a rotational symmetry relationship of 120° between each other. (**F**) HAADF-STEM image of the heteroepitaxial BSO/AO, as viewed along the *b* axis of the thin film. The inset images are a magnified region of the film (left) and the FFT of the film region (right). The white dashed rectangle indicates a unit cell of BSO.

set of atoms in these cells of Bi_6O_n (n = 6 to 12) with different oxygen loss (fig. S2). A comparison of the formation energies of the 69 known bismuth oxide compounds in the Open Quantum Materials Database showed that Bi_6O_9 is strongly favored over the others and also possesses a wide bandgap and is the most stable structure. Indeed, the preparation of the film requires the addition of Sm element to stabilize the structure. We used energy dispersive spectrometer (EDS) to analyze the composition of the film and (001) STO substrate separately, and the chemical composition ratio we obtained was Bi:Sm:O = 1.8:0.2:3 (figs. S3 and S4). In addition, the valence analysis using x-ray photoelectron spectroscopy (XPS) confirmed the results of EDS, which was similar to the atomic ratio of the precursor (fig. S5 and table S1).

General structures

We grew BSO films on an inexpensive single crystal (0001) AO substrate using the chemical solution method of sol-gel spin coating (*30*). The x-ray diffraction (XRD) patterns showed only diffraction peaks from the directions of (0006) AO substrate and (001) films of BSO with an out-of-plane lattice parameter of about 9.137 Å (Fig. 1A). This observation suggests that the films are epitaxially grown, which is also confirmed by the phi scans and reciprocal space mappings (RSMs) discussed below. To further confirm that the presence of Sm can stabilize the formation of this phase, we investigated varying the content of Sm from 5 to 15% (fig. S6). The film without the Sm substitution consists of a main phase of Bi_6O_7 and some Bi_2O_3 phases, which highlights the importance of Sm in stabilizing the ferroelectric structure. Ab initio molecular dynamics simulation results show that Sm has a stronger oxygen binding ability than Bi (Fig. 1B and fig. S7). When the thickness is reduced down to one unit cell, the ferroelectric phase can be maintained by the addition of Sm (fig. S8). Moreover, the introduction of Sm reduces the structure formation energy by 0.41 eV per atom. We used XRD phi scanning, wide-range RSM, and fast Fourier transform (FFT) to reveal the in-plane lattice matching relationship between BSO films and hexagonal AO substrates. The XRD phi scans are collected along the reflection of the (101) BSO film and the (11$\bar{2}$6) substrate (Fig. 1C). The phi scan of the (101) planes of the film show 12 diffraction peaks, of which six diffraction peaks correspond to the (11$\bar{2}$6) diffraction peaks of the hexagonal AO substrate. This features a four-axis symmetric structure of films with three different orientations on the six-axis symmetric substrate, which confirms an in-plane epitaxial relationship with the substrate (Fig. 1D). We provide wide-range RSMs of the sample in the (Q_x, Q_y) and (Q_x, Q_z) planes (Fig. 1E and fig. S9). The epitaxial relationship between thin film and substrate shown by RSMs is consistent with phi scanning results. RSMs about the (105) plane

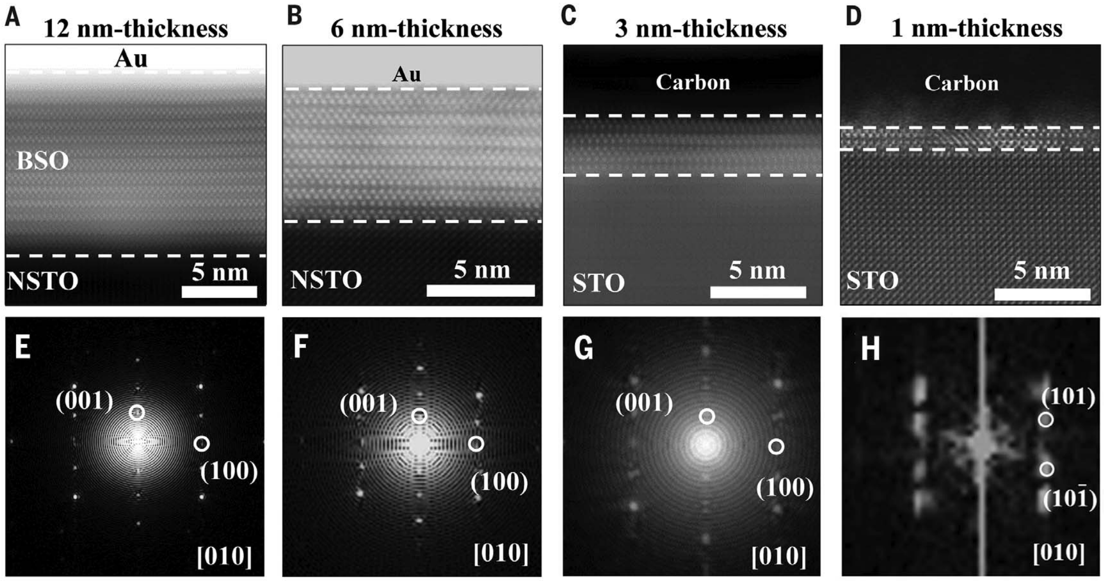


Fig. 2. Characterization of ultrathin BSO films. (**A** to **D**) The HAADF-STEM images of the BSO films grown on the STO-based [STO or Nb:STO (NSTO)] substrate have thicknesses of 12 nm (A), 6 nm (B), 3 nm (C), and 1 nm (D). The white dashed lines indicate the up or down interface of the films. (**E** to **H**) The FFT patterns corresponding to the films shown in (A) to (D), respectively.

of the film have been carried out (fig. S9C), which indicate a T-like phase structure with an in-plane lattice parameter of 3.94 Å and an out-of-plane lattice parameter of 9.24 Å.

The direct evidence for the layered structure in the film presented in this work is provided by the spherical aberration-corrected HAADF-STEM images (Fig. 1F and fig. S10A). We observed flat and high-quality films. The bright spots correspond to Bi ($Z = 83$, where Z is the atomic number)/Sm ($Z = 62$) columns, owing to the Z^2-dependent image contrast (*31*). Because Sm is randomly distributed in the position of Bi, it is difficult to distinguish the exact occupation sites of the Sm (figs. S11 to S14). The film is arranged in a regular layered arrangement with a period of three BiO layers, which is similar to the fluorite structure along the *c*-axis direction. A large spacing appears between each of the two groups of three BiO layers, indicating a different layered structure of bismuth oxide than has been previously observed. The out-of-plane and in-plane lattice parameters are 9.26 and 3.97 Å, respectively, which correspond to the results of XRD and RSMs. The corresponding FFT pattern (inset of Fig. 1F) was identified as the [010] zone axis, which is consistent with the simulated BSO electron diffraction pattern (fig. S10B). This confirms that the film has a T-like phase structure, which is the same as the RSMs scan result. The continuity and periodicity of the phase along the *a* and *c* axes can be clearly seen in the FFT. In addition, we analyzed the epitaxial relationship between the BSO film and the AO substrate by adjusting the focus and contrast (figs. S15 and S16).

Interestingly, the growth of this layered BSO film is extremely flexible and has little dependence on the types of substrates. Under the same conditions, the high-quality BSO film can also be successfully obtained on other lattice-mismatched substrates with different crystal structures, such as (001) STO and Au/SiO_2/Si substrates (figs. S17 and S18). We confirmed the epitaxial orientation matching relationship of BSO/AO and BSO/STO along [001]/[0001] and [001]/[001], respectively (figs. S19 and S20). We obtained the full width at half maximum (FWHM) of ω-scanning for the film and the substrate at a specific crystal plane to prove crystallinity (fig. S21). The FWHM of the (004) BSO film and (0006) AO substrate are about 0.0122° and 0.0123°, respectively. The FWHM of the (004) film grown on the STO substrate and (002) STO substrate are about 0.0291° and 0.0303°, respectively. The FWHM of the films grown on these two substrates are almost the same as those of their respective substrates, suggesting that BSO films grown by the chemical solution method generally have a high crystalline quality, whether they are grown on a single-crystal (0001) AO substrate or (001) STO substrate. This would be ascribed to the design idea of layered structure based on the spontaneous arrangement in the in-plane direction of the crystal atoms.

STEM analysis for ultrathin BSO film

We demonstrated that the film still has a high crystalline quality and high flatness in the ultrathin state. We prepared a batch of single-phase BSO films with thicknesses of 12, 6, 3, and 1 nm on the STO-based substrates. The thickness of the sample can be controlled by the concentration of the precursor by a linear relationship (figs. S22 and S23). The HAADF-STEM images and corresponding FFT patterns are shown in Fig. 2. First, we directly observed that all BSO films have high flatness without showing the characteristics of "ripples," and the BSO films are continuously arranged in Bi atomic layers (Fig. 2, A to D, and fig. S24). Notably, the structure of the BSO film does not collapse when approaching a thickness of one unit cell (1-nm thickness); instead, it remains layered, and the chemical ratio is still maintained (Fig. 2, E to H, and figs. S25 and S26).

Second, the FFT patterns of all BSO films show bright and regularly arranged diffraction spots (the positions of diffraction spots are the same as those in Fig. 1F), which show that they all grow in the form of single crystals. X-ray reflectivity (XRR) and XRD fitting results also confirmed the high crystal quality and smooth interface of BSO films (fig. S23 and table S2). As the thickness of the film decreases, the diffraction peaks move to low angles, indicating the gradually increasing lattice parameter *c*, an observation that is similar to the results of TEM (fig. S23 and table S3). We could attribute this observation to the compressive strain caused by the surface effect that is acting on the film (*32*). In addition, we also found a strain concentration region at the Bi layer at the BSO/AO (STO) interface, whereas the strain of other Bi layers that extend toward the *c* axis is much weaker than that at the interface (fig. S27). The successful preparation of high-quality BSO films with a thickness of 1 nm is very likely due to the fact that the two Bi layers at the interface bear most of the strain from the substrate to maintain the normal growth of the films, which also lays a foundation for the measurement of the macroscopic ultrathin ferroelectric properties.

Ferroelectric hysteresis loop

Ferroelectric hysteresis loops of ultrathin films are extremely difficult to measure. Influenced

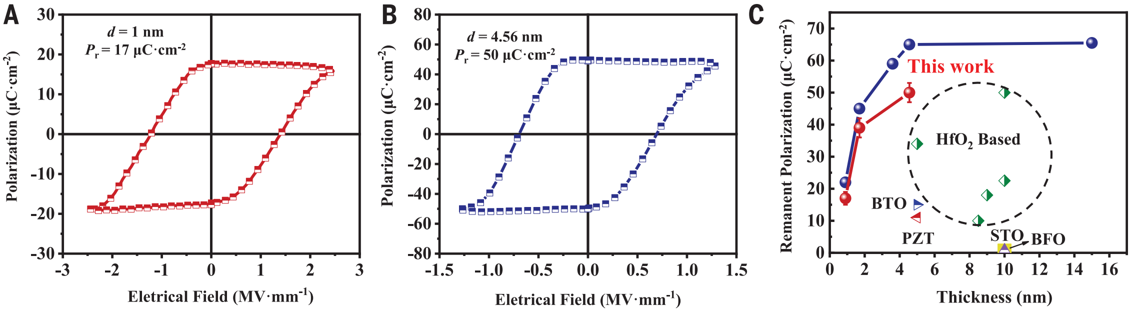


Fig. 3. Characterization of macro ferroelectricity. (**A** and **B**) The polarization hysteresis loops of the films with thicknesses of 1 nm (A) and 4.56 nm (B) obtained by the PUND mode measurement under an electric field with a frequency of 1 kHz. *d*, film thickness; P_r, remanent polarization. (**C**) The relationship between the thickness of the BSO film and the remanent polarization and a comparison with other ferroelectric systems (such as traditional perovskite systems and doped hafnium oxide systems). The blue and red spheres in the plot represent the dynamic hysteresis mode conventional measurements and PUND measurements of this work, respectively. In PUND mode, the contribution of nonferroelectric switching can be subtracted to obtain the true ferroelectric polarization (figs. S28 and S29). The green diamonds within the dashed circle indicate the HfO_2-based sample data points. The blue triangle, red triangle, purple triangle, and yellow square indicate the BTO, PZT, STO, and BFO sample points, respectively. The error bars denote standard deviations.

by size effect and film quality, the suppression of surface charges and the existence of leakage current cause the film to lose its original ferroelectricity. We obtained a high-quality ferroelectric hysteresis loop in the BSO film with a single–unit cell thickness of ~1 nm, which had a remanent polarization as large as 17 μC cm^{-2} (Fig. 3A and fig. S30A). Making this sort of observation in a traditional perovskite system, a doped hafnium oxide system, or a two-dimensional ferroelectric system has been challenging with ultrathin films of thicknesses down to 1 nm. The ferroelectricity of the $BiFeO_3$ freestanding film with a thickness of three unit cells (*14*), $Hf_{0.5}Zr_{0.5}O_2$ with a thickness of 1 nm (*9*), and $CuInP_2S_6$ film with a thickness of 4 nm (*11*) are all indirectly characterized by domain switching that is observed by applying a bias voltage. The macroscopic ferroelectric hysteresis loop is direct evidence to confirm whether the single–unit cell–thick film has ferroelectricity, which suggests that BSO ferroelectric thin films have great potential for applications in nanoelectronic devices. The remanent polarization of the BSO film at 1 nm is relatively higher than that of other ultrathin ferroelectric films that have been reported, such as $BaTiO_3$ (BTO, 5 nm, 15 μC cm^{-2}) (*8*), $BiFeO_3$ (BFO, 10 nm, 1 μC cm^{-2}) (*33*), $PbZr_{0.2}Ti_{0.8}O_3$ (PZT, 5 nm, 11 μC cm^{-2}) (*34*), and STO (10 nm, 1 μC cm^{-2}) (*35*).The remanent polarization of the BSO film with a thickness of 4.56 nm increases to 50 μC cm^{-2} (Fig. 3B and fig. S30B), which is the highest value among ultrathin ferroelectric films of thicknesses less than 5 nm, as compared with the hafnium oxide–based ferroelectric films that have been reported (5 nm, 34 μC cm^{-2}) (*10*, *36*–*38*) (Fig. 3C). By using the semiempirical method (*39*), as a displacement-type ferroelectric, we calculated the polarization by the displacement. The atomic displacement of Bi is about 0.22 Å as determined through STEM image analysis (fig. S32), which is close to the theoretical prediction of 0.20 Å. We calculated the spontaneous polarization of the film to be about 49.8 to 53.4 μC cm^{-2}. We obtained more hysteresis loops for the devices, indicating the ferroelectric repeatability of the films (fig. S30). In addition, by adjusting the parameters in positive-up-negative-down (PUND) mode, we obtained hysteresis loops under different conditions to obtain more ferroelectric information (fig. S31).

As with traditional perovskite systems, the ferroelectricity of the BSO film is also affected by the thickness. The remanent polarization decreases with reduced thickness (Fig. 3C). The size effect is probably due to the existence of a certain "dead layer" in the film (*40*, *41*). The "dead layer" usually has a low dielectric constant, which results in a decrease in the actual voltage that is assigned to the thinner film and a smaller remanent polarization. Nevertheless, the polarization value obtained for the films presented in this work is much higher than the conventional value. There are some reasons for the high polarization of these films at 1-nm thickness. First, Sm can preserve the original structure of the ferroelectric phase at a thickness of 1 nm (fig. S7). The layered structure and the high tolerance to vacancy are also beneficial to maintaining ferroelectric structural stability at low dimensions. The stability of the ferroelectric phase will overcome the structural instability caused by the increase in surface energy and defects due to the size reduction. At the same time, the ferroelectric phase stability can also overcome the increase in depolarization field to maintain high polarization. Second, the polarization can enhance with increasing axial ratio when the thickness decreases. The displacement polarization also can increase from surface to interface. These results should be ascribed to strain effects and charge transfer (*42*) (fig. S33), which will overcome the polarization attenuation caused by size effect.

The excellent fatigue and retention characteristics of atomic-scale BSO films and the virtually nonimprinting phenomenon at high temperatures confirm the great potential of BSO films for a wide range of device applications (fig. S34). T_c is an important parameter for ferroelectric materials. We have tried to explore the potential phase transition of this newly characterized ferroelectric compound through theoretical calculation and temperature-dependent XRD, dielectric, and ferroelectric tests, which indicate that the T_c of ultrathin BSO films should be 493 K (fig. S35).

PFM characterization

We carried out PFM measurements to investigate the ferroelectric switching properties of the films presented in this work. The PFM phase images after a box-in-box writing with a tip bias of positive and negative voltage demonstrate well-defined regions of phase contrast, which corresponds to remanent polarization states, for BSO films with thicknesses of 1, 2.1, and 3.4 nm (Fig. 4, A to C). This indicates that the polarization states can be rewritten, highlighting switchable polarization for the ultrathin films especially down to one unit cell; this finding was also confirmed by the amplitude images (fig. S36). Notably, unpoled areas at the edge show the similar phase contrast as positively poled areas, demonstrating that original BSO films exhibit spontaneous polarizations. In the respective square area, we selected multiple straight lines across the area where all voltages are applied to observe the phase lag of the overall area (fig. S37). The results show that the phase lags of the films with thicknesses of 1, 2.1, and 3.4 nm are 70° to 80°, 150° to 160°, and 160° to 180°, respectively (table S4). Then we randomly chose a position and measured the local amplitude and phase hysteresis loop (Fig. 4, E and F, and fig. S38). All the BSO films

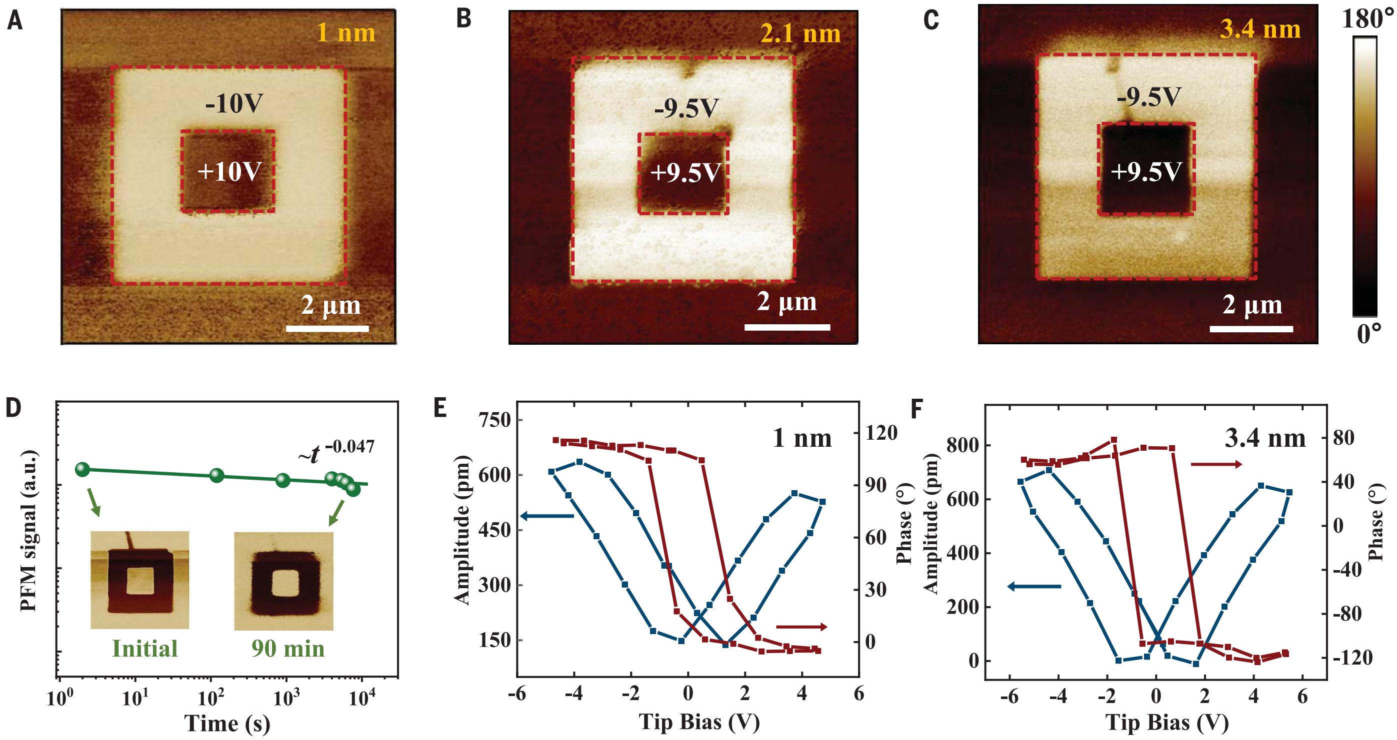


Fig. 4. PFM of BSO thin films. (**A** to **C**) The out-of-plane phase image after box-in-box writing with a tip bias in the BSO thin films with thicknesses of 1 nm (A), 2.1 nm (B), and 3.4 nm (C) by PFM. The entire detection area is 8 μm by 8 μm. The red dashed squares indicate the boundaries of different polarized areas and are used to guide eye. The color scale bar shows the degree of phase. (**D**) PFM signal as a function of delay time measured at room temperature after switching in a 1-nm-thick BSO film. The inset images show the initial phase image and one obtained 90 min later. (**E** and **F**) Local PFM measurement results for films with thicknesses of 1 nm (E) and 3.4 nm (F), including both the amplitude and phase hysteresis loop. The red lines indicate the local phase, and the blue lines indicate the local amplitude.

with different thicknesses show neat butterfly curves.

Surface topology inspections before and after PFM measurement and analysis of local PFM data after changing ac amplitudes and dc measurement frequency were analyzed to prove the ferroelectric nature of the BSO thin films (figs. S39 to S41). In addition, BSO films with a thickness of 1 nm show excellent retention properties (Fig. 4D and fig. S42). The PFM signal–time diagram predicts that the polarization of the film can be maintained for several days or even longer after fitting. The solid line is the simulation curve of signal decay, which is in line with the power law decay, $P(t) \propto t^{-\alpha}$, where t is decay time and α is the decay exponent. The α of the 1-nm-thick BSO film is 0.047, which is far better than that of the reported conventional 12–unit cell–thick ferroelectric BTO film (α = 0.14) (*35*). The long-term ferroelectric retention indicates that BSO films with a thickness of 1 nm have excellent ferroelectric stability, which is different from that of nonferroelectric films. All piezoelectric responses of the above films prove the ferroelectric switching. The topography obtained by PFM proves that the BSO film prepared by the chemical method has high quality. The BSO film with a thickness of 1 nm grows uniformly, and the root-mean-square roughness is 0.105 nm (fig. S37A and table S4).

Theoretical calculation for the structure and ferroelectricity

To further understand the atomic structure, we performed a high-throughput DFT crystal structure prediction within the structure space of Bi_6O_9 that combined the genetic-algorithm implemented in USPEX (Universal Structure Predictor: Evolutionary Xtallography) with information from the HAADF-STEM structures. In this section, unless otherwise specifically noted, all the structures are constrained to match the in-plane lattice constants of substrates with a T-like lattice constant of 3.97 Å. Figure S43A shows the formation-energy profile of 120 predicted structures with the chemical formula Bi_6O_9. Several low-lying structures are predicted to be noncentrosymmetric (see the crystal structures in fig. S43, B to D). In particular, we found the structure in fig. S43D with space group *Pmm*2 to open a bandgap of around 1.2 eV by hybrid DFT calculations, indicating excellent insulating performance. The specific structural details of *Pmm*2 Bi_6O_9 can be found in table S6, and the detailed densities of states calculated by different exchange functionals with or without inclusion of spin-orbit coupling are available in figs. S44 and S45. For a material to be regarded as a ferroelectric material, it first needs to be an insulator. In addition, it is better to have a continuous and smooth transition between the noncentrosymmetric state and the centrosymmetric phase for the displacive ferroelectrics. By considering the group-subgroup relations (*43*), a phase with the space group of *Pmmm* is found to be the corresponding centrosymmetric structure of the *Pmm*2 Bi_6O_9. The specific structure of *Pmmm* Bi_6O_9 is provided in table S6. Figure 5A displays the free-energy variation of Bi_6O_9 as a function of normalized polar displacements λ between the centrosymmetric and noncentrosymmetric structures, which exhibit a typical double-well energy landscape that is available in ferroelectric materials. The energy per atom monotonically decreases from the centrosymmetric (paraelectric) structure to the noncentrosymmetric (ferroelectric) structure, indicating continuous and spontaneous paraelectric-ferroelectric transitions under the critical temperatures. Notably, the energy difference between the centrosymmetric structure and the noncentrosymmetric structure is about 24 meV per atom [comparable to that of BTO (*44*)], which implies the relatively high stability of the polar phase of Bi_6O_9. Combining the double-well

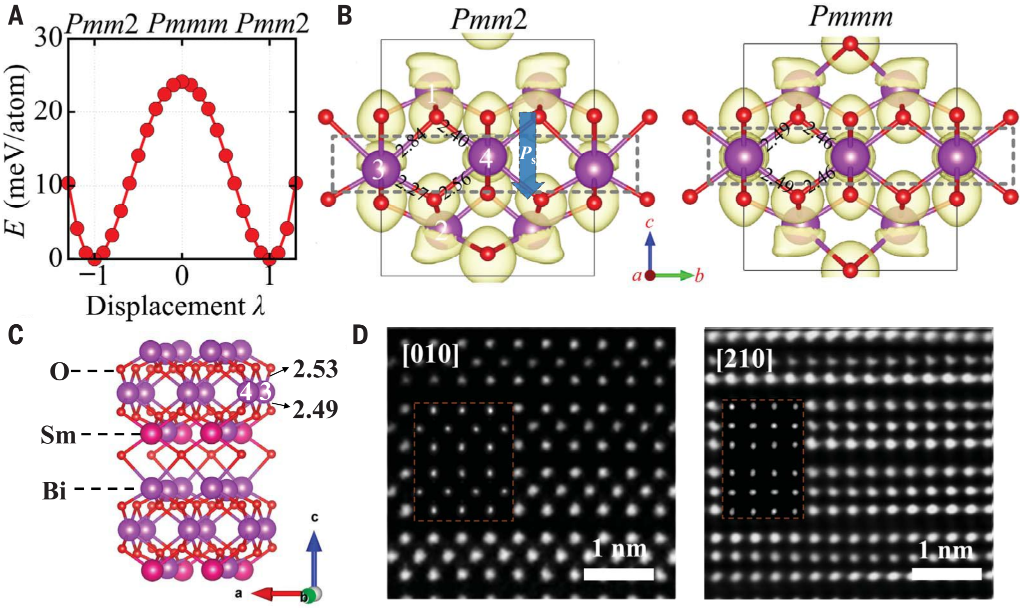


Fig. 5. The BSO structure confirmed by DFT and HAADF-STEM. (**A**) Total energy of Bi_6O_9 as a function of the normalized polar displacements λ of Bi_6O_9 under the epitaxial strain of 3.97 Å. *E*, total energy. (**B**) The ELF of ferroelectric and paraelectric phases of Bi_6O_9. The isovalue is set to 0.53. The marked change in ELF is highlighted by the dashed rectangles. The black numbers label the bond lengths of Bi–O, and the white numbers label the four inequivalent Bi atoms. The blue arrow points in the direction of spontaneous polarization. (**C**) The ferroelectric structure of Sm-substituted Bi_6O_9, as predicted by DFT. (**D**) The HAADF-STEM images of the [010] and [210] directions as a comparison with the simulated HAADF images based on the structure model (brown dashed boxes).

energy landscape with the insulating properties in electronic structure calculations, we have proven that Bi_6O_9 is a new oxide ferroelectric. Therefore, the modern polarization theory based on the Berry phase method can be applied to Bi_6O_9. The spontaneous polarization is calculated to be around 30 μC cm^{-2}, which is consistent with the polarizations measured in our thin film samples (17 to 50 μC cm^{-2}).

In the Bi-based ferroelectric materials, the lone-pair electrons of Bi play a large role in the spatial inversion symmetry breaking by exploiting so-called lone-pair stereochemical activity (*45*). To study the ferroelectric mechanism of Bi_6O_9, the electron localization function (ELF), which is a powerful tool for identifying the role of lone-pair electrons in driving the nonpolar-polar transitions (*46*, *47*), is used to reveal real-space visualization of the lone-pair electrons. The ELFs of *Pmm*2 and *Pmmm* Bi_6O_9 are comparatively shown in Fig. 5B. There are four symmetry-inequivalent positions of Bi atoms in the ferroelectric phase, which are therefore marked as “1” to “4” in Fig. 5B. In the transition from the paraelectric *Pmmm* phase to the ferroelectric *Pmm*2 phase, the ELF of Bi-3 and Bi-4 in the O_8 hexahedron cages transform from the spherically symmetric distribution to the lobe-like asymmetric distribution, which implies that the lone-pair electrons of Bi-3 and Bi-4 are the driving force of the ferroelectricity by breaking the symmetry. We found that the ELFs of Bi-1 and Bi-2 are also slightly changed during phase transition. However, their ELFs are oppositely distributed along the +*c* and −*c* directions, which causes the dipoles to mostly cancel each other out and only results in a very small contribution to the ferroelectricity. The roles of lone-pair electrons of Bi can also be understood by analyzing the element-projected density of states (DOS) and orbital projected DOS of Bi in fig. S45 because the lone-pair electrons are believed to stabilize the ferroelectricity through sp hybridizations (*48*). We found that the s states of Bi-3 and Bi-4 are much stronger than those of Bi-1 and Bi-2 in the energy range from −2 eV to the Fermi level, which implies that Bi-3 and Bi-4 have stronger hybridization with the p states than Bi-1 and Bi-2. This is consistent with the ELF analysis and further confirms the important role of lone-pair electrons of Bi-3 and Bi-4 in driving the ferroelectric transition. Next, to simulate the Sm-substituted Bi_6O_9, we considered all of the possible substituted configurations in which one Sm substitutes for one Bi within the unit cell of *Pmm*2 Bi_6O_9; a detailed comparison of all the possible structures can be found in fig. S46. The best structure match corresponds to a lowest-lying configuration, and its crystal structure is shown in Fig. 5C. By analyzing the interatomic distances between Bi and O for Bi-3 and Bi-4 in Fig. 5C, Bi-3 and Bi-4 are found to be deviated from the center of the O_8 hexahedron cage, which indicates that polarization remains in the Sm-substituted Bi_6O_9. In addition, the DOS calculated by hybrid functional HSE06 in fig. S47 shows that the Sm-substituted Bi_6O_9 opens a bandgap of 2 eV. Our calculations thus suggest that the ferroelectricity is preserved in the presence of Sm that is substituted in the Bi_6O_9. To compare the predicted crystal structure with the actual samples, we compared the crystal structure of Sm-substituted Bi_6O_9 with the images and found that it reproduces well the atomic structures along the [010] and [210] directions that were revealed by the HAADF-STEM images, which confirms the accuracy of the predicted structure (fig. S48). To confirm the crystal structure of BSO films with a thickness of 1 nm, we compared the predicted structure of Bi_5SmO_9 in integrated differential phase contrast (iDPC)–STEM (fig. S49). At the same time, Fig. 5D shows the HAADF-STEM images that were simulated along the directions of BSO film [010] and [210], which are highly consistent and used to support the accuracy of the predicted structure. The simulation model is shown in fig. S50. In addition, we observed that matching between BSO film and STO substrate is achieved by a BiO and TiO layer of substrate. Therefore, a possibility of charge transfer between Bi^{3+} and Ti^{4+} at the interface exists, which would be a factor for the enhanced displacement polarization at the interface as described above.

Conclusions

We designed a ferroelectric with layered structure of bismuth oxide and prepared the BSO thin film with good crystallinity through the sol-gel method, which can be grown on a variety of substrates. The film can still achieve macropolarization at a thickness of 1 nm at room temperature, with a high remanent polarization of 17 μC cm^{-2}. We confirmed the ferroelectric properties with measurements of

writing domain and local butterfly curves in PFM. We obtained the structure of the BSO film through DFT calculations and confirmed that it is a different type of room-temperature ferroelectric film than previously observed. This provides a promising route for future research of ferroelectric materials, and these ultrathin ferroelectric films are highly suitable for future nanoelectronic devices.

REFERENCES AND NOTES

1. J. Junquera, P. Ghosez, *Nature* **422**, 506–509 (2003).
2. D. D. Fong *et al*., *Science* **304**, 1650–1653 (2004).
3. S. Salahuddin, S. Datta, *Nano Lett.* **8**, 405–410 (2008).
4. T. Watanabe, A. Saiki, K. Saito, H. Funakubo, *J. Appl. Phys.* **89**, 3934–3938 (2001).
5. C. G. Duan, R. F. Sabirianov, W. N. Mei, S. S. Jaswal, E. Y. Tsymbal, *Nano Lett.* **6**, 483–487 (2006).
6. S. Venkatesan *et al*., *Phys. Rev. B* **78**, 104112 (2008).
7. L. A. Bursill, P. J. Lin, *Nature* **311**, 550–552 (1984).
8. Y. S. Kim *et al*., *Appl. Phys. Lett.* **86**, 102907 (2005).
9. S. S. Cheema *et al*., *Nature* **580**, 478–482 (2020).
10. T. S. Böscke, J. Müller, D. Bräuhaus, U. Schröder, U. Böttger, *Appl. Phys. Lett.* **99**, 102903 (2011).
11. F. Liu *et al*., *Nat. Commun.* **7**, 12357 (2016).
12. Y. Zhou *et al*., *Nano Lett.* **17**, 5508–5513 (2017).
13. C. Cui *et al*., *Nano Lett.* **18**, 1253–1258 (2018).
14. D. Ji *et al*., *Nature* **570**, 87–90 (2019).
15. H. J. Lee *et al*., *Science* **369**, 1343–1347 (2020).
16. S. S. Cheema *et al*., *Science* **376**, 648–652 (2022).
17. C. A. P. de Araujo, J. D. Cuchiaro, L. D. McMillan, M. C. Scott, J. F. Scott, *Nature* **374**, 627–629 (1995).
18. B. H. Park *et al*., *Nature* **401**, 682–684 (1999).
19. K. S. Knight, *Mineral. Mag.* **56**, 399–409 (1992).
20. B. Aurivillius, *Ark. Kemi* **1**, 463–480 (1949).
21. B. Aurivillius, *Ark. Kemi* **1**, 499–512 (1949).
22. L. Li *et al*., *Nano Lett.* **17**, 6575–6582 (2017).
23. L. Li *et al*., *Mater. Today Nano* **6**, 100037 (2019).
24. H. Irie, M. Miyayama, T. Kudo, *J. Appl. Phys.* **90**, 4089–4094 (2001).
25. J. Yang *et al*., *Nat. Mater.* **18**, 970–976 (2019).
26. L. Manna, L. W. Wang, R. Cingolani, A. P. Alivisatos, *J. Phys. Chem. B* **109**, 6183–6192 (2005).
27. J. F. Scott, *Ferroelectric Memories* (Springer, 2000).
28. A. Matsumoto, Y. Koyama, I. Tanaka, *Phys. Rev. B* **81**, 094117 (2010).
29. R. Punn, A. M. Feteira, D. C. Sinclair, C. Greaves, *J. Am. Chem. Soc.* **128**, 15386–15387 (2006).
30. Materials and methods are available as supplementary materials.
31. G. Catalan *et al*., *Nat. Mater.* **10**, 963–967 (2011).
32. L. Zhang *et al*., *Science* **361**, 494–497 (2018).
33. Y. T. Liu, C.-S. Ku, S.-J. Chiu, H.-Y. Lee, S.-Y. Chen, *ACS Appl. Mater. Interfaces* **6**, 443–449 (2014).
34. V. Nagarajan *et al*., *J. Appl. Phys.* **100**, 051609 (2006).
35. D. Lee *et al*., *Science* **349**, 1314–1317 (2015).
36. Y. Wei *et al*., *Nat. Mater.* **17**, 1095–1100 (2018).
37. U. Schroeder *et al*., *Inorg. Chem.* **57**, 2752–2765 (2018).
38. Y. Yun *et al*., *Nat. Mater.* **21**, 903–909 (2022).
39. S. C. Abrahams, S. K. Kurtz, P. B. Jamieson, *Phys. Rev.* **172**, 551–553 (1968).
40. V. C. Lo, *J. Appl. Phys.* **94**, 3353–3359 (2003).
41. F. Yang, F. Zhang, G. Hu, Z. Zong, M. Tang, *Appl. Phys. Lett.* **106**, 172903 (2015).
42. S. Zhang *et al*., *Adv. Mater.* **29**, 1703543 (2017).
43. U. Muller, *International Tables for Crystallography* (Wiley, 2011).
44. Y.-W. Fang *et al*., *Sci. Bull.* **60**, 156–181 (2015).
45. O. Diéguez, O. E. González-Vázquez, J. C. Wojdeł, J. Íñiguez, *Phys. Rev. B* **83**, 094105 (2011).
46. Y.-W. Fang, H. Chen, *Commun. Mater.* **1**, 1–8 (2020).
47. R. Seshadri, N. A. Hill, *Chem. Mater.* **13**, 2892–2899 (2001).
48. R. E. Cohen, *Nature* **358**, 136–138 (1992).
49. X. He, K. Jin, *Phys. Rev. B* **94**, 224107 (2016).

ACKNOWLEDGMENTS

Funding: This work was supported by the National Key Research and Development Program of China (2018YFA0703700, 2017YFE0119700, and 2020YFA0406202), the National Natural Science Foundation of China (21801013, 51774034, 51961135107, 62104140, 12175235, 22090042, 12074016, 11704041, and 12274009), the Fundamental Research Funds for the Central Universities (FRF-IDRY-19-007 and FRF-TP-19-055A2Z), the National Program for Support of Top-notch Young Professionals, the Young Elite Scientists Sponsorship Program by CAST (2019-2021QNRC), and Lingang Laboratory Open Research Fund (grant LG-QS-202202-11). Use of the Beijing Synchrotron Radiation Facility (1W1A beamlines, China) of the Chinese Academy of Sciences is acknowledged. Y.-W.F. acknowledges the support of Masaki Azuma's group during his stay at the Tokyo Institute of Technology. Y.L. acknowledges the support of the Beijing Innovation Team Building Program (grant no. IDHT20190503), the Beijing Natural Science Foundation (Z210016), the Research and Development Project from the Shanxi-Zheda Institute of Advanced Materials and Chemical Engineering (2022SX-TD001), and the General Program of Science and Technology Development Project of Beijing Municipal Education Commission (KM202110005003). **Author contributions:** L.Z. and J.T. conceived the idea of the work. L.Z. and Q.Y. designed the research. Q.Y., L.Z., J.H., Y.J., and R.Y. fabricated the films and performed the initial tests. Y.-W.F. and O.D. performed and interpreted the theoretical calculations. J.H., Y.L., M.S., S.D., D.Z., and X.Z. performed and analyzed the STEM experiments. Z.W. and H.W. provided the fitting of XRR and XRD. Y.D. and Z.L. performed and analyzed the XRD results. L.F., J.C., and X.X. conducted the ferroelectric properties measurements. Q.Y. and L.Z. wrote the manuscript with contributions from others. All authors discussed the results and commented on the manuscript. L.Z., Y.L., and J.T. guided the projects. **Competing interests:** There are no competing interests, including patents related to the work. **Data and materials availability:** All data are presented in the main text and supplementary materials. **License information:** Copyright © 2023 the authors, some rights reserved; exclusive licensee American Association for the Advancement of Science. No claim to original US government works. https://www.science.org/about/science-licenses-journal-article-reuse

SUPPLEMENTARY MATERIALS

science.org/doi/10.1126/science.abm5134
Materials and Methods
Figs. S1 to S50
Tables S1 to S6
References (*50–87*)

Submitted 23 September 2021; resubmitted 28 November 2022
Accepted 23 February 2023
10.1126/science.abm5134

3D POROUS MATERIALS

Programming 3D curved mesosurfaces using microlattice designs

Xu Cheng[1,2]†, Zhichao Fan[1,2,3]†, Shenglian Yao[4], Tianqi Jin[1,2], Zengyao Lv[1,2], Yu Lan[1,2], Renheng Bo[1,2], Yitong Chen[1,5], Fan Zhang[1,2], Zhangming Shen[1,2], Huanhuan Wan[3], Yonggang Huang[6,7], Yihui Zhang[1,2]*

Cellular microstructures form naturally in many living organisms (e.g., flowers and leaves) to provide vital functions in synthesis, transport of nutrients, and regulation of growth. Although heterogeneous cellular microstructures are believed to play pivotal roles in their three-dimensional (3D) shape formation, programming 3D curved mesosurfaces with cellular designs remains elusive in man-made systems. We report a rational microlattice design that allows transformation of 2D films into programmable 3D curved mesosurfaces through mechanically guided assembly. Analytical modeling and a machine learning–based computational approach serve as the basis for shape programming and determine the heterogeneous 2D microlattice patterns required for target 3D curved surfaces. About 30 geometries are presented, including both regular and biological mesosurfaces. Demonstrations include a conformable cardiac electronic device, a stingray-like dual mode actuator, and a 3D electronic cell scaffold.

Three-dimensional (3D) cellular microstructures are ubiquitous in living organisms, where they play diverse, irreplaceable roles in 3D shape formation (*1*–*4*), synthesis and transport of nutrients (*5*, *6*), and regulation of growth and reproduction (*7*, *8*). For example, the nonuniformly distributed cellular microstructures in the *Physalis philadelphica* berry and the *Silene vulgaris* flower, which form closed cages, offer a sufficient stiffness to support their oval calyx sacs (Fig. 1A, left and middle left); the intricate, vascular networks in cabbage leaves can locally shrink and unilaterally thicken at reduced temperatures, leading to the formation of a multilayer spherical shape (Fig. 1A, middle right); and the honeycomb-like cellular microstructures with hexagonal chambers throughout the cell wall of the *Stephanopyxis turris* diatom enhance the efficiency of its photosynthesis (Fig. 1A, right) (*1*). Because of the high surface areas, large pore volumes, and excellent mechanical and thermal properties of cellular structures, cellular designs have been exploited in the development of materials and functional systems (*9*, *10*). Examples include lattice materials and foams with high specific stiffness, specific strength, and impact resistance (*3*, *11*–*15*); porous electrodes with small ion diffusion distances and large percentages of active materials for high-power lithium ion batteries (*16*, *17*); artificial tissues and organs with hierarchical vascularized networks capable of oxygen and nutrient supply and waste removal (*5*, *6*, *18*); electromagnetic metamaterials capable of blocking, absorbing, enhancing, or bending electromagnetic waves (*19*); and metal-organic frameworks for water-splitting and oxygen-reduction reactions (*20*).

Inspired by cellular biological surfaces such as those shown in Fig. 1A, we developed a microlattice design strategy as a powerful route to achieve the desired stiffness distribution of 2D microfilms, thereby allowing their transformation into programmable 3D curved mesosurfaces using mechanically guided assembly. We established both an analytical model and a machine learning–based computational approach for the inverse design of target 3D curved mesosurfaces from 2D microlattice patterns with optimized distributions of porosity and cell sizes. Although inverse design methods of 2D-to-3D assembly have been reported for strategies relying on spatial stiffness control of thin films using thickness engineering (*21*, *22*), soft active materials with programmable strain distributions (*23*–*27*), or constrained optimization of geometries and rotations of unit cells in kirigami and origami tessellations (*28*–*31*), the limitations of applicable materials and length scales have impeded their utility in 3D microelectronic devices (*32*, *33*).

[1]Applied Mechanics Laboratory, Department of Engineering Mechanics, Tsinghua University, Beijing 100084, P.R. China. [2]Laboratory of Flexible Electronics Technology, Tsinghua University, Beijing 100084, P.R. China. [3]College of Mechanical and Vehicle Engineering, Hunan University, Changsha 410082, P.R. China. [4]School of Materials Science and Engineering, University of Science and Technology Beijing, Beijing 100083, P.R. China. [5]Department of Automation, Tsinghua University, Beijing 100084, P.R. China. [6]Querrey Simpson Institute for Bioelectronics, Northwestern University, Evanston, IL 60208, USA. [7]Departments of Civil & Environmental Engineering, Mechanical Engineering, and Materials Science & Engineering, Northwestern University, Evanston, IL 60208, USA.
*Corresponding author. Email: yihuizhang@tsinghua.edu.cn
†These authors contributed equally to this work.

Microlattice design strategy for curvature programming of 3D mesosurfaces

Figure 1 illustrates the key concepts and capabilities of the bioinspired microlattice design strategy. This strategy introduces a 2D thin film with an engineered lattice pattern consisting of spatially varying triangular units and micrometer-sized ribbons. The triangle lattice design is exploited instead of cellular designs with circular holes because of the relieved stress concentration and the excellent adaptability to complexly shaped edges (fig. S1). Figure 1B presents a schematic illustration of the microlattice design strategy using a circular design domain $\mathfrak{R}$ as an example. We used triangular lattices to discretize the prescribed design domain (fig. S2), dividing the domain into N triangular units with M lattice nodes. L_{ik} (where k = 1, 2, 3) and φ_i are the side length and the porosity of the i^{th} triangular unit (where $i = 1, \ldots, N$); φ_i = 0 and 1 denote two limit conditions, i.e., the solid material region without any porosity and the region without any material, respectively. Considering the stretching-dominated mechanism of the triangular lattice, the effective modulus (E_i) scales with the relative density ($\bar{\rho}_i = 1 - \varphi_i$) of the unit, i.e., $E_i \propto (1 - \varphi_i)$, and therefore the distribution of microlattice porosity serves as a crucial parameter to adjust the stiffness distribution. We use Ω to denote the set of nodes (with M_{bond} nodes in total) that are bonded with a prestretched elastomer (prestrains, ε_X and ε_Y) in the mechanical assembly. Accordingly, the in-plane displacements $\boldsymbol{D_j}$ ($\boldsymbol{D_j} = [d_{jX}, d_{jY}]$, $j = 1, 2, \ldots, M_{\text{bond}}$) are applied to this node set Ω to trigger the 2D-to-3D assembly, where d_{jX} and d_{jY} are the displacement components of the j^{th} node along X and Y directions. Once the porosity distribution φ_i, the node set Ω of bonding sites, and the prestrain (ε_X and ε_Y) are given, the 3D mesosurface resulting from the mechanical assembly can be determined, corresponding to a forward problem. Figure S3 provides a set of examples with the same square-shaped design domain $\mathfrak{R}$, bonding sites, and uniaxial prestrain (30%). Assigning different porosity (φ_i) distribution results in distinct 3D surface geometries, indicating a crucial role of porosity distribution in tailoring the assembled mesosurface geometry.

The practical utility of the microlattice strategy requires a rational inverse design method as the theoretical basis. Herein, the inverse design problem focuses on determining the porosity distribution, bonding sites, and prestrain for a target 3D surface and a prescribed number (N) of triangular units. An octopus-like mesosurface serves an example to illustrate the key procedure of the inverse design (Fig. 1C). The design target (fig. S4A) is derived by simplifying the complex biological surface, which consists of an axisymmetric “head” region and eight curvy “tentacles.” Discretizing the head region into eight pieces of subsurfaces interconnected in the central region allows utility of a beam theory–based model (see the supplementary text for details) to obtain distributions of bending stiffness and porosity in the 2D precursor. The various tentacle shapes can be also reproduced using

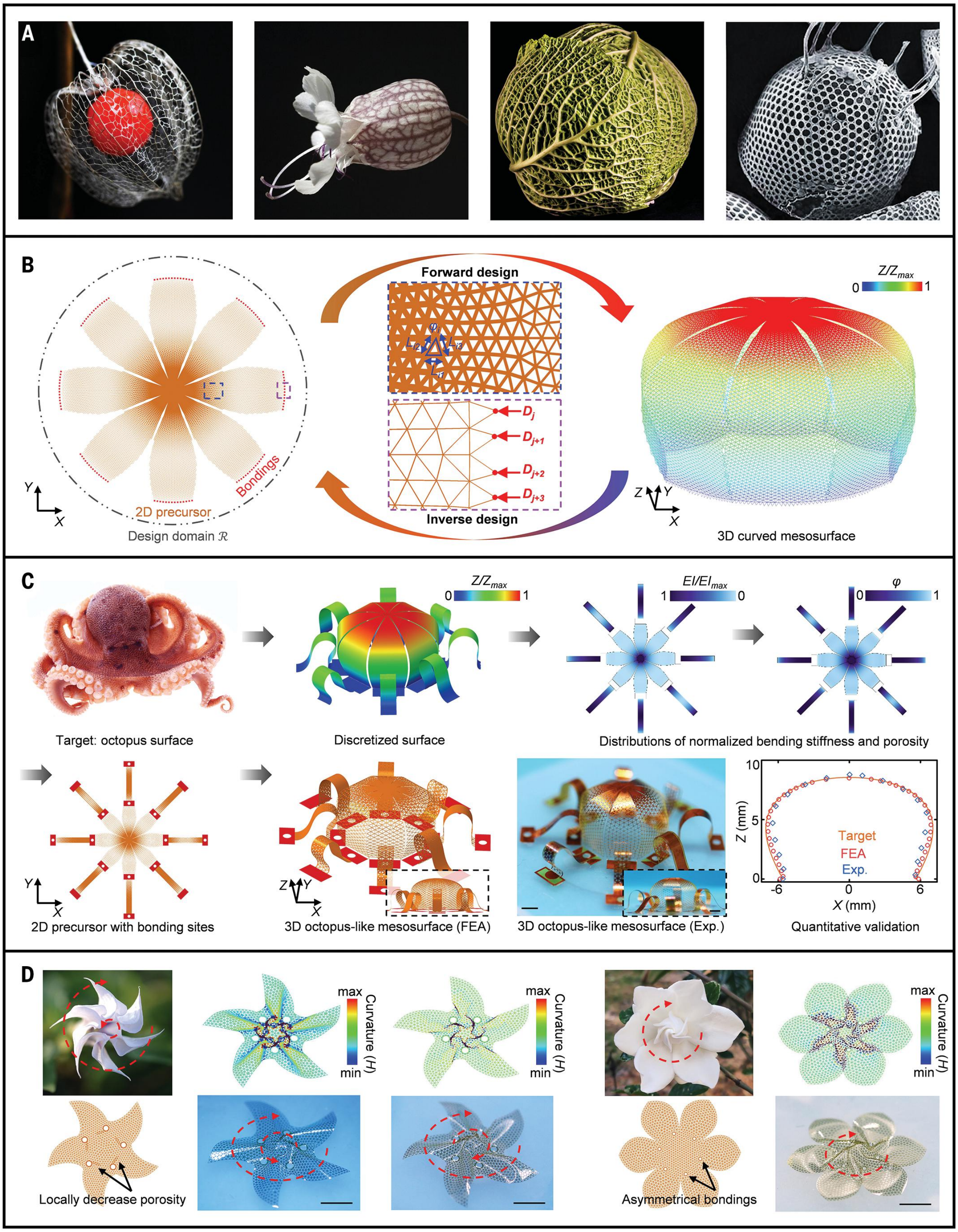


Fig. 1. Conceptual illustrations of curvature programming of 3D mesosurfaces by bioinspired microlattice design strategy. (**A**) Optical images of a *Physalis philadelphica* berry (left) and *S. vulgaris* flower (middle left) with oval, reticular calyx sacs; multilayer spherical cabbage leaves with intricate, vascular networks (middle right); and an *S. turris* diatom with a honeycomb-like cellular cell wall [reproduced with permission from Jantschke *et al.* (*1*), copyright 2014, The Royal Society of Chemistry]. (**B**) Schematic illustrations of forward and inverse designs of 3D curved mesosurfaces in the framework of the bioinspired microlattice design strategy. Here, φ_i and L_{ik} (where k = 1, 2, 3) represent the porosity and side lengths of triangular unit cell numbered i in the design domain $\Re$, respectively, and $\boldsymbol{D_j}$ is the displacement vector (d_{jX}, d_{jY}) of the node numbered j in the bonding regions. (**C**) FEA and experimental results of the inverse design of an octopus-like mesosurface with an optimized microlattice pattern based on a discretized approach. (**D**) Two flower mesostructures (left: *D. stramonium*, right: *G. jasminoides* Ellis) and bioinspired designs with bonding sites distributed inside the 2D microlattice. Scale bars, 2 mm.

this model. Then, the 2D microlattice pattern can be generated, along with the node set of bonding sites. The assembled 3D surface geometry based on finite element analysis (FEA) and experimental measurements are both in excellent agreement with the design target (Fig. 1C and fig. S4, B and C). The maximum principal strain is <1% in most regions of the octopus-like mesosurface, indicating that the fracture failure would not occur in commonly used electronic materials (e.g., Si, Au, Cu, and Ti) during assembly (fig. S4B). Here, the microfabrication technologies (materials and methods and figs. S5 to S9) allowed fabrication of patterned 2D microlattice in a bilayer of 200 nm Cu and 12 μm polyimide (PI), with a minimum ribbon width of 10 μm. The experiments of mechanically guided assembly followed procedures similar to those reported previously (fig. S10) (*34*, *35*).

The microlattice design strategy confers a locally discrete yet globally continuous geometric feature of the microfilm, which enables a discreteness-mediated deformation mechanism inaccessible to solid microfilms. Such a discreteness-mediated deformation mechanism mainly occurs in microfilms with inner bonding sites, where localized deformations usually develop. A circular-shaped microfilm serves as an example to describe this mechanism, in which four symmetrically distributed inner bonding sites are assigned (fig. S11). Although the structural geometry and loading conditions are symmetric with regard to the X and Y axes, the buckling deformations display two possible modes that are mediated by the discreteness. For solid or densely distributed microlattice films, a chiral mode involving twisting deformations is more energetically favorable (fig. S11, B and C). When the microlattice is sufficiently sparse to accommodate bending-dominated deformations of ribbon components, the symmetric mode becomes more energetically favorable. Although the solid microfilm shows a chiral buckling mode, the twisting orientation is random and not controllable. Harnessing the discreteness-mediated deformation of microlattice films offers an avenue to 3D mesosurfaces with controlled chirality, e.g., by introducing slightly reduced porosity at the intermediate region of two bonding sites (fig. S12). Figure 1D and fig. S13 present two mesosurfaces inspired by *Datura stramonium* and *Gardenia jasminoides* Ellis, in which the chirality is tailored by the porosity-governed method (see the supplementary text).

Microlattice design methods for the rational assembly of 3D mesosurfaces

A beam theory–based model allows the inverse design of 2D ribbon mesostructures and axis-symmetric mesosurfaces (Fig. 2 and figs. S14 to S20). By homogenizing a straight, ribbon-shaped microlattice as a solid ribbon structure and using the Euler-Bernoulli beam theory, the key design parameters [including the porosity $\varphi(S)$ and the prestrain ε_{pre}] for a target ribbon can be obtained analytically (see the supplementary text and figs. S14 to S16). Most axis-symmetric 3D surfaces are nondevelopable and therefore cannot be assembled directly from geometrically continuous 2D films without involving large membrane strains (e.g., >5%), which are not tolerable for most inorganic electronic materials. We introduce a discretization-based approximation method to allow utility of the beam theory–based model in the inverse design of axis-symmetric mesosurfaces. The method divides the target surface uniformly into n subsurfaces (fig. S17), each of which can be considered as a ribbon with a nonuniform width. Then, the porosity distribution $\varphi(S)$ and the prestrain ε_{pre} can be determined for the target subsurface. Figure 2A presents a hemispherical mesosurface approximated with 10 subsurfaces (supplementary text), where optical images and numerical simulations of the assembled 3D mesosurface are in close accordance with the target surface. The experiments used a bilayer of 200 nm Si and 8 μm PI in the fabrication, and the resulting hemispherical mesosurface has a diameter of ~2 mm (movie S1). Similarly, the proposed method allows for the inverse design of spherical caps (100 nm Au or Ti and 8 μm PI) (fig. S18, A to C) and hemi-ellipsoidal mesosurfaces (100 nm Au or Ti and 12 μm PI) with various aspect ratios (3, 2/3, and 1/3) (fig. S18, D to F). Fairly close 3D mesosurfaces can be obtained through use of only 10 subsurfaces in the discretization (Fig. 2A and fig. S18, A to F). These results illustrate the effectiveness of the inverse design method based on the microlattice strategy.

Introducing inner bonding sites allows the curvature of the assembled 3D mesosurface to vary its sign, thereby expanding the range of 3D mesosurfaces. Figure 2B presents a volcano-like mesosurface (100 nm Ti and 8 μm PI) with a crateriform concavity (~1.4 mm in diameter) at the central region. Assigning a high level of porosity (90%) to the joint region of inner and outer surfaces enables programmable folding deformations to reproduce the geometric feature of the slope discontinuity (movie S2). With use of a single inner bonding site, donut-like 3D mesosurfaces can also be accurately attained (fig. S18, G and H). Adding more inner bonding sites allows combination of two or more customized 3D mesosurfaces, enriching the accessible range of axis-symmetric mesosurfaces. Figure 2C, fig. S18I, and movie S3 provide two palace-like mesostructures composed of a torus at the outer region and a cylinder (or a hemisphere) at the inner region. Approximately closed-form geometries are also possible, with two examples shown in Fig. 2, D and E, and fig. S19, D and E.

The above beam theory–based model also allows for the inverse design of 3D mesosurfaces with rotational symmetries, including complex biomimetic mesosurfaces reconstructed from real plants. For example, the blueberry flower has five petals and a style, and their shapes can be reconstructed through discrete-point sampling to serve as our design target (Fig. 2F, left, and fig. S20A). Then, the bilayer 2D precursor patterns and the prestrain can be determined through the inverse design method (Fig. 2F, middle left, and fig. S20B). The resulting biomimetic microlattice structure is shown in the middle of Fig. 2F. Similarly, a biomimetric *P. philadelphica* berry surrounded with a closed oval calyx sac can be inversely designed and fabricated (Fig. 2G and fig. S20, C and D). This inverse design method can be further extended to curvy mesosurfaces with a slight degree of asymmetry. In this case, the mesosurface is discretized into a certain number of uneven curvy ribbons, and each ribbon component can be reproduced by optimizing the porosity distribution and prestrain. Two examples are provided in Fig. 2, H and I, and fig. S21, where the design targets mimic a garden spider's abdomen and an asymmetric flowerpot.

Design of a strain-limiting frame to connect bonding sites of as-assembled 3D mesosurfaces allows their isolation from the bulky elastomeric substrate without altering their geometric configurations (fig. S22). On the basis of this facile isolation method, freestanding 3D mesosurfaces with diverse configurations are fabricated, including an octopus head–like mesosurface, a hemi-ellipsoidal mesosurface, and spherical caps, with the lateral size spanning from ~600 μm to ~14 mm (Fig. 2J and fig. S23). Mechanics modeling suggested that the stiffness ratio between the 3D mesostructure and the strain-limiting frame is the dominant parameter that affects the shape fixation (see the supplementary text and fig. S24). In addition, the extended material compatibility, broad applicable length scales, and rich structural topology (Fig. 2, J and K, and figs. S25 to S27) suggest versatile capabilities of the microlattice strategy for designing 3D functional devices and microsystems.

If the target 3D surface cannot be discretized into a group of symmetric ribbons, then the above beam theory–based model considering only bending deformations will not work. Introducing a machine learning algorithm allows for the establishment of a powerful inverse design method for 3D mesosurfaces with both symmetric and asymmetric configurations. Using the seashell surface as an example (Fig. 3A), the method starts with discretizing the 3D curved surface into a set of 3D feature points (X_i, Y_i, Z_i, i = 1 … N_P, where N_p is the total point number) using strategic cuts that can capture key geometric features (i.e., radial

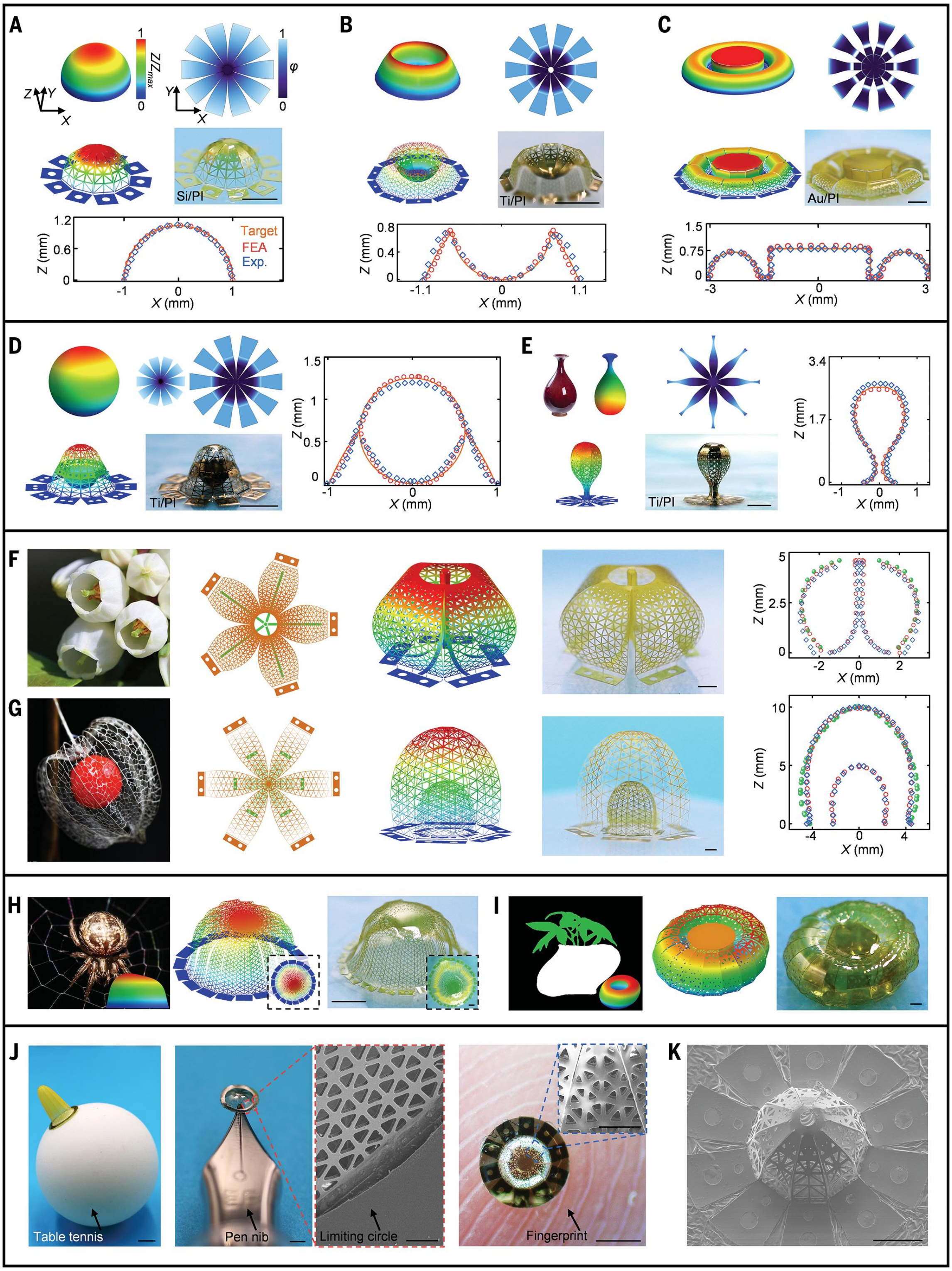


Fig. 2. Inverse designs of 3D curved mesosurfaces based on an analytical model. (**A** to **C**) Target geometry, porosity distribution of the 2D precursor pattern, and corresponding FEA and experimental results for a hemispherical mesosurface (A), a volcano-like mesosurface (B), and a palace-like mesosurface (C). (**D** and **E**) Inverse design of closed-form 3D mesosurfaces: a suspended spherical mesosurface (D) and a vase-like mesosurface (E). (**F** and **G**) Inverse design of two plant mesosurfaces with bilayer layouts: blueberry flower (F) and *P. philadelphica* berry (G). Green dots are sampled from the plant surfaces. (**H**) Target geometry, FEA, and experimental results of an asymmetric surface that resembles the curved abdomen of a garden spider. (**I**) Similar results for the inverse design of an asymmetric flowerpot. (**J**) 3D isolated mesosurfaces with different aspect ratios and length scales (from millimeter to micrometer). Scale bars, 5 mm, 1 mm, and 500 μm in the three optical images from left to right, respectively, and 100 μm in the SEM images. (**K**) SEM image of a hemispherical microsurface (30 nm Ti and 2.7 μm PI). Scale bars: (A) to (I), 1 mm; (K), 100 μm.

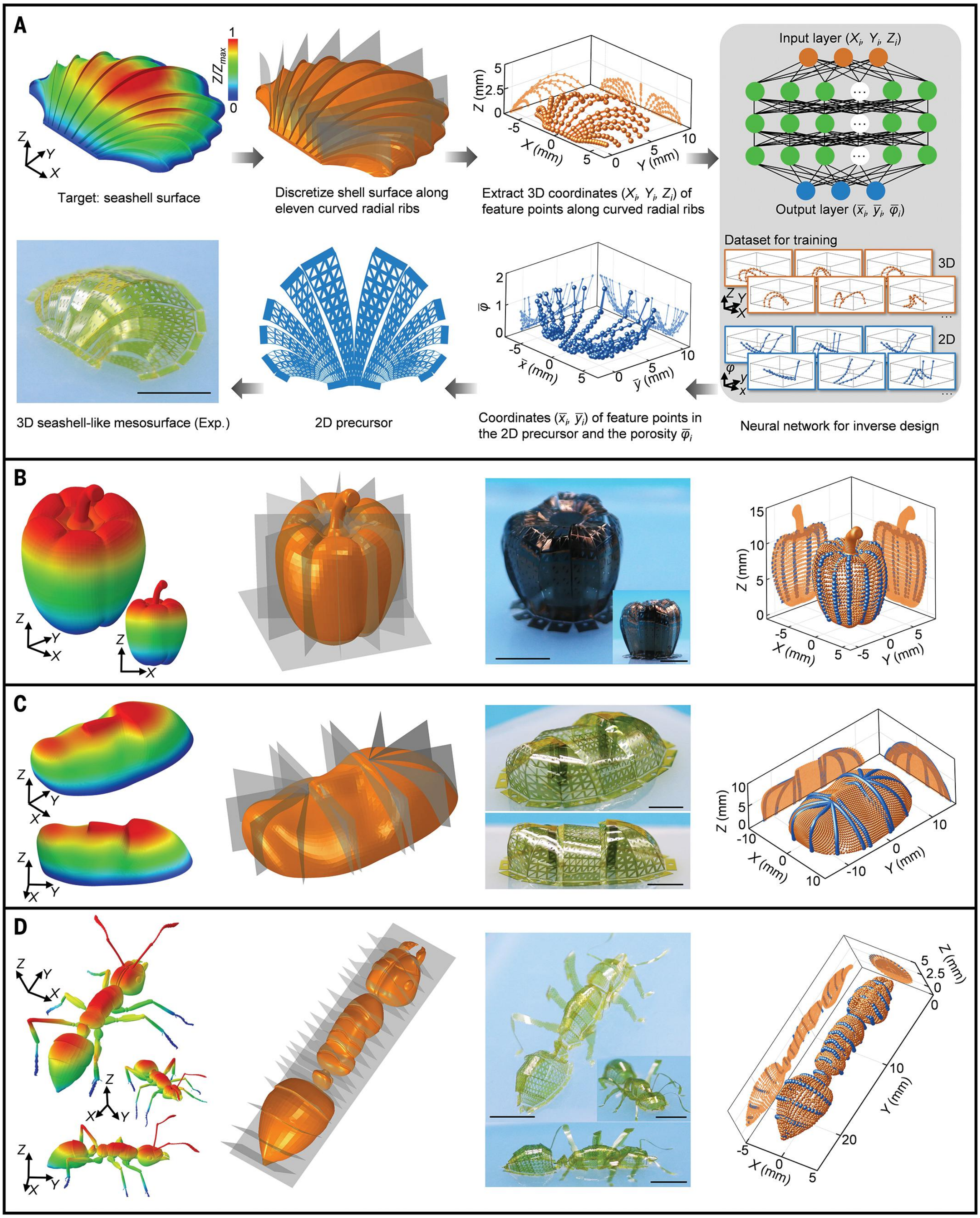


Fig. 3. Inverse designs of 3D complex mesosurfaces using a point cloud–based machine learning method. (**A**) Schematic illustrations of the process of the inverse design for a seashell mesosurface (20 nm Ti and 7 μm PI). (**B**) Target geometries, discretization strategies, experimental results, and comparisons between the computed point cloud (blue) and the design target (orange) for a pimento-like mesosurface (200 nm Ti and 7 μm PI), which is divided into discretized ribbon components using a set of planes across a central line. (**C**) Similar results for a mask-like mesosurface (20 nm Ti and 7 μm PI) with regional discretization through radial and parallel cuts. (**D**) Similar results for an ant-like surface (20 nm Ti and 7 μm PI) based on a cutting strategy similar to CT scanning. Scale bars, 5 mm.

ribs in this example). A point cloud–based artificial neural network (*36*) is exploited to predict the 2D point coordinates ($\bar{x}_i, \bar{y}_i$) and their corresponding porosity ($\bar{\varphi}_i$) on the basis of the training by generating a dataset through FEA (see the supplementary text and figs. S28 to S32). Then, the 2D microlattice pattern containing 12 separate ribbons and bonding sites can be generated, given the optimal set of ($\bar{x}_i$, $\bar{y}_i, \bar{\varphi}_i$) and prescribed meshing method. The loadings [i.e., displacements (Δ_x, Δ_y) and rotation angle (Θ) of bonding sites in the X–Y plane] applied to the 2D ribbon precursors can be determined directly by the coordinates of bonding edges in the 2D precursor and

target seashell surface. Considering the negligible axial elongation or compression of ribbon components during buckling deformations, each ribbon component typically requires a distinct loading condition, indicating that the entire seashell surface cannot be formed through a single-step assembly on the same substrate. Each ribbon component is assembled on a separate substrate (see the supplementary text) and then transferred onto the same platform using the aforementioned strain-limiting frame to form the entire 3D mesosurface (figs. S33 and S34). Quantitative comparisons of feature-point coordinates in target seashell surface, FEA, and experiments show a high degree of agreement (fig. S35). Refining the discretization with more strategic cuts leads to an enhanced agreement of the resulting mesosurface and the design target (fig. S36).

As illustrated above, the mapping between 3D complex mesosurfaces and 2D microlattice films is actually simplified into the one between a set of 3D point cloud (X_i, Y_i, Z_i) and another ($\bar{x}_i$, $\bar{y}_i$, $\bar{\varphi}_i$). Therefore, the computational cost could be reduced considerably to facilitate the inverse design of complex 3D

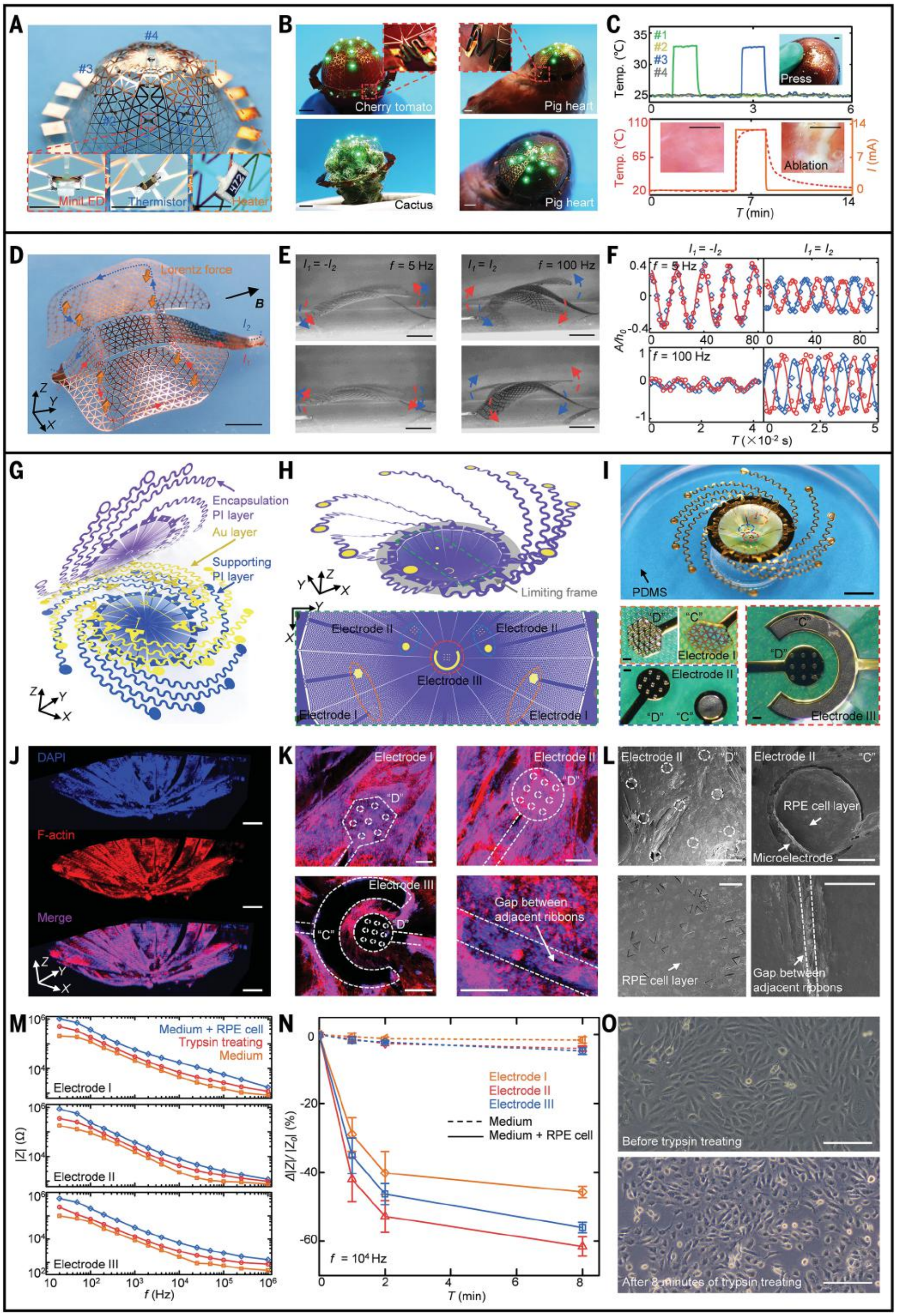


Fig. 4. Applications of 3D curved mesosurfaces based on bioinspired microlattice designs. (**A**) Optical image of a breathable, hemispherical electronic device that integrates mini-LEDs, chip thermistors, and a heater. (**B**) Conformal electronic device wrapped around the cherry tomato, cactus, and apical region of a pig heart. (**C**) Measured temperature change of the heart surface (top) under a finger press and during the thermal ablation therapy in a local region of the heart (bottom). Scale bars: (A) and (C), 1 mm; (B), 5 mm. (**D**) Optical image of a stingray-like actuator with two circuits arranged on two sides of the body. (**E** and **F**) Optical images and amplitude responses of two vibration modes (left: top-down mode; right: left-right mode) of the 3D actuator excited by Lorentz forces. A and h_0 are the vibrational amplitude and initial height of front tips of two "fins," respectively. Scale bars, 5 mm. (**G** to **I**) Schematic illustrations of the 2D precursor designs (G), FEA results of assembled 3D configurations (H), and corresponding experimental results (I) of an electronic cell scaffold. Scale bars in (I), 5 mm (top) and 100 μm (bottom). (**J** and **K**) Fluorescence-stained images and magnified images of the electronic cell scaffold with RPE cells. Scale bars: (J), 1 mm; (K), 200 μm. (**L**) SEM images of local regions after freeze-drying. Scale bars, 100 μm. (**M**) Impedance curves for electrodes I, II, and III with three different conditions. (**N**) Relative changes of the impedance at 10 kHz as a function of the trypsin treating time for three different electrodes. The average values of four independent experiments are shown with SD values. (**O**) Optical images of the RPE cells before and after 8 min of trypsin treating. Scale bars, 20 μm.

surfaces. The strategy used to discretize the target surface is important in this method. For 3D surfaces with an approximate rotational symmetry, a set of planes that cross a central line can divide the mesosurface into discretized ribbon components. The pimento and carambola serve as two mesosurfaces that can be inversely designed following this discretization strategy (Fig. 3B and figs. S37 and S38, A and B). Extraction of spatial coordinates of feature points allows a quantitative shape comparison between biomimetic microlattice structures and target surfaces (Fig. 3B and figs. S37, right, and S39, A and B). For mesosurfaces without a clear symmetry, the target surface can be first divided into certain subsurface parts according to the geometric feature, and then each part can be further discretized using an appropriate strategy (e.g., radial or parallel cuts). As an example, Fig. 3C and figs. S38C and S39C present results of an inverse design for a target surface that resembles a face mask. Here, the inverse design begins with cutting the surface into three parts, followed by discretizing these parts into five, three, and five ribbon components, for the "forehead," "nose," and "chin" parts, respectively. Figure 3D illustrates the use of the proposed inverse design method in generating an ant-like mesostructure in which the main body part is discretized using a cutting strategy similar to computed tomography (CT) scanning. The six legs and two tentacles are designed separately and then added to the main body part after its assembly. The entire ant-like microlattice structure consisting of 4034 microtriangles and 7826 microribbons accurately reproduces the design target (Fig. 3D and figs. S38D and S39D), showing the capability of the point cloud–based method in designing highly complex 3D mesosurfaces.

Device applications based on bioinspired microlattice designs

The bioinspired microlattice designs allow the construction of 3D electronic systems with the desired curvature distributions for either conforming to or replicating the curvy surfaces of biological tissues and organs. Figure 4A presents a breathable, hemispherical electronic device for cardiac sensing, optical stimulation, and thermal ablation. This device consists of 11 blue mini-LEDs, four chip thermistors, and one heater, and copper wires (250 nm) sitting on PI microlattice frames (10 μm) serve as the electrical connection (fig. S40). Here, we introduce optimized serpentine structures as strain-limiting frames in which the as-assembled hemispherical shape can not only be well maintained in the freestanding state, but can also be deformable to adapt to nonspherical surfaces to yield high signal-to-noise ratio temperature sensing (Fig. 4B and Fig. 4C, top; fig. S41; and movie S4). The microlattice design not only reduces physical constraints [e.g., interfacial adhesion and wrinkles (*37*, *38*); fig. S41F] on the heart, but also provides microchannels for the lubricating fluid in the pericardium to avoid pericardiosymphysis. This device could be used for the treatment of heart arrhythmias (*39*). An array of blue micro-LEDs could perform optogenetic therapy with large area of optical stimulation, and the microheater is capable of localized thermal ablation to suppress abnormal electrical signals on the heart surface (Fig. 4C, bottom).

Biomimetic 3D mesostructures that imitate the dynamic characteristics of living organisms are also possible using the microlattice designs. Figure 4D, fig. S42, and movie S5 show a stingray-like 3D mesostructure with a curved body and a pair of "fan-shaped fins." Two circuits integrated with the fins can generate periodically varying Lorentz forces to the 3D mesostructure under a fixed magnetic field ($\boldsymbol{B}$) along the body length direction (Fig. 4D and fig. S42). Different vibration modes can be excited by varying current directions in the two circuits and adjusting their frequency (Fig. 4, E and F). The difference between measured resonant frequencies (5 and 100 Hz) of these two modes is evident, because of their distinct deformation features.

Development of 3D biological models and platforms that mimic in vivo 3D microenvironments has important implications for investigating fundamental behaviors (e.g., growth, apoptosis, and pathogenesis) of cells. For example, the retinal pigment epithelium (RPE) cells in the 3D curved surface of the outer blood–retinal barrier–vascular complex are essential in transporting biological molecules between the retina and blood, but existing culture models of RPE cells are limited to 2D planar geometries (*40*). A spherical cap–shaped electronic cell scaffold with integrated sensing capabilities is presented here (Fig. 4, G to I; supplementary text; and fig. S43), in which the curvature radius (~7.5 mm) is close to that of rabbit RPE. RPE cells were planted on the 3D scaffold, and then cultured for 15 days with the medium changed every 2 days. Figure 4, J and K, provides fluorescent staining images of RPE cells growing on the electronic scaffold. It can be seen that RPE cells are uniformly spread across the whole curved surface because of the relatively closed configuration and micrometer-sized lattices (5 to 62 μm in microribbon length, which is similar in size to the RPE cells) of the 3D scaffold. As evidence, Figs. 4K, bottom right, and 4L and fig. S44 show that RPE cells could cross the gaps between adjacent ribbon components of the curved mesosurface to connect with each other. Results of impedance measurements based on the 3D electronic scaffold are shown in Fig. 4, M and N. Because RPE cells behave as dielectric materials when immersed in culture media under electrical stimulation (*41*, *42*), a distinct increase of impedance can be observed after growth of RPE cells on the scaffold (Fig. 4M). To test the sensitivity of impedance measurements to physiological activities of RPE cells, a trypsin solution was used to treat these cells, and the time responses of impedance were recorded (Fig. 4N). As the time of trypsin treating increases, the impedance drops rapidly and eventually stabilizes because trypsin causes RPE cells to contract and partially detach from the scaffold, as evidenced by the optical images shown in Fig. 4O and fig. S45. These results suggest the 3D electronic cell scaffold as a noninvasive platform for studying real-time, spatial distributions of physiological activities (e.g., growth and apoptosis) of cells.

Conclusion

The bioinspired microlattice design strategy and inverse design methods presented herein allow for the rational assembly of 2D films into desired 3D mesosurfaces with diverse geometries, from regular surfaces (e.g., hemispherical, spherical, hemi-ellipsoidal, and hemi-toroidal surfaces) to highly complex surfaces (e.g., those resembling a volcano, flower, fruit, octopus, and ant). In principle, the microlattice designs are applicable to a broad set of materials, including but not limited to those demonstrated in this work (silicon, metals, chitosan, polyimide, SU8, and laser-induced graphene). Compared with previous strategies (*21*–*24*) for local stiffness control, the proposed microlattice design enables fundamental advances in realizable geometries, applicable materials, and length scales of the assembled 3D surfaces (see the supplementary text). Demonstrations in conformal 3D cardiac electronic devices, a bionic dual-mode actuator, and a 3D electronic cell scaffold suggest promising application opportunities in bioelectronics, microelectromechanical systems, and microrobotics. Additionally, the microlattice strategy can be used to design optical devices such as optical metasurfaces with angle-dependent reflectance (fig. S46).

REFERENCES AND NOTES

1. A. Jantschke, C. Fischer, R. Hensel, H. G. Braun, E. Brunner, *Nanoscale* **6**, 11637–11645 (2014).
2. E. E. Kuchen *et al*., *Science* **335**, 1092–1096 (2012).
3. F. V. Senhora, E. D. Sanders, G. H. Paulino, *Adv. Mater.* **34**, e2109304 (2022).
4. W. Li *et al*., *Nat. Electron.* **4**, 134–142 (2021).
5. B. Grigoryan *et al*., *Science* **364**, 458–464 (2019).
6. L. Neufeld *et al*., *Sci. Adv.* **7**, eabi9119 (2021).
7. K. J. I. Lee *et al*., *PLOS Biol.* **17**, e3000427 (2019).
8. D. A. Dickerson, *Adv. Biol.*e2200067 (2022).
9. S. Li *et al*., *Nature* **592**, 386–391 (2021).
10. D. M. Sussman *et al*., *Proc. Natl. Acad. Sci. U.S.A.* **112**, 7449–7453 (2015).
11. J. R. Greer, V. S. Deshpande, *MRS Bull.* **44**, 750–757 (2019).
12. S. J. Yeo, M. J. Oh, P. J. Yoo, *Adv. Mater.* **31**, e1803670 (2019).
13. S. N. Khaderi *et al*., *Extreme Mech. Lett.* **10**, 15–23 (2017).
14. L. R. Meza, J. M. J. Schormans, J. J. C. Remmers, V. S. Deshpande, *J. Mech. Phys. Solids* **125**, 276–297 (2019).
15. A. J. D. Shaikeea, H. Cui, M. O'Masta, X. R. Zheng, V. S. Deshpande, *Nat. Mater.* **21**, 297–304 (2022).
16. W. Li, J. Liu, D. Zhao, *Nat. Rev. Mater.* **1**, 16023 (2016).

17. Z. Qu *et al.*, *Adv. Energy Mater.* **12**, 2200714 (2022).
18. G. J. Pahapale *et al.*, *Adv. Sci. (Weinh.)* **9**, e2104649 (2022).
19. D. Schurig *et al.*, *Science* **314**, 977–980 (2006).
20. H. Hu *et al.*, *Nat. Chem.* **13**, 358–366 (2021).
21. Z. Fan *et al.*, *Adv. Mater.* **32**, e1908424 (2020).
22. M. Liu, L. Domino, D. Vella, *Soft Matter* **16**, 7739–7750 (2020).
23. J. H. Pikul *et al.*, *Science* **358**, 210–214 (2017).
24. J. W. Boley *et al.*, *Proc. Natl. Acad. Sci. U.S.A.* **116**, 20856–20862 (2019).
25. H. Aharoni, Y. Xia, X. Zhang, R. D. Kamien, S. Yang, *Proc. Natl. Acad. Sci. U.S.A.* **115**, 7206–7211 (2018).
26. A. Nojoomi, J. Jeon, K. Yum, *Nat. Commun.* **12**, 603 (2021).
27. K. Liu, F. Hacker, C. Daraio, *Sci. Robot.* **6**, eabf5116 (2021).
28. G. P. T. Choi, L. H. Dudte, L. Mahadevan, *Nat. Mater.* **18**, 999–1004 (2019).
29. R. Guseinov, C. McMahan, J. Pérez, C. Daraio, B. Bickel, *Nat. Commun.* **11**, 237 (2020).
30. L. Jin, A. E. Forte, B. Deng, A. Rafsanjani, K. Bertoldi, *Adv. Mater.* **32**, e2001863 (2020).
31. C. Baek, A. G. Martin, S. Poincloux, T. Chen, P. M. Reis, *Phys. Rev. Lett.* **127**, 104301 (2021).
32. M. Kim *et al.*, *Nat. Electron.* **3**, 546–553 (2020).
33. C. Becker *et al.*, *Nat. Commun.* **13**, 2121 (2022).
34. S. Xu *et al.*, *Science* **347**, 154–159 (2015).
35. Y. Zhang *et al.*, *Nat. Rev. Mater.* **2**, 17019 (2017).
36. Y. Guo *et al.*, *IEEE Trans. Pattern Anal. Mach. Intell.* **43**, 4338–4364 (2021).
37. C. Zhang, Y. K. Hao, B. Li, X. Q. Feng, H. Gao, *Soft Matter* **14**, 1681–1688 (2018).
38. X. Lin *et al.*, *Nat. Biomed. Eng.* **3**, 632–643 (2019).
39. J. Park *et al.*, *Sci. Transl. Med.* **8**, 344ra86 (2016).
40. D. Kent *et al.*, *Exp. Eye Res.* **76**, 213–219 (2003).
41. A. G. Montaño-Figueroa *et al.*, *Biosens. Bioelectron.* **128**, 37–44 (2019).
42. A. Bussooa *et al.*, *Adv. Sci. (Weinh.)* **7**, 1902999 (2020).

ACKNOWLEDGMENTS

We thank J. A. Rogers from Northwestern University for inspiring discussions. **Funding:** This work was supported by the National Natural Science Foundation of China (grants 12050004 and 12225206 to Y.Z. and grant 31800813 to S.Y.); the Tencent Foundation (XPLORER Prize to Y.Z.); and the Institute for Guo Qiang, Tsinghua University (grant 2021GQG1009 to Y.Z.). **Author contributions:** Y.Z. designed and supervised the research. X.C., Z.F., and Y.Z. led the structural designs and mechanics modeling with assistance from T.J., Y.C., H.W., and Y.H. X.C. led the fabrication work with assistance from Y.L. and Z.S. S.Y. and X.C. led the design and characterization of electronic cell scaffold with assistance from Z.F. X.C. and F.Z. led the design and characterization of dual-mode actuators. Z.L., X.C., and R.B. led the metasurface design and simulations. Y.Z. and X.C. wrote the manuscript and designed the figures. All authors commented on the manuscript. **Competing interests:** The authors declare no competing interests. **Data and materials availability:** All data are available in the main text or the supplementary materials. **License information:** Copyright © 2023 the authors, some rights reserved; exclusive licensee American Association for the Advancement of Science. No claim to original US government works. https://www.science.org/about/science-licenses-journal-article-reuse

SUPPLEMENTARY MATERIALS

science.org/doi/10.1126/science.adf3824
Materials and Methods
Supplementary Text
Figs. S1 to S46
References (*43–50*)
Movies S1 to S5

Submitted 18 October 2022; accepted 1 March 2023
10.1126/science.adf3824

COMPARATIVE EMOTION

Evolutionarily conserved role of oxytocin in social fear contagion in zebrafish

Ibukun Akinrinade[1]†‡, Kyriacos Kareklas[1]†, Magda C. Teles[1], Thais K. Reis[1], Michael Gliksberg[2], Giovanni Petri[3,4], Gil Levkowitz[2,5], Rui F. Oliveira[1,6,7]*

Emotional contagion is the most ancestral form of empathy. We tested to what extent the proximate mechanisms of emotional contagion are evolutionarily conserved by assessing the role of oxytocin, known to regulate empathic behaviors in mammals, in social fear contagion in zebrafish. Using oxytocin and oxytocin receptor mutants, we show that oxytocin is both necessary and sufficient for observer zebrafish to imitate the distressed behavior of conspecific demonstrators. The brain regions associated with emotional contagion in zebrafish are homologous to those involved in the same process in rodents (e.g., striatum, lateral septum), receiving direct projections from oxytocinergic neurons located in the pre-optic area. Together, our results support an evolutionary conserved role for oxytocin as a key regulator of basic empathic behaviors across vertebrates.

Emotional contagion, described as the ability to match the emotional state of another individual, has been considered the most ancestral form of empathy, on top of which more complex forms of empathic behaviors, such as consolation and helping, have evolved (e.g., rodents, elephants, dolphins, and primates) (*1*–*3*). Emotional contagion relies on simple perception-action mechanisms and provides important adaptive advantages to social living species (*1*). It enhances social cohesion and the establishment of social bonds, as well as promoting the rapid spread of fear among group members once a threat (e.g., predators) is detected, which allows individuals to survive potential dangers without directly experiencing them (*3*). Therefore, emotional contagion is expected to be phylogenetically ancient, being present even in species with less elaborate social cognition. Indeed, social contagion of fear has been recently described in zebrafish (*Danio rerio*), consisting of transmission of the alarm response (i.e., distress behavior consisting in erratic movement and freezing) to observers and increases in observer cortisol levels similar to those of target individuals (*4*–*6*). Moreover, behavioral responses are influenced by familiarity, with familiar distressed target fish eliciting stronger alarm responses in observers (*5*). The extent to which the distress behavior observed in zebrafish in response to alarmed conspecifics are phenomenologically similar to emotional contagion, can also be argued through comparison with mammalian models of emotional contagion, such as facial expressions in orangutans (*7*) and freezing in rodents (*8*). We investigated whether social transmission of the alarm response in zebrafish shares the same proximate mechanisms that have been described for social fear contagion in mammals. We focused on the oxytocin signaling system because nonapeptides of the oxytocin family are evolutionarily conserved across vertebrates (*9*) and have been implicated in the regulation of emotional contagion in rodents (*10*, *11*) and fear recognition in humans (*12*, *13*).

[1]Integrative Behavioral Biology Lab, Instituto Gulbenkian de Ciência, Oeiras 2780-156, Portugal. [2]Department of Molecular Cell Biology, Weizmann Institute of Science, Rehovot 7610001, Israel. [3]ISI Foundation and ISI Global Science Foundation, Torino 10126, Italy. [4]CENTAI Institute, Torino 10138, Italy. [5]Department of Molecular Neuroscience, Weizmann Institute of Science, Rehovot 7610001, Israel. [6]ISPA-Instituto Universitário, Lisboa 1149-041, Portugal. [7]Champalimaud Neuroscience Program, Champalimaud Centre for the Unknown, Lisbon 1400-038, Portugal.
*Corresponding author. Email: ruiol@ispa.pt
†These authors contributed equally to this work.
‡Present address: Department of Physiology and Pharmacology, Cumming School of Medicine, University of Calgary, 2500 University Drive NW, Calgary Alberta T2N 1N4, Canada.

Oxytocin signaling is necessary and sufficient for social fear contagion

We used zebrafish mutant lines for the ligand (*oxt*) and the two receptors (*oxtr* and *oxtrl*) of the zebrafish oxytocin nonapeptide CYISNCPIG-NH_2 (isotocin) (*9*) to assess the role of oxytocin in social fear contagion. In zebrafish, as in other Ostariophysi fish species, injured individuals release an alarm substance from their skin into the water, originally termed Schreckstoff (fear substance), which is detected through olfaction eliciting a distress response consisting of erratic movement followed by freezing behavior (*14*). The sight of conspecifics in distress also elicits the expression of this response in observers, indicating the occurrence of social fear contagion in zebrafish (*4*–*6*) (Fig. 1). Therefore, we have used an experimental paradigm in which a naïve observer fish watches an unfamiliar conspecific shoal in a neighboring tank (i.e., without chemical communication), to which we have administered either water (control) or the alarm substance (Fig. 1A). Given that freezing behavior was a more consistent distress response in wild types than erratic movement (Fig. 1, B to K), we have used it as a readout for fear contagion. Observer individuals of all wild-type (WT) control lines (i.e., $oxt^{+/+}$, $oxtr^{+/+}$, and $oxtrl^{+/+}$) significantly increased their freezing behavior when exposed to a distressed shoal. By contrast, observer individuals of all mutant lines (i.e., $oxt^{-/-}$, $oxtr^{-/-}$, and $oxtrl^{-/-}$) failed to significantly increase their freezing behavior when exposed to a distressed shoal (Fig. 1, C, E, and G). This indicates that oxytocin signaling is necessary for social fear contagion in zebrafish. Moreover, we administered exogenous oxytocin to the ligand mutants and their controls to assess whether it could recue the social fear contagion phenotype. We also injected another group of ligand mutants and their respective control with the vehicle solution to control for putative stressful effects of the injection. Mutants injected with oxytocin also significantly increased their freezing behavior when exposed to distressed conspecifics, indicating that oxytocin is both necessary and sufficient for social fear contagion (Fig. 1, E and G). These results also suggest the lack of compensatory actions by the vasotocin system, which is known to crosstalk with the oxytocinergic system.

Oxytocin modulates the activity of ventral forebrain regions associated with social fear contagion

To characterize the neural circuits associated with emotional contagion in zebrafish we examined the expression of a neuronal activity marker, phospho-S6 ribosomal protein (pS6), in a set of forebrain and midbrain areas involved in social decision-making across vertebrates [i.e., social decision-making network (*15*)]. Significant changes were identified in two of these areas, the ventral (Vv) and central nucleus (Vc) of the ventral telencephalic area (Fig. 2A). The Vv is a putative homolog of the mammalian lateral septum and the Vc of the mammalian striatum (*15*). Notably, the expression, recognition, and sharing of emotions in humans also relies on the regulation of activity in these forebrain areas by oxytocin, even if higher order empathic functions are dependent on neocortical circuits (*16*–*19*). In zebrafish, we find that both areas exhibit a decrease in activity associated with the expression of freezing behavior in observer wild types and an increase in activity with the lack of response in *oxtr* mutants (Fig. 2B). This suggests that zebrafish distress behavior during contagion is mediated by decreases in inhibitory cell activity and that overactivation of these cells in mutants prevents the expression of this behavior. To test this hypothesis, we used a double reporter line for both excitatory (glutamate: *vglut2/dsRed*) and inhibitory (γ-aminobutyric acid, GABA: *gad1b/GFP*) neurotransmission (Fig. 2C). Compared with controls, during contagion the Vv indeed exhibits greater activity in inhibitory cells ($\chi^2_{1,13} = 5.09$, $p = 0.024$), but the Vc instead exhibits increased activity in excitatory cells ($\chi^2_{1,13} = 9.90$, $p = 0.002$). Notably, the oxytocinergic modulation of GABAergic inhibition is also

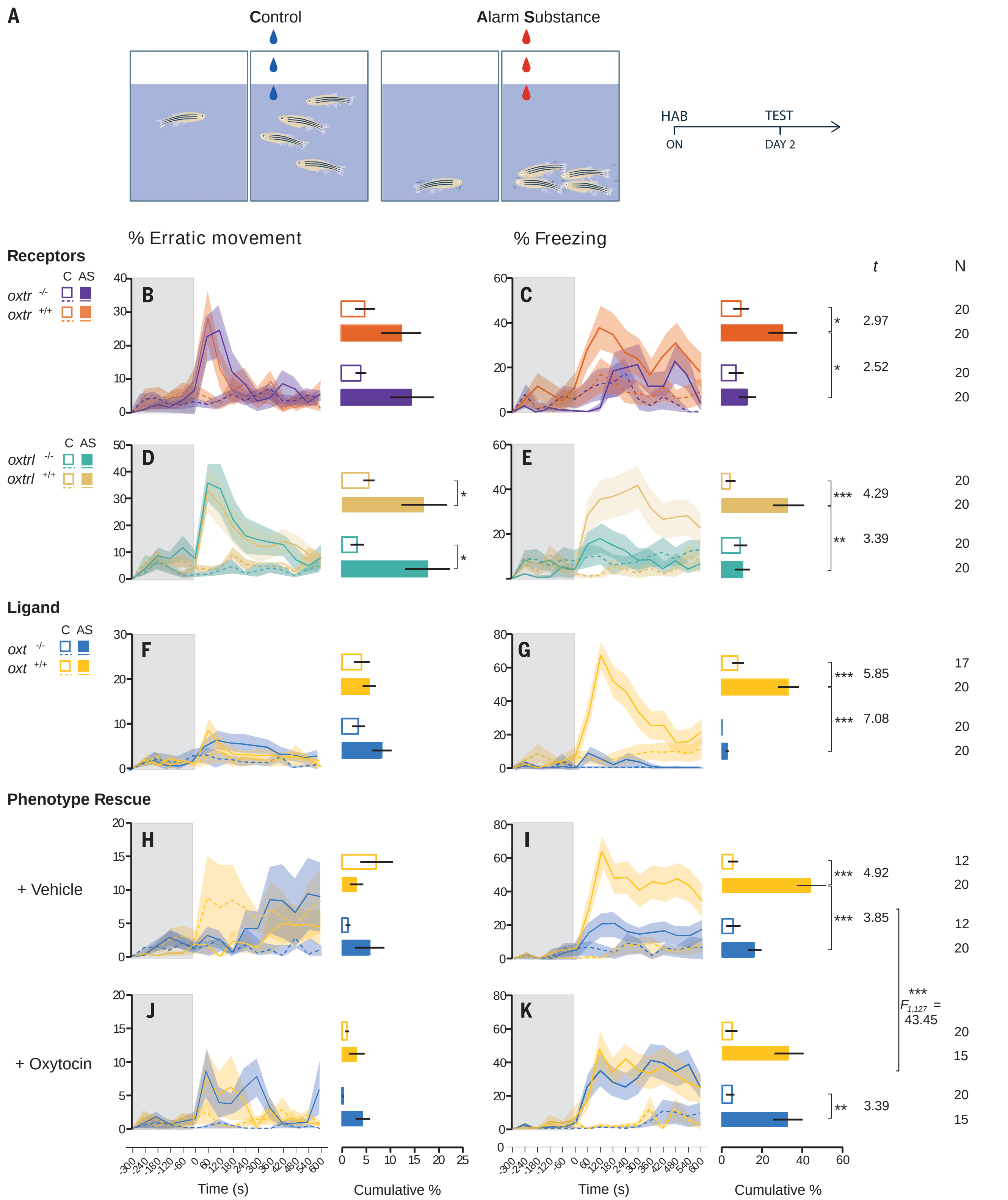
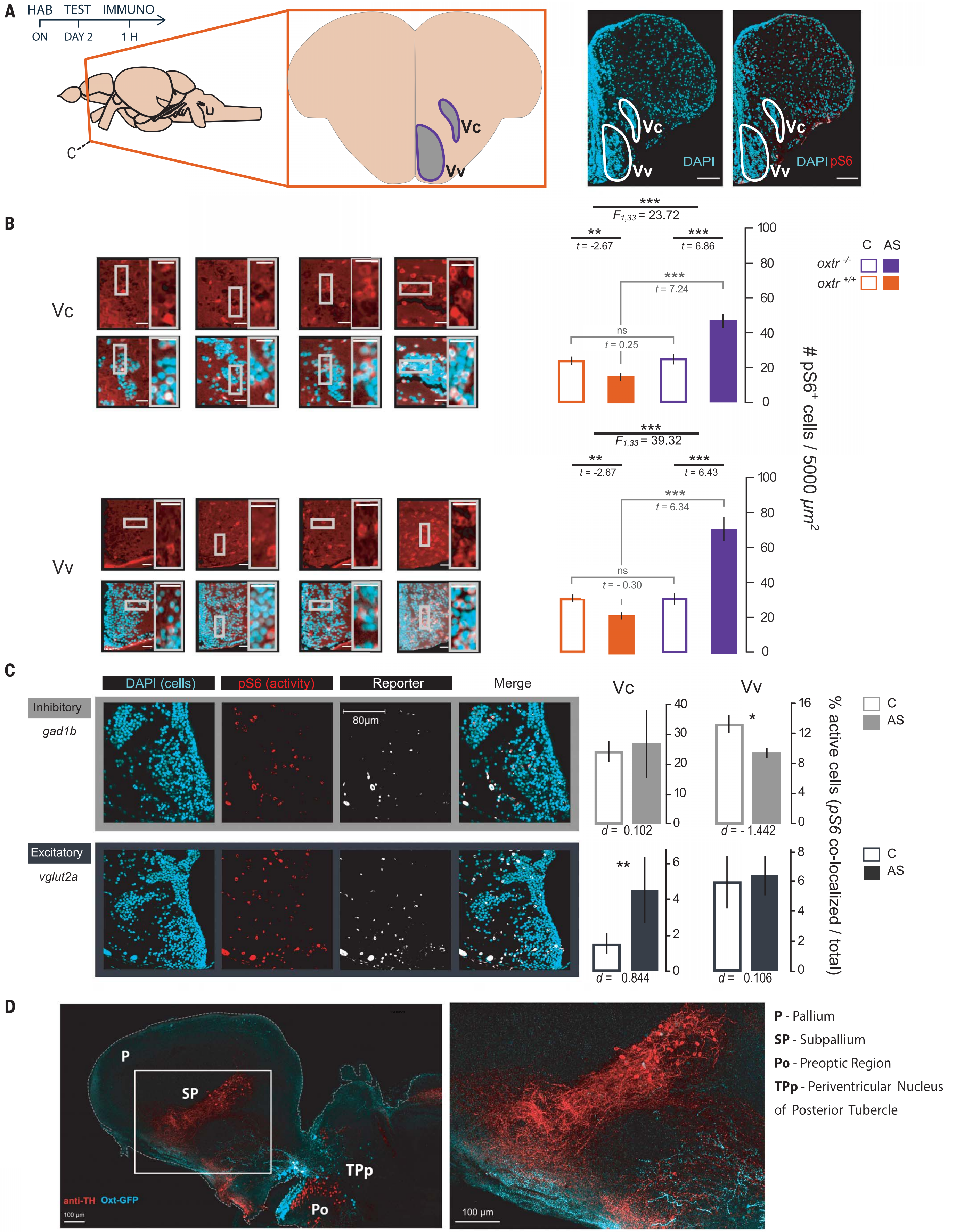
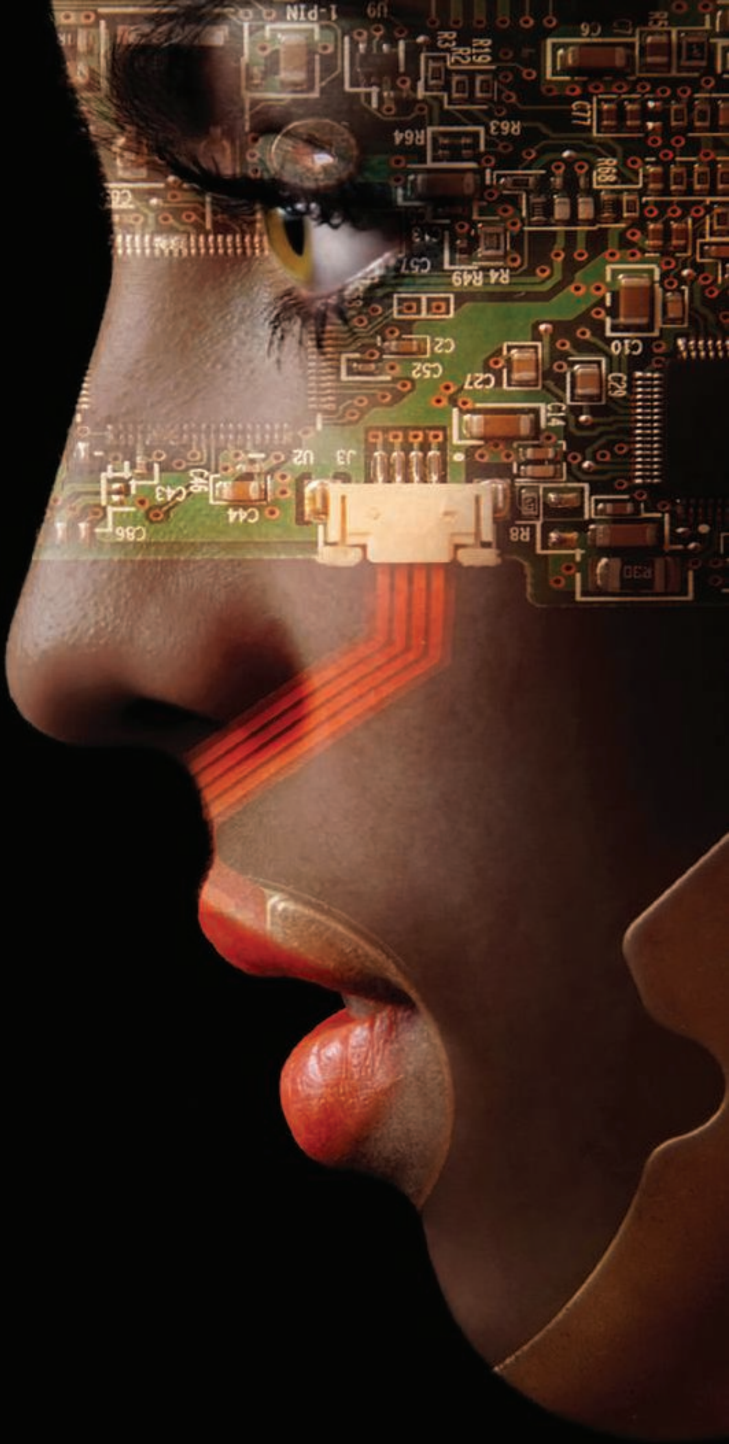


Fig 1. Oxytocin effects on the social transmission of distress. (**A**) Schematic and schedule (HAB, habituation; ON, overnight) of the social contagion paradigm. Droplets represent administration of vehicle (blue) and alarm substance (AS, red) to control and experimental groups. (**B** to **K**) (Left) temporal dynamics of freezing and erratic movement response across treatments for mutant *oxtr*$^{(-/-)}$, *oxtrl*$^{(-/-)}$, *oxt*$^{(-/-)}$, and ligand rescue with intraperitoneal (i.p.) oxytocin (OXT) to *oxt*$^{(-/-)}$ fish, compared with WT controls. Shaded area indicates time before AS or vehicle administration. (Right) percentage of freezing and erratic movement (mean ± SEM) after vehicle and AS administration. [Two-way analysis of variance (ANOVA) with post hoc Welch's *t*-test, **P* < 0.05, ***P* < 0.01, ****P* < 0.001.]


A
HAB TEST IMMUNO
ON DAY 2 1 H
C
Vc
Vv
DAPI
DAPI pS6
B
Vc
Vv
***
F1,33 = 23.72
**
t = -2.67
***
t = 6.86
***
t = 7.24
ns
t = 0.25
***
F1,33 = 39.32
**
t = -2.67
***
t = 6.43
***
t = 6.34
ns
t = - 0.30
pS6+ cells / 5000 μm2
C AS
oxtr -/-
oxtr +/+
C
DAPI (cells)
pS6 (activity)
Reporter
Merge
Inhibitory
gad1b
Excitatory
vglut2a
80μm
Vc
Vv
d = 0.102
d = - 1.442
d = 0.844
d = 0.106
% active cells (pS6 co-localized / total)
C
AS
D
P
SP
TPp
Po
anti-TH Oxt-GFP
100 μm
P - Pallium
SP - Subpallium
Po - Preoptic Region
TPp - Periventricular Nucleus of Posterior Tubercle



Share **Your Robotics Research** with the **World**.

Shaping the future of robotics with high impact research!

As a multidisciplinary online-only journal, *Science Robotics* publishes original, peer-reviewed, research articles that advance the field of robotics. The journal provides a central forum for communication of new ideas, general principles, and original developments in research and applications of robotics for all environments.

Submit your research today. Learn more at: **science.org/journal/scirobotics**

Twitter: @SciRobotics
Facebook: @ScienceRobotics

Science Robotics
AAAS

Fig 2. Oxytocin receptor deletion alters nodal neuronal activation. (**A**) Schedule of behavioral assay and immuno-staining; anatomical localization of the two brain areas responding to fear contagion: the central nucleus (Vc) and the ventral nucleus of the ventral telencephalon (Vv), with representative hemicoronal sections identified by DAPI (cyan) and patterns of neuronal activity shown by pS6 (magenta) through immunostaining. (**B**) Quantification of the density (cells per 5000 μm^2) of pS6 positive cells in each brain area, Vc and Vv; panels show representative examples (left to right: WT control, WT alarm, mutant control, mutant alarm; scale = 20 μm). (**C**) Quantified activity in cells (pS6 and DAPI) identified as either excitatory (glutaminergic: *vglut2a*) or inhibitory (GABAergic: *gad1b*) in double reporter lines (*vglut2a*:dsRed / *gad1b*:GFP) compared between the observation of control (C) or alarm-response (AS) in demonstrators (linear mixed model, with pS6 as covariate; Cohen's *d* quantifies effect size), with representative microscopy examples shown in panels. [Results are shown as mean ± SEM; *P < 0.05, **P < 0.01, *** P < 0.001.] (**D**) Representative example of sagittal brain slice (confocal maximum intensity z-stack) showing immunostained *oxt* positive neuronal fibers (yellow) projecting to the Vv in the subpallium of adult zebrafish with TH cell groups (pink) also projecting to the Vv.

exhibited in the lateral septum of mice during social fear transmission (*17*).

The zebrafish Vv conserves the role of the mammalian lateral septum as a functional connectivity area between the social behavior and mesolimbic system (*15*). Thus, the decreasing inhibition when distress is observed enables otherwise suppressed signals during control conditions to be relayed between areas of the network. By contrast, the Vc conserves the role of the striatum as part of the mesolimbic reward pathway for downstream other-oriented motor and motivational controls (*16*, *18*), which explains the excitatory increases similar to those noted in parts of the striatum in mice (*19*). Because the proportion of active cells during social fear contagion that were either inhibitory or excitatory was a minority (Vc 31.26% and Vv 15.86%), the overall decreased activity may relate to other oxytocin-induced changes in local cells, likely due to shifts in connectivity across the network. Oxytocin regulation of these ventral forebrain areas relies on projections from oxytocin neurons in the pre-optic area (Fig. 2D), and is confirmed by the expression of both zebrafish oxytocin receptors in these areas (*oxtr*, *oxtrl*; fig. S1), which is also in agreement with the pattern of brain distribution of *oxtr* in other teleost fish (*20*). Notably, both receptors are also expressed across most nodes of the social decision-making network, but the expression of the primary receptor (*oxtr*) is distinctly greater and more widespread (fig. S1). Thus, we examined the effect of *oxtr* expression on patterns of functional connectivity across the social decision-making network.

Oxytocin modulates functional connectivity across brain regions in response to social contagion

To study functional connectivity, we constructed networks representing coactivation patterns during social fear contagion and control treatments, for both wild types and *oxtr* mutants, with positive and negative correlations between nodes indicating excitatory and inhibitory patterns respectively. Although functional distributions differ between wild types and mutants under both control and treatment conditions, average inhibition and excitation notably differ only under the fear contagion treatment (fig. S2). Networks were tested for both excitatory and inhibitory distributions across genotypes and treatments, and for computed average levels of each [probability in sample space, p(ω)]. Under control conditions wild types and mutants show differences in the network distribution (excitation: KS = 0.23, $P < 10^{-4}$; inhibition: KS = 0.55, $P < 10^{-6}$), but negligible differences in average signals (only inhibition: U = 3492, $P < 10^{-5}$, Cohen's d = 0.18). Under treatment, *oxtr* mutants exhibited both higher average excitation (U = 5744, $P < 10^{-6}$, Cohen's d = 0.67) and inhibition (U = 1972, $P < 10^{-6}$, Cohen's d = 0.68), as well as greater differences in distribution (excitation: KS = 0.49, $P < 10^{-6}$; inhibition: KS = 0.73, $P < 10^{-6}$). Overall, the absence of emotional contagion in *oxtr* mutants was paralleled by a segregated pattern of functional connectivity (excitatory: KS = 0.38, $P < 10^{-6}$; inhibitory: KS = 0.50, $P < 10^{-4}$) with significantly greater average excitation in their brain network (U = 5680, $P < 10^{-6}$, Cohen's d = 0.49) than wild types displaying the socially transmitted distress behavior. In line with our findings in the reporter line, the Vv of the wild type loses all its inhibitory connectivity during treatment compared with the control, but in mutants inhibitory connectivity is partially retained—namely to the anterior tuberal nucleus. By contrast, the Vc of wild types maintains inhibitory connectivity during contagion, shifting only in target nodes and reducing strong neighboring connections, which may explain the overall reduced activity. We also confirm that it exhibits excitatory links, most of which are to non-neighboring nodes and which do not appear in *oxtr* mutants. These include the habenula (HAV), the lateral hypothalamic nucleus, and the posterior dorsal telencephalic area, which are involved in fear and alarm responses (*6*, *21*). Node centrality also radically shifted in ranking between the brain networks of wild types and *oxtr* mutants, and with fear contagion compared with the control (fig. S3 and table S1). In turn, only a single preserved submodule (at $z > 3$, $P < 0.01$) was shared between wild types and *oxtr* mutants under the fear contagion treatment, and it constitutes the dorsal and ventral habenula, the posterior pre-optic area and the magnocellular preoptic nucleus. Considering the implications of the habenular nuclei in zebrafish fear responses and that the pre-optic area responds to the alarm substance (*6*, *21*), this submodule is likely involved in processing fear stimulation in both groups. Notably, although the submodule is isolated in *oxtr* mutants, in wild types it is integrated in a larger module together with ventral and dorsal areas of the telencephalon, and the ventral zone of the periventricular nucleus. This indicates that oxytocin drives greater functional integration when animals are exposed to distressed conspecifics.

Oxytocin regulates the recognition of emotion-like states needed for social fear contagion

The observed social transmission of fear in zebrafish can be regarded simply as behavior contagion based on motor imitation or as emotional contagion, which requires recognition of the demonstrator's state (i.e., emotion) and which triggers an automatic representation of the same state in the observer, causing an equivalent expression of behavior (*22*). Although zebrafish match both the behavior and cortisol levels of distressed individuals (*4*), this may be due to either recognizing and sharing the internal state of others or because the behavior of others signals local danger (e.g., predators) (*14*), which triggers proportional physiological and behavioral changes. Therefore, we decided to test state recognition explicitly by separating (in time) the moment the observer sees the distressed conspecific (observation phase) from a second moment (test phase), when the observer must discriminate between the demonstrator previously observed in distress and the individual that was relaxed (i.e., only swimming). If observers can make this discrimination, it means that when they expressed alarm behavior in response to the observed distress behavior of conspecifics (observation phase), they were not merely responding with motor imitation but were able to encode information on the behavioral state of demonstrators, which they subsequently used to discriminate between the two demonstrators when they are in a similar behavioral state (test phase). To this end, observers of *oxt*, *oxtr*, and *oxtrl* mutants and their respective WT controls were first exposed to two simultaneous prerecorded video playbacks of the same demonstrator in conflicting states: neutral (swimming) and periodic distress (three bouts of erratic movement and freezing). Observers were then exposed to two videos both showing the demonstrator in the neutral state,

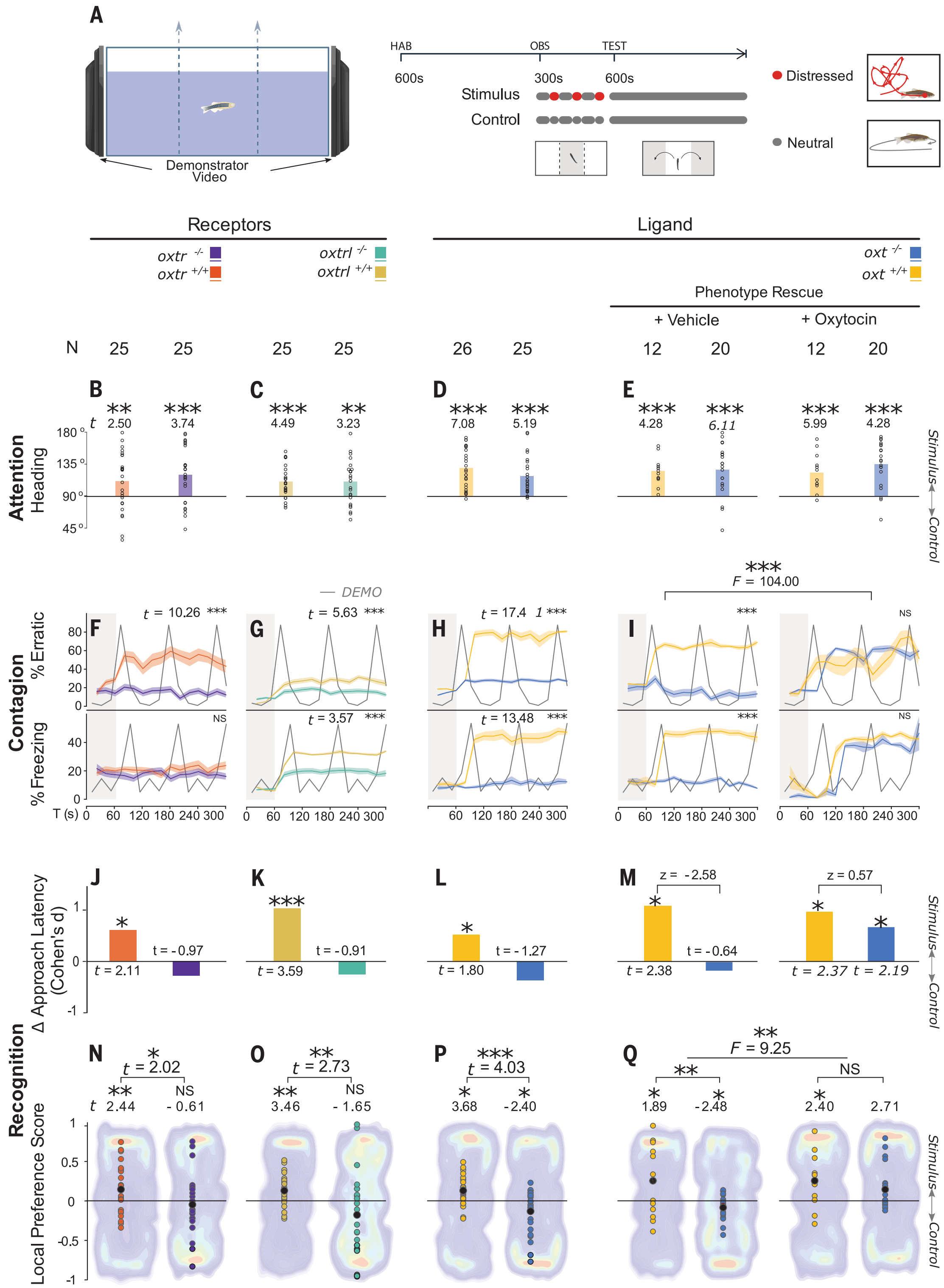


Fig. 3. Content validity of fear transmission by state recognition. (**A**) Video playback tests enabled the controlled assessment of stimulus versus state recognition across two experimental phases: a 5-min observation of two conflicting videos presenting the same demonstrator in either a neutral state (control) or periodically distressed (stimulus) and a 10-min local preference test while both videos displayed the demonstrator in a neutral state. During observation attention was measured by (**B** to **E**) the absolute heading toward the stimulus video (0 to 180°; one-sample *t*-tests, $\mu \neq 90°$) and (**F** to **I**) temporal changes in the proportion time erratic and freezing following analogous behavior in the stimulus video, which were compared between genotype and treatment (linear mixed models, full factorial). During tests (**J** to **M**) differences in latency to first approach the stimulus compared with the control location were tested (Welch's two-sample *t*-tests; effect-size comparisons: *z* tests, $d_1 \neq d_2$, $|z| \geq 1.96$ at $\alpha = 0.05$ two-sided) and (**N** to **Q**) local preference scores, calculated from cumulative durations, were also compared (one-sample *t*-tests, $\mu \neq 0$; genotypic comparisons: Welch's two-sample *t*-tests; genotype times treatment: two-way ANOVA with post hoc Fisher's LSD). Heat maps are representative examples with the least deviation from the mean. [$^{NS}P > 0.05$, $^{*}P < 0.05$, $^{**}P < 0.01$, $^{***}P < 0.001$.]

in which recognition was tested through local preferences based on the previously observed conflicting states (Fig. 3A).

During observation, fish oriented toward erratic movement and freezing and thus attention shifted to the distressed behavior and not the level of movement (fig. S4). Notably, orientation preferences were not different between any of the oxytocin mutants and WT controls (Fig. 3, B to E). By contrast, the wild types replicated the distress behavior of the demonstrators whereas the oxytocin mutants failed to do so. However, the administration of oxytocin to the ligand mutant (*oxt*) rescued the distress contagion (Fig. 3, F to I, and fig. S5). This replicated the results of the live demonstrator experiment regarding the necessary and sufficient role of oxytocin and further shows that attention is not moderating these effects. Notably, during the test phase wild type observers were motivated to approach and preferred being near the previously distressed demonstrator, whereas oxytocin mutants did not express a motivation to approach

the previously distressed demonstrator (Fig. 3, J to M) and preferred being near the demonstrator that remained in a neutral state (Fig. 3, N to Q). This indicates that oxytocin is necessary and sufficient for zebrafish to recognize the distress from the neutral behavior in the same conspecific, suggesting the occurrence of an oxytocin-dependent emotion recognition in zebrafish (*23*, *24*). This is in line with responses in humans and mammals that implicate the recognition of a fearful state in others and not simply their behavior (*25*, *26*). Moreover, because distressed behavior in zebrafish signals local predation risk (*14*), our findings also show that oxytocin promotes interaction with distressed others despite heightened local risk. Such other-oriented acts that involve individual costs and benefits for others are typically referred to as prosociality, which is well-defined in mammals where it is also regulated by oxytocin (*2*, *21–23*). In this case the benefit for the receiver can be due to the buffering of distress in the presence of others, which has been also described in zebrafish (*21*). Thus, approaching and interacting with a distressed individual may prove to be a prosocial behavior in zebrafish, but further evidence is needed.

Discussion

The oxytocin regulation of social transmission of fear in zebrafish described here supports its evolutionary conserved role in emotional contagion, given its similar effects in mammals, where exogeneous administration of oxytocin increases observational fear responses (*10*, *11*). Furthermore, in both zebrafish and rodents, oxytocin also regulates emotion recognition (*25*, *27*), which is the cognitive basis for emotional contagion. Therefore, it is plausible that oxytocin has been recruited early in the evolution of nonapeptides to regulate ancestral empathic behaviors in group living species, and that it has been evolutionarily coopted to regulate more complex empathic behaviors, such as consolation and helping (*26*, *28–30*), in species with more complex cognitive abilities. However, to what extent the social contagion of fear observed in zebrafish and in mammals is homologous, or represents a case of convergent evolution, remains an open question. Although at this stage the homology hypothesis is more parsimonious as it requires fewer evolutionary transitions for the observed similarities, more comparative research across different relevant species is needed to disentangle these two hypotheses. From a human translational research perspective our results contribute to the validation of a phylogenetically distant model of emotional contagion.

REFERENCES AND NOTES

1. F. B. de Waal, *Annu. Rev. Psychol.* **59**, 279–300 (2008).
2. F. B. M. de Waal, S. D. Preston, *Nat. Rev. Neurosci.* **18**, 498–509 (2017).
3. A. Pérez-Manrique, A. Gomila, *Wiley Interdiscip. Rev. Cogn. Sci.* **13**, e1560 (2022).
4. R. F. Oliveira, A. I. Faustino, *Commun. Integr. Biol.* **10**, 44329 (2017).
5. P. F. Silva, C. G. de Leaniz, A. C. Luchiari, *Anim. Behav.* **153**, 95–103 (2019).
6. J. S. Pinho, M. Castilho, J. S. Sollari, R. F. Oliveira, *Genes Brain Behav.* **19**, e12688 (2020).
7. M. Davila Ross, S. Menzler, E. Zimmermann, *Biol. Lett.* **4**, 27–30 (2008).
8. J. Hernandez-Lallement, P. Gómez-Sotres, M. Carrillo, *Neurosci. Biobehav. Rev.* **132**, 1229–1248 (2022).
9. C. Theofanopoulou, G. Gedman, J. A. Cahill, C. Boeckx, E. D. Jarvis, *Nature* **592**, 747–755 (2021).
10. F. Zoratto *et al*., *Neuropharmacology* **143**, 250–267 (2018).
11. M. T. Pisansky, L. R. Hanson, I. I. Gottesman, J. C. Gewirtz, *Nat. Commun.* **8**, 2102 (2017).
12. C. F. Zink, A. Meyer-Lindenberg, *Horm. Behav.* **61**, 400–409 (2012).
13. S. Shahrestani, A. H. Kemp, A. J. Guastella, *Neuropsychopharmacology* **38**, 1929–1936 (2013).
14. N. Speedie, R. Gerlai, *Behav. Brain Res.* **188**, 168–177 (2008).
15. L. A. O'Connell, H. A. Hofmann, *Science* **336**, 1154–1157 (2012).
16. C. Lamm, M. Rütgen, I. C. Wagner, *Neurosci. Lett.* **693**, 49–53 (2019).
17. R. Menon *et al*., *Curr. Biol.* **28**, 1066–1078.e6 (2018).
18. J. Lieberz *et al*., *Neuropsychopharmacology* **45**, 1134–1140 (2020).
19. M. Moaddab, B. I. Hyland, C. H. Brown, *Mol. Cell. Neurosci.* **68**, 323–330 (2015).
20. L. S. Huffman *et al*., *J. Chem. Neuroanat.* **44**, 86–97 (2012).
21. A. I. Faustino, A. Tacão-Monteiro, R. F. Oliveira, *Sci. Rep.* **7**, 44329 (2017).
22. S. D. Preston, F. B. de Waal, *Behav. Brain Sci.* **25**, 1–20, discussion 20–71 (2002).
23. V. Ferretti, F. Papaleo, *Genes Brain Behav.* **18**, e12544 (2019).
24. E. G. I. Nieuwburg, A. Ploeger, M. E. Kret, *Neurosci. Biobehav. Rev.* **123**, 24–47 (2021).
25. V. Ferretti *et al*., *Curr. Biol.* **29**, 1938–1953.e6 (2019).
26. J. P. Burkett *et al*., *Science* **351**, 375–378 (2016).
27. M. M. Rogers-Carter *et al*., *Nat. Neurosci.* **21**, 404–414 (2018).
28. L. F. Li *et al*., *Psychoneuroendocrinology* **103**, 14–24 (2019).
29. A. Yamagishi, J. Lee, N. Sato, *Behav. Brain Res.* **393**, 112790 (2020).
30. S. W. Chang, J. W. Barter, R. B. Ebitz, K. K. Watson, M. L. Platt, *Proc. Natl. Acad. Sci. U.S.A.* **109**, 959–964 (2012).

ACKNOWLEDGMENTS

We thank all members of G. Levkowitz's and R. Oliveira's laboratories for fruitful discussions; Instituto Gulbenkian de Ciência (IGC) Advanced Imaging Facility for technical support; IGC's Fish Facility for animal care and valuable advice; IGC's Histopathology Facility for technical support and valuable advice. **Funding:** This work was funded by a research grant from Fundação para a Ciência e a Tecnologia (FCT, Portugal; ref. PTDC/BIA-COM/30627/2017) awarded to R.F.O.; I.A. was supported by a PhD Fellowship from FCT (PD/BD/106005/2014); K.K. and M.C.T. were supported by postdoc FCT fellowships (2021.01659.CEECIND and PTDC/BIA-COM/31956/2017, respectively). The G.L. laboratory is supported by Israel Science Foundation (1511/16), United States-Israel Binational Science Foundation (2017325), Nella and Leon Benoziyo Center for Neurological Diseases, Richard F. Goodman Yale/Weizmann Exchange Program and Estate of Emile Mimran. G.L. is an incumbent of the Elias Sourasky Professorial Chair. The Advanced Imaging Facility of IGC is supported by the grant PPBI-POCI-01-0145-FEDER-022122, and the Fish Facility is part of Congento, which is supported by grant LISBOA-01-0145-FEDER-022170; both of these grants are cofinanced by the Lisbon Regional Operational Programme (Lisboa 2020), under the Portugal 2020 Partnership Agreement, through the European Regional Development Fund (FEDER) and FCT (Portugal). **Author contributions:** Conceptualization: R.F.O., I.A., and K.K. Funding acquisition: R.F.O., I.A., and G.L. Investigation: I.A., K.K., M.C.T., T.K.R., M.G., and G.P. Methodology: G.L., G.P., and R.F.O. Visualization: I.A., K.K., M.C.T., M.G., and G.P. Writing – original draft: R.F.O., I.A., and K.K. Writing – review and editing: I.A., K.K., M.C.T., T.K.R., M.G., G.P., G.L., and R.F.O. I.A. and K.K. contributed equally to this study, and first authorship was decided alphabetically. **Competing interests:** The authors declare no competing interests. **Data and materials availability:** All data are available in the manuscript or the supplementary material.

License information: Copyright © 2023 the authors, some rights reserved; exclusive licensee American Association for the Advancement of Science. No claim to original US government works. https://www.sciencemag.org/about/science-licenses-journal-article-reuse

SUPPLEMENTARY MATERIALS

science.org/doi/10.1126/science.abq5158
Materials and Methods
Figs. S1 to S6
Tables S1 and S2
Data S1
References (*31–46*)

View/request a protocol for this paper from *Bio-protocol*.

Submitted 14 April 2022; accepted 6 February 2023
10.1126/science.abq5158

CLIMATE ADAPTATION

The evolution of white-tailed jackrabbit camouflage in response to past and future seasonal climates

Mafalda S. Ferreira[1,2,3,4]*†, Timothy J. Thurman[3], Matthew R. Jones[3], Liliana Farelo[1,4], Alexander V. Kumar[5,6], Sebastian M. E. Mortimer[3], John R. Demboski[7], L. Scott Mills[5,8], Paulo C. Alves[1,2,4,5], José Melo-Ferreira[1,2,4]*‡, Jeffrey M. Good[3,5]*‡

The genetic basis of adaptive traits has rarely been used to predict future vulnerability of populations to climate change. We show that light versus dark seasonal pelage in white-tailed jackrabbits (*Lepus townsendii*) tracks snow cover and is primarily determined by genetic variation at endothelin receptor type B (*EDNRB*), corin serine peptidase (*CORIN*), and agouti signaling protein (*ASIP*). Winter color variation was associated with deeply divergent alleles at these genes, reflecting selection on both ancestral and introgressed variation. Forecasted reductions in snow cover are likely to induce widespread camouflage mismatch. However, simulated populations with variation for darker winter pelage are predicted to adapt rapidly, providing a trait-based genetic framework to facilitate evolutionary rescue. These discoveries demonstrate how the genetic basis of climate change adaptation can inform conservation.

Preservation of genetic diversity is a primary goal of conservation biology (*1*), reflecting the critical role that genetic variation plays in promoting rapid adaptation to environmental change (*2*, *3*). Although there has been progress in dissecting the genetic basis of adaptation in some species (*4*–*6*), rarely has such information been used to guide the conservation of populations (*7*, *8*). These shortcomings reflect the difficulties of genetic mapping in natural populations (*9*) and using genotype-to-phenotype maps to facilitate adaptive responses (*7*).

Circannual shifts in morphology, physiology, and behavior cued by changes in photoperiod allow many species to buffer the challenges of seasonal environments (*10*). Seasonal molts to winter-white pelage and plumage have evolved in at least five animal families to maintain crypsis in snow-covered environments (*11*). Winter coloration has been directly tied to survival in snowshoe hares (*12*, *13*), and several species appear vulnerable to camouflage mismatch caused by global snow cover declines (*14*–*18*). We examined how snow cover variation has shaped the evolution and future adaptive potential of winter camouflage in white-tailed jackrabbits (*Lepus townsendii*), a North American species undergoing widespread population declines (*19*).

Winter coat color tracks variation in snow cover across the white-tailed jackrabbit range

Winter coat color varies from brown to white across the white-tailed jackrabbit distribution (*11*, *20*). We used 1312 georeferenced records to estimate a species distribution model (Fig. 1 and figs. S1 and S2A) (*21*) and used climate covariates and 196 museum specimens with mostly white or brown pelage to build a probabilistic model of winter coloration across the range (Fig. 1A and tables S1 and S2).

Consistent with previous work (*11*), the probability of an animal having white pelage increased with snow cover duration and a correlate of snow seasonality (mean diurnal temperature range) and decreased with an index of snow transience (isothermality; table S1). Our model predicted a mosaic of winter-white or -brown populations separated by zones of intermediate coat color probabilities. We found a steep winter color gradient between the Rocky Mountains and the Great Plains of Colorado (Fig. 1C), which included a previously described population with continuous coat color variation (*20*).

The genetic basis of winter coat color

To dissect the genetic basis of winter color variation, we sequenced (62.5×; table S3 and data S1 and S2) and assembled a white-tailed jackrabbit genome (48.03 Mb scaffold N50; table S3). We also sequenced 74 genomes from the coat color polymorphic zone in Colorado (Fig. 1C) to low coverage (~1.8×; table S4), of which seven genomes were also resequenced to moderate coverage (~12.2×; data S1 and table S5). Analysis of 239,834 unlinked single nucleotide polymorphisms (SNPs) showed weak population structure partitioned across two genetic clusters not broadly coincident with coat color variation (fig. S3E; between-cluster weighted fixation index, F_{ST} = 0.036). Spectrophotometric analysis of six dorsal regions (fig. S4) uncovered considerable variation in dorsal brightness, hue, and contrast (n = 61 specimens, 51% variance in the first principal component (PC1) figs. S4 and S5, A and D); variegation (14.6% variance in PC2; figs. S4 and S5, B and E); and mottling (7.5% variance in PC3; figs. S4 and S5, C and F).

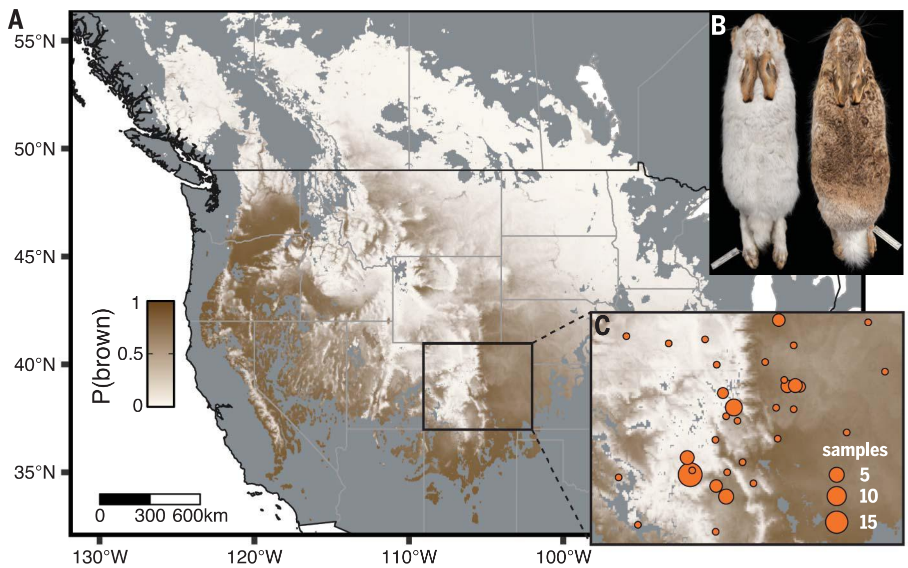


Fig. 1. Winter coat color variation in white-tailed jackrabbits. (**A**) Probability of winter-brown coats across the modeled white-tailed jackrabbit distribution. (**B**) Representative winter coat color variation [Photo credit: IV.ZM.4312.P @ Denver Museum of Nature & Science]. (**C**) Sampling locations used for association mapping across Colorado, scaled by sample size.

[1]CIBIO, Centro de Investigação em Biodiversidade e Recursos Genéticos, InBIO Laboratório Associado, Universidade do Porto, Vairão, Portugal. [2]Departamento de Biologia, Faculdade de Ciências da Universidade do Porto, Porto, Portugal. [3]Division of Biological Sciences, University of Montana, Missoula, MT, USA. [4]BIOPOLIS Program in Genomics, Biodiversity and Land Planning, CIBIO, Vairão, Portugal. [5]Wildlife Biology Program, College of Forestry and Conservation, University of Montana, Missoula, MT, USA. [6]US Fish and Wildlife Service, Fort Collins, CO, USA. [7]Zoology Department, Denver Museum of Nature & Science, Denver, CO, USA. [8]Office of Research and Creative Scholarship, University of Montana, Missoula, MT, USA.
***Corresponding author. Email: sferreira.mafalda@gmail.com (M.S.F); jmeloferreira@cibio.up.pt (J.M.-F.); jeffrey.good@umontana.edu (J.M.G)**
†Present address: Department of Medical Biochemistry and Microbiology, Uppsala University, Uppsala, Sweden.
‡These authors contributed equally to this work.

White versus brown categories used in our binary phenotypic model (Fig. 1) consistently partitioned continuous color variation along PC1 (fig. S4B). Genome-wide association tests between 5,557,716 SNPs and PC1 of the spectrophotometric data revealed significant associations robust to population structure on two scaffolds, each containing one gene involved in melanogenesis (Fig. 2 and fig. S6).

One association centered on corin serine peptidase (*CORIN*; Fig. 2B; $P = 7.26 \times 10^{-16}$), a serine peptidase expressed in hair follicles that acts as a downstream suppressor of the agouti signaling protein (*ASIP*) (*22*). Loss-of-function mutations in *CORIN* have been associated with enlarged pheomelanin bands and lighter pelage in tigers (*23*) and mice (*24*). The other association centered on the endothelin receptor type B (*EDNRB*, Fig. 2D; $P = 3.31 \times 10^{-22}$), a G protein-coupled receptor essential to developmental migration and differentiation of melanocyte precursors (*25*, *26*). *EDNRB* mutations cause white piebald spotting due to absence of melanocytes (*27*). For both genes, top associated variants were noncoding, consistent with a regulatory basis of seasonal camouflage variation.

We also performed association tests on all 74 jackrabbits, binning color as white or brown, and found two additional associations. One overlapped a noncoding region ($P = 1.29 \times 10^{-14}$; figs. S6B and S7) near genes from the α2-macroglobulin gene family, which have been linked to reproduction (*28*–*30*), and may reflect a correlated seasonal trait. The other overlapped *ASIP* ($P = 1.38 \times 10^{-14}$; fig. S6B), a well-known signaling protein that shifts melanogenesis to lighter phaeomelanin production or inhibits pigment production (*31*). *ASIP* has been associated with discrete winter coat color polymorphisms in snowshoe and mountain hares (*6*, *32*).

We next used mass spectrometry to generate high-confidence genotypes for 59 jackrabbits with spectrophotometric data at 34 linked SNPs (average within-gene $r^2 \geq 0.93$) across *CORIN* (n = 13 SNPs), *EDNRB* (n = 9 SNPs), and *ASIP* (n = 12 SNPs) (fig. S8 and data S1 and S3). *CORIN* ($P = 6.82 \times 10^{-9}$) and *EDNRB* ($P = 7.73 \times 10^{-12}$) alleles remained strongly associated with PC1 (tables S6 and S7), showing largely additive (Fig. 2, C and E; all $P > 0.05$, dominance deviation test; tables S8 and S9) and independent effects ($P > 0.05$; Fig. 2F, fig. S9, and table S10). *ASIP* was not associated when including the other genes as covariates (tables S6 and S7), but we detected epistatic interactions between the top associated SNPs at *ASIP* and *CORIN* ($P < 0.05$; table S10), consistent with known molecular interactions between these genes (*22*). A linear model of the top associated SNPs from each gene explained 65% of phenotypic variation (model D, table S11). Although a precise estimate of effect sizes awaits more sampling, winter camouflage in white-tailed jackrabbits

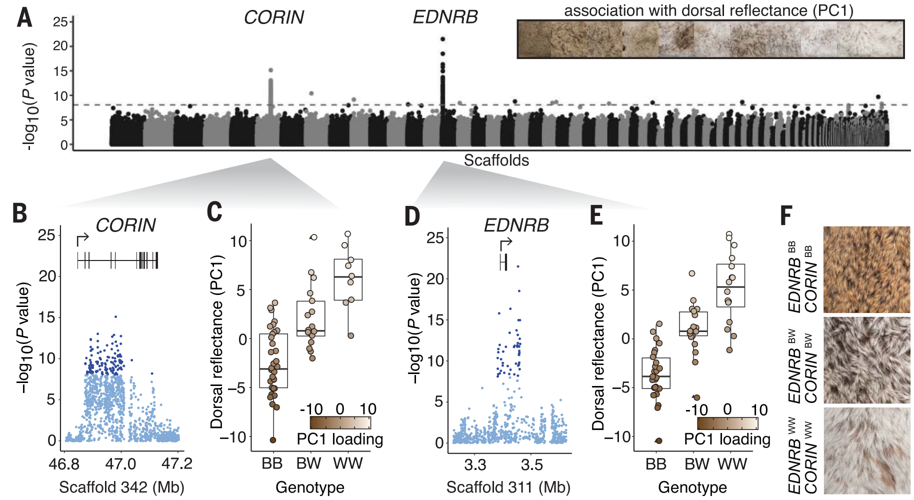


Fig. 2. The genetic basis of winter coat color variation. (**A**) Genome-wide associations ($-\log_{10}P$ values; 5,557,716 SNPs) with winter coat color (inset: dorsal photos ordered by PC1) of 61 jackrabbits (dashed line, Bonferroni-corrected $P = 0.05$). (**B** to **E**) Local associations, gene structures, and dorsal reflectance across assayed diploid genotypes (BB, homozygous brown; BW, heterozygous; WW, homozygous white) for *CORIN* (B and C) and *EDNRB* (D and E). Significant associations are highlighted in dark blue (Bonferroni-corrected $P \leq 0.05$). (**F**) Dorsal images of specimens with double homozygous or heterozygous *CORIN* and *EDNRB* genotypes [Photo credit: IV.ZM.4312.P @ Denver Museum of Nature & Science].

appears to be primarily determined by large-effect additive genetic variation at *CORIN* and *EDNRB*, with a minor contribution of *ASIP*.

Multigenic winter camouflage adaptation is shaped by selection on ancient genetic polymorphisms and gene flow between species

Genome-wide comparisons among white-tailed jackrabbit genomes revealed increased scaled absolute genetic divergence between winter-white and winter-brown associated alleles of *CORIN*, *EDNRB*, and *ASIP* (Z-score ≥ 3; Fig. 3A and fig. S10), indicating that seasonal camouflage variation did not arise from recent mutations in white-tailed jackrabbits. To examine the history of these genes, we combined white-tailed jackrabbit genomes with 10 new and 19 previously published (*6*, *32*–*36*) genomes (~7.5 to 33.5×; table S5) from nine other *Lepus* species, including four showing seasonal camouflage (data S1). Genome-wide analysis clustered white-tailed jackrabbits with three other color-changing species (Fig. 3B, fig. S11, and table S12). *CORIN*, *EDNRB*, and *ASIP* showed discordant local genealogies whereby winter-brown alleles from white-tailed jackrabbits grouped with black-tailed jackrabbits, a winter-brown species, whereas winter-white alleles grouped with closely related winter-white species (Fig. 3B and fig. S12). The estimated divergence time between the white and brown haplotypes exceeded 3 million years (Myr) at all three genes [*EDNRB* = 4.2 Myr (95% highest posterior density (HPD) 3.3 to 5.0 Myr); *CORIN* = 3.3 Myr (95% HPD 2.9 to 4.3 Myr); *ASIP* = 3.1 Myr (95% HPD 2.4 to 3.7 Myr); fig. S13], suggesting a common ancestor near the onset of *Lepus* diversification (*37*).

Deep phylogenetic discordance at each gene could reflect gene flow from another species (*38*). Consistent with this, divergence (d_{xy}) across an ~88-kb interval overlapping *ASIP* was reduced between black-tailed jackrabbits and the white-tailed jackrabbit brown allele relative to simulated expectations (Fig. 3C; fig. S14, B and C; and table S13). By contrast, the white allele showed normal levels of divergence compared to other winter-white hares (Fig. 3D and fig. S14D). Black- and white-tailed jackrabbits occupy similar prairie habitats with overlapping ranges and show substantial genome-wide introgression (D-statistic = 0.19, $P << 0.0001$; 4% admixture (f_G), $P << 0.0001$). The persistence of introgressed alleles, a binary association (fig. S6B), and a central role in color evolution (*31*) suggest that *ASIP* contributes to a component of color variation not captured by our measurements. This is the third instance of introgression at *ASIP* contributing to winter camouflage in hares (Fig. 3B) (*6*, *32*), suggesting that some genes may be evolutionary hotspots for adaptive introgression (*39*).

The evolutionary processes shaping variation at *CORIN* and *EDNRB* were less clear. Divergence (d_{xy}) between black-tailed jackrabbits and the brown-associated intervals of both genes were not unusually shallow (Fig. 3C), as expected with recent introgression. However, closer inspection revealed local phylogenetic variation that is consistent with ancient gene flow (fig. S14). Although the causative mutations remain unknown, the top associated

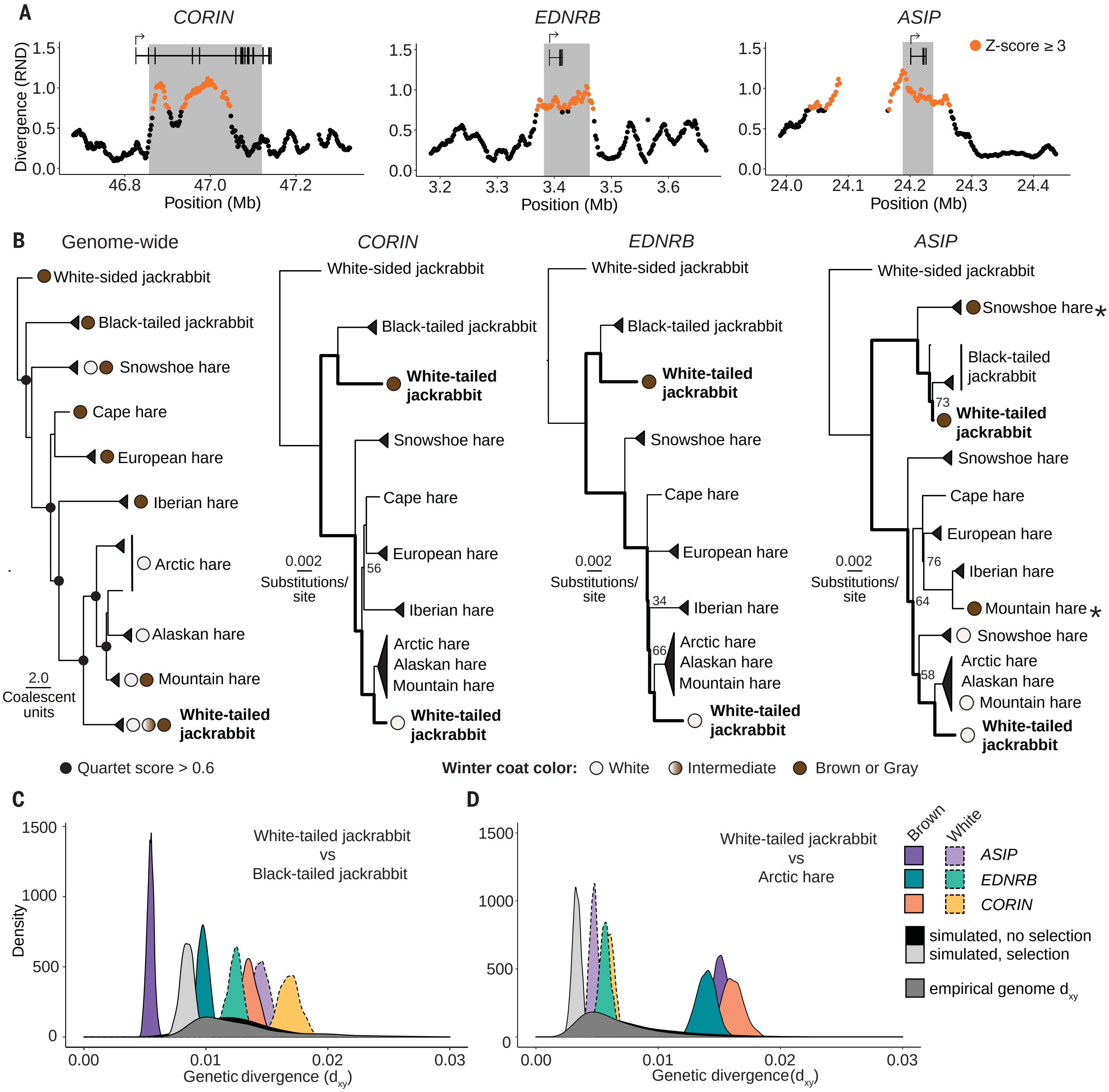


Fig. 3. Evolution of winter coat color variation. (**A**) Scaled absolute genetic divergence (RND) in 20-kb sliding windows (dots, 2-kb step size) between one homozygous winter-white and winter-brown genome. Association intervals are gray, orange dots are windows of elevated divergence (RND Z-score ≥ 3), and gaps represent missing data in the reference assembly. (**B**) Phylogenies of *CORIN*, *EDNRB*, and *ASIP* (associated intervals) differed from the multispecies coalescent tree (43,430 50-kb windows, fig. S11). An asterisk denotes species for which winter pelage variation has previously been associated with introgression (*6*, *33*). Branches with bootstrap support <80 are labeled. (**C** and **D**) Empirical and simulated distributions of genetic divergence (d_{xy}) genome-wide and for *CORIN*, *EDNRB*, and *ASIP* between white-tailed jackrabbits and (C) black-tailed jackrabbits or (D) Arctic hares.

SNPs at both genes fell outside putative introgression tracts. These patterns suggest a history of recombination among ancient color alleles at *CORIN* and *EDNRB*, likely maintained by long-term spatially varying selection (*40*). Collectively, these findings indicate that multigenic winter camouflage adaptation (Fig. 1), shaped by selection on standing and introgressed variation (Fig. 3), has long been important to white-tailed jackrabbit survival.

Future climate change vulnerability and adaptive potential of seasonal camouflage variation

Seasonal snow cover is predicted to decline over the next century (*41*), which may reduce the adaptive value of winter-white coats (*11*).

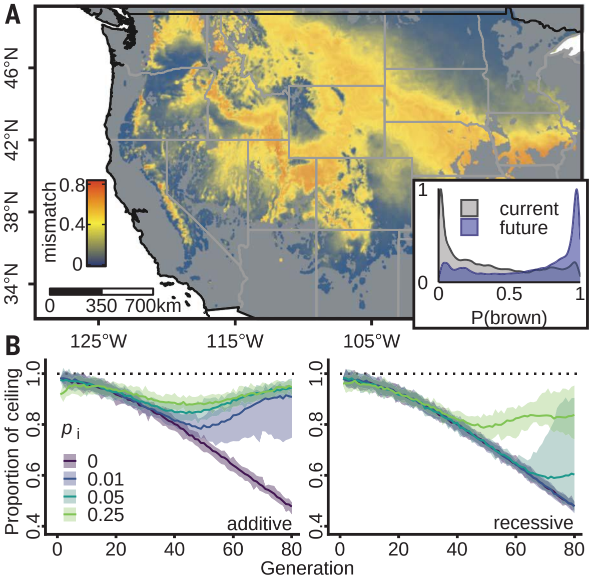


Fig. 4. Adaptation to future climate-induced mismatch. (**A**) Predicted phenotypic mismatch ($\Delta P_{(brown)}$) in 2080 using RCP8.5 forecasts of snow residence time, mean diurnal temperature range, and isothermality (inset: predicted probability shifts toward winter-brown across the USA range). (**B**) Simulated size trajectories of populations (30 replicates; lines, averages; ribbons, 95% quantiles) experiencing future camouflage mismatch ($\Delta P_{(brown)}$ = 0.75) shown as a proportion of the population ceiling (dotted line) assuming standing variation of additive (left panel) or recessive (right panel) brown alleles at *CORIN* and *EDNRB*.

To understand how jackrabbit camouflage might evolve in response to climate change, we forecasted winter coat color probabilities for the year 2080 on the basis of correlates of snow residence time, seasonality, and transience (Fig. 4A and fig. S2, D to F). We used forecasts under a high–CO_2 emissions scenario [Representative Concentration Pathway (RCP) 8.5] to model challenging, though not unlikely (*42*), conditions that jackrabbits may experience in the future. Under this model, winter-brown coats ($P_{(brown)} \geq 0.8$) will be strongly favored across much of the southern (USA) range (~49% at $P_{(brown)} \geq 0.8$ in 2080; fig. S2, B to F), a 3.1-fold increase over historical conditions (16% at $P_{(brown)} \geq 0.8$). Although the rate of mismatch will depend on which emissions scenario transpires, future reductions in snow cover are likely to induce widespread camouflage mismatch (Fig. 4A) given strong correlations of forecasted parameters across emission scenarios (*21*).

Previous work proposed that standing variation for seasonal camouflage could promote rapid evolutionary rescue in species threatened by diminished snow cover (*11*). To understand if the genetic basis of camouflage inferred from Colorado populations may facilitate evolutionary rescue more broadly, we sequenced 69 additional white-tailed jackrabbit genomes from across the range (~2.1×; table S14). Although winter phenotypes were mostly unknown for these samples, we found low genetic structure (F_{ST} = 0.020 Colorado versus North Dakota) and color-associated polymorphisms outside of Colorado at all three genes (fig. S15). Moreover, the presence of white alleles at the three genes was positively correlated with snow cover duration across the range (r = 0.33 to 0.46, $p < 0.05$; fig. S16). Therefore, multigenic color-associated variation appears functionally relevant and broadly shared across the range.

Next, we simulated the capacity for populations with the largest forecasted mismatch ($\Delta P_{(brown)}$ = 0.75) to adapt to changes in snow cover. Focusing on large-effect variation at *CORIN* and *EDNRB*, we found that populations without winter-brown alleles trended toward extinction, whereas populations with winter-brown alleles could adapt rapidly. Evolutionary rescue was likely even under a high-emissions scenario and when adaptive winter-brown alleles were initially rare (Fig. 4B and figs. S17 and S18). However, the efficacy of selection depended on genetic dominance. Fully recessive winter-brown variation, as found in other hares (*6*, *32*), was associated with slower responses and larger population declines (Fig. 4B and fig. S18). Thus, the capacity for evolutionary rescue to buffer against future population declines in this and other species confronted by seasonal mismatch (*11*) will depend on local demography, the genetic architecture of adaptive traits, and frequencies of adaptive alleles (*3*).

Toward a framework for prioritizing and facilitating conservation efforts

Optimism that standing variation could enable evolutionary rescue in the face of camouflage mismatch is tempered by widespread population declines in white-tailed jackrabbits caused by habitat alteration, extermination, shifts in predator communities, and climate change (*19*) coupled with the emerging threat of rabbit hemorrhagic disease virus (*43*). Using regional conservation assessments (*19*), we found that populations predicted to harbor winter-brown variation ($P_{(brown)} \geq 0.8$) have disproportionately experienced local declines or extirpations (Pearson's χ^2 test P value = 2.2×10^{-16}; Cramér's V = 0.31; fig. S2C). Given these threats, our predictive map of climate-induced camouflage mismatch (Fig. 4A) provides an initial framework for prioritizing conservation efforts. Adaptive potential may be enhanced through local management actions aimed at reducing anthropogenic stressors and promoting connectivity between populations harboring critical winter-brown variation. Our findings also enable quantification of color-associated variation in vulnerable populations by using any DNA source without knowledge of winter phenotypes. In the absence of connectivity or standing variation, our simulations suggest that local adaptation could be accelerated by modest amounts of human-assisted gene flow to mismatched populations (*44*).

Safeguarding the adaptive potential of populations is central for conservation (*1*), yet the genetic basis of adaptation is rarely incorporated into applied conservation planning (*11*, *45*). Landscape genomic approaches have proven useful for uncovering adaptive genetic variation and climate change vulnerability without knowledge of phenotypes (*46*, *47*). Our results show why a deeper understanding of the genetic basis of adaptive traits may also be needed to predict future responses of populations threatened by climate change and how such insights may be applied to facilitate evolutionary rescue.

REFERENCES AND NOTES

1. O. H. Frankel, M. E. Soulé, *Conservation and Evolution* (Cambridge Univ. Press, Cambridge, 1981).
2. R. A. Bay *et al.*, *Am. Nat.* **189**, 463–473 (2017).
3. M. Kardos, G. Luikart, *Am. Nat.* **197**, 511–525 (2021).
4. S. Lamichhaney *et al.*, *Science* **352**, 470–474 (2016).
5. R. D. H. Barrett *et al.*, *Science* **363**, 499–504 (2019).
6. M. R. Jones *et al.*, *Science* **360**, 1355–1358 (2018).
7. M. Kardos, A. B. A. Shafer, *Trends Ecol. Evol.* **33**, 827–839 (2018).
8. T. Q. Thompson *et al.*, *Proc. Natl. Acad. Sci. U.S.A.* **116**, 177–186 (2019).
9. J. M. Cohen, M. J. Lajeunesse, J. R. Rohr, *Nat. Clim. Chang.* **8**, 224–228 (2018).
10. B. Helm *et al.*, *Proc. Biol. Sci.* **280**, 20130016 (2013).
11. L. S. Mills *et al.*, *Science* **359**, 1033–1036 (2018).
12. M. Zimova, L. S. Mills, J. J. Nowak, *Ecol. Lett.* **19**, 299–307 (2016).
13. E. C. Wilson, A. A. Shipley, B. Zuckerberg, M. Z. Peery, J. N. Pauli, *Conserv. Lett.* **12**, e12614 (2019).
14. L. S. Mills *et al.*, *Proc. Natl. Acad. Sci. U.S.A.* **110**, 7360–7365 (2013).
15. K. Atmeh, A. Andruszkiewicz, K. Zub, *Sci. Rep.* **8**, 7648 (2018).
16. S. M. Sultaire *et al.*, *Proc. Biol. Sci.* **283**, 20153104 (2016).
17. S. Pedersen, M. Odden, H. C. Pedersen, *Ecosphere* **8**, e01722 (2017).
18. E. C. Wilson, B. Zuckerberg, M. Z. Peery, J. N. Pauli, *Biol. Conserv.* **249**, 108731 (2020).
19. D. E. Brown, A. T. Smith, J. K. Frey, B. R. Schweiger, *J. Fish Wildl. Manag.* **11**, 341–352 (2020).
20. R. M. Hansen, G. D. Bear, *J. Mammal.* **44**, 420–422 (1963).
21. Supplementary Materials Online.
22. D. Enshell-Seijffers, C. Lindon, B. A. Morgan, *Development* **135**, 217–225 (2008).
23. X. Xu *et al.*, *Cell Res.* **27**, 954–957 (2017).
24. E. Avigad Laron, E. Aamar, D. Enshell-Seijffers, *J. Invest. Dermatol.* **139**, 257–259 (2019).
25. M. Takeo *et al.*, *Cell Rep.* **15**, 1291–1302 (2016).
26. H. Li *et al.*, *Sci. Rep.* **7**, 7272 (2017).
27. K. Hosoda *et al.*, *Cell* **79**, 1267–1276 (1994).
28. H. Kashiwagi, H. Ishimoto, *Sci. Rep.* **10**, 1–13 (2020).

29. C. Tayade, S. Esadeg, Y. Fang, B. A. Croy, . *Mol. Cell. Endocrinol.* **245**, 60–66 (2005).
30. R. Sayegh, J. T. Awwad, C. Maxwell, B. Lessey, K. Isaacson, *J. Clin. Endocrinol. Metab.* **80**, 1021–1026 (1995).
31. M. Manceau, V. S. Domingues, R. Mallarino, H. E. Hoekstra, *Science* **331**, 1062–1065 (2011).
32. I. Giska *et al*., *Proc. Natl. Acad. Sci. U.S.A.* **116**, 24150–24156 (2019).
33. M. R. Jones, L. S. Mills, J. D. Jensen, J. M. Good, *Am. Nat.* **196**, 316–332 (2020).
34. M. R. Jones, L. S. Mills, J. D. Jensen, J. M. Good, *Evolution* **74**, 2033–2045 (2020).
35. F. A. Seixas, P. Boursot, J. Melo-Ferreira, *Genome Biol.* **19**, 91 (2018).
36. F. Seixas, thesis, University of Porto and University of Montpellier, Porto and Montpellier (2017).
37. M. S. Ferreira *et al*., *Syst. Biol.* **70**, 593–607 (2021).
38. S. Joly, P. A. McLenachan, P. J. Lockhart, *Am. Nat.* **174**, E54–E70 (2009).
39. M. Moest *et al*., *PLOS Biol.* **18**, e3000597 (2020).
40. D. Charlesworth, *PLOS Genet.* **2**, e64 (2006).
41. G. T. Pederson *et al*., *Science* **333**, 332–335 (2011).
42. C. R. Schwalm, S. Glendon, P. B. Duffy, *Proc. Natl. Acad. Sci. U.S.A.* **117**, 19656–19657 (2020).
43. J. Asin *et al*., *Transbound. Emerg. Dis.* **69**, e394–e405 (2021).
44. S. N. Aitken, M. C. Whitlock, *Annu. Rev. Ecol. Evol. Syst.* **44**, 367–388 (2013).
45. J. C. Teixeira, C. D. Huber, *Proc. Natl. Acad. Sci. U.S.A.* **118**, e2015096118 (2021).
46. O. Razgour *et al*., *Proc. Natl. Acad. Sci. U.S.A.* **116**, 10418–10423 (2019).
47. R. A. Bay *et al*., *Science* **359**, 83–86 (2018).
48. M. S. Ferreira, MafaldaSFerreira/wtjr_camouflage, v. 1.0.0 (2022); https://doi.org/10.5281/zenodo.7324926.
49. T. J. Thurman, tjthurman/wtjr_sdm, v. 0.9.0 (2022); https://doi.org/10.5281/zenodo.7373507.

ACKNOWLEDGMENTS

L. Rossier, T. Williams, N. Herrera, B. Davis, E. Larson, J. Sweatman, M. McLaughlin, USDA Wildlife Services (North and South Dakota), and Colorado Parks and Wildlife (Gunnison and Monte Vista) assisted in sample collection. We thank L. Olson, E. Braker, E. Rickart, A. Hornsby, E. Westwig, N. Duncan, A. Doll and J. Stephenson for access to museum collections and R. Wicker for specimen photographs (IV.ZM.4312.P ©DENVER MUSEUM OF NATURE & SCIENCE). We thank P. Boursot, J. Jensen, M. Kardos, members of EVOCHANGE, the UNVEIL Network and CIBIO-InBIO, T. Wheeler, and the UM Genomics Core for helpful discussions and experimental support. Sequencing was performed at Novogene Technology Co., Ltd (Davis, CA), and UC Davis Genome Center (Davis, CA). Computational resources were provided by Griz Shared Computing Cluster and CIBIO New-Gen platform. **Funding:** National Science Foundation (NSF), EPSCoR grant (OIA-1736249) (J.M.G.). Fundação para a Ciência e a Tecnologia (FCT), "2CHANGE" PTDC/BIA-EVL/28124/2017, cofunded by ERDF through COMPETE 2020 POCI-01-0145-FEDER-028124 (J.M.-F.). FCT, PhD grant PD/BD/108131/2015 (POPH-QREN funds from ESF and Portuguese MCTES/FCT) (M.S.F.). FCT, 2021.00150. CEECIND (J.M.-F). NSF, DEB-1907022 (L.S.M., J.M.G.), DGE-1702043 (M.R.J.), DGE-1313190 (M.R.J.), and PRFB-1907243 (T.J.T.). Society for the Study of Evolution, Rosemary Grant Graduate Student Research Award (M.S.F.). European Society for Evolutionary Biology, Godfrey Hewitt Mobility Award (M.S.F.). Fundação Luso-Americana para o Desenvolvimento, Portugal-United States of America Research Networks Program (M.S.F., P.C.A.). European Union's Seventh Framework Programme, grant no. 286431 (CIBIO New-Gen). GenomePT POCI-01-0145-FEDER-022184. National Institutes of Health Shared Instrumentation Grant 1S10OD010786-01 (UC Davis Genome Center). **Author contributions:** Conceptualization: M.S.F., L.S.M., P.C.A., J.M.-F., J.M.G. Supervision: J.M.-F., J.M.G. Data Curation: M.S.F., T.J.T. Validation: M.S.F., T.J.T. Investigation: M.S.F., T.J.T., P.C.A., J.M.G., M.R.J., L.F., S.M.E.M. Formal analysis: M.S.F., T.J.T., A.V.K. Resources: L.S.M., J.R.D., J.M.-F., J.M.G. Funding acquisition: M.S.F., L.S.M., P.C.A., M.R.J., T.J.T., J.M.-F., J.M.G. Visualization: M.S.F., T.J.T., J.M.-F., J.M.G. Writing – original draft: M.S.F., J.M.-F., J.M.G. Writing – review and editing: All authors **Competing interests:** None declared. **Data and materials availability:** Sequence data are available in NCBI (BioProject PRJNA726805, SAMN19037327-SAMN19037409, SAMN30246380-SAMN30246447; BioProjects PRJNA420081, PRJNA242290, PRJNA399194, PRJNA561428, PRJNA564335; data S1). Genotype, spectrophotometry data, and the annotated *L. townsendii* reference genome are deposited in Figshare (https://figshare.com/s/0a2dce1d3a6cf15d0e3d) and NCBI (PRJNA729659, PRJNA729660). Analysis code and related resources are archived in Zenodo (*48*, *49*).

License information: Copyright © 2023 the authors, some rights reserved; exclusive licensee American Association for the Advancement of Science. No claim to original US government works. https://www.sciencemag.org/about/science-licenses-journal-article-reuse

SUPPLEMENTARY MATERIALS

science.org/doi/10.1126/science.ade3984
Materials and Methods
Figs. S1 to S18
Tables S1 to S14
Data S1 to S4
References (*50*–*121*)
MDAR Reproducibility Checklist

Submitted 13 August 2022; accepted 27 February 2023
10.1126/science.ade3984

NANOMATERIALS

Direct synthesis and chemical vapor deposition of 2D carbide and nitride MXenes

Di Wang[1], Chenkun Zhou[1], Alexander S. Filatov[1], Wooje Cho[1], Francisco Lagunas[2], Mingzhan Wang[3], Suriyanarayanan Vaikuntanathan[1], Chong Liu[3], Robert F. Klie[2], Dmitri V. Talapin[1,3,4]*

Two-dimensional transition-metal carbides and nitrides (MXenes) are a large family of materials actively studied for various applications, especially in the field of energy storage. MXenes are commonly synthesized by etching the layered ternary compounds, called MAX phases. We demonstrate a direct synthetic route for scalable and atom-economic synthesis of MXenes, including compounds that have not been synthesized from MAX phases, by the reactions of metals and metal halides with graphite, methane, or nitrogen. The direct synthesis enables chemical vapor deposition growth of MXene carpets and complex spherulite-like morphologies that form through buckling and release of MXene carpet to expose fresh surface for further reaction. The directly synthesized MXenes showed excellent energy storage capacity for lithium-ion intercalation.

MXenes, where M stands for early transition metal (such as Ti, V, Nb, or Mo) and X is C or N, are a large family of two-dimensional (2D) transition-metal carbides and nitrides. Since the discovery of $Ti_3C_2T_x$ (T = O, OH, and F) in 2011 (*1*), MXenes have been commonly synthesized from crystalline MAX phases (where A is typically Al, Si, or Ga) through selective etching of A atoms with hydrofluoric acid (HF)–containing solutions (*1*–*3*) or Lewis acidic molten salts (*4*, *5*), followed by the delamination of the MXene sheets (*6*). Interest in MXenes continues to grow because of their potential applications in energy storage (*7*, *8*), electromagnetic interference (EMI) shielding (*9*, *10*), transparent conductive layers (*11*), superconductivity (*5*), and catalysis (*12*). Moreover, the aforementioned T components in MXenes can be replaced with covalently bonded surface groups, including organic molecules, either during etching of the MAX phases (*4*, *13*), or through postsynthetic modifications of surface groups (*5*). As such, opportunities are available to combine the benefits of 2D MXenes, such as a low diffusion barrier for cation intercalation (*14*), excellent electrical and thermal conductivity (*3*), and nearly endless tailorability of molecular surface groups.

Preparations of MXenes through high-temperature synthesis and chemical etching of MAX (*15*) or non-MAX (*16*, *17*) phases require high energy consumption, show poor atom economy, and use large amounts of hazardous HF or Lewis acidic molten salts. The development of direct synthetic methods would facilitate practical applications of the rapidly developing family of functional MXenes. An ideal approach would involve a reaction of inexpensive precursors into MXenes bypassing intermediate MAX phases. In 2019, Druffel *et al.* reported the synthesis of Y_2CF_2 with a MXene-like structure from the solid-state reaction between YF_3, Y metal, and graphite (*18*), based on the previously reported synthesis of Sc, Y, and Zr metal carbide halides by Hwu *et al.* in 1986 (*19*).

Among about 100 known MXene structures, Ti MXenes show some of the best combinations of physical and chemical properties (*20*) relevant to a variety of applications (*21*). We show that Ti_2CCl_2 and Ti_2NCl_2 MXenes can be directly synthesized from Ti metal, titanium chlorides ($TiCl_3$ or $TiCl_4$), and various carbon or nitrogen sources, including graphite, CH_4, or N_2. The directly synthesized MXenes (denoted as DS-MXenes) can be delaminated, and their surface groups can be replaced with other molecules through nucleophilic substitution or completely removed by means of reductive elimination (*5*). Besides convenience and scalability, the direct synthesis routes offer synthetic modalities not compatible with traditional MAX etching methods. For example, we demonstrated chemical vapor deposition (CVD) synthesis of extended carpets of Ti_2CCl_2, Ti_2NCl_2, Zr_2CCl_2, and Zr_2CBr_2 MXene sheets oriented perpendicular to the substrate. Such orientations make MXene surfaces easily accessible for ion intercalation (*7*, *22*) and chemical or electrochemical transformations (*23*, *24*) by exposing edge sites with high catalytic activity (*25*, *26*).

Direct synthesis of Ti_2CCl_2 MXene

The synthesis of DS-Ti_2CCl_2 was accomplished through the high-temperature reaction between Ti, graphite, and $TiCl_4$ (Fig. 1A). Titanium and graphite were ground into a fine powder in a 3:1.8 molar ratio and combined with 1.1 molar equivalent $TiCl_4$. The mixture was sealed in a quartz ampoule and heated to 950°C in 20 min, and the temperature was maintained until the reaction was finished; typically, 2 hours is sufficient for maximum yield of MXene. The reaction could be performed on a multigram scale (fig. S1) and should be easily amenable to further scaling.

Powder x-ray diffraction (XRD) and structural analysis by means of Rietveld refinement of the as-synthesized reaction products (Fig. 1B) revealed the presence of a Ti_2CCl_2 MXene phase with the lattice parameters a = 3.2284(2) Å and c = 8.6969(1) Å (numbers in parentheses are standard uncertainties), which are near the values reported for Ti_2CCl_2 MXene synthesized by etching of Ti_2AlC MAX phase with Lewis acidic molten salt (referred to as MS-MXenes) (*5*). Cubic TiC_x (x = 0.5 to 1) was often present as a by-product but could be efficiently removed through its precipitation from nonaqueous dispersions of the raw product prepared, for example, by means of ultrasonic dispersion in propylene carbonate (PC) or delamination of DS-Ti_2CCl_2 with n-butyllithium (n-BuLi) (Fig. 1C).

The formation of Ti_2CCl_2 MXene was observed initially at ~850°C, and the yield of MXene was maximal at 950°C (fig. S2A). TiC_x became the dominant reaction product at temperatures >1000°C. At 950°C, the formation of Ti_2CCl_2 phase was observed after 2 hours, and the ratio between Ti_2CCl_2 and TiC_x in products did not change substantially after increasing reaction time from 2 hours to 10 days at this temperature (fig. S2B). This finding naturally raises a question whether MXene was the kinetic or thermodynamic product of the reaction. We noticed that MXene phase did not form when we attempted to react TiC_x with Ti and $TiCl_3$ or $TiCl_4$ (fig. S2C). However, prolonged heating of purified MS-Ti_2CCl_2 at 950°C resulted in a partial conversion into TiC_x (fig. S3). We concluded from these observations that Ti_2CCl_2 was a kinetically favored phase forming in competition with TiC_x.

The XRD patterns of DS-Ti_2CCl_2 synthesized from $TiCl_3$ or $TiCl_4$ were similar (fig. S4B), as were scanning electron microscopy (SEM) images of the products' morphology, represented by large MXene stacks (Fig. 1D and figs. S5 and S6). A high-resolution high-angle annular dark field (HAADF) scanning transmission electron microscopy (STEM) image of DS-Ti_2CCl_2 oriented along the $[2\bar{1}\bar{1}0]$ zone axis and its corresponding electron energy loss spectroscopy (EELS) elemental maps are shown in Fig. 1, F and G, respectively. The center-to-center distance between MXene sheets calculated from the HAADF image is 0.87 ± 0.06 nm (fig. S7), which is in agreement with the value of 0.87 ± 0.02 nm measured with XRD on multiple samples. DS-Ti_2CCl_2 MXene sheets contained Ti and

[1]Department of Chemistry and James Franck Institute, University of Chicago, Chicago, IL 60637, USA. [2]Department of Physics, University of Illinois Chicago, Chicago, IL 60607, USA. [3]Pritzker School of Molecular Engineering, University of Chicago, Chicago, IL 60637, USA. [4]Center for Nanoscale Materials, Argonne National Laboratory, Argonne, IL 60439, USA.
*Corresponding author. Email: dvtalapin@uchicago.edu

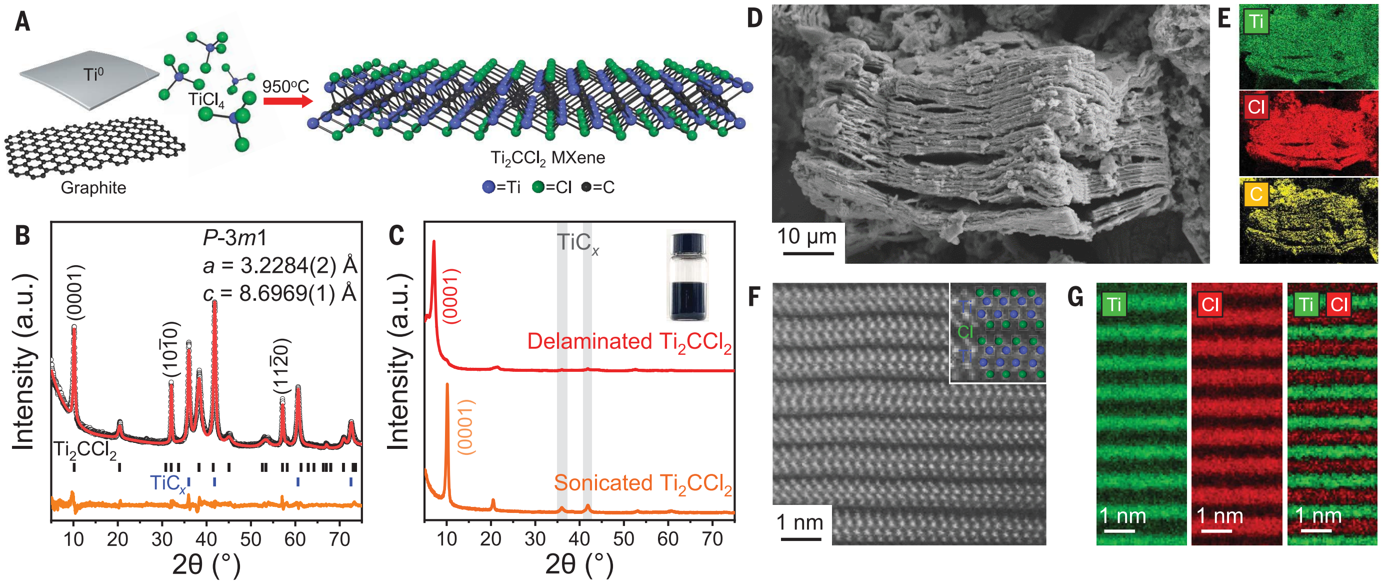


Fig. 1. Direct synthesis and characterization of DS-Ti_2CCl_2 MXene. (**A**) Schematic diagram of the synthesis. (**B**) XRD pattern and Rietveld refinement of DS-Ti_2CCl_2 prepared by reacting Ti, graphite, and $TiCl_4$ at 950°C. (**C**) XRD patterns of dispersible delaminated and sonicated DS-Ti_2CCl_2 MXenes. (Inset) Colloidal solution of the delaminated DS-Ti_2CCl_2. (**D**) SEM image and (**E**) EDX elemental mapping of a DS-Ti_2CCl_2 stack. (**F**) High-resolution HAADF image and (**G**) EELS atomic column mapping representing the layered structure of DS-Ti_2CCl_2.

Cl with an atomic ratio of 49.9:50.1 (fig. S8), which is near the ideal 1:1 stoichiometry. This ratio suggested that the full coverage of MXene surfaces with Cl was achieved. In comparison, the MXenes synthesized by using the traditional MAX-exfoliation route are often deficient in surface coverage, with a typical stoichiometry of $Ti_2CCl_{1.5–1.7}$ (*5*). The formation of Cl-terminated titanium carbide sheets was further confirmed by characteristic binding energies (fig. S9) in the x-ray photoelectron spectroscopy (XPS) (*27*). All these features, together with the assessment of crystal quality from linewidths in Raman spectra (fig. S10), confirmed the high degree of structural perfection of our DS-Ti_2CCl_2 product.

As-synthesized DS-Ti_2CCl_2 MXene stacks could be delaminated and solution-processed as individual 2D monolayers (Fig. 1C and fig. S11). For delamination, multilayer MXene was first intercalated with Li^+ by treatment with 2.5 M *n*-BuLi hexane solution (fig. S12A) (*5*, *28*) then shaken with polar solvents such as *N*-methylformamide (NMF) or 2,6-difluoropyridine (DFP) to form a suspension of delaminated 2D sheets (fig. S13). Insoluble by-products were selectively precipitated by a mild centrifugation at 240 g for 15 min (fig. S12B). In delaminated DS-Ti_2CCl_2, the (0001) diffraction peak shifted to a lower 2θ angle of 7.02°, corresponding to the enlarged *d*-spacing of 12.54 Å, from the original 8.70 Å. A similar *d*-spacing expansion was found in delaminated $Ti_3C_2Cl_2$ MXenes (from 11.08 to 14.96 Å) (*5*). Delamination of DS-Ti_2CCl_2 MXenes can be performed on a multigram scale, producing ~25 g·liter^{-1} colloidal dispersions that can be stable for months under N_2 atmosphere (fig. S14).

CVD of MXenes

CVD is a versatile technique for synthesizing films, heterostructures, and complete devices by reacting gaseous precursors on a substrate. Although transition-metal carbides and nitrides such as Mo_2C, Mo_2N, and TiC_x can be grown with CVD (*29*–*31*), such a synthetic option has not been previously available for MXenes. We introduce the direct synthesis of MXenes through CVD and show a route to new morphologies of MXenes with more easily accessible surfaces and exposed catalytically active edges.

We grew MXenes by CVD at 950°C on a Ti surface with a CH_4 and $TiCl_4$ gas mixture diluted in Ar (Fig. 2A). After the exposure for 15 min, the as-synthesized product (denoted as CVD-Ti_2CCl_2) was characterized by means of XRD (Fig. 2B). According to the Rietveld refinement, the lattice parameters a = 3.2225(2) Å and c = 8.7658(8) Å matched well with the reported values for Ti_2CCl_2 MXene (*5*). Raman spectra (Fig. 2C) also confirmed the purity of Ti_2CCl_2 MXene. High-resolution STEM-EELS (fig. S15) and EDX analysis (fig. S16) confirmed the crystallinity and stoichiometry of CVD-Ti_2CCl_2. The center-to-center interlayer distance of 0.88 ± 0.05 nm calculated from STEM images (fig. S17) was typical for Ti_2CCl_2 MXenes. SEM images showed a substrate fully covered with a wrinkled layer of Ti_2CCl_2 (Fig. 2D). Such a carpet of Ti_2CCl_2 MXene sheets grown perpendicular to the substrate would be difficult for traditionally synthesized MXenes to achieve. This morphology, previously observed for other CVD-grown 2D materials such as MoS_2 (*32*), appeared particularly promising for efficient ion intercalation, such as in supercapacitors (*7*, *22*).

We used direct CVD synthesis to produce MXenes that have not been previously prepared by the etching of MAX phases. For example, Zr_2CCl_2 and Zr_2CBr_2 MXenes were synthesized by exposing a Zr foil to CH_4 and $ZrCl_4$ or $ZrBr_4$ vapor at 975°C. These two zirconium MXenes appeared in the same general morphology as that of the titanium MXenes, adopting vertically aligned carpet-like structure on the surface of the Zr foil (fig. S18). Arguably the most intriguing product of the direct synthesis was phase-pure nitride Ti_2NCl_2 MXene formed through the reaction of Ti foil with $TiCl_4$ and N_2 above 640°C (Fig. 2, A to C and E, and figs. S19 and S20). Nitride MXenes have been predicted to have a variety of attractive properties, including ferromagnetism and higher conductivity as compared with that of carbide MXenes (*33*). However, the challenge of making nitride MXenes by traditional methods of etching nitride MAX phases lies in higher energies needed to extract "A" atoms from corresponding MAX phase—for example, Al from $Ti_{n+1}AlN_n$ (*34*). The nitride MXene sheets can dissolve in HF solution because of their lower stability (*35*). To date, only a few nitride MXenes have been synthesized, and experimental realization of chloride-terminated nitride MXenes has not been achieved. Our

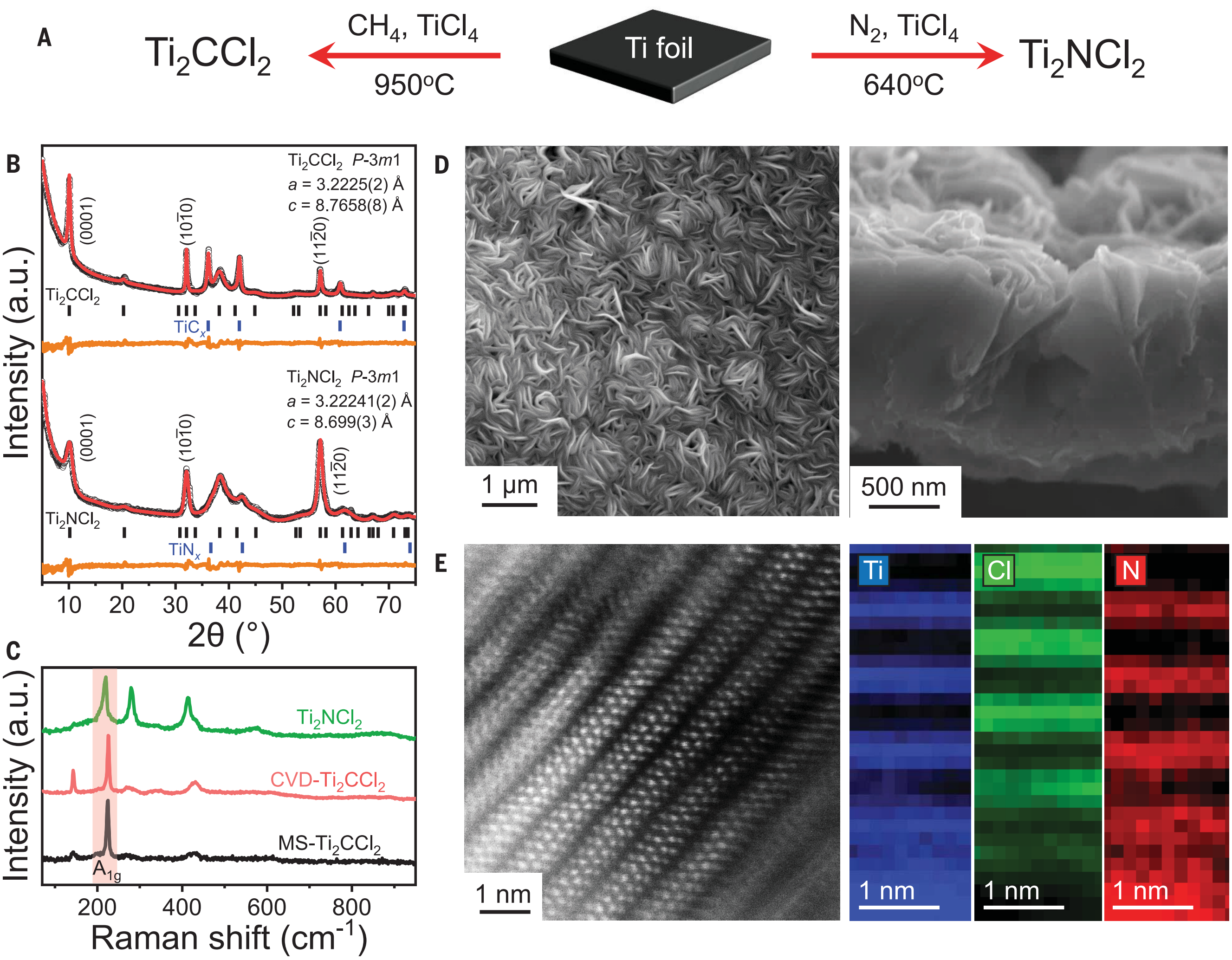


Fig. 2. CVD growth of MXenes. (**A**) Schematic diagram of the CVD reactions. (**B**) XRD patterns and Rietveld refinement for CVD-Ti_2CCl_2 and CVD-Ti_2NCl_2. (**C**) Raman spectra of CVD-Ti_2CCl_2 and CVD-Ti_2NCl_2 MXenes in comparison with that of a traditional MS-Ti_2CCl_2 MXene, which was synthesized by etching Ti_2AlC MAX phase with $CdCl_2$ molten salt. (**D**) Frontal and cross-sectional SEM images of CVD-Ti_2CCl_2. (**E**) High-resolution HAADF images and EELS elemental mapping of CVD-Ti_2NCl_2.

CVD method, using N_2 as the nitrogen source, further demonstrates the versatility of bottom-up MXene syntheses. These reactions can be useful beyond MXenes synthesis. Given that $TiCl_4$ plays the key role in Ti metallurgy (Kroll process) and in synthesis of TiO_2 from titanium ores (chloride process), both being on the millions of tons annually, the above reactions may create interesting opportunities, such as nitrogen fixation as a side process in conventional TiO_2 synthesis.

CVD growth of hierarchically structured MXenes

During the CVD synthesis of Ti_2CCl_2 MXene, gaseous reagents react with the titanium surface (*36*). As the thickness of growing MXene carpet increases, the diffusion of gaseous reagents toward the reaction zone (Fig. 3A) would slow down, and the growth of the MXene carpet would be expected to be self-limiting. However, we observed a new growth regime that allowed MXenes to bypass this kinetic bottleneck through the sequence of growth stages captured by ex situ SEM studies (fig. S21) and shown schematically in Fig. 3B. The uniform growth of the MXene carpet (Fig. 2D) was followed by the formation of "bulges" (Fig. 3C) that further evolved into spherical MXene "vesicles" (Fig. 3D). Next, these vesicles detached from the substrate (Fig. 3, F and G). The process could repeat itself, the exposed fresh surfaces enabling continuous synthesis of MXenes. After a prolonged CVD reaction, metal titanium was completely consumed (fig. S22). The internal structure of CVD-MXene vesicles was composed of Ti_2CCl_2 sheets radiating from the center and oriented normal to the surface (Fig. 3H and fig. S23). Imaging of a fragmented vesicle (Fig. 3E) and individual vesicles dissected with a focused ion beam (FIB) revealed a small void at the vesicle centers (fig. S24). Small TiC_x crystallites have been often found around the central void of MXene vesicles (figs. S25 and S26), suggesting that buckling of MXene carpet can be initiated by TiC_x nucleated under the growing MXene carpet.

The complexity of hierarchical organization of CVD-Ti_2CCl_2 vesicles is unusual for MXenes. The formation of "flower-like" morphologies—observed, for example, for graphene (*37*)—typically resulted from anisotropic growth initiated by a spherical seed acting as center. However, in the case of CVD-grown MXenes, spherical vesicles emerged from the planar MXene carpet. Their possible growth mechanism can be derived from a recent theoretical work, inspired by the nonequilibrium evolution of cell and organelle membranes, that illustrated how membrane growth could lead

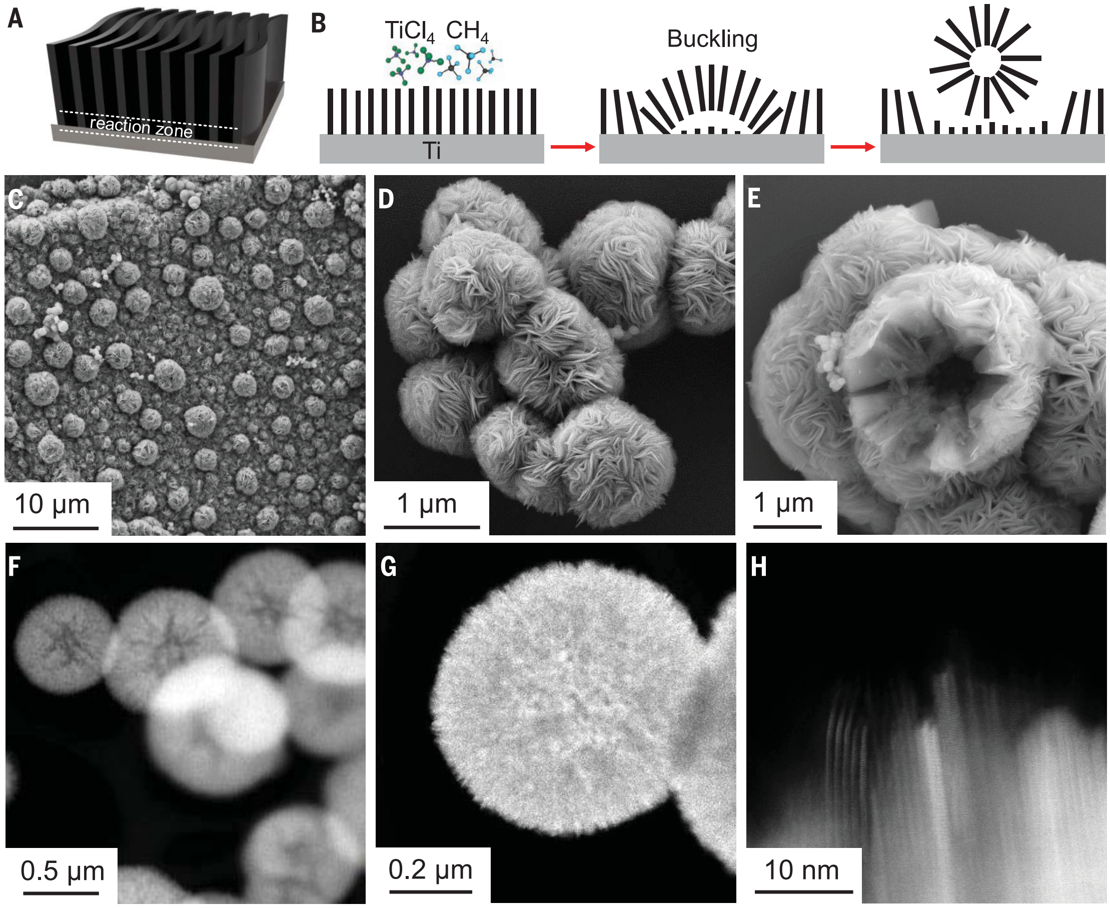


Fig. 3. Morphologies of CVD-Ti_2CCl_2. (**A** and **B**) Schematic diagrams illustrating the (A) reaction zone and (B) proposed buckling mechanism of CVD-Ti_2CCl_2 through which microspheres are formed. (**C** to **E**) SEM images show that morphology of CVD-Ti_2CCl_2 can be varied by tuning reaction conditions. (C) Microspheres growing on carpets. (D) Individual microspheres. (E) A fragmented microsphere showing a hollow center. (**F** to **H**) STEM analysis further shows that vertically aligned MXene sheets constitute the microspheres, while a void is left at the center.

to a variety of nontrivial geometries similar to our experimentally observed MXene vesicles (*38*).

The MXene carpet formed at an early stage of CVD growth (Fig. 2C) and loosely attached to the substrate can be approximated as an elastic 2D membrane. The energetics of such an elastic membrane can be defined through the surface area and local curvature by using a Helfrich Hamiltonian with a surface tension and bending rigidity terms, proportional to the surface tension γ and the bending rigidity κ, respectively (*39*). When $\gamma, \kappa > 0$, the membrane naturally prefers a flat geometry under equilibrium conditions (*40*). However, when new material is constantly added to the sheet, the standard equilibrium description fails to predict its shape and stability (*41*). During a CVD process, new MXene sheets keep nucleating and growing on the surface of Ti foil. The addition of new materials to a substrate with a fixed area creates substantial in-plane stress within MXene carpet, which can be relaxed by out-of-plane wrinkling or buckling where flexible MXene carpet detaches from rigid Ti surface (*42*, *43*). Viewed in the context of the above-described elastic sheet model, the growth of MXenes induced a negative surface tension in an effective free-energy landscape (supplementary text 2).

Van der Waals–bonded 2D MXene sheets can efficiently slide against each other, which creates only a small elastic penalty for the formation of buckled and curved geometries. Ultimately, these deformations can collapse into spherical vesicles that detach and refresh the substrate for further growth, as schematically shown in Fig. 3B. We found that gas reagent flow rate has a strong effect on the morphology of the CVD product. Flat carpets and bulges were favored at different flow rates (fig. S27), further suggesting that hierarchical morphology of CVD-grown MXenes results from the interplay of complex reaction kinetics rather than from templated growth. We emphasize that detailed mechanistic understanding of MXene vesicles growth will require additional computational and experimental studies. We simply propose a plausible mechanism to help explain the observed phenomenology.

Electrochemical energy storage

MXenes are known for their excellent pseudocapacitive energy storage properties that stem from the combination of large surface-to-volume ratio and high electrical conductivity. Ti_2CT_x MXenes show some of the highest predicted and experimentally observed capacities among all studied MXene materials (*20*, *44*). We investigated the Li-ion storage properties of electrodes prepared from DS-Ti_2CCl_2 and CVD-Ti_2CCl_2. We performed electrochemical characterizations on DS-Ti_2CCl_2 using a two-electrode (Li coin cell) configuration. A conducting additive, 10 wt % Super P carbon black, was added following the standard approach. The first several cyclic voltammetry (CV) cycles of a delaminated DS-Ti_2CCl_2 electrode recorded at a scan rate of 0.5 $mV \cdot s^{-1}$ within the electrochemical potentials from 0.2 to 3.0 V versus Li^+/Li (fig. S28A) showed

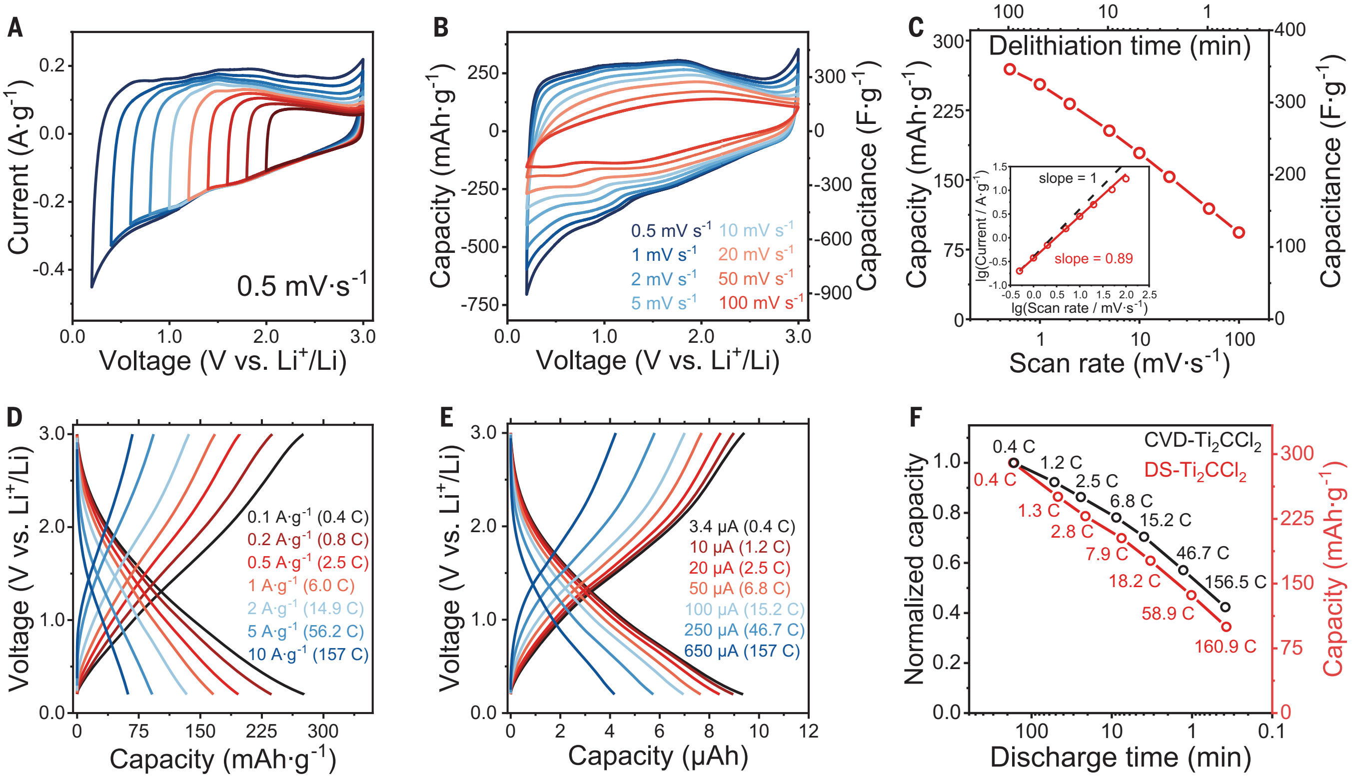


Fig. 4. Electrochemical energy storage properties of Ti_2CCl_2 MXenes. (**A**) Cyclic voltammetry (CV) profiles of delaminated DS-Ti_2CCl_2 with various negative cut-off potentials at a scan rate of 0.5 mV·s^{-1}. (**B**) CV profiles of delaminated DS-Ti_2CCl_2 at different scan rates from 0.5 to 100 mV·s^{-1}. Differential capacity Q was derived from differential capacitance C. (**C**) Change of DS-MXene electrode capacity and capacitance versus the discharge time during CV scan recorded at various potential scan rates. (Inset) b-value determination. (**D**) Galvanostatic charge-discharge (GCD) profiles of DS-Ti_2CCl_2 from current densities of 0.1 to 10 A·g^{-1}. (**E**) GCD profiles of CVD-Ti_2CCl_2 from current densities of 3.4 to 650 μA. (**F**) Normalized galvanostatic discharge capacity of CVD-Ti_2CCl_2 and DS-Ti_2CCl_2 electrodes from 0.4 to ~160 C. Absolute capacity of DS-Ti_2CCl_2 is shown in the secondary y axis as a reference.

redox peaks that can be assigned to the formation of a solid electrolyte interphase (SEI) layer (*4*, *45*). After the third CV cycle, the specific capacitance of DS-MXene electrode stabilized at 341 F·g^{-1} (which corresponds to a capacity of 265 mA·hour·g^{-1}) (fig. S28B), which is in a good agreement with previously reported data for MS-Ti_2CCl_x MXene (*44*). The rectangular CV profile without redox peaks suggests a pseudocapacitive energy storage mechanism for delaminated MXenes (*46*), which is further supported by the consistency of the rectangular CV profiles recorded with different negative cut-off potentials (Fig. 4A).

The charge storage kinetics were investigated by measuring the dependence of electrochemical current i on the potential scan rate v (supplementary text 3). In theory, the current scales with scan rate as $i \sim v^b$, where a b-value of 1 corresponds to a capacitive process, and a b-value of 0.5 is typical for battery-type energy storage (*47*). CV profiles of delaminated DS-Ti_2CCl_2 MXene at scan rates from 0.5 to 100 mV·s^{-1} are shown in Fig. 4B. The specific lithiation capacities and capacitances, versus charge-discharge times and scan rates calculated from the CV profiles, are plotted in Fig. 4C. The Fig. 4C inset shows the i versus v plotted in logarithmic scale from 0.5 to 100 mV·s^{-1}. We observed a linear relationship with a slope of $b \approx 0.89$ for scan rates that ranged from 0.5 to 20 mV·s^{-1}, indicating a capacitive-like charge storage for the delaminated DS-Ti_2CCl_2 electrodes. Galvanostatic charge-discharge (GCD) profiles of a DS-Ti_2CCl_2 electrode are shown Fig. 4D. About 48% capacity was maintained from a current density of 0.1 to 2 A·g^{-1}, which is comparable with previously reported values for Cl-terminated MXenes (*44*, *48*). A maximum capacity of 286 mA·hour·g^{-1} was recorded at a specific current of 0.1 A·g^{-1} within 0.1 to 3.0 V (fig. S29), which is slightly higher than previously reported value for the optimized performance of MS-Ti_2CCl_x MXene (*44*). These electrochemical studies further confirm excellent electrochemical characteristics of DS-Ti_2CCl_2 MXene.

The high-rate performance of MXenes is sensitive to electrode microstructure such as flake size, flake orientation, and pore size distribution (*49*). For example, restacking of exfoliated MXene sheets can reduce the surface area that is easily accessible for intercalating ions, which is a well-known problem of 2D materials (*50*). New morphologies, such as CVD-grown MXene carpets and vesicles with individual sheets oriented normal to the substrate (Fig. 3), can facilitate the development of MXenes for fast electrochemical energy storage. To preserve the as-synthesized morphology, CVD-Ti_2CCl_2 grown on Ti foil (fig. S30) was directly used as an electrode for an electrochemical cell. Galvanostatic plots at various current densities highlight the high-power performance of CVD-Ti_2CCl_2 electrode with vertically oriented MXene sheets in Li^+ intercalation processes (Fig. 4E). The CVD electrode further shows a slightly better high-rate performance than that of delaminated MXene from 0.4 C to ~160 C (Fig. 4F). The b-value of CVD-Ti_2CCl_2 was calculated as 0.93 (fig. S31D), which indicates an energy storage mechanism closer to that of a freely diffusing capacitor. A better understanding of ion transport in complex morphologies of CVD-grown MXenes, as well as charge transport between individual MXene vesicles, should help to further

optimize the electrochemical performance of DS- and CVD-grown MXenes.

REFERENCES AND NOTES

1. M. Naguib *et al*., *Adv. Mater.* **23**, 4248–4253 (2011).
2. J. Halim *et al*., *Chem. Mater.* **26**, 2374–2381 (2014).
3. M. Ghidiu, M. R. Lukatskaya, M. Q. Zhao, Y. Gogotsi, M. W. Barsoum, *Nature* **516**, 78–81 (2014).
4. Y. Li *et al*., *Nat. Mater.* **19**, 894–899 (2020).
5. V. Kamysbayev *et al*., *Science* **369**, 979–983 (2020).
6. O. Mashtalir *et al*., *Nat. Commun.* **4**, 1716 (2013).
7. Y. Xia *et al*., *Nature* **557**, 409–412 (2018).
8. M. Naguib *et al*., *J. Am. Chem. Soc.* **135**, 15966–15969 (2013).
9. A. Iqbal *et al*., *Science* **369**, 446–450 (2020).
10. F. Shahzad *et al*., *Science* **353**, 1137–1140 (2016).
11. K. Hantanasirisakul *et al*., *Adv. Electron. Mater.* **2**, 1600050 (2016).
12. H. Zhou *et al*., *Nat. Commun.* **12**, 5510 (2021).
13. M. A. Hope *et al*., *Phys. Chem. Chem. Phys.* **18**, 5099–5102 (2016).
14. G. R. Bhimanapati *et al*., *ACS Nano* **9**, 11509–11539 (2015).
15. M. Naguib *et al*., *ACS Nano* **6**, 1322–1331 (2012).
16. J. Zhou *et al*., *Angew. Chem. Int. Ed.* **55**, 5008–5013 (2016).
17. J. Halim *et al*., *Adv. Funct. Mater.* **26**, 3118–3127 (2016).
18. D. L. Druffel *et al*., *Chem. Mater.* **31**, 9788–9796 (2019).
19. S. J. Hwu, R. P. Ziebarth, S. Vonwinbush, J. E. Ford, J. D. Corbett, *Inorg. Chem.* **25**, 283–287 (1986).
20. B. Anasori, M. R. Lukatskaya, Y. Gogotsi, *Nat. Rev. Mater.* **2**, 16098 (2017).
21. A. VahidMohammadi, J. Rosen, Y. Gogotsi, *Science* **372**, 1165–1178 (2021).
22. X. L. Li *et al*., *Adv. Energy Mater.* **10**, 2001394 (2020).
23. H. Wang *et al*., *Adv. Mater.* **30**, e1704561 (2018).
24. C. J. Zhang *et al*., *Chem. Mater.* **29**, 4848–4856 (2017).
25. Y. R. Luo *et al*., *Joule* **3**, 279–289 (2019).
26. X. Yang, N. Gao, S. Zhou, J. Zhao, *Phys. Chem. Chem. Phys.* **20**, 19390–19397 (2018).
27. V. Natu *et al*., *Matter* **4**, 1224–1251 (2021).
28. D. Voiry *et al*., *Nat. Chem.* **7**, 45–49 (2015).
29. C. Xu *et al*., *Nat. Mater.* **14**, 1135–1141 (2015).
30. Y. L. Hong *et al*., *Science* **369**, 670–674 (2020).
31. O. Ledain *et al*., *Phys. Procedia* **46**, 79–87 (2013).
32. C. Stern *et al*., *Sci. Rep.* **8**, 16480 (2018).
33. H. Kumar *et al*., *ACS Nano* **11**, 7648–7655 (2017).
34. I. R. Shein, A. L. Ivanovskii, *Comput. Mater. Sci.* **65**, 104–114 (2012).
35. M. Naguib, V. N. Mochalin, M. W. Barsoum, Y. Gogotsi, *Adv. Mater.* **26**, 992–1005 (2014).
36. J. Gavillet *et al*., *Phys. Rev. Lett.* **87**, 275504 (2001).
37. S. Y. Wang *et al*., *Carbon* **120**, 103–110 (2017).
38. J. Binysh, T. R. Wilks, A. Souslov, *Sci. Adv.* **8**, eabk3079 (2022).
39. G. Salbreux, F. Jülicher, *Phys. Rev. E* **96**, 032404 (2017).
40. A. D. Pezzutti, H. Hernández, *J. Phys. Conf. Ser.* **1603**, 012003 (2020).
41. Z. Hua *et al*., *Nat. Commun.* **10**, 5406 (2019).
42. B. Li, Y. P. Cao, X. Q. Feng, H. J. Gao, *Soft Matter* **8**, 5728–5745 (2012).
43. D. J. Schmidt *et al*., *ACS Nano* **3**, 2207–2216 (2009).
44. G. Ma *et al*., *Nat. Commun.* **12**, 5085 (2021).
45. R. M. Gnanamuthu, C. W. Lee, *Mater. Chem. Phys.* **130**, 831–834 (2011).
46. S. Fleischmann *et al*., *Nat. Energy* **7**, 222–228 (2022).
47. N. Elgrishi *et al*., *J. Chem. Educ.* **95**, 197–206 (2018).
48. L. Liu *et al*., *ACS Nano* **16**, 111–118 (2022).
49. M. R. Lukatskaya *et al*., *Nat. Energy* **2**, 17105 (2017).
50. J. Wang, V. Malgras, Y. Sugahara, Y. Yamauchi, *Nat. Commun.* **12**, 3563 (2021).

ACKNOWLEDGMENTS

The authors express their appreciation to I. Golovina for helping with atomic force microscopy measurements. We thank Y. Han and G. Yan for helpful discussions about electrochemical measurements and G. Olack for helping with SEM data analysis. We are also grateful to A. Nelson for a critical reading and editing of the manuscript and M. Talapin for help with artwork. **Funding:** The work on direct MXene synthesis was supported by the National Science Foundation under award DMR-2004880, and CVD synthesis was supported by the US Department of Defense Air Force Office of Scientific Research under grants FA9550-22-1-0283 and FA9550-20-1-0104. Electrochemical studies were supported by the Advanced Materials for Energy-Water Systems (AMEWS) Center, an Energy Frontier Research Center funded by the US Department of Energy (DOE), Office of Science, Basic Energy Sciences. W.C. and S.V. were supported by the University of Chicago Materials Research Science and Engineering Center, which is funded by the National Science Foundation under award DMR-2011854. S.V. acknowledges support from the National Science Foundation under grant DMR-1848306. F.L. and R.F.K. at UIC were supported by a grant from the National Science Foundation (NSF-DMR 1831406). Acquisition of UIC JEOL ARM200CF was supported by an MRI-R2 grant from the National Science Foundation (DMR-0959470). The Gatan Continuum GIF acquisition at UIC was supported by an MRI grant from the National Science Foundation (DMR-1626065). FIB-SEM was performed at the Canadian Centre for Electron Microscopy, a Canada Foundation for Innovation Major Science Initiatives funded facility. The work also used resources of the Center for Nanoscale Materials, a DOE Office of Science User Facility operated for the DOE Office of Science by Argonne National Laboratory under contract DE-AC02-06CH11357. **Author contributions:** D.W. performed and designed the experiments, analyzed data, and cowrote the paper. C.Z. carried out Raman measurements and data analysis. A.S.F. contributed to x-ray measurements and data analysis. W.C. contributed to TEM analysis of delaminated MXene and building the CVD system. F.L. and R.F.K. performed high-resolution STEM studies and image analysis. M.W. and C.L. contributed to the electrochemistry measurements and data analysis. S.V. performed simulations and interpretation of the morphology of CVD-MXenes. D.V.T. conceived and designed experiments and simulations, analyzed data, cowrote the paper, and supervised the project. All authors discussed the results and commented on the manuscript. **Competing interests:** D.W. and D.V.T. are inventors on patent application US 63/399,931 submitted by the University of Chicago, which covers direct synthesis and CVD of MXenes. **Data and materials availability:** All data needed to evaluate the conclusions in the paper are present in the paper or the supplementary materials. The samples can be provided by the authors upon reasonable request under a materials transfer agreement with the university. Correspondence and requests for materials should be addressed to D.V.T. (dvtalapin@uchicago.edu).

License information: Copyright © 2023 the authors, some rights reserved; exclusive licensee American Association for the Advancement of Science. No claim to original US government works. https://www.science.org/about/science-licenses-journal-article-reuse

SUPPLEMENTARY MATERIALS

science.org/doi/10.1126/science.add9204
Materials and Methods
Supplementary Notes
Figs. S1 to S34
Tables S1 to S5
References (*51*–*59*)

Submitted 13 July 2022; accepted 31 January 2023
10.1126/science.add9204

3D PRINTING

A silicone-based support material eliminates interfacial instabilities in 3D silicone printing

Senthilkumar Duraivel[1], Dimitri Laurent[2], Didier A. Rajon[2], Georg M. Scheutz[3], Abhishek M. Shetty[4], Brent S. Sumerlin[3], Scott A. Banks[5], Frank J. Bova[2], Thomas E. Angelini[1,5,6]*

Among the diverse areas of 3D printing, high-quality silicone printing is one of the least available and most restrictive. However, silicone-based components are integral to numerous advanced technologies and everyday consumer products. We developed a silicone 3D printing technique that produces precise, accurate, strong, and functional structures made from several commercially available silicone formulations. To achieve this level of performance, we developed a support material made from a silicone oil emulsion. This material exhibits negligible interfacial tension against silicone-based inks, eliminating the disruptive forces that often drive printed silicone features to deform and break apart. The versatility of this approach enables the use of established silicone formulations in fabricating complex structures and features as small as 8 micrometers in diameter.

Silicone elastomer's resistance to heat, chemical agents, weathering, ozone, moisture, and ultraviolet (UV) irradiation makes it critical for manufacturing countless products, including electronic devices, automobiles, aircraft, and medical devices (*1*). Silicone elastomers have been used in medical devices for many years (*2*), and their applications include embedded sensors (*3*), flexible electronics (*4*), soft robotics (*5*), and additive manufacturing (*6*). Silicone structures can be fabricated by using conventional techniques such as molding, or advanced techniques such as soft lithography and 3D printing (*7–9*). However, 3D printing with silicone generally results in low-quality products because of challenges created by the interfacial behaviors of silicone pre-elastomer in its liquid state. These challenges can be partially addressed by using an embedding support material that flows around the translating printing nozzles while trapping deposited inks in space, providing stability to printed structures (*10–14*). However, even under such stabilizing conditions, the interfacial tension between printed inks and their support media drives the deformation and breakup of printed structures before they solidify (Fig. 1, A and B) (*9*, *15*). Modifying silicone inks with additives can stabilize 3D printed structures (*16*, *17*), yet a versatile approach to additive manufacturing with unmodified silicone inks remains elusive. One route to achieving high-quality 3D silicone printing without ink modification is to eliminate the disruptive role of interfacial tension by using support materials that are chemically similar to the printed inks they stabilize (Fig. 1C). Thus, there is a critical need to develop support materials that are chemically similar to poly(dimethylsiloxane) (PDMS) inks.

[1]Department of Materials Science and Engineering, University of Florida, Gainesville, FL 32603, USA. [2]Department of Neurosurgery, University of Florida College of Medicine, Gainesville, FL 32608, USA. [3]George and Josephine Butler Polymer Research Laboratory, Center for Macromolecular Science and Engineering, Department of Chemistry, University of Florida, Gainesville, FL 32611, USA. [4]Advanced Technical Center, Anton Paar USA, Ashland, VA 23005, USA. [5]Department of Mechanical and Aerospace Engineering, University of Florida, Gainesville, FL 32611, USA. [6]J. Crayton Pruitt Family Department of Biomedical Engineering, University of Florida, Gainesville, FL 32611, USA.
***Corresponding author. Email: t.e.angelini@ufl.edu**

We describe a method for 3D printing precise, intricately detailed structures made from PDMS that makes use of a support material exhibiting negligible interfacial tension when in contact with silicone inks. We call this method additive manufacturing at ultralow interfacial tension (AMULIT). The AMULIT support material is a packed inverse emulsion composed of aqueous droplets in a continuum of silicone oil. The ultralow interfacial tension between the AMULIT support material and PDMS inks enabled us to print features with diameters as small as 8 μm. We achieved high-performance printing by tuning the elasticity and flow properties of this support material, which allowed us to fabricate complicated shapes such as brain aneurysm models and functional trileaflet heart valves. We demonstrated that the AMULIT technique does not require specialized inks by using several different commercially available PDMS formulations to print various structures. With mechanical testing, we found that 3D printed structures produced by using AMULIT were more extensible than their molded counterparts and equally robust. We also found that these structures have a smooth surface finish at the macroscale and microscale roughness, which is facilitated by the low interfacial tension between PDMS inks and the AMULIT support medium. Our results show that the AMULIT 3D printing technique could be used to fabricate intricate silicone structures for biomaterial design and surgical simulators, and they introduce the possibility of expanding the method for printing with other materials.

Results

Formulation and testing of AMULIT support material

To formulate an AMULIT support medium for 3D printing with PDMS inks, we prepared inverse emulsions in which silicone oil was the continuous phase and varied the aqueous droplet packing fraction, ϕ, and the average droplet radius, a, between samples; ϕ and a can be tuned independently to determine an emulsion's rheological properties and its corresponding performance as a printing support medium (*18*). We expected a to strongly influence the printed feature roughness because the material interfaces will not spontaneously flatten under conditions of ultralow interfacial tension. Thus, we formulated small emulsion droplets and chose ϕ on the basis of the emulsions' rheological properties (fig. S1). The elastic shear modulus, G', and yield stress, σ_y, of each formulation, were measured with rheological tests (materials and methods and fig. S2). For AMULIT printing, we chose an emulsion having σ_y = 9 Pa and G' = 320 Pa; the emulsion with these properties is weak enough to flow around a translating printing needle yet strong enough to support complex 3D printed structures (*9*, *10*). For this formulation, we estimated the Reynolds number near the translating nozzle during a typical print to be 10^{-6} to 10^{-2}, which indicates that irregular flow patterns should be suppressed (supplementary text). For all formulations, we found that emulsions made from pure water droplets in silicone oil were extremely cloudy and inhibited visualizing the printing process. To make optically clear emulsions, we matched the refractive indices of the two phases by adding glycerol to the droplets, which allowed the 3D printing process to be imaged at the macroscale with photography and at the microscale with confocal fluorescence microscopy (CFM) (Fig. 1, D to G, and fig S3).

To test the role of interfacial tension in embedded 3D printing, we compared the performance of the AMULIT support medium with an all-aqueous support medium made from packed hydrogel microparticles swollen in water. In both cases, we 3D printed features made from a fluorescent PDMS liquid and imaged the ink-support interfaces using CFM (materials and methods). We formulated the packed microgels to have σ_y = 10 Pa and G' = 550 Pa, values comparable to those of the AMULIT material. Examining the 3D fluorescence images, we found that printed silicone features broke up and formed spherical droplets within the aqueous support. When a liquid ink is printed into a packed granular support medium, the smallest stable feature has a diameter given by $d_{\min} \approx 2\gamma/\sigma_y$, where γ is the interfacial tension between the ink and the support medium (*15*). For the aqueous medium, γ = 25 mN/m, so $d_{\min}$ was ≈5 mm,

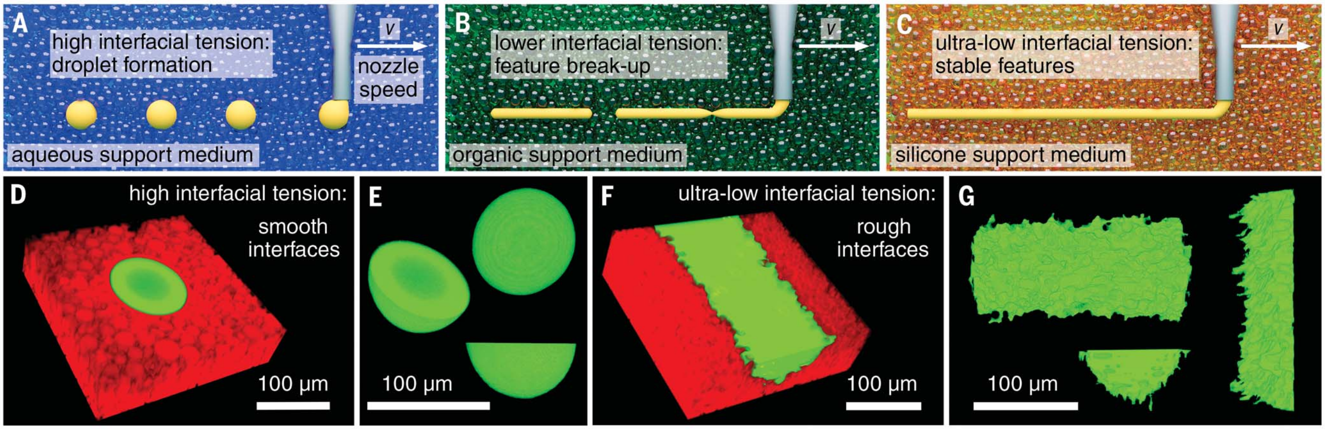


Fig. 1. Interfacial tension drives feature breakup in embedded 3D printing. (**A**) High interfacial tension between aqueous support materials and silicone inks destabilizes 3D printed features, driving them to break into spherical droplets. (**B**) Intermediate interfacial tension between organic support materials and silicone inks provides some stability but limits minimum stable feature size. (**C**) Ultralow interfacial tension between silicone oil–based support materials and silicone inks eliminates interfacial instabilities, removing the limits on minimum stable feature size. (**D**) CFM image showing silicone-based inks (green) that break into droplets when printed into support materials made from aqueous microgels (red). (**E**) A droplet digitally isolated from the support and examined from different angles. The droplet appears nearly spherical and exhibits a smooth surface. (**F**) By contrast, the silicone-based ink (green) remains continuous and retains its shape indefinitely after printing into a silicone-based support material (red). (**G**) When viewed from different angles, the printed features exhibit roughness with a characteristic length scale of the microparticles composing the support material, facilitated by ultralow interfacial tension.

50 times the 100-μm diameter of the printed feature (Fig. 1, D and E). Thus, the breakup of the feature into droplets was expected. By contrast, the 100-μm diameter silicone feature printed into the AMULIT support material remained intact, indicating that $\gamma < 0.5$ mN/m. To better estimate γ between a PDMS ink and the AMULIT support medium, we performed a series of test prints in which $d_{\min}$ was measured for multiple values of σ_y, finding that $\gamma \approx 0.08$ mN/m (fig. S4). We also observed that the characteristic roughness length scale at the feature surface was about one order of magnitude smaller than the feature diameter, from which we would estimate $\gamma \approx 0.05$ mN/m. These results indicate that the AMULIT approach can potentially achieve features 300 to 500 times smaller than those achievable when printing PDMS into an aqueous support medium having the same material properties.

Complex device fabrication using the AMULIT technique

The improvement in complexity, quality, and functionality of PDMS vessel models traced in the published literature parallels a decrease in interfacial tension of silicone inks against their embedding materials. For example, hydrocarbon support materials (*9*) improved on aqueous support materials (*19*). As a first test of the AMULIT method's capabilities, we printed a model brain aneurysm; models with accurate vasculature are needed for improved patient simulators to train neurosurgeons in cerebrovascular procedures. Current simulated tissues provide unrealistic tactile feedback, lack small-diameter intracranial angioarchitecture, and often exclude the aortic arch and extracranial vascular anatomy that determine which catheters and instruments are used in each procedure (*20*, *21*).

To create a model, we collected a 3D angiogram of a patient's brain aneurysm using x-ray computed tomography (XRCT). The 3D scan was segmented and processed to create a series of 3D printing trajectories (Fig. 2A and materials and methods). We used Gelest ExSil 100 silicone pre-elastomer, which can be formulated to have material properties that mimic a wide range of tissues. A snapshot from a video of the printing process demonstrates how the translating needle flows easily through the jammed emulsion, which traps the deposited silicone in place (Fig. 2B and movie S1). The printed structure was cured at 60°C for 24 hours and then imaged with XRCT (Fig. 2C). Horizontal and vertical slices through the 3D scan revealed that the highly branched, complex printed network of vessels is hollow, with an average wall thickness of ≈400 μm (Fig. 2D and movie S2). The CT scan of the printed structure was used to create a 3D model for quantitative comparison with the original angiogram. The registration between the patient-derived model and the printed model is excellent; 68% of the printed-surface locations lie within 500 μm of their programmed locations, and 95% lie within 1 mm (Fig. 2, E and F).

Our ability to accurately model brain vasculature raises the question of whether such fine structures can be manufactured to be both highly compliant and physically robust. The artificial aortic heart valve belongs to a class of devices with such requirements. Native aortic heart valves are subject to dynamic mechanical loads during the cardiac cycle (*22*). Prosthetic replacement is widely used to treat aortic valve failure, yet the predominantly used mechanical valves and allogeneic- or xenogeneic-tissue valve replacements often result in mechanical failure, hemolysis, blood coagulation, or structural degradation due to calcification. A potential alternative is an artificial silicone valve prosthesis; silicone is established in vascular applications because of its hemocompatibility and durability (*22*–*27*). The AMULIT 3D printing method can be used to replicate the intricate semilunar shape of the thin aortic leaflets in manufactured silicone valves. We designed a model heart valve based on physiologically representative dimensions of the different valve components (Fig. 2, G and H, and fig. S5) (*28*). We used a UV-curable silicone formulation, Silopren UV Electro-225-1 (Momentive), as the ink and printed it into the AMULIT material (Fig. 2I). To create highly flexible leaflets, we printed the structure by translating the needle tip at a speed of 2 mm/s and depositing material at a rate of 125 μL/hour, producing features ≈150 μm in diameter. Correspondingly, we chose a layer spacing of 100 μm for good layer adhesion. The printed model was then UV cured, removed from the AMULIT material, washed with detergent, and rinsed in deionized water (materials and methods). The cured part had a final wall thickness of ≈250 μm. Despite having very thin, flexible walls, the model valves were physically robust enough to connect to pipe

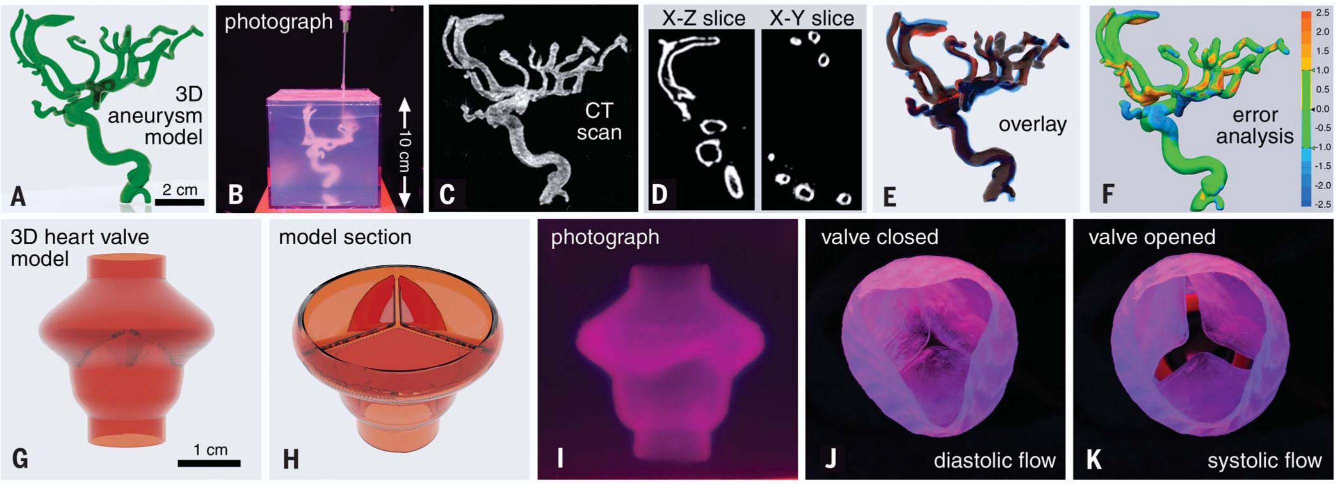


Fig. 2. AMULIT printing of brain aneurysm and aortic heart valve models. (**A**) Brain aneurysm models for surgical simulations comprise complex, interconnected, hollow tubes with intricate details. (**B**) Photograph of the aneurysm model being printed into the AMULIT material. (**C**) CT imaging of the 3D printed model within the printing container shows the complexity of the printed aneurysm. (**D**) Slices through the CT scan show that the printed structure exhibits the hollow channels of the patients' neurovasculature. (**E** and **F**) The printed structure overlays well with the patient's neurovasculature, and quantitative error analysis demonstrates agreement between the two (±1 mm error range corresponds to 95% of all points). (**G** and **H**) A model tricuspid aortic heart valve designed by using the geometric measurements of the native heart valve. (**I**) A silicone heart valve model printed in a single seamless trajectory with a wall thickness of 250 μm within the AMULIT support medium and cured under a UV lamp. (**J** and **K**) Once cured and washed, the valve model is robust enough to be coupled with a water supply, simulating transvalvular flow of the cardiac cycle. The thin leaflets of the valve are observed to open and close during the systolic and diastolic flow of the simulation.

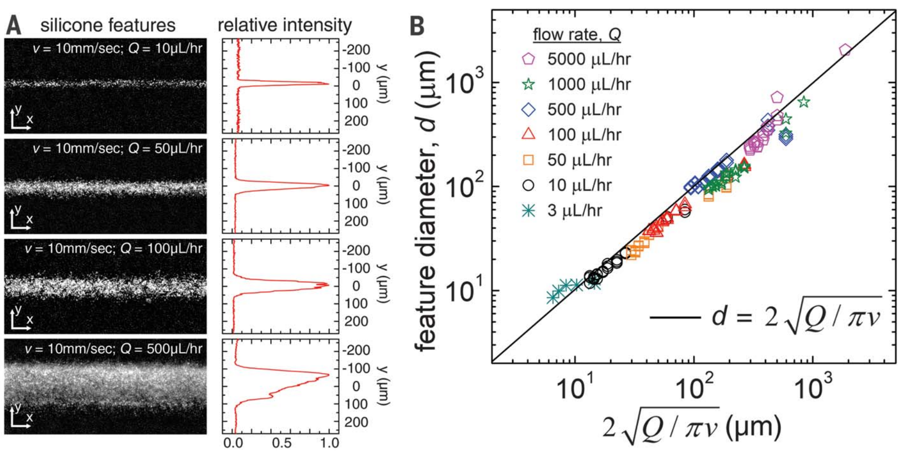


Fig. 3. Control of AMULIT printed feature size. (**A**) (Left) Intensity-inverted images. These images are averaged along the *x* axis, yielding an intensity profile across each feature. (Right) A Gaussian function is fit to the intensity profile to determine the diameter of the printed line. We measured printed feature diameter with brightfield microscopy, varying the translation speed, ν, of the printing nozzle and the ink deposition rate, *Q*. (**B**) Feature diameter of the printed silicone is controllable and can be predicted from a fluid continuity equation with no fitting parameters.

fittings and simulate transvalvular blood flow through cyclic pumping of water (movie S3). During the negative flow of the pulse representing the diastolic cycle, the valves remained closed with very little deflection on the thin leaflets (Fig. 2J), and during the positive pulse corresponding to the systolic cycle, the leaflets deflected, opening the valve and letting the water flow (Fig. 2K).

AMULIT performance: Feature size and print quality

The wall thicknesses of the brain vasculature and heart valve models were set by using a combination of feature diameter and layer spacing. The feature diameter, *d*, for different prints, can be chosen by selecting a combination of nozzle translation speed, ν, and material deposition rate, *Q*. To systematically explore how well *d* can be predicted with the AMULIT technique, we printed a series of linear features using the Smooth-On Mold Max 10 PDMS formulation at different combinations of ν and *Q* and then measured *d* (Fig. 3A and materials and methods).We predicted the relationship between *d*, *Q*, and ν, given by $\pi\ (d/2)^2 = Q/\nu$, according to basic fluid continuity. Performing many experiments at different combinations of *Q* and ν, we found that this prediction matched the measured feature diameter very well with no adjustable parameters (Fig. 3B). These printed features were stable over time; the change in measured feature size over the course of 120 min postprinting was found to be negligible (fig. S6). We were able to fabricate stable silicone features as small as 8 μm in diameter using the AMULIT printing technique; the smallest stable feature diameter we have seen previously demonstrated with unmodified silicone was 40 μm, although smaller unstable features were also reported (*9*). A feature diameter of 10 μm was previously achieved by modifying silicone ink with emulsion droplets (*16*, *29*). To print these very fine features, we formulated an AMULIT support material with an increased yield stress using droplets 1 μm in diameter (fig. S1); the high-magnification images in Fig. 1F indicate that larger droplets would impose interfacial roughness comparable to these small feature diameters.

We have shown that highly controlled 3D printing with PDMS is possible with the AMULIT

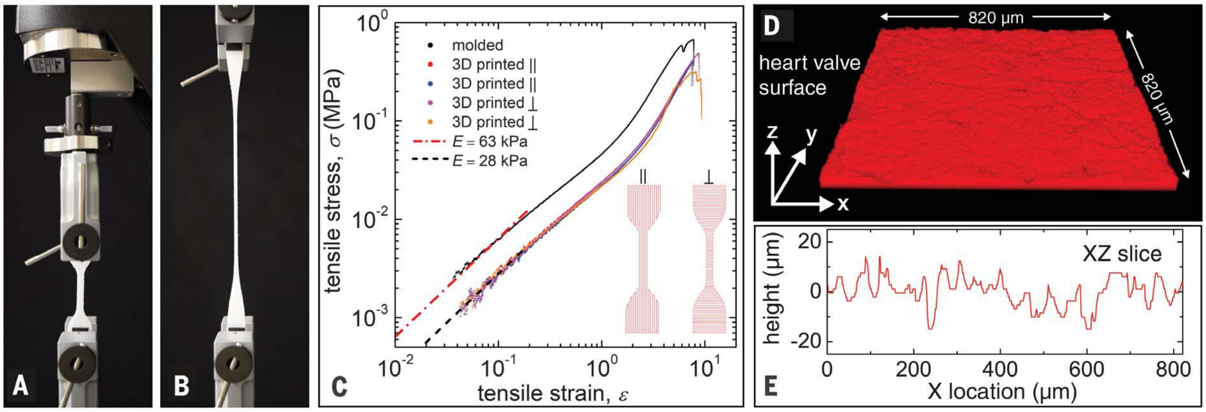


Fig. 4. Material and surface properties of the AMULIT printed silicone structures. (**A** and **B**) Silicone tensile specimens are subject to unidirectional tensile stress and are stretched to failure. (**C**) Tensile stress-strain curves of the specimens printed with their features oriented parallel and perpendicular to the tensile force show linear stress-strain relationships at low strains and exhibit an elastic modulus of 28 kPa. (**D** and **E**) Surface profiles of the printed silicone heart valves exhibit microroughness with an RMS value of 5.5 μm, likely determined by the emulsion droplet radius and the ultralow interfacial tension with the AMULIT support material.

technique, and the functionality of the heart valve model suggests that such structures may be sufficiently compliant and durable for use in applications. To test the mechanical performance of printed silicone structures, we fabricated tensile specimens using PlatSil-71 RTV (room-temperature vulcanizing) (Polytek) silicone formulation following ASTM standard D412 Type C specifications. To test the role of layer-to-layer adhesion in the mechanical integrity of the samples, we printed them with their extruded features oriented in both the longitudinal and lateral directions with respect to the long axis of the specimen geometry. The printed structures were cured at 60°C for 4 hours and then tested by using an Instron 5943 at a loading rate of 500 mm/min (Fig. 4, A and B). The tensile stress-strain data showed that both the lateral and longitudinal print specimens differed negligibly from one another and had the same elastic modulus of 28 kPa (Fig. 4C). All printed specimens exhibited linear stress-strain relationships at low strain levels and repeatable stress-strain curves at higher strains, failing at strains greater than 1000%. Comparing these results with the performance of molded specimens, we found that all the stress-strain curves had the same shape but that printed structures failed at higher strains than molded structures, whereas molded structures exhibited elastic moduli approximately twice those of printed structures. This softening effect could arise from systematic heterogeneities in the printed structures inherent to the 3D printing process. Additionally, we conducted fatigue tests, imposing 10^5 cycles of ±10% strain, alternately stretching and buckling the samples. Subsequent tensile tests showed that the printed structures exhibited less fatigue than did their molded counterparts; the elastic modulus dropped by 18% for the cast samples and 14% for the printed structures (fig. S7).

As a final assessment of the quality of structures fabricated with the AMULIT printing technique, we investigated the surface finish of fabricated parts. The ultralow interfacial tension between the silicone and the AMULIT support material was expected to produce microrough surfaces on the printed shapes. Using CFM, we imaged a segment of the heart valve model immersed in a rhodamine solution, visualizing and quantifying the surface roughness in 3D. We found the root mean square (RMS) roughness to be 6.54 ± 0.95 μm (mean and standard error, respectively) which is comparable to the average diameter of emulsion droplets used in these tests, ≈4 μm. Thus, we expect a smaller roughness with smaller emulsion droplets such as those used to print very fine features (Fig. 3B). This value is also comparable to the roughness of PDMS structures printed into support materials that exhibit a high interfacial tension against silicone inks (*9*), so it may be limited by other factors. In either case, our results demonstrate that eliminating disruptive interfacial driving forces with the AMULIT technique enables precise silicone printing without reducing surface quality or mechanical performance of fabricated structures. The added role of emulsion droplet size in surface roughness may enable a printed structure's optical properties to be tuned while independently controlling its mechanical performance through ink composition or feature diameter.

Conclusions

The AMULIT 3D printing method eliminates the disruptive effects of interfacial tension between printed inks and their support materials. Our results show that AMULIT printing can be used to make precise, smooth, strong, and functional devices from commercially available PDMS formulations. The versatility of the AMULIT technique eliminates the need to formulate specialized PDMS inks for 3D applications and broadens the toolbox for researchers and industrial manufacturers seeking to 3D print PDMS-based devices, while improving on previous silicone printing methods. The AMULIT strategy hinges on formulating support materials that are chemically similar to the inks they support—in this case, PDMS inks printed into a continuum of PDMS oil—although the same principle could be used with aqueous polymers. Despite the chemical similarity between the ink and the support medium, we never observed intermixing between the two materials that interfered with printing quality. The very low Reynolds number exhibited during embedded 3D printing with materials such as those we used should facilitate the formation of ink–support interfaces (*30*), potentially stabilized by an effective interfacial tension (*31*) or a form of liquid–liquid phase separation (*32*), likely influenced by the jammed emulsion phase. Additionally, weak attractive interactions between the emulsion droplets may help to retain them on their side of the interfaces (*33*–*35*). In the near term, we envision the AMULIT method to be useful in 3D printing for a wide range of applications beyond silicone-based devices, given the diversity and availability of polymer systems and the simplicity of formulating AMULIT support materials.

REFERENCES AND NOTES

1. H. H. Moretto, M. Schulze, G. Wagner, in *Ullmann's Encyclopedia of Industrial Chemistry* (Wiley VCH, 2011), pp. 23–26.
2. A. Rahimi, A. Mashak, *Plast. Rubber Compos.* **42**, 223–230 (2013).
3. X. Ruan *et al.*, *Adv. Mater. Technol.* **5**, 2000171 (2020).

4. A. Nathan *et al*., *Proc. IEEE* **100**, 1486–1517 (2012).
5. O. D. Yirmibeşoğlu *et al*., in *2018 IEEE International Conference on Soft Robotics* (*RoboSoft*), Livorno, Italy, 24 to 28 April 2018 (IEEE, 2018), pp. 295–302.
6. F. Liravi, E. Toyserkani, *Addit. Manuf.* **24**, 232–242 (2018).
7. V. Ozbolat *et al*., *ACS Biomater. Sci. Eng.* **4**, 682–693 (2018).
8. T. Femmer, A. J. Kuehne, M. Wessling, *Lab Chip* **14**, 2610–2613 (2014).
9. C. S. O'Bryan *et al*., *Sci. Adv.* **3**, e1602800 (2017).
10. T. Bhattacharjee *et al*., *Sci. Adv.* **1**, e1500655 (2015).
11. T. Bhattacharjee *et al*., *Soft Matter* **14**, 1559–1570 (2018).
12. G. Ovarlez, Q. Barral, P. Coussot, *Nat. Mater.* **9**, 115–119 (2010).
13. L. Mohan, C. Pellet, M. Cloitre, R. Bonnecaze, *J. Rheol.* (*N.Y.N.Y.*) **57**, 1023–1046 (2013).
14. J. R. Seth, L. Mohan, C. Locatelli-Champagne, M. Cloitre, R. T. Bonnecaze, *Nat. Mater.* **10**, 838–843 (2011).
15. C. S. O'Bryan, A. Brady-Miné, C. J. Tessmann, A. M. Spotz, T. E. Angelini, *Soft Matter* **17**, 3886–3894 (2021).
16. B. M. Rauzan, A. Z. Nelson, S. E. Lehman, R. H. Ewoldt, R. G. Nuzzo, *Adv. Funct. Mater.* **28**, 1707032 (2018).
17. C. Perrinet, E. J. Courtial, A. Colly, C. Marquette, R. Fulchiron, *Adv. Mater. Technol.* **5**, 1901080 (2020).
18. T. G. Mason, J. Bibette, D. A. Weitz, *Phys. Rev. Lett.* **75**, 2051–2054 (1995).
19. T. J. Hinton, A. Hudson, K. Pusch, A. Lee, A. W. Feinberg, *ACS Biomater. Sci. Eng.* **2**, 1781–1786 (2016).
20. M. Waqas *et al*., *Neurosurgery* **87**, E445–E453 (2020).
21. T. Scullen, J. D. Nerva, P. S. Amenta, A. S. Dumont, *Neurosurgery* **87**, E454–E455 (2020).
22. F. B. Coulter *et al*., *Matter* **1**, 266–279 (2019).
23. M. A. Punchard *et al*., *Ann. Biomed. Eng.* **37**, 1322–1330 (2009).
24. R. N. Ghriallais, L. McNamara, M. Bruzzi, *J. R. Soc. Interface* **10**, 20120965 (2013).
25. L. Rouleau, J. Rossi, R. L. Leask, *J. Biomech. Eng.* **132**, 071015 (2010).
26. J. Martorell *et al*., *Cardiovasc. Res.* **103**, 37–46 (2014).
27. M. Balcells *et al*., *Circulation* **121**, 2192–2199 (2010).
28. W. Sun, C. Martin, T. Pham, *Annu. Rev. Biomed. Eng.* **16**, 53–76 (2014).
29. Z.-T. Xie, D.-H. Kang, M. Matsusaki, *Soft Matter* **17**, 8769–8785 (2021).
30. K. J. LeBlanc *et al*., *ACS Biomater. Sci. Eng.* **2**, 1796–1799 (2016).
31. D. Truzzolillo, L. Cipelletti, *Soft Matter* **13**, 13–21 (2016).
32. S. Duraivel *et al*., *Biophys. Rev.* **3**, 031307 (2022).
33. V. V. Erramreddy, S. Ghosh, *Langmuir* **30**, 11062–11074 (2014).
34. A. Z. Nelson, R. H. Ewoldt, *Soft Matter* **13**, 7578–7594 (2017).
35. A. Z. Nelson *et al*., *Curr. Opin. Solid State Mater. Sci.* **23**, 100758 (2019).
36. S. Duraivel, T. E. Angelini, Heart Valve Maker, v2.0, Zenodo (2023); https://doi.org/10.5281/zenodo.7643835.

ACKNOWLEDGMENTS

The authors thank Anton Paar for use of their MCR 702 rheometer through the Anton Paar VIP research program. **Funding:** No funding was received. **Author contributions:** Conceptualization: S.D. and T.E.A. Methodology: S.D., D.L., D.A.R., G.M.S., A.M.S., B.S.S., S.A.B., F.J.B., and T.E.A. Investigation: S.D., D.L., D.A.R., A.M.S., and T.E.A. Visualization: S.D., D.L., D.A.R., A.M.S., B.S.S., S.A.B., F.J.B., and T.E.A. Funding acquisition: B.S.S., S.A.B., F.J.B., and T.E.A. Project administration: T.E.A. Supervision: B.S.S., F.J.B., and T.E.A. Writing – original draft: S.D. and T.E.A. Writing – review and editing: S.D., D.L., D.A.R., G.M.S., A.M.S., B.S.S., S.A.B., F.J.B., and T.E.A. **Competing interests:** S.D., B.S.S., and T.E.A are inventors on a US patent application (PCT/US2021/037346). All other authors declare that they have no competing interests. **Data and materials availability:** All data are available in the manuscript and the supplementary material; code for the design and generation of print trajectories for the heart valve model is freely accessible at Zenodo (*36*).

License information: Copyright © 2023 the authors, some rights reserved; exclusive licensee American Association for the Advancement of Science. No claim to original US government works. https://www.science.org/about/science-licenses-journal-article-reuse

SUPPLEMENTARY MATERIALS

science.org/doi/10.1126/science.ade4441
Materials and Methods
Supplementary Text
Figs. S1 to S7
Movies S1 to S3

Submitted 17 August 2022; accepted 17 February 2023
10.1126/science.ade4441

RESEARCH ARTICLE SUMMARY

PLANT SCIENCE

Elucidation of the pathway for biosynthesis of saponin adjuvants from the soapbark tree

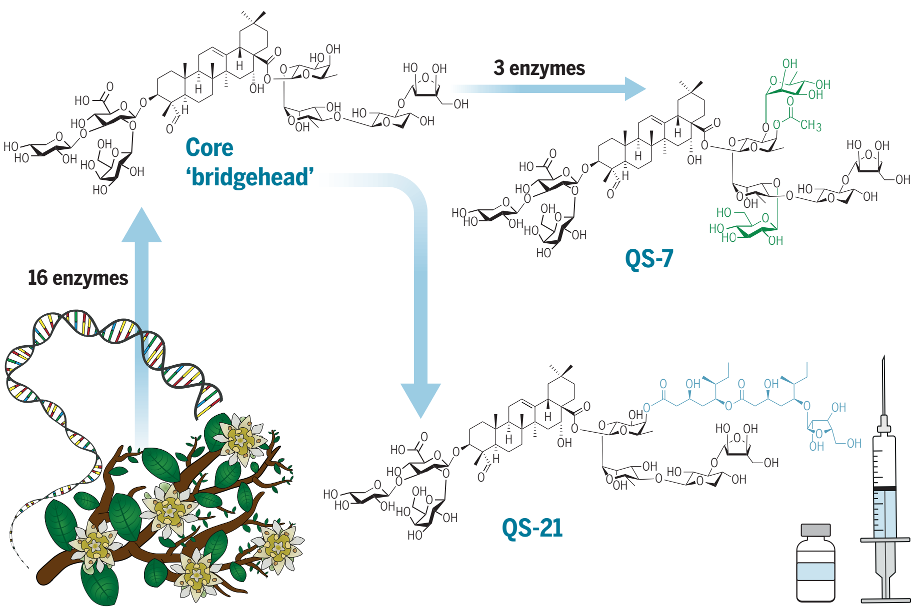
James Reed†, Anastasia Orme†, Amr El-Demerdash†, Charlotte Owen, Laetitia B. B. Martin, Rajesh C. Misra, Shingo Kikuchi, Martin Rejzek, Azahara C. Martin, Alex Harkess, Jim Leebens-Mack, Thomas Louveau, Michael J. Stephenson, Anne Osbourn*

INTRODUCTION: Adjuvants are immunostimulatory substances that are added to vaccines to boost the immune response. Until recently, the only adjuvants available for clinical use were aluminum salts, either alone (alum) or in proprietary mixtures, and oil-in-water emulsions containing squalene, which have relatively low potency and substantial side effects, respectively. Natural surfactants (saponins) have been used as adjuvants in veterinary medicine for almost a century. The first saponin adjuvant, AS01, has recently been approved for use in the human shingles vaccine Shingrix and the malaria vaccine Mosquirix. It is also a promising adjuvant candidate for a tuberculosis vaccine. AS01 is a liposome-based formula that contains monophosphoryl lipid A and a saponin known as QS-21, which act synergistically to induce strong antibody and helper T cell responses. QS-21 is one of >100 structurally related QS saponins produced by the Chilean soapbark tree (*Quillaja saponaria*). These include QS-7 and QS-17, which, together with QS-21, are included in the Novovax NVX-CoV2373 COVID-19 vaccine. Because of their chemical complexity, the only current commercial source of QS saponins is the bark of the soapbark tree. The increasing demand for these highly valuable molecules has led to growing interest in the possibility of developing environmentally sustainable, "free-from-tree" strategies to access these compounds in other ways.

RATIONALE: The biosynthetic pathway for QS saponins is not known. Elucidation of the genes and enzymes from the soapbark tree comprising the "instruction manual" for making QS saponins would provide insights into how these molecules are biosynthesized and diversified. It would also pave the way for new routes to access and engineer natural and new-to-nature immunostimulants.

RESULTS: We first sequenced the genome of the soapbark tree. Then, using genome mining and combinatorial transient expression in *Nicotiana benthamiana*, a wild relative of tobacco, we identified a total of 16 enzymes that together enable the production of advanced QS pathway intermediates that represent a bridgehead for adjuvant bioengineering. We also discovered a further three enzymes needed to make QS-7, a saponin with comparable adjuvant properties to QS-21 and low toxicity that is present in low abundance in *Q. saponaria* bark extract. Our work opens up the possibility of producing QS-7 and other related QS molecules in a heterologous expression system.

CONCLUSION: We have elucidated the pathway for the biosynthesis of advanced QS intermediates. Using our transient plant expression system, we were able to purify all of the intermediates at preparative scale, showing the power of this platform for rapid access to these molecules. We further demonstrate the production of the vaccine adjuvant QS-7. A number of plant natural products, including QS saponins and foxglove cardiac glycosides, have a D-fucose moiety, but the biosynthetic pathway to this sugar in plants was not previously known. In the present work, a route to D-fucosylation was discovered in which D-fucose is formed in situ from a 4-keto-6-deoxy-D-glucose attached to the saponin scaffold rather than being synthesized before transfer. Although the levels of QS-7 produced in *N. benthamiana* were low, they were comparable to those found in many tissues of *Q. saponaria*, with the exception of bark, which is about threefold higher. The availability of the complete gene sets for the biosynthesis of the heptasaccharide triterpene glycoside bridgehead QS saponins and QS-7 now present an opportunity for future endeavors to optimize production in heterologous expression systems with the ultimate aim of attaining commercial-scale yields. The availability of the complete genome sequence of *Q. saponaria*, coupled with our powerful and rapid transient expression platform, open up opportunities to access QS-21 and a diverse array of other saponins. This provides the potential to ultimately generate designer saponins with optimal immunostimulatory activity and low toxicity using metabolic engineering approaches. ■



Genomics-driven elucidation of saponin biosynthesis in the soapbark tree. The soapbark tree (*Q. saponaria*) produces >100 structurally related QS saponins, including the vaccine adjuvants QS-7 and QS-21. Transient combinatorial expression of a total of 16 enzymes in tobacco enabled the production of an advanced bridgehead for adjuvant bioengineering that can be used to access QS-7, paving the way for new routes to access and engineer natural and new-to-nature immunostimulants.

The list of author affiliations is available in the full article.
*Corresponding author. Email: anne.osbourn@jic.ac.uk
†These authors contributed equally to this work.

READ THE FULL ARTICLE AT
https://doi.org/10.1126/science.adf3727

PLANT SCIENCE

Elucidation of the pathway for biosynthesis of saponin adjuvants from the soapbark tree

James Reed[1]†, Anastasia Orme[1]†‡, Amr El-Demerdash[1]†§, Charlotte Owen[1], Laetitia B. B. Martin[1], Rajesh C. Misra[1], Shingo Kikuchi[1], Martin Rejzek[1], Azahara C. Martin[1], Alex Harkess[2,3], Jim Leebens-Mack[4], Thomas Louveau[1]¶, Michael J. Stephenson[1], Anne Osbourn[1]*

The Chilean soapbark tree (*Quillaja saponaria*) produces soap-like molecules called QS saponins that are important vaccine adjuvants. These highly valuable compounds are sourced by extraction from the bark, and their biosynthetic pathway is unknown. Here, we sequenced the *Q. saponaria* genome. Through genome mining and combinatorial expression in tobacco, we identified 16 pathway enzymes that together enable the production of advanced QS pathway intermediates that represent a bridgehead for adjuvant bioengineering. We further identified the enzymes needed to make QS-7, a saponin with excellent therapeutic properties and low toxicity that is present in low abundance in *Q. saponaria* bark extract. Our results enable the production of *Q. saponaria* vaccine adjuvants in tobacco and open the way for new routes to access and engineer natural and new-to-nature immunostimulants.

Vaccination is a huge success story in the fight against infectious diseases. Vaccines frequently require an adjuvant component (an immunostimulant) to enhance the immune response to the antigen. However, to date, only a few adjuvants have been licensed for human use. Triterpene glycosides (saponins) from the Chilean soapbark tree (*Quillaja saponaria*) have proven to be highly effective adjuvants because of their ability to elicit both antibody and cellular immune responses (*1*). These saponins are collectively known as QS saponins. The QS-21 fraction, comprising isomeric forms of a complex triterpene saponin, is an immune potentiator used in the adjuvant AS01. AS01 has been licensed for use in two human vaccines: the GSK vaccines Shingrix and Mosquirix, for shingles and malaria, respectively. A mixture of QS saponins, including QS-21, QS-17, and QS-7, is also included in Matrix-M, a combination adjuvant used in the NVX-CoV2373 COVID-19 vaccine produced by Novavax (*2*). QS-17 is a glycosylated derivative of QS-21. QS-7 has the same core structure as QS-21, but the two saponins differ in the nature of their modifications at the C-28 position. QS-7 has a simple acetyl group instead of the long (C-18) acyl chain present in QS-21, and there are also differences in the C-28 sugar moieties (Fig. 1A). Because of their chemical complexity, the only current commercial source of these saponins is the bark of the soapbark tree itself. However, these key immunogenic saponins represent only a portion of >100 structurally related molecules produced by *Q. saponaria* (*3*), so they require extensive purification. This issue is further exacerbated by variations in saponin content and composition between individual trees caused by environmental and genetic factors (*4*–*6*). Although a number of saponin biosynthetic enzymes have been characterized in recent years from taxonomically diverse plant species [e.g., (*7*–*10*)], much remains to be learned about the enzymes that generate the enormous structural diversity of saponins. Indeed, QS-21 has a total of seven different types of glycosidic moieties, including unusual sugars such as D-fucose, D-apiose, and L-arabinofuranose, for which the cognate enzymes are not yet known. Understanding the biosynthetic pathways for QS saponins will therefore provide new insights into how these molecules are made and diversified. It will further open up opportunities to produce saponins optimized for their immunostimulatory properties and low toxicity in heterologous hosts for use in the vaccines of the future.

Results

Biosynthesis of the quillaic acid scaffold

Triterpenes are biosynthesized from the linear isoprenoid precursor 2,3-oxidosqualene (**1**), which can be cyclized into >100 different diverse scaffold products (*11*). The most common of these scaffolds is β-amyrin (**2**). The core structure of QS-7, QS-21, and QS-17 is quillaic acid (QA) (**5**), which is based on β-amyrin but has oxidized groups at the C-16α, C-23, and C-28 positions (Fig. 1B). We therefore initiated our investigations of saponin biosynthesis in *Q. saponaria* by searching for the enzymes required for β-amyrin biosynthesis and oxidation.

QS saponins are normally extracted commercially from bark. At the time of starting this work, transcriptome data derived from *Q. saponaria* leaves were available through the 1000 Plants (1KP) Project (*12*). We obtained saplings of *Q. saponaria* from a UK nursery [John Innes Centre (JIC) accession no. S10; hereafter referred to as *Q. saponaria* S10] and verified the presence of QS-21 in the leaves, consistent with previous reports (*13*) (fig. S1). A BLAST search against the 1KP data was conducted using a characterized β-amyrin synthase (GgbAS1; GenBank accession no. AB037203) from licorice (*Glycyrrhiza glabra*) as a query (*14*). This revealed a single full-length candidate with 88% amino acid sequence identity to GgbAS1. We used gene-specific primers (data S1) to clone the corresponding sequence from cDNA prepared from the leaves of *Q. saponaria* S10. We then investigated the function of this candidate by *Agrobacterium*-mediated transient expression in the leaves of *Nicotiana benthamiana*. Gas chromatography–mass spectrometry (GC-MS) analysis of leaf extracts revealed a peak with the same retention time and mass spectrum as an authentic β-amyrin standard (**2**), confirming that this enzyme (hereafter referred to as QsbAS1) is indeed a β-amyrin synthase (fig. S2).

We next considered candidates for oxidation of β-amyrin (**2**). Most known triterpene oxidases are members of the cytochrome P450 monooxygenase (CYP) superfamily (*8*). Of these, the CYP716 family is commonly associated with triterpene biosynthesis and includes enzymes known to perform C-28 and C-16α oxidation (*8*, *15*). A BLAST search of the 1KP *Q. saponaria* transcriptome dataset was performed using a known C-28 oxidase from *Medicago truncatula* (CYP716A12; GenBank accession no. FN995112) (*16*), a saponin-producing species that, like *Q. saponaria*, belongs to the Fabales order. From this, the two highest scoring hits were selected for further investigation. Transient expression of the first of these, *CYP716A224*, with *QsbAS1* in *N. benthamiana* resulted in near total conversion of β-amyrin (**2**) to oleanolic acid (**3**) (fig. S3). The second enzyme, CYP716A297, showed very little activity toward β-amyrin. However coexpression of both *CYP716A224* and *CYP716A297* in combination with *QsbAS1* resulted in the formation of a new product that we identified as echinocystic acid (**4**) using an authentic standard (fig. S3). These two CYPs are therefore able to oxidize two (C-28 and C-16α) of the three positions that are oxidized in QA (**5**) (Fig. 1C). In searching for the final oxidase, we compiled a list of all CYP sequences in the 1KP *Q. saponaria* transcriptome dataset that appeared to be full length ($n = 35$). After eliminating enzymes that were closely related to known CYPs associated with primary metabolism, we were left with 26 candidates, of which 17 were successfully cloned and transiently expressed in *N. benthamiana* (data S2). Using

[1]John Innes Centre, Norwich Research Park, Norwich NR4 7UH, UK. [2]Department of Crop, Soil, and Environmental Sciences, Auburn University, Auburn, AL 36849, USA. [3]HudsonAlpha Institute for Biotechnology, Huntsville, AL 35806, USA. [4]Department of Plant Biology, University of Georgia, Athens, GA 30602, USA.
*Corresponding author. Email: anne.osbourn@jic.ac.uk
†These authors contributed equally to this work.
‡Present address: Illumina Centre, Great Abington, Cambridge CB21 6DF, UK.
§Present address: Department of Chemistry, Faculty of Sciences, Mansoura University, Mansoura 35516, Egypt.
¶Present address: GTP Technology, Immeuble Gould, 31670 Labège, France.

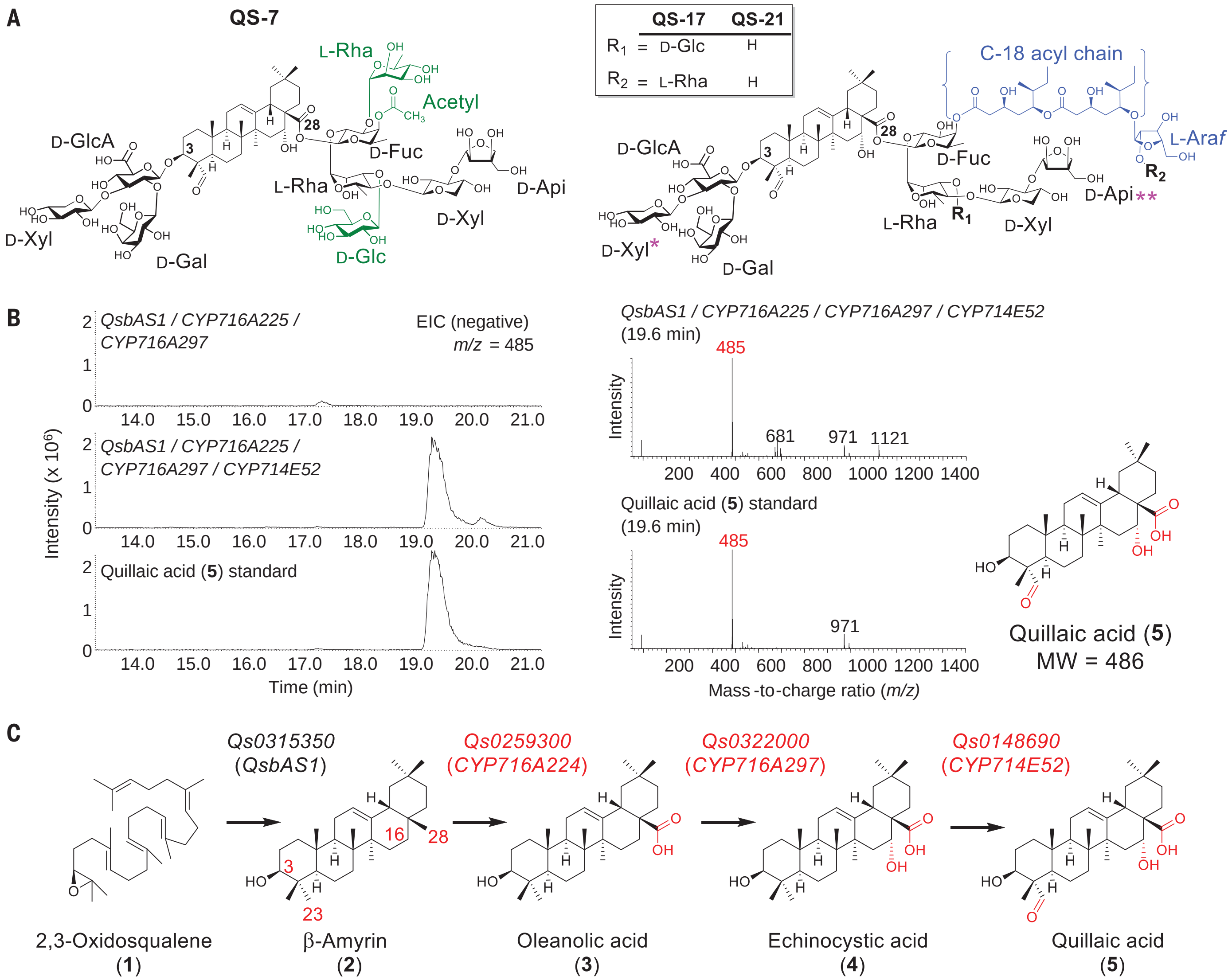


Fig. 1. Reconstitution of the steps to QA. (**A**) QS-7 and QS-21 share a core structure (shown in black) consisting of the triterpene scaffold QA; a branched trisaccharide at C-3 featuring D-glucuronic acid (D-GlcA), D-galactose (D-Gal), and D-xylose (D-Xyl); and a linear tetrasaccharide at C-28 featuring D-fucose (D-fuc), L-rhamnose (L-Rha), D-Xyl, and D-apiose (D-Api). This core structure is common to about one third of all reported QS saponins. It should be noted that QS-21 variants also exist with L-rhamnose in place of D-Xyl at C-3 (*) and D-Xyl in place of D-Api at C-28 (**). QS-17 is a glycosylated derivative of QS-21. Both have a D-glucose (D-Glc) attached to the L-Rha of the C-28 sugar chain (as shared with QS-7), whereas QS-17 also has an additional L-Rha attached to the L-arabinofuranose (L-Ara*f*) of the C-18 acyl chain. (**B**) LC-MS extracted ion chromatograms (EIC) for *N. benthamiana* leaf extracts after coexpression of the β-amyrin synthase QsbAS1 with the CYPs CYP716A224 (a C-28 oxidase), CYP716A297 (a C16α oxidase), and CYP714E52 (a C-23 oxidase). The combination of all four enzymes resulted in the production of the QS scaffold, QA (*m/z* = 485) (**5**). Top, extract from control leaves that are not expressing the C-23 oxidase. (**C**) Biosynthetic route to QA: QsbAS1, β-amyrin synthase; CYP716A224, C-28 oxidase; CYP716A297, C16α oxidase; and CYP714E52, C-23 oxidase. The structure of QA was confirmed by NMR (fig. S4). Note that CYP714E52 was also found to be active on oleanolic acid. The resulting product is anticipated to be the C-23 aldehyde of oleanolic acid (gypsogenin) (fig. S46).

this approach, a single candidate, *CYP714E52*, was identified, which, when coexpressed with *QsbAS1*, *CYP716A224*, and *CYP716A297*, resulted in the production of QA (**5**) in *N. benthamiana* (Fig. 1B). We then performed large-scale transient expression by vacuum agro-infiltration of 209 plants, purified ~30 mg of this product, and confirmed its structure as QA (**5**) by ^{1}H nuclear magnetic resonance (^{1}H NMR) spectroscopy (fig. S4 and Fig. 1C). A phylogenetic tree showing the relatedness of the three CYPs required for QA biosynthesis to other previously characterized triterpene modifying CYPs from plants is shown in fig. S5.

Generation of a pseudochromosome-level genome assembly for Q. saponaria

Genes for plant-specialized metabolic pathways are commonly coexpressed and may also be physically colocalized or "clustered" within the genome (*17*). Coexpression analysis requires the availability of RNA-sequencing (RNA-seq) data for multiple different tissues and/or treatments, whereas discovery of biosynthetic gene clusters is dependent on the availability of a genome assembly, neither of which was available for *Q. saponaria*. To facilitate discovery of the saponin biosynthetic steps downstream of QA, we therefore generated de novo transcriptome and genome sequence resources for *Q. saponaria* S10. RNA-seq data were generated for six different tissues, primordia, expanding leaves, mature leaves,

old leaves, green stems, and roots, using Illumina HiSeq4000. QS-21 was present in all tissues examined (fig. S1). The estimated genome size of *Q. saponaria* based on flow cytometry was 411 Mbp (*18*). PacBio long-read sequencing and Hi-C (high-throughput/resolution chromosome conformation capture) were used to generate a chromosome-scale assembly (table S1, fig. S6, and materials and methods). The draft genome was annotated by RNA-seq read alignment, filtering, gene model generation, and selection of final gene models (table S1, fig. S7, and materials and methods). Karyotype analysis revealed 28 chromosomes, consistent with a haploid chromosome number of 14 (Fig. 2A). The 14 scaffolds therefore represent the 14 chromosomes of *Q. saponaria* S10. Synteny analysis provided evidence for a whole-genome duplication event in *Q. saponaria* S10 (Fig. 2B), consistent with hypothesized polyploidy events observed across members of the Fabales (*19*).

Investigation of the expression profiles of the characterized QA biosynthesis genes in different *Q. saponaria* tissues revealed that these genes are highly coexpressed (Fig. 2C), with the highest absolute expression in leaf primordia and the lowest in old leaves (Fig. 2C and fig. S8), suggesting that it may be possible to identify further candidate downstream QS pathway genes on the basis of coexpression using these genes as bait.

We next mined the *Q. saponaria* genome assembly using plantiSMASH, an algorithm designed to predict biosynthetic gene clusters (BGCs) in plant genomes (*20*). plantiSMASH predicted a total of 51 candidate clusters, of which 34 were assigned to the "saccharide" and/or "terpene" classes (fig. S9 and data S3) and so may be relevant to triterpene glycoside (i.e., saponin) biosynthesis. The four QA biosynthetic genes, *QsbAS1*, *CYP714E52*, *CYP716A224*, and *CYP716A297*, are not physically clustered with each other. However, the gene encoding one of the CYPs required for QA biosynthesis (*CYP716A297*) is located adjacent to a saccharide biosynthetic gene cluster (cluster 45) that includes genes predicted to encode sugar

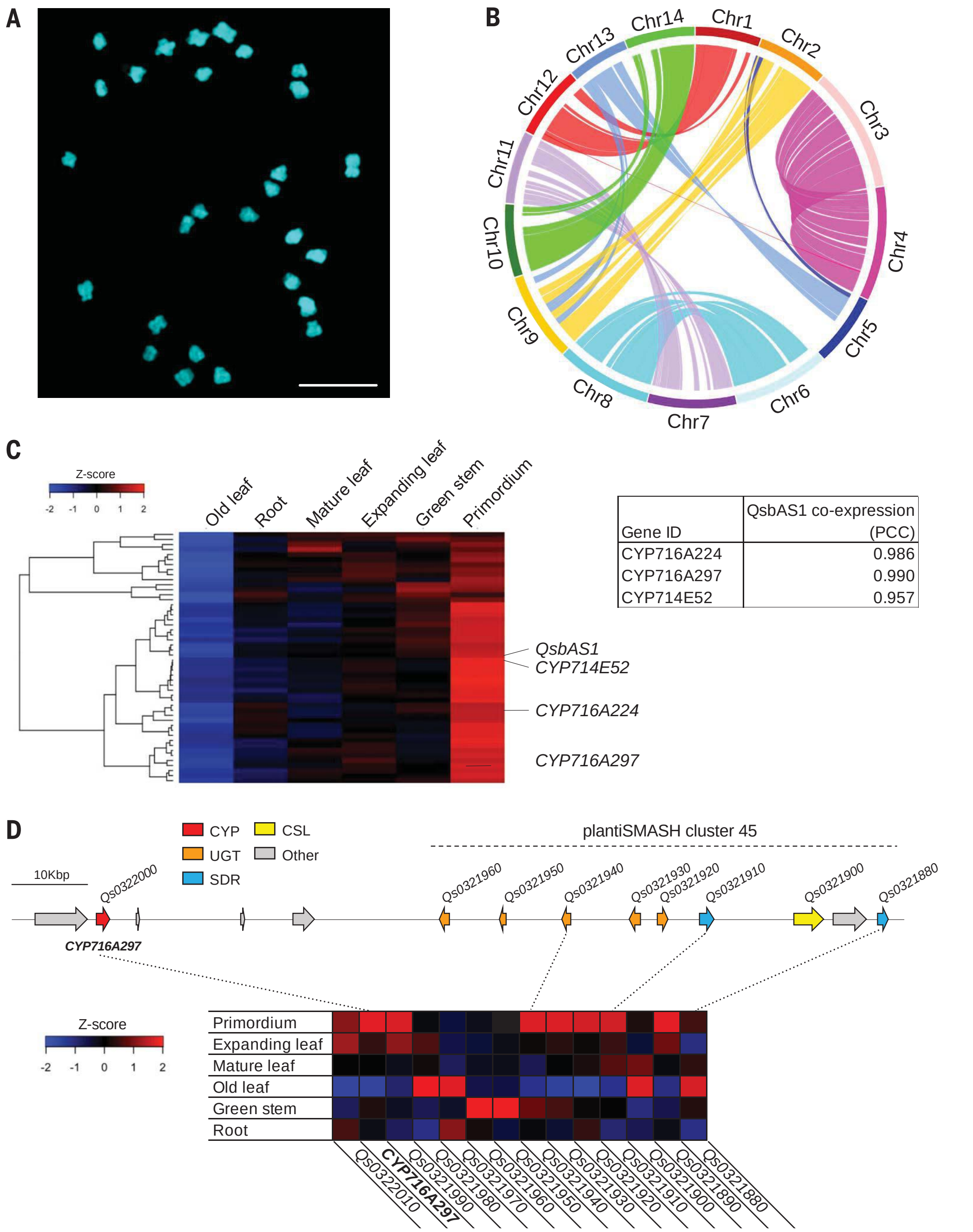


Fig. 2. Generation of the *Q. saponaria* genome and transcriptome sequences resources. (**A**) Karyotype analysis of *Q. saponaria* S10 meristem tissue at mitotic metaphase I revealing 28 chromosomes. Scale bar, 5 μm. (**B**) Circular synteny plot showing the 14 chromosomes of *Q. saponaria* S10. Syntenic blocks (indicated by the colored lines) provide evidence of a whole-genome duplication event. (**C**) Hierarchical clustering of the top 50 *Q. saponaria* genes that are coexpressed with *QsbAS1*, as calculated by the PCC value of *z* scores (generated from DESeq2 VST-transformed read quantification values). The four QA biosynthetic genes (labeled) show tight coexpression and are expressed most strongly in primordial tissue. PCC values for the three QA CYPs with QsbAS1 are shown to the right. (**D**) A biosynthetic gene cluster (45) predicted by plantiSMASH is located on chromosome 11, very close to the QA biosynthesis gene *CYP716A297*. Several of the genes in this region also show high expression in primordial tissue.

transferases and other enzymes with potential functions in specialized metabolism (Fig. 2D). Some of these genes have similar expression profiles to *CYP716A297*, potentially suggesting a functional association (Fig. 2D).

Addition of the C-3 sugar chain

Having discovered the biosynthetic steps to QA (**5**) (Fig. 1C), we next focused on identifying the enzymes required for the addition of sugars at the C-3 and C-28 positions of the QA scaffold. The enzymes typically responsible for glycosylation of plant natural products belong to glycosyltransferase 1 (GT1) family (*21*, *22*). GT1 enzymes use uridine diphosphate (UDP)–activated sugar donors to transfer sugar units onto small molecules, so they are referred to as UDP-dependent glycosyltransferases (UGTs). We therefore mined the *Q. saponaria* genome annotation to find all predicted full-length (>410 amino acids) UGT genes by searching with InterPro code IPR002213. This yielded a total of 166 predicted UGT genes, which were then prioritized on the basis of their strength of coexpression with *QsbAS1* [Pearson correlation coefficient (PCC) cutoff of 0.7] and their absolute gene expression levels in primordia [transcripts per million (TPM) >1600], resulting in a shortlist of 20 UGT genes (table S2). The two most highly coexpressed UGTs, *Qs0321930* and *Qs0321920* (PCC 0.987 and 0.985, respectively), were colocated in the BGC shown in Fig. 2D, along with a third coexpressed UGT gene, *Qs0321940* (PCC 0.956). This cluster also contains a gene for another class of carbohydrate-active enzyme, *Qs0321900*, which is predicted to encode a cellulose synthase–like (CSL) protein. *Qs0321900* is not coexpressed with *QsbAS1* (PCC –0.59), although it is expressed at moderate levels in primordial tissue. Another unlinked but closely related predicted CSL gene, *Qs0000870*, is very highly coexpressed with *QsbAS1* (PCC 0.992), suggestive of a role in the QS pathway. We cloned all 20 UGT candidates and both CSL genes to evaluate their functions.

Coexpression of each of the UGT and CSL genes with the four QA pathway genes was performed by transient expression in *N. benthamiana* and modification of QA (**5**) monitored by untargeted liquid chromatography–mass spectrometry (LC-MS). No conversion of QA (**5**) was observed when the UGT candidates were coexpressed. However, when either of the two CSL genes was coexpressed with the QA pathway genes, LC-MS analysis of leaf extracts revealed a peak with a mass corresponding to QA plus D-glucuronic acid and a concomitant reduction in QA (**5**) levels (Fig. 3A). We then scaled up our transient plant expression experiments. After vacuum infiltration of 104 *N. benthamiana* plants coexpressing the QA pathway genes with *CSL1*, we were able to purify 9.5 mg of product (data S4). We also obtained 2.1 mg of the product of coexpression of the QA pathway genes with *CSL2* (from 80 *N. benthamiana* plants) (data S4). ^{1}H NMR analysis revealed that the spectra for the two products were identical (fig. S10). Extensive 2D NMR analysis (COSY, HSQC, HMBC, and ROESY) confirmed that both products were 3-*O*-{β-D-glucopyranosiduronic acid}-QA (**6**; hereafter abbreviated as QA-Mono) (tables S3 and S4).

Phylogenetic analysis revealed that CSL-1 and CSL-2 belong to the CSL-M subfamily, so they are hereafter referred to as CSLM1 and CSLM2 (fig. S11). Although CSL proteins have not traditionally been regarded as small-molecule glycosyltransferases, two other examples have recently been reported from other plant species (*9*, *23*). The strong coexpression of *CSLM2* with *QsbAS1* suggests that CSLM2 may be primarily responsible for QA-Mono (**6**) biosynthesis in *Q. saponaria*.

We next screened our suite of cloned UGT candidates for the ability to glycosylate QA-Mono (**6**). Coexpression of *Qs0123860* (ranked third in table S2 based on coexpression with *QsbAS1*) with the QA pathway genes and *CSLM1* resulted in a new product with the mass of QA-GlcA plus a hexose (Fig. 3B). After scale-up by vacuum infiltration of 104 *N. benthamiana* plants, 7.3 mg of this product was purified and its structure determined to be 3-*O*-{β-D-galactopyranosyl-(1→2)-β-D-glucopyranosiduronic acid}-QA (**7**; hereafter abbreviated as QA-Di) by NMR (COSY, HSQC, HMBC, and ROESY) (table S5 and data S4). Thus, *Qs0123860* (UGT73CU3) encodes a QA-3-*O*-glucuronoside-β-1,2-galactosyltransferase capable of adding the second sugar to the C-3 position of *Q. saponaria* saponins.

Another round of coexpression experiments led to the identification of two UGTs that were able to further glycosylate QA-Di (**7**). One of these, *Qs0283870,* generated a product with a mass consistent with addition of a pentose, whereas the product of the second, *Qs0283850*, had a mass consistent with addition of a deoxyhexose (Fig. 3B). It is known that saponins from *Q. saponaria* show variation in the terminal sugar of the C-3 oligosaccharide chain and that either D-xylose or L-rhamnose can occur at this position (*3*, *5*, *24*). After large-scale vacuum infiltration, the two products were purified and their structures determined by extensive 2D NMR as 3-*O*-{β-D-xylopyranosyl-(1→3)-[β-D-galactopyranosyl-(1→2)]-β-D-glucopyranosiduronic acid}-QA (**8**; hereafter abbreviated as QA-TriX) (21.6 mg purified) and 3-*O*-{α-L-rhamnopyranosyl-(1→3)-[β-D-galactopyranosyl-(1→2)]-β-D-glucopyranosiduronic acid}-QA (**9**; hereafter abbreviated as QA-TriR) (43.3 mg purified), respectively (tables S6 and S7 and data S4). Thus, *Qs0283870* (UGT73CX1) encodes a xylosyltransferase and *Qs0283850* (UGT73CX2) a rhamnosyltransferase. These genes are ranked sixth and 13th, respectively, in table S2 on the basis of their coexpression with *QsbAS1*. Phylogenetic analysis revealed that all three UGTs, UGT73CU3, UGT73CX1, and UGT73CX2, belong to subgroup D of the GT1 family (fig. S12). This subgroup includes several other enzymes that are known to glycosylate triterpenes from both monocots and dicots (*21*). In summary, CSLM1/2, together with the three UGT enzymes characterized here, collectively enable the conversion of QA (**5**) to either QA-TriX (**8**) or QA-TriR (**9**) (Fig. 3C).

Addition of the C-28 sugar chain

QS-7, QS-21, and QS-17 share a common core consisting of the QA scaffold, the C-3 sugar chain, and a tetrasaccharide moiety at C-28 consisting of D-fucose, L-rhamnose, D-xylose, and D-apiose (Fig. 1A). These molecules differ in the nature of the other sugar and acyl groups attached to the C-28 sugar chain. A survey of the structures of saponins reported from *Q. saponaria* indicated that C-3 glycosylation is likely to precede the modifications at the C-28 position (fig. S13). Our results thus far were consistent with this hypothesis. Having successfully reconstituted the pathway for addition of the C-3 trisaccharide chain, we next turned our attention to elucidating the steps needed for glycosylation at C-28. The sugar that is linked directly to the QA scaffold at this position is D-fucose, which is attached through an ester linkage. The UGT gene *Qs0321930* (*UGT74BX1*) shows the highest level of coexpression with *QsbAS1* (PCC 0.987) (table S2) and is located in biosynthetic gene cluster 45 (Fig. 2D). Furthermore, *Qs0321930* is the only gene on the UGT candidate list that is predicted to encode a member of subgroup L of the GT1 family (fig. S12), a subgroup known to contain ester-forming UGTs (*21*). Indeed, transient expression of *Qs0321930*, together with the previously identified *Q. saponaria* saponin biosynthesis genes (the four QA genes, *CSLM2*, *UGT73CU3*, and *UGT73CX1*, producing **8**), resulted in formation of small amounts of a new product with a mass consistent with addition of a deoxyhexose, which we anticipated to be the C-28 fucoside of **8** (**10**; hereafter abbreviated as QA-TriX-F) (fig. S14). UDP-α-D-fucose has been suggested to be limiting in *N. benthamiana*, which could account for the low abundance of the new product (*9*). Nevertheless, screening of additional UGT candidates against the putative QA-TriX-F (**10**) resulted in the identification of a UGT in subgroup A capable of adding a further deoxyhexose, with a mass consistent with addition of L-rhamnose as the second sugar in the C-28 sugar chain, to form QA-TriX-FR (**12**) (fig. S14). The activity of this putative rhamnosyltransferase, *UGT91AR1*, was dependent on the presence of D-fucose. The gene encoding it, *Qs0321920*, has the second-highest level of coexpression with *QsbAS1* (PCC 0.985; table S2) and is located in biosynthetic gene cluster 45 adjacent to the putative fucosyltransferase gene (*UGT74BX1*), with which it

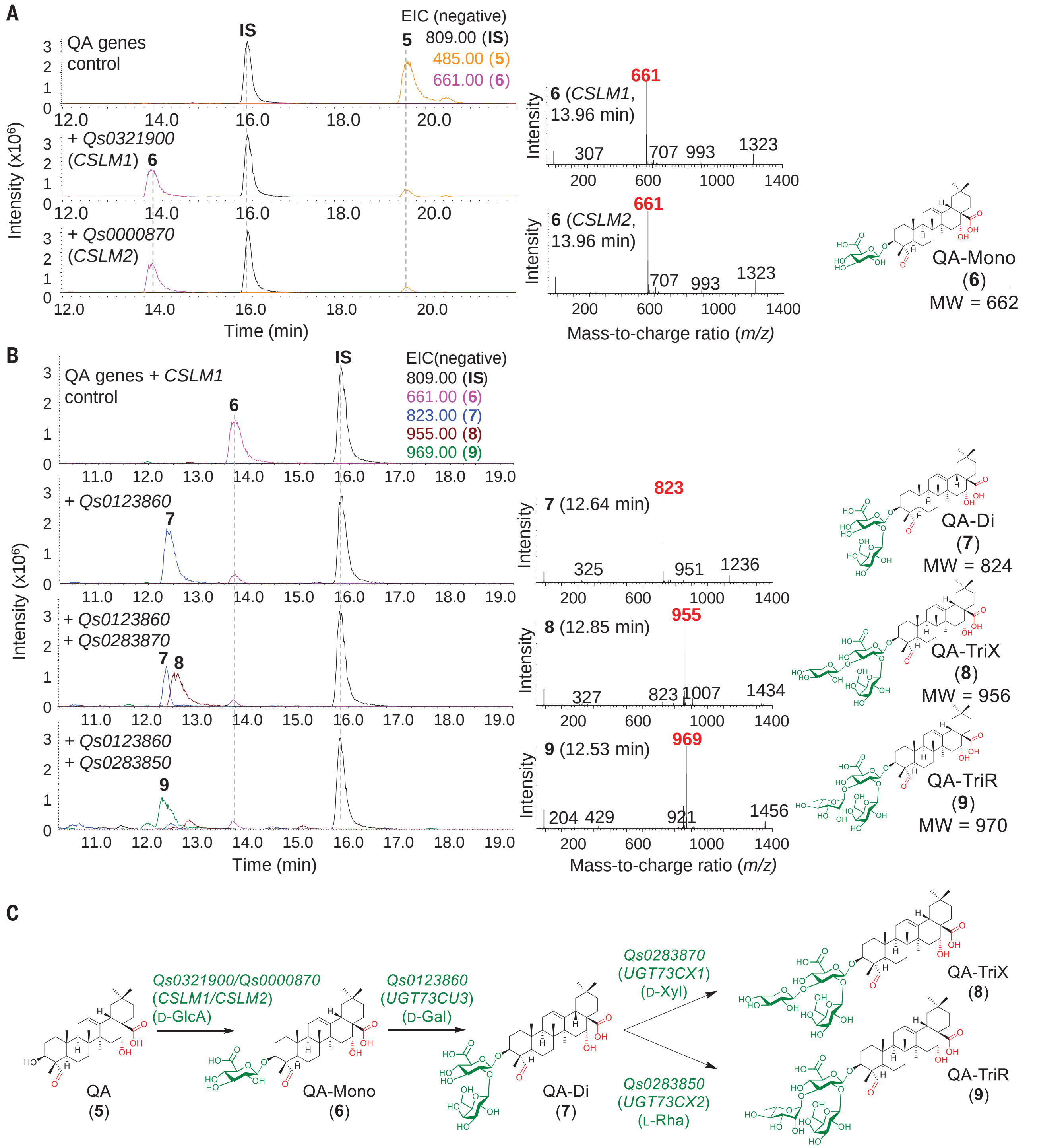


Fig. 3. Addition of the C-3 sugar chain. (**A**) LC-MS EIC of *N. benthamiana* leaf extracts showing that coexpression of either of the predicted CSL genes, *CSLM1* or *CSLM2*, with the four QA genes results in the conversion of QA to a new more polar product (retention time 14 min). The mass spectra (right) indicate that the product is the same for *CSLM1* and *CSLM2* and are consistent with addition of glucuronic acid to QA to form QA-Mono (**6**). IS, internal standard (digitoxin). (**B**) LC-MS EIC of *N. benthamiana* leaf extracts after coexpression with UGT candidates that add additional sugars at the C-3 position. A control sample from leaves expressing the QA pathway plus glucuronosyltransferase (CSLM1) is shown at the top. The second panel shows that further coexpression of *Qs0123860* resulted in conversion of QA-Mono (**6**) to a new product consistent with addition of a galactose to form QA-Di (**7**). Coexpression of either *Qs0283870* (third panel) or *Qs0283850* (bottom panel) with the QA-Di gene set resulted in conversion of QA-Di (**7**) to new products. The *Qs0283870* product was consistent with the addition of a xylose to form QA-TriX (**8**), whereas the *Qs0283850* product was consistent with the addition of a rhamnose to form QA-TriR (**9**). The mass spectra of these products and structures are shown to the right of the chromatograms. (**C**) Summary of the pathway from QA (**5**) to QA-TriX (**8**) and QA-TriR (**9**). The structures of compounds **6** to **9** were all confirmed by NMR after large-scale infiltration and purification (tables S3 to S7 and data S4).

Recent PhD?

Boost your career by applying to the *Science* and SciLifeLab's Prize for young scientists

If selected as a winner, you will have your essay published by ***Science***, win up to USD 30,000 and be invited to Sweden during our 10th anniversary celebration to receive your prize, present your research and meet with leading scientists in your field.

Science & SciLifeLab

PRIZE

For Young Scientists

Knut and Alice Wallenberg Foundation

SciLifeLab

Science AAAS

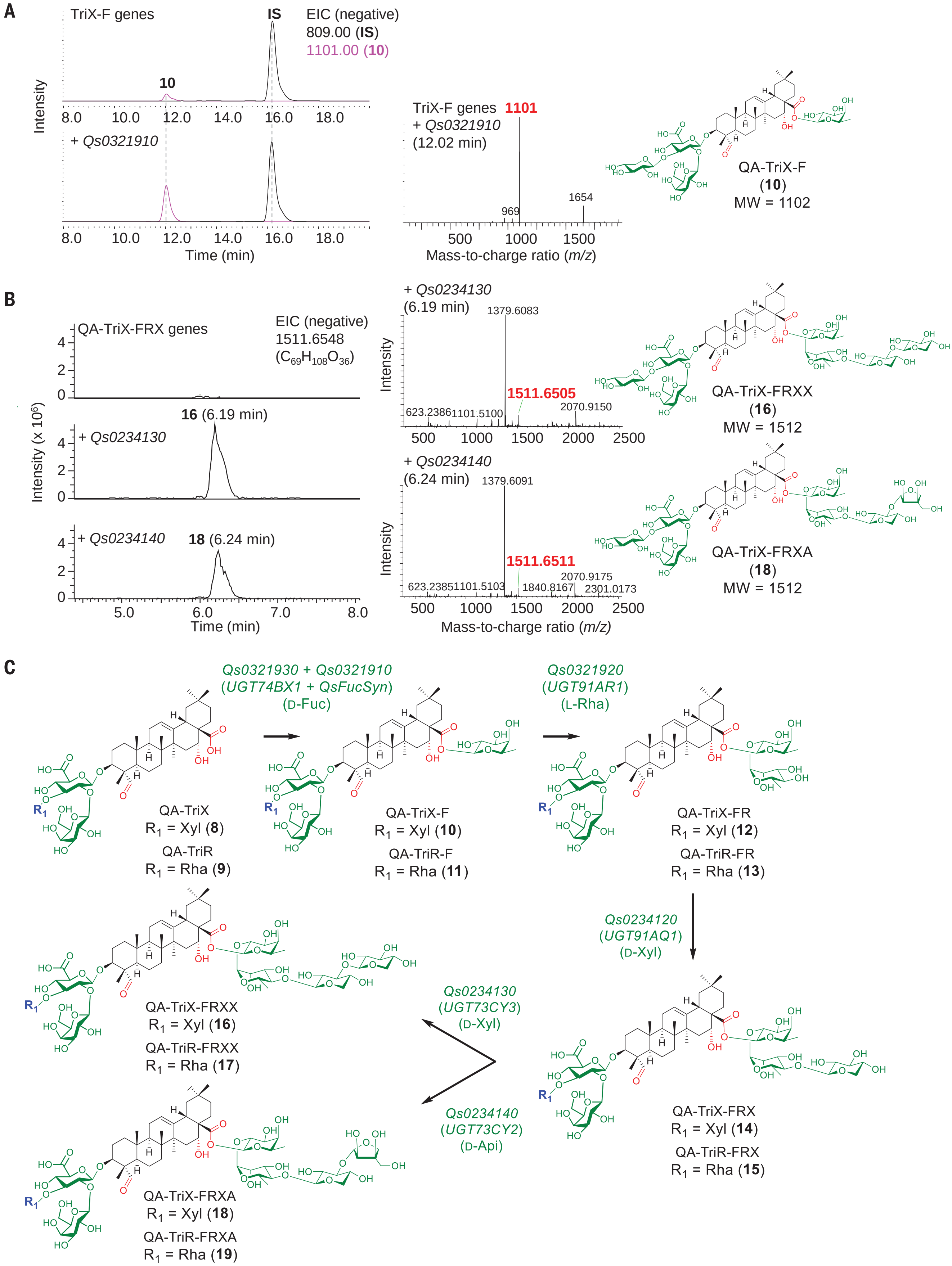

A
TriX-F genes
IS
EIC (negative)
809.00 (IS)
1101.00 (10)
10
Intensity
8.0 10.0 12.0 14.0 16.0 18.0
+ Qs0321910
Time (min)
TriX-F genes 1101
+ Qs0321910
(12.02 min)
969
1654
500 1000 1500
Mass-to-charge ratio (m/z)
QA-TriX-F
(10)
MW = 1102
B
QA-TriX-FRX genes
EIC (negative)
1511.6548
(C69H108O36)
Intensity (x 10^6)
16 (6.19 min)
+ Qs0234130
+ Qs0234140
18 (6.24 min)
5.0 6.0 7.0 8.0
Time (min)
+ Qs0234130
(6.19 min)
1379.6083
1511.6505
623.2386
1101.5100
2070.9150
QA-TriX-FRXX
(16)
MW = 1512
+ Qs0234140
(6.24 min)
1379.6091
1511.6511
623.2385
1101.5103
1840.8167
2070.9175
2301.0173
QA-TriX-FRXA
(18)
MW = 1512
500 1000 1500 2000 2500
Mass-to-charge ratio (m/z)
C
Qs0321930 + Qs0321910
(UGT74BX1 + QsFucSyn)
(D-Fuc)
Qs0321920
(UGT91AR1)
(L-Rha)
QA-TriX
R1 = Xyl (8)
QA-TriR
R1 = Rha (9)
QA-TriX-F
R1 = Xyl (10)
QA-TriR-F
R1 = Rha (11)
QA-TriX-FR
R1 = Xyl (12)
QA-TriR-FR
R1 = Rha (13)
Qs0234120
(UGT91AQ1)
(D-Xyl)
QA-TriX-FRXX
R1 = Xyl (16)
QA-TriR-FRXX
R1 = Rha (17)
Qs0234130
(UGT73CY3)
(D-Xyl)
Qs0234140
(UGT73CY2)
(D-Api)
QA-TriX-FRXA
R1 = Xyl (18)
QA-TriR-FRXA
R1 = Rha (19)
QA-TriX-FRX
R1 = Xyl (14)
QA-TriR-FRX
R1 = Rha (15)

Fig. 4. Addition of the C-28 sugar chain. (**A**) LC-MS EIC of *N. benthamiana* leaf extracts after transient expression of the gene set for production of QA-TriX-F (**10**). Only low amounts of **10** accumulate in *N. benthamiana* (top). However, coexpression of the short-chain dehydrogenase encoded by *Qs0321910* results in marked increases in the yield of this product (bottom), as well as increases in further downstream products (fig. S15). (**B**) Identification of the terminal xylosyl- and apiosyltransferases required for synthesis of the linear tetrasaccharide at C-28. The gene set for production of QA-TriX-FRX (**14**) was transiently coexpressed in *N. benthamiana* (top). Further coexpression of either *Qs0234130* (middle) or *Qs0234140* (bottom) resulted in the appearance of new products with identical masses (consistent with addition of pentoses) and slight differences in retention times. Large-scale infiltration, purification, and NMR analysis of the products using the QA-TriR-FRX (**15**) scaffold determined that *Qs0234130* is the terminal xylosyltransferase, whereas *Qs0234140* is the terminal apiosyltransferase (tables S9 and S10). (**C**) Summary of the biosynthetic pathway for the C-28 tetrasaccharide chain. The structures of compounds **11**, **13**, **15**, **17**, and **19** were all confirmed by NMR after large-scale infiltration and purification (tables S8 to S12).

shares only ~30% amino acid sequence identity. A further round of screening identified another subgroup A UGT encoded by *Qs0234120* (*UGT91AQ1*) that appeared to modify QA-TriR-FR by addition of a pentose, suggesting that this may be the C-28 xylosyltransferase producing QA-TriX-FRX (**14**) (fig. S14).

In contrast to the QA C-3 glycosides, only trace amounts of the three putative C-28 glycosides were observed, with large quantities of unconverted precursor QA-TriX (**8**) remaining (fig. S14). It was apparent that the poor conversion from the QA-TriX (**8**) product to QA-TriX-F (**10**) was likely to represent a substantial bottleneck, impeding further pathway elucidation and structural verification of the products. Biosynthetic gene cluster 45 also harbors two predicted short chain dehydrogenase/reductase (SDR) genes. One of these, *Qs0321910*, is located immediately adjacent to the *UGT91AR1* gene and has a similar expression pattern to the QS enzymes characterized so far (coexpression with *QsbAS1*, PCC 0.871) (Fig. 2D). Most of the known sugar nucleotide–interconverting enzymes are members of the SDR superfamily (*25*, *26*). Transient coexpression of this SDR enzyme with the gene set for QA-TriX-F (**10**) biosynthesis resulted in substantial increases in the levels of the QA-TriX-F (**10**) product, suggesting that the SDR has a role in D-fucosylation, potentially by converting an endogenous UDP-sugar substrate in *N. benthamiana* to UDP-D-fucose, thereby furnishing enhanced FucT activity (Fig. 4A). Further, coexpression of the additional C-28 sugar transferases, including *UGT91AR1* and *UGT91AQ1*, demonstrated that the amounts of the relevant products [QA-TriX-FR (**12**) and QA-TriX-FRX (**14**), respectively] were likewise substantially increased in the presence of the *Qs0321910* SDR (fig. S15).

We next exploited the new SDR to perform large-scale transient expression experiments in *N. benthamiana* to purify the new UGT products. During the previous purifications of the C-3 QA trisaccharide products, we obtained approximately twofold higher yields of the the C-3 rhamnose [QA-TriR (**9**)] compared with the C-3 xylose version [QA-TriX (**8**)] (data S4). We therefore opted to generate and purify the putative C-28 glycosides on the basis of the QA-TriR (**9**) scaffold. After infiltration of 100 to 200 *N. benthamiana* plants, the products were purified and their identities confirmed by extensive 1D and 2D NMR analysis as follows: UGT74BX1 product (3-*O*-{α-L-rhamnopyranosyl-(1→3)-[β-D-galactopyranosyl-(1→2)]-β-D-glucopyranosiduronic acid}-28-*O*-{β-D-fucopyranosyl ester}-QA) (**11**) (hereafter abbreviated as QA-TriR-F) (1 mg purified); UGT91AR1 product (3-*O*-{α-L-rhamnopyranosyl-(1→3)-[β-D-galactopyranosyl-(1→2)]-β-D-glucopyranosiduronic acid}-28-*O*-{α-L-rhamnopyranosyl-(1→2)-β-D-fucopyranosyl xester}-QA) (**13**) (hereafter abbreviated as QA-TriR-FR) (43.9 mg purified); and the UGT91AQ1 product (3-*O*-{α-L-rhamnopyranosyl-(1→3)-[β-D-galactopyranosyl-(1→2)]-β-D-glucopyranosiduronic acid}-28-*O*-{β-D-xylopyranosyl-(1→4)-α-L-rhamnopyranosyl-(1→2)-β-D-fucopyranosyl ester}-QA) (**15**) (hereafter abbreviated as QA-TriR-FRX) (3.1 mg purified) (tables S8 to S10 and data S4).

The terminal sugar in the linear tetrasaccharide at C-28 in saponins such as QS-21 can be either D-xylose or D-apiose (Fig. 1A). Having identified the enzymes that add the first three sugars in the C-28 sugar chain, we performed a final round of screening to identify the sugar transferases that add these sugars. This led to the identification of two further functional UGTs that each generated a product consistent with QA-TriX-FRX plus a pentose, but with slightly different retention times (Fig. 4B). The genes encoding these enzymes, *Qs0234130* and *Qs0234140* (ranked 14th and 18th, respectively, in table S2), were both located in the chromosome 7 biosynthetic gene cluster 31 with the previously characterized C-28 xylosyltransferase *UGT91AQ1* (data S3). This region is syntenic to the chromosome 11 biosynthetic gene cluster 45, suggesting that the two clusters may share a common evolutionary origin and may have arisen as a consequence of genome duplication (fig. S16). We also found that a predicted UDP-D-apiose/UDP-D-xylose synthase gene, *Qs0088320*, was highly expressed in *Q. saponaria* leaf primordia. This gene was not physically clustered with the previously characterized saponin biosynthesis genes but showed strong coexpression with them (coexpression with *QsbAS1*, PCC 0.943). Transient expression of this putative UDP-apiose/UDP-xylose synthase (QsAXS) with either *Qs0234130* or *Qs0234140* resulted in a marked increase (~11-fold) in the amount of the *Qs0234140* product generated (fig. S17).

We next performed large-scale transient expression in *N. benthamiana* and purified each of the two new UGT products using the QA-TriR-FRX scaffold (**15**). Their structures were determined by extensive 1D and 2D NMR as (3-*O*-{α-L-rhamnopyranosyl-(1→3)-[β-D-galactopyranosyl-(1→2)]-β-D-glucopyranosiduronic acid}-28-*O*-{β-D-xylopyranosyl-(1→3)-β-D-xylopyranosyl-(1→4)-α-L-rhamnopyranosyl-(1→2)-β-D-fucopyranosyl ester}-QA) (**17**) (*Qs0234140*; 13.2 mg purified) (hereafter abbreviated as QA-TriR-FRXX) and (3-*O*-{α-L-rhamnopyranosyl-(1→3)-[β-D-galactopyranosyl-(1→2)]-β-D-glucopyranosiduronic acid}-28-*O*-{β-D-apiofuranosyl-(1→3)-β-D-xylopyranosyl-(1→4)-α-L-rhamnopyranosyl-(1→2)-β-D-fucopyranosyl ester}-QA) (**19**) (*Qs0234130;* 13.2 mg purified) (hereafter abbreviated as QA-TriR-FRXA) (tables S11 and S12 and data S4). Thus, *Qs0234130* (*UGT73CY3*) encodes the terminal xylosyltransferase, and *Qs0234140* (*UGT73CY2*) encodes the terminal C-28 apiosyltransferase (Fig. 4C). The importance of QsAXS in boosting the *Qs0234140* product suggests that UDP-α-D-apiose may be lacking in *N. benthamiana*. The fully characterized pathway up to this point is shown in Fig. 5. About one third of characterized QS saponins are derived from these scaffolds (*24*), making this an important branch point for saponin diversification.

Mechanism for D-fucosylation

Given the importance of the SDR encoded by *Qs0321910* for enhancing D-fucosylation and subsequent addition of the sugar chain at C-28, we sought to further understand the function of this enzyme. We hypothesized that this enzyme would be responsible for the production of UDP-D-fucose. Despite the fact that plant sugar biosynthetic pathways are generally well characterized, the biosynthetic route to D-fucose in plants is unknown. In bacteria, dTDP-D-glucose is converted to dTDP-4-keto-6-deoxy-D-glucose by a dTDP-D-glucose 4,6-dehydratase. The 4-keto group of this intermediate is then reduced by dTDP-4-keto-6-deoxy-D-glucose reductase to form dTDP-D-fucose (Fig. 6A) (*27*). The first of these steps is shared with dTDP-L-rhamnose biosynthesis, and indeed it is known that plants synthesize the analogous UDP-L-rhamnose from UDP-D-glucose through UDP-4-keto-6-deoxy-D-glucose (*28*). Because UDP-4-keto-6-deoxy-D-glucose would be expected to be present in plant cells as part of UDP-L-rhamnose biosynthesis, we hypothesized that the *Qs0321910* SDR may function as a 4-ketoreductase. Furthermore,

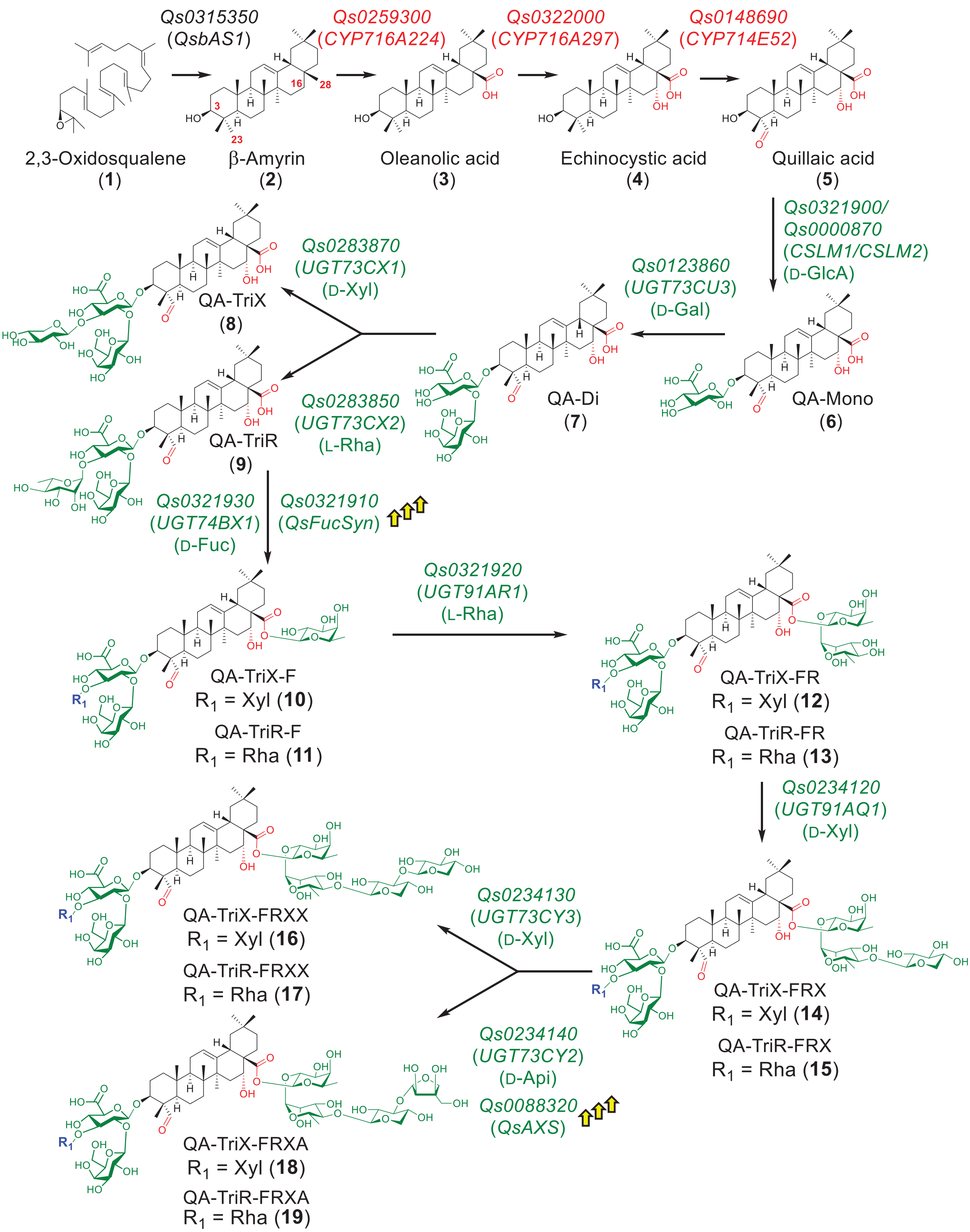


Fig. 5. Complete pathway to compounds 16 to 19. A summary giving full compound names, abbreviations, isolated yields, retention times, and *m/z* data, as well as the set of genes transiently expressed in *N. benthamiana* for each compound is provided as data S4.

phylogenetic analysis of this SDR revealed that it is a member of the SDR114C family (fig. S18), as previously defined by Moummou *et al.* (*29*). Several members of this family have been shown to reduce carbonyl groups to alcohols in alkaloid and terpenoid biosynthesis (*29*–*32*), consistent with our proposal that the *Qs0321910* SDR may perform C-4 reduction of UDP-4-keto-6-deoxy-D-glucose to form UDP-D-fucose.

To test this hypothesis, we purified the *Qs0321910* SDR for functional analysis in vitro (fig. S19). The anticipated UDP-4-keto-6-deoxy-D-glucose substrate is not commercially available. Therefore, to generate this compound from UDP-D-glucose, we cloned and purified a characterized UDP-D-glucose 4,6-dehydratase from the *Acanthocystis turfacea* chlorella virus 1 (ATCV-1 UGD, GenBank accession no. YP_001427025.1)

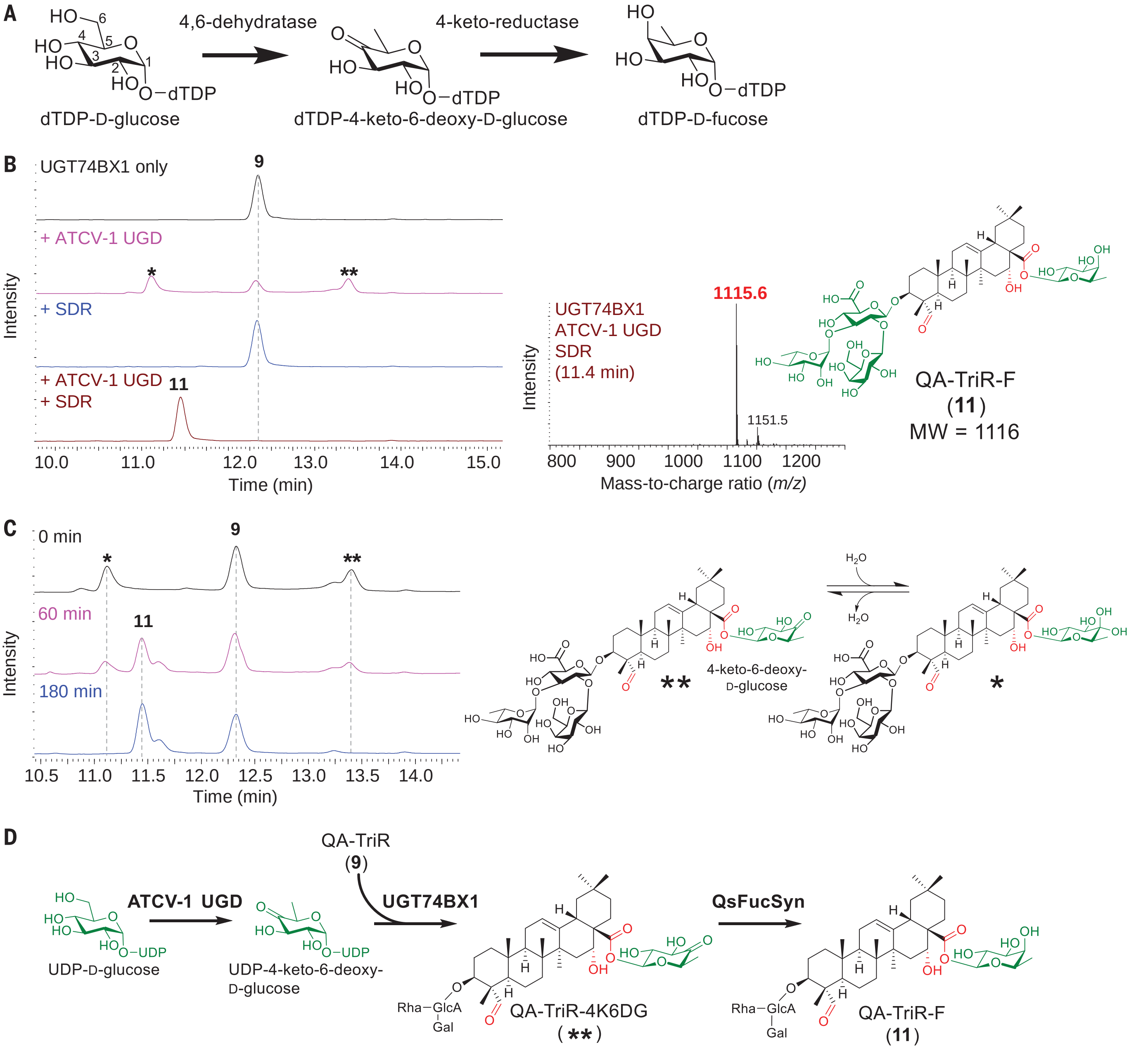


Fig. 6. Characterization of the SDR encoded by *Qs0321910*. (**A**) Biosynthesis of D-fucose in bacteria. dTDP-D-glucose is converted in a two-step process to dTDP-D-fucose through dTDP-4-keto-6-deoxy-D-glucose. (**B**) In vitro production of QA-TriR-F (**11**) from QA-TriR and UDP-D-glucose. Top, QA-TriR (**9**) incubated with UDP-D-glucose and UGT74BX1 only. The addition of ATCV-1 UGD (which converts UDP-D-glucose to UDP-4-keto-6-deoxy-glucose) resulted in new products anticipated to be QA-TriR-4K6DG (**) and its hydrate (*) (second from top). No conversion of QA-TriR was observed with the addition of the SDR alone (third from top). However, the combination of ATCV-1 UGD and SDR resulted in total conversion of QA-TriR (**9**) to QA-TriR-F (**11**). Mass spectra for the QA-TriR-4K6DG (**) and its hydrate (*) are shown in fig. S47. (**C**) The SDR reduces the QA-TriR-4K6DG product to form QA-TriR-F (**11**). QA-TriR was incubated with UDP-D-glucose in the presence of ATCV-1 UGD and UGT74BX1, resulting in the formation of QA-TriR-4K6DG (**) and its hydrate (*). This enzyme mixture was inactivated by boiling before addition of the SDR. LC-MS analysis of the reaction at 0 min (top), 60 min (middle), and 180 min (bottom) revealed the formation of QA-TriR-F with consumption of QA-TriR-4K6DG (**) and its hydrate (*), demonstrating that the SDR reduces the 4-keto-6-deoxy-glucose attached to QA-TriR to form the D-fucose in QA-TriR-F (**11**). (**D**) Proposed biosynthetic pathway to QA-TriR-F (**11**) from QA-TriR (**9**) and UDP-D-glucose.

(*33*) (fig. S19). We also purified the *Q. saponaria* UGT74BX1 (fig. S19). In a single reaction, we combined UDP-D-glucose with the purified QA-TriR (**9**) product and the *Qs0321910* SDR, ATCV-1 UGD, and UGT74BX1 enzymes. Subsequent LC-MS analysis confirmed the conversion of QA-TriR (**9**) to QA-TriR-F (**11**). We also demonstrated that the production of **11** was dependent on the presence of both ATCV-1 UGD and the *Qs0321910* SDR, consistent with the anticipated pathway (Fig. 6B). Although coincubation of UGT74BX1 and SDR alone did not result in any new products, the combination of UGT74BX1 and ATCV-1 UGD resulted in partial conversion of **9** to a product with a mass consistent with the addition of 4-keto-6-deoxy-D-glucose (hereafter abbreviated as QA-TriR-4K6DG), suggesting that the UGT74BX1 can use UDP-4-keto-6-deoxy-D-glucose as a substrate (Fig. 6B). Furthermore, LC-MS analysis of leaf extracts from plants transiently expressing the QA-TriX-F (**10**) gene set (with the SDR excluded) also revealed a peak with a mass consistent with QA-TriX-4K6DG. This peak was larger than the QA-TriX-F (**10**) peak (fig. S20). A medicagenic acid-3-*O*-glucuronide (MA-GlcA) C-28 D-fucosyltransferase (SOAP6 - UGT74BB2) was recently described from spinach (*9*). Transient expression of this enzyme in *N. benthamiana*, along with the relevant MA-GlcA enzymes, has been reported to yield a new product with the mass of MA-GlcA plus a deoxyhexose (*9*), suggesting that a similar phenomenon may be occurring.

We next attempted to ascertain a direct link between the *Qs0321910* SDR and UDP-D-fucose production in vitro. To this end, UDP-D-glucose was first incubated with ATCV-1 UGD, and the reaction was monitored by NMR. Initially, as anticipated, we observed the formation of UDP-4-keto-6-deoxy-D-glucose. However, the addition of the SDR did not result in the production of UDP-D-fucose (fig. S21) despite clear evidence that the purified *Qs0321910* SDR was functional in our initial in vitro experiment. Furthermore, we were unable to detect UDP-D-fucose after transient expression of the SDR in *N. benthamiana* (fig. S22). The identification of these sugar nucleotides was confirmed with NMR-verified standards.

The failure of the *Qs0321910* SDR to convert UDP-4-keto-6-deoxy-D-glucose to UDP-D-fucose in vitro, coupled with the observation that UGT74BX1 appears to use UDP-4-keto-6-deoxy-D-glucose as a substrate, suggested that our initial model was incorrect. We therefore considered a new model in which UDP-4-keto-6-deoxy-D-glucose may serve as a sugar donor for UGT74BX1, forming the QA-TriR-4K6DG product. The 4-keto-6-deoxy-D-glucose (attached to the QA-TriR) would then be reduced at the C-4 position to give the observed QA-TriR-F (**11**) product. To test this, we performed a modified version of our initial in vitro assay by combining QA-TriR with UDP-D-glucose, ATCV-1 UGD, and UGT74BX1. As before, we observed conversion of QA-TriR to a new product consistent with the addition of 4-keto-6-deoxy-D-glucose, forming QA-TriR-4K6DG. We next heat inactivated the ATCV-1 UGD/UGT74BX1 enzyme mixture before adding the *Qs0321910* SDR. Subsequent LC-MS analysis revealed the conversion of the putative QA-TriR-4K6DG to a new product identified as QA-TriR-F (Fig. 6C). Our results indicate that the SDR encoded by *Qs0321910* SDR does not operate at the sugar nucleotide level, but rather reduces 4-keto-6-deoxy-D-glucose to D-fucose after transfer to the QA-TriR backbone (Fig. 6D). We therefore named this SDR QsFucSyn.

Three further steps for production of QS-7

The enzymes discovered up until this point allowed us to make the advanced saponin pathway heptasaccharide intermediates **16**, **17**, **18**, and **19** (Fig. 5). We next searched for the steps needed to make QS-7 (Fig. 1A). Three additional modifications to the C-28 sugar chain are needed to convert **18** into QS-7, specifically the addition of two sugars, L-rhamnose and D-glucose, and an acetyl group (Fig. 7). During our screen for the terminal C-28 glycosyltransferases, we detected putative glucosyltransferase activity for *Qs0321940* (*UGT91AP1*), and coexpression with the enzyme set for **18** resulted in a product anticipated to be the glucoside of **18** (fig. S23). The gene encoding this enzyme is located within the chromosome 11 biosynthetic gene cluster 45 (Fig. 2D) and is coexpressed with the known QS genes (ranked seventh in table S2; coexpression with *QsbAS1* PCC 0.956). *Qs0321940* may therefore encode a glucosyltransferase implicated in QS-7 biosynthesis (fig. S23). Two more steps would then be required to achieve biosynthesis of QS-7, namely the addition of an L-rhamnose and an acetyl group at the C-3 and C-4 positions of D-fucose, respectively. On the basis of the structures of known saponins from *Q. saponaria*, acetylation appears to precede rhamnosylation (fig. S24) (*24*). We shortlisted 10 candidate *Q. saponaria* BAHD acyltransferase genes on the basis of their levels of coexpression with *QsbAS1* (PCC ≥ 0.9, TPM ≥1600) (table S13), successfully cloned and screened seven for activity toward the full heptasaccharide scaffold **18**, and identified a single enzyme (encoded by *Qs0206480*, PCC 0.900) that generated a product with a mass consistent with addition of an acetyl group (fig. S25). *Qs0206480* (*QsACT1*) is located on chromosome 13 and is not clustered with any of the previously characterized genes. We next screened the remaining unassigned UGT candidates for their ability to modify this putative acetylated substrate and identified two enzymes that gave products that likely corresponded to the addition of either L-rhamnose or D-glucose encoded by *Qs0023500* (*UGT73B44*, ranked 17th in table S2) or *Qs0213660* (*UGT73B43*, ranked 20th in table S2), respectively (fig. S26). These two UGTs belong to subgroup D of the UGT1 family and share 72% amino acid sequence identity. The genes encoding them are not located in predicted biosynthetic gene clusters. Coexpression of these two enzymes, together with the gene set for **18**, did not result in a product featuring both sugars, suggesting that the UGTs compete for the same position (fig. S26). Indeed, saponins featuring either L-rhamnose or D-glucose at the C-3 position of fucose have been isolated from *Q. saponaria* (*24*, *34*, *35*), with QS-7 featuring L-rhamnose. This therefore strongly suggested that *Qs0023500* rhamnosyltransferase is the last outstanding step for QS-7 biosynthesis. We therefore coexpressed the gene set for **18** with the newly discovered candidate glucosyltransferase (*Qs0321940*), acetyltransferase (*Qs0206480*), and rhamnosyltransferase (*Qs0023500*) genes. Subsequent LC-MS analysis revealed a small peak with the same retention time and mass as a QS-7 standard (Fig. 7). Quantification of the QS-7 levels in *N. benthamiana* (7.9 μg/g dry leaf weight) revealed them to be comparable to those found in many tissues of *Q. saponaria*, with the exception of bark, which was about threefold higher (fig. S27). After large-scale infiltration of 410 *N. benthamiana* plants and fractionation by reversed-phase high-performance liquid chromatography (HPLC) (see the materials and methods) ~11 mg of semipure (3 to 5%) QS-7 was obtained. Subsequent 1D and 2D NMR analysis enabled us to assign the structure of this compound as QS-7 (**20**) on the basis of comparison with published data (*34*) (figs. S28 to S43). Furthermore, our recorded ^{1}H NMR spectrum showed complete superimposition with the chemical shifts of a pure QS-7 standard under identical conditions (figs. S44 and S45). Together, these results demonstrate the successful elucidation of the QS-7 pathway and its reconstitution in a heterologous host.

Conclusion

We report the characterization of a total of 14 *Q. saponaria* enzymes that enable the biosynthesis of the advanced heptasaccharide triterpene glycoside intermediates **16**, **17**, **18**, and **19**. We further identify two other enzymes required for efficient glycosylation with the rare sugars D-fucose and D-apiose. A biosynthetic pathway for D-fucose had not previously been characterized despite the widespread occurrence of this sugar in the plant kingdom (*21*). We initially expected the glycosyltransferase UGT74BX1 to add D-fucose to QA-TriR (**9**) (Fig. 5), but we and others found no evidence of this sugar nucleotide in representative dicot plants (*36*). Here, we provide evidence for a different route to D-fucosylation in which UDP-4-keto-6-deoxy-D-glucose serves as the sugar donor for UGT74BX1, with the 4-keto-6-deoxy-D-glucose

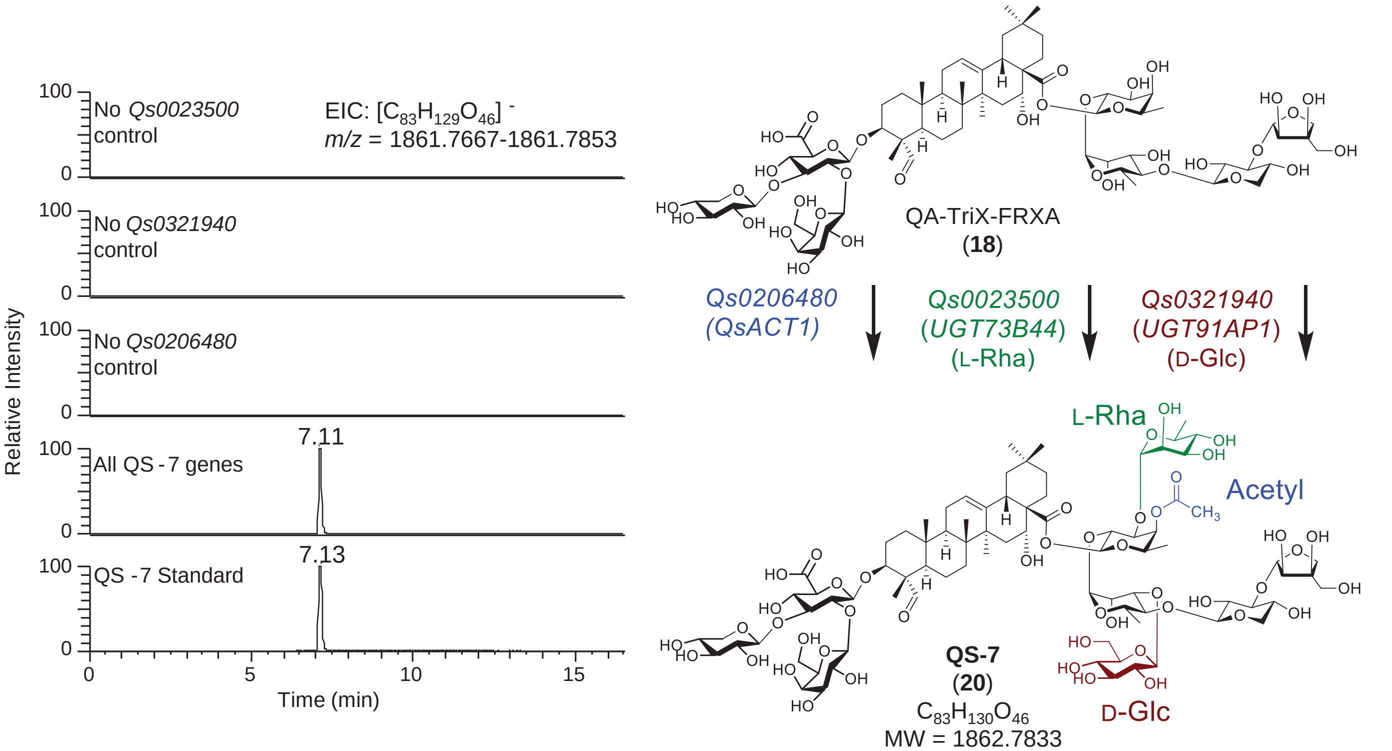


Fig. 7. Production of QS-7. Gene set for production of the core heptasaccharide QA-TriX-FRXA (**18**) was transiently coexpressed in *N. benthamiana*, along with the *Qs0206480*, *Qs032140*, and *Qs0206480* genes. LC-MS of *N. benthamiana* leaf extracts revealed a peak with the exact mass and retention time of an authentic QS-7 (**20**) standard. This peak was absent if any one of the *Qs0206480*, *Qs032140*, or *Qs0206480* genes was omitted. Large-scale infiltration and purification allowed the isolation of a small quantity of semipure QS-7 from *N. benthamiana* and structural confirmation by NMR (tables S14 and S15).

moiety attached at the C-28 position of the saponin scaffold then being subsequently reduced in situ to yield D-fucose. This discovery raises broader questions about the origin of D-fucose moieties found in other plant natural products [e.g., foxglove cardiac glycosides (*37*)].

Using our transient plant expression platform, we have been able to purify all of the QS pathway intermediates from QA to QA-TriR-FRXA in milligram quantities (in some cases tens of milligrams), demonstrating the power of transient plant expression for rapid access to these molecules. We further demonstrate the production of the vaccine adjuvant QS-7 (**20**). QS-7, unlike QS-21, has negligible toxicity toward animal cells (*1*). However, despite its promise as an adjuvant, supply of this saponin is limited by its low abundance in *Q. saponaria* bark extracts. Although the levels of QS-7 in *N. benthamiana* were also low, our work opens up for the first time the possibility of producing QS-7 and other related QS molecules in a heterologous expression system. Clearly, optimization of the biosynthetic process with the aim of attaining commercial-scale production levels is beyond the scope of the current work, but our results now make this a very attractive ambition. The availability of the complete genome sequence and comprehensive transcriptome resources for *Q. saponaria* opens up opportunities to use this "instruction manual" to access QS-21 and a diverse array of other QS saponins. Collectively, these advances will enable investigation of the poorly understood relationship between QS saponin structure and adjuvant activity, and ultimately the generation of designer saponins with optimal immunostimulatory activity and low toxicity through metabolic engineering approaches.

Methods summary

Detailed materials and methods can be found in the supplementary materials.

Q. saponaria plant material and saponin quantification

A *Q. saponaria* sapling (~1 m tall) was obtained from Burncoose Nurseries (Cornwall, UK) and maintained in a glasshouse (24°C, 16 hours light). We gave this plant JIC accession no. S10. Extracts (80% methanol) of freeze-dried tissues (young, mature, and old leaves, primordium, green stem, bark, and root, with four biological replicates) were analyzed using a Thermo Scientific QExactive Hybrid Quadrupole-Orbitrap Mass spectrometer HPLC, and saponin content determined relative to standard curves generated using purified QS-7 and QS-21 samples obtained from Desert King (San Diego, CA, USA).

Generation of sequence resources for Q. saponaria

Genes for the biosynthesis of QA were identified by mining the assembled 1KP transcriptome derived from *Q. saponaria* leaves (downloaded from https://www.onekp.com/public_data.html) for candidate oxidosqualene cyclase (OSC) and CYP sequences using BLASTP. For discovery of the remaining QS pathway genes, we generated de novo transcriptome data for six different *Q. saponaria* tissues using Illumina HiSeq4000 PE150 and a draft genome assembly using PacBio Sequel sequencing. A Hi-C library was prepared using the Phase Genomics Plant Hi-C 2.0 Kit (Seattle, WA) and sequenced with Illumina PE75. The draft contig assembly was scaffolded into 14 pseudomolecules using Phase Genomics Proximo software. After RNA-seq–guided genome annotation, the completeness of the gene space was assessed by BUSCO analysis (*38*).

Cloning and transient expression

Oligonucleotide primers were designed on the basis of predicted gene sequences and flanked with attB sites for Gateway cloning (data S1). RNA extracted from primordia and young leaves

was used for cDNA synthesis. RNA isolation was performed using a Qiagen RNeasy Plant Mini kit with the modified protocol according to (*39*). Candidate sequences were amplified, cloned into pDONR207 using BP clonase (ThermoFisher), and sequenced (Eurofins) before being introduced into the binary expression vector pEAQ-*HT*-DEST1 (*40*) for transient expression in *N. benthamiana*. For ease of performing infiltrations, in some cases, multiple genes were incorporated into a single binary vector using Golden Gate cloning (*41*, *42*). For screening of candidate genes, agro-infiltrations were performed at a small scale using a needleless syringe (*43*, *44*). For purification of compounds, large-scale vacuum infiltrations were performed as described previously (*44*). Leaf material was harvested 5 days after infiltration and frozen at –80°C before lyophilization for 24 to 72 hours. All experiments included coexpression of the truncated feedback-insensitive mevalonate pathway enzyme 3-hydroxy-3-methylglutaryl-CoA reductase (tHMGR) to boost triterpene yield (*44*).

Metabolite analysis

Standards were obtained from the following sources: oleanolic acid was from Merck; echinocystic acid and QA were from Extrasynthese; and QS-7 and QS-21 were from Desert King. The internal standards coprostanol (GC-MS) and digitoxin (LC-MS) were obtained from Merck. Leaf extracts were analyzed by GC-MS or LC-MS depending on the polarity of the compounds under investigation. Full details of the methods used for metabolite analysis, scale-up and purification of compounds for structural determination by NMR, investigation of QsFucSyn activity, and sugar nucleotide analysis are provided in the full materials and methods in the supplementary materials.

REFERENCES AND NOTES

1. C. R. Kensil, U. Patel, M. Lennick, D. Marciani, *J. Immunol.* **146**, 431–437 (1991).
2. A. King, (Chemistry World, 2022); https://www.chemistryworld.com/news/soapbark-branches-out-to-fill-essential-role-in-vaccine-recipes/4015836.article.
3. G. C. Kite, M. J. Howes, M. S. Simmonds, *Rapid Commun. Mass Spectrom.* **18**, 2859–2870 (2004).
4. A. S. Grandón *et al.*, *Nat. Prod. Commun.* **8**, 1697–1700 (2013).
5. L. P. Iglesias, J. G. Castro, V. A. Artze-Vargas, R. O. Peredo, U.S. Patent No. 11,254,699 (2022).
6. S. Copaja, C. Blackburn, R. Carmona, *Wood Sci. Technol.* **37**, 103–108 (2003).
7. K. Miettinen *et al.*, *Nucleic Acids Res.* **46**, D586–D594 (2018).
8. K. Malhotra, J. Franke, *Beilstein J. Org. Chem.* **18**, 1289–1310 (2022).
9. A. Jozwiak *et al.*, *Nat. Chem. Biol.* **16**, 740–748 (2020).
10. Y. Li *et al.*, *Nat. Commun.* **12**, 2563 (2021).
11. R. Xu, G. C. Fazio, S. P. Matsuda, *Phytochemistry* **65**, 261–291 (2004).
12. One Thousand Plant Transcriptomes Initiative, *Nature* **574**, 679–685 (2019).
13. T. Schlotterbeck, M. Castillo–Ruiz, H. Cañon–Jones, R. S. Martín, *Econ. Bot.* **69**, 262–272 (2015).
14. H. Hayashi *et al.*, *Biol. Pharm. Bull.* **24**, 912–916 (2001).
15. K. Miettinen *et al.*, *Nat. Commun.* **8**, 14153 (2017).
16. M. Carelli *et al.*, *Plant Cell* **23**, 3070–3081 (2011).
17. G. Polturak, Z. Liu, A. Osbourn, *Curr. Opin. Green Sustain. Chem.* **33**, 100568 (2022).
18. S. Garcia *et al.*, *Collect. Bot.* **29**, 7–16 (2010).
19. S. B. Cannon *et al.*, *Mol. Biol. Evol.* **32**, 193–210 (2015).
20. S. A. Kautsar, H. G. Suarez Duran, K. Blin, A. Osbourn, M. H. Medema, *Nucleic Acids Res.* **45**, W55–W63 (2017).
21. T. Louveau, A. Osbourn, *Cold Spring Harb. Perspect. Biol.* **11**, a034744 (2019).
22. S. Rahimi *et al.*, *Biotechnol. Adv.* **37**, 107394 (2019).
23. S. Y. Chung *et al.*, *Nat. Commun.* **11**, 5664 (2020).
24. J. D. Fleck *et al.*, *Molecules* **24**, 171 (2019).
25. Y. Yin, J. Huang, X. Gu, M. Bar-Peled, Y. Xu, *PLOS ONE* **6**, e27995 (2011).
26. Y. Kallberg, U. Oppermann, B. Persson, *FEBS J.* **277**, 2375–2386 (2010).
27. Y. Yoshida, Y. Nakano, T. Nezu, Y. Yamashita, T. Koga, *J. Biol. Chem.* **274**, 16933–16939 (1999).
28. T. Oka, T. Nemoto, Y. Jigami, *J. Biol. Chem.* **282**, 5389–5403 (2007).
29. H. Moummou, Y. Kallberg, L. B. Tonfack, B. Persson, B. van der Rest, *BMC Plant Biol.* **12**, 219 (2012).
30. H. W. Choi *et al.*, *Plant Physiol.* **148**, 383–401 (2008).
31. T. Czechowski *et al.*, *Proc. Natl. Acad. Sci. U.S.A.* **119**, e2203890119 (2022).
32. J. Ziegler *et al.*, *Plant J.* **48**, 177–192 (2006).
33. M. Parakkottil Chothi *et al.*, *J. Virol.* **84**, 8829–8838 (2010).
34. S. Guo, L. Kenne, *Phytochemistry* **54**, 615–623 (2000).
35. S. Guo, L. Kenne, *Phytochemistry* **55**, 419–428 (2000).
36. M. Pabst *et al.*, *Anal. Chem.* **82**, 9782–9788 (2010).
37. W. Kreis, A. Hensel, U. Stuhlemmer, *Planta Med.* **64**, 491–499 (1998).
38. M. Manni, M. R. Berkeley, M. Seppey, F. A. Simão, E. M. Zdobnov, *Mol. Biol. Evol.* **38**, 4647–4654 (2021).
39. D. J. MacKenzie, M. A. McLean, S. Mukerji, M. Green, *Plant Dis.* **81**, 222–226 (1997).
40. F. Sainsbury, E. C. Thuenemann, G. P. Lomonossoff, *Plant Biotechnol. J.* **7**, 682–693 (2009).
41. C. Engler, R. Kandzia, S. Marillonnet, *PLOS ONE* **3**, e3647 (2008).
42. E. Weber, C. Engler, R. Gruetzner, S. Werner, S. Marillonnet, *PLOS ONE* **6**, e16765 (2011).
43. F. Sainsbury, P. Saxena, K. Geisler, A. Osbourn, G. P. Lomonossoff, *Methods Enzymol.* **517**, 185–202 (2012).
44. J. Reed *et al.*, *Metab. Eng.* **42**, 185–193 (2017).

ACKNOWLEDGMENTS

We thank M. Stocks and G. Pope (PBL Technology) for advice and support; R. Melton and M. Ambrose (JIC) for help in sourcing plant material; JIC Horticultural Services for assistance with plant cultivation; the JIC Metabolomics, NMR, and Chemistry platforms for assistance with instruments and method development; Norwich Bioscience Institutes (NBI) Research Computing for computational support; D. Nelson and the UGT Nomenclature Committee for formal assignment of the *Q. saponaria* CYPs and UGTs, respectively; and R. Field and our industrial collaborators for their comments and productive discussions. **Funding:** This work was supported by JIC Innovation Fund Award KEC IF29 2018 AO29 (A.Os.); Biotechnological and Biological Sciences Research Council (BBSRC) Super Follow-on-Fund award BB/R005508/1 (R.C.M., S.K., A.E.-D., and A.Or.); industrial funding (J.R., R.C.M., S.K., A.E.-D., C.O., M.R., and A.Or.); joint Engineering and Physical Sciences Research Council/ Biotechnological and Biological Sciences Research Council (BBSRC)-funded OpenPlant Synthetic Biology Research Centre grant BB/ L014130/1 (M.S. and A.Os.); and the John Innes Foundation (C.O. and A.Os.), and the BBSRC Institute Strategic Programme Grant "Molecules from Nature – Products and Pathways" (BBS/E/J/000PR9790 to T.L. and A.Os.). **Author contributions:** J.R. and A.Os. conceived and designed the project. L.M. performed QS-21 and QS-7 profiling of *Q. saponaria* tissues, QS-7 quantification in *N. benthamiana*, and generation of transcriptome resources. J.R. and L.M. performed purification of genomic DNA. A.H. prepared the Hi-C library. C.O., A.H., and J.L.-M. performed computational analysis of the genome assembly. C.O., A.Or., J.R., L.M., and T.L. performed bioinformatics analysis (including gene discovery, coexpression analysis, and phylogenetics). J.R., A.Or., L.M., T.L., and S.K. performed cloning and screening of candidate enzymes. R.C.M. generated the GoldenGate vectors. J.R. and M.S. performed the initial scale-up of QA production and NMR analysis. A.E.D. performed the full scale-up, purification, and structural analysis of pathway intermediates and QS-7. A.C.M. performed karyotyping. S.K. performed the enzyme purification and in vitro glycosylation assays. M.R. performed the synthesis, purification, and NMR analysis of sugar nucleotides. M.R. and J.R. performed the sugar nucleotide profiling. J.R. and A.Os. wrote the manuscript with input from all authors. **Competing interests:** J.R., A.Or., T.L., L.M., and A.Os. are inventors of patents arising from this work. The remaining authors declare no competing interests. **Data and materials availability:** The fully assembled and annotated *Q. saponaria* genome sequence has been deposited under NCBI BioProject ID PRJNA914519. RNASeq reads are deposited under NCBI BioProject ID PRJNA914309 (SRA accessions SRR22829626 - SRR22829649). The sequences of the genes characterized in this study can also be found in GenBank as follows: *QsbAS1* (*Qs0315350*), OQ107256; *CYP716A224* (*Qs0259300*), OQ107260; *CYP716A297* (*Qs0322000*), OQ107248; *CYP714E52* (*Qs0148690*), OQ107266; *CSLM1* (*Qs0321900*), OQ107253; *CSLM2* (*Qs0000870*), OQ107265; *UGT73CU3* (*Qs0123860*), OQ107259; *UGT73CX2* (*Qs0283850*), OQ107255; *UGT73CX1* (*Qs0283870*), OQ107254; *UGT74BX1* (*Qs0321930*), OQ107250; *UGT91AR1* (*Qs0321920*), OQ107251; *UGT91AQ1* (*Qs0234120*), OQ107264; *UGT73CY3* (*Qs0234130*), OQ107263; *UGT73CY2* (*Qs0234140*), OQ107262; *UGT73B44* (*Qs0023500*), OQ107261; *UGT91AP1* (*Qs0321940*), OQ107249; *UGT73B43* (*Qs0213660*), OQ107257; *Apiose/xylose synthase* (*Qs0088320*), OQ107247; *QsFucSyn* (*Qs0321910*), OQ107252; and *QsACT1* (*Qs0206480*), OQ107258. All of the above *Q. saponaria* genes characterized in this study are available as expression constructs (either as DNA preparations or in the relevant microbial strains) from A.Os. under a material transfer agreement with Plant Bioscience Ltd.

License information: Copyright © 2023 the authors, some rights reserved; exclusive licensee American Association for the Advancement of Science. No claim to original US government works. https://www.science.org/about/science-licenses-journal-article-reuse

SUPPLEMENTARY MATERIALS

science.org/doi/10.1126/science.adf3727
Materials and Methods
Figs. S1 to S53
Tables S1 to S16
References (*45*–*69*)
Data S1 to S5
MDAR Reproducibility Checklist

View/request a protocol for this paper from *Bio-protocol*.

Submitted 18 October 2022; accepted 2 February 2023
10.1126/science.adf3727

WORKING LIFE

By **Jessica Larsen**

Embrace compassion

"Do we have permission to give your father a blood transfusion? A tracheotomy?" I was a 19-year-old college student. My father had fallen into a coma a few weeks earlier and I was his next of kin, responsible for his medical decisions. Suddenly I was spending my weekends driving to the hospital 3 hours away in friends' borrowed cars after spending the week juggling coursework, a part-time job, and phone calls from the hospital, sometimes during class or in the middle of the night. I told my professors the general outline of what was going on so I could leave class when my father's doctors called, but for the most part I kept my struggles private. I wanted to be seen as strong and capable, and I worried my professors would think I was making excuses.

The call about the blood transfusion and tracheotomy came the night before an exam. The blood transfusion was an easy decision; it is a relatively safe procedure. The tracheotomy was another story. I had to decide how my father would feel if he came out of his coma and had a hole in his throat for the rest of his life. Ultimately, I declined.

After a few hours of restless sleep, I was hardly in a state to take the exam. I told my professor what had happened the previous night and requested an alternative exam date, which was denied. My score on that exam reflected the turmoil I was going through, not my knowledge of the material. This experience made me even more reluctant to be vulnerable and honest about my struggles. When I soon had to make the devastating decision to take my father off life support, I only told a few trusted mentors.



"I have learned to value my students' growth and learning over others' perceptions."

Despite that trauma, I was able to make it through my studies and, 8 years later, I became a professor myself. As a new faculty member, I felt I needed to adopt a tough classroom persona to earn my colleagues' respect and keep students from taking advantage of me. My demeanor wasn't unlike that of the professor who denied me the exam extension years earlier, and it did not reflect my actual character.

Then, the pandemic hit. I was too tired to keep up the act, and my students needed compassion and support. So, I shared the story about my father's illness and death to acknowledge that life goes on outside of my classroom and grades are not the most important thing in the world. I told my students I knew they might be suffering and wanted them to know that if they came to me needing help, I would understand.

The response was immediate and powerful. Students became unafraid to share their stories with me and ask for support. My connections with them deepened and I could mentor them on a new level. I changed nothing about the way I delivered course material, but student exam scores improved, as did my teaching evaluations. Students could see that although the class was rigorous and I pushed them to learn the material, I cared about their well-being and wanted them to succeed.

Some of my colleagues perceive me as being "too close" to the students and think my class is not rigorous enough. In the past, I worried such impressions would affect my chance for promotion and advancement. But I have learned to value my students' growth and learning over others' perceptions.

A fellow professor recently asked me, "If this works so well, why didn't you do it sooner?" All I can say is that vulnerability is really hard. It involves sharing of yourself as fully as you are able, including admitting wrongdoing and acknowledging that you can't always be your best self. Far from being a sign of weakness, it requires a ton of strength.

Exposing your imperfections, connecting with students on a deeper level, and creating space for them—and you—to grow will always be challenging, but it is worth it. I cannot know everything that is going on in every student's life, but I can always choose compassion. ■

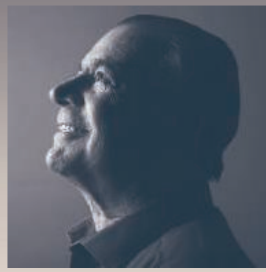
Jessica Larsen is a professor at Clemson University. Send your career story to SciCareerEditor@aaas.org.

ILLUSTRATION: ROBERT NEUBECKER

Your Legacy to Science

AN ESTATE GIFT TO THE
AMERICAN ASSOCIATION FOR THE ADVANCEMENT OF SCIENCE





Since 1848, our founding year, the American Association for the Advancement of Science (AAAS) has been deeply committed to advancing science, engineering and innovation around the world for the benefit of all people.

By making AAAS a beneficiary of your will, trust, retirement plan or life insurance policy, you become a member of our 1848 Society, joining Thomas Edison, Alexander Graham Bell and the many distinguished individuals whose vision led to the creation of AAAS and our world-renowned journal, *Science*, so many years ago.

Unlike many of its peers, *Science* is not for-profit. Your estate gift would provide long-term financial stability and durable annual income that will support operations and competitive innovation for years to come. **This support is vital.**

"As a teacher and instructor, I bear responsibility for the younger generations. If you have extra resources, concentrate them on organizations, like AAAS, that are doing work for all."

—Prof. Elisabeth Ervin-Blankenheim, 1848 Society member

If you intend to include AAAS in your estate plans, provide this information to your lawyer or financial adviser:

Legal Name: American Association for the Advancement of Science
Federal Tax ID Number: 53-0196568
Address: 1200 New York Avenue, NW, Washington, DC 20005

If you would like more information on making an estate gift to AAAS, cut out and return the form below or send an email to philanthropy@aaas.org. Additional details are also available online at **www.aaas.org/1848Society**.

1848 SOCIETY AAAS

cut here

Yes, I would like more information about joining the AAAS 1848 Society.

PLEASE CONTACT ME AT:

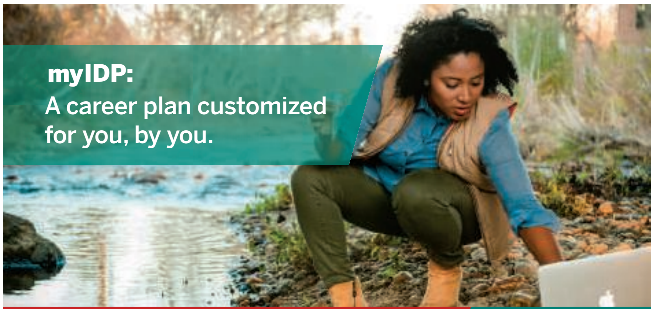
Name: ____________________

Address: ____________________

City: ____________ State: ______ Zip code: ________ Country: ______

Email: ____________________ Phone: ____________

RETURN THIS FORM TO:
AAAS Office of Philanthropy and Strategic Partnerships • 1200 New York Avenue, NW • Washington, DC 20005 USA



For your career in science, there's only one Science

Features in myIDP include:

- Exercises to help you examine your skills, interests, and values.
- A list of 20 scientific career paths with a prediction of which ones best fit your skills and interests.

myIDP

Visit the website and start planning today!
myIDP.sciencecareers.org

ScienceCareers AAAS In partnership with:

FASEB Federation of American Societies for Experimental Biology
UMASS University of Massachusetts Medical School
UCSF University of California San Francisco
UIC
BURROUGHS WELLCOME FUND

UNIVERSITY OF IOWA CARVER COLLEGE OF MEDICINE
University of Iowa Health Care

CHAIR, DEPARTMENT OF BIOCHEMISTRY AND MOLECULAR BIOLOGY
THE UNIVERSITY OF IOWA
ROY J. AND LUCILLE A. CARVER COLLEGE OF MEDICINE

The Carver College of Medicine at the University of Iowa seeks candidates for the position of **Chair and Department Executive Officer, Department of Biochemistry and Molecular Biology**. The successful candidate will be a nationally prominent academic leader with a strong record of achievement in research, education, and mentorship. The UI Department of Biochemistry and Molecular Biology has a distinguished research and teaching faculty, and a nationally recognized research program, with outstanding faculty who are national and international leaders in their respective research areas. The department encompasses a diverse set of research programs spanning mechanisms of DNA repair, Gene Expression, Protein Trafficking, Signal Transduction, and Molecular Dynamics, Metabolism and Cellular Organization. Strong core facilities for protein crystallography, NMR, and single-molecule biochemistry underpin the research of the department. The department supports the training of medical students, educators, and researchers through its long-standing PhD graduate program, and the department serves as a home for undergraduate majors in Biochemistry.

The search committee will accept nominations and applications until the position is filled. Applications should include a current curriculum vitae and/or biosketch, as well as a cover letter outlining the candidate's interest in the position, as well as the attributes and qualifications making them suitable for the role. Cover letters including statements on administration experience, teaching philosophy, faculty mentorship, and a commitment to diversity, equity, and inclusion are strongly encouraged. Confidential inquires regarding this position can be addressed to the search committee chair.

To apply for this position, visit our website at:
https://jobs.uiowa.edu/jobSearch/facultyDetailDisplay.php?requisitionNumber=74746&fromComm=Y
(Requisition #074746)

The University of Iowa is an equal opportunity/af rmative action employer. All quali ed applicants are encouraged to apply and will receive consideration for employment free from discrimination on the basis of race, creed, color, religion, national origin, age, sex, pregnancy (including childbirth and related conditions), disability, genetic information, status as a U.S. veteran, service in the U.S. military, sexual orientation, gender identity, or associational preferences.

